Microwave and millimeter radiometry for the characterization and quantification of ice and snow clouds

Victoria Sol Galligani

THÈSE

PRÉSENTÉE À

L' OBSERVATOIRE DE PARIS

ÉCOLE DOCTORALE D'ASTRONOMIE ET D'ASTROPHYSIQUE D'ILE DE FRANCE

PAR **Victoria Sol GALLIGANI**

POUR OBTENIR LE GRADE DE: **DOCTEUR EN PHYSIQUE**

LA RADIOMÉTRIE MICRO-ONDE ET MILLIMÉTRIQUE POUR LA CARACTÉRISATION ET QUANTIFICATION DES NUAGES DE GLACE ET DE LA NEIGE

DIRECTRICE DE RECHERCHE: **Catherine PRIGENT, LERMA**

CO-DIRECTEUR DE RECHERCHE: **Carlos JIMENEZ, LERMA**

SOUTENUE À PARIS LE 14 JANVIER 2014 DEVANT LE JURY COMPOSÉ DE

1. Didier PELAT ..... Président
2. Hélène CHEPFER ..... Rapporteuse
3. Jean-Pierre CHABOUREAU ..... Rapporteur
4. Thérèse ENCRENAZ ..... Examinatrice
5. Patrick ERIKSSON ..... Examinateur
6. Julien DELANOË ..... Examinateur
7. Catherine PRIGENT ..... Directrice
8. Carlos JIMENEZ ..... Co-directeur

l'Observatoire de Paris | LERMA

Laboratoire d'Etude du Rayonnement et de la Matière en Astrophysique

Thèse cofinancée par le CNES et Astrium

LERMA - Laboratoire d'Etude du Rayonnement et de la Matière en Astrophysique

A mi papá, en sus gabinetes espaciales ...

This document is based on a modified version of a LaTeX template provided *Prof. Johan Carlson.*

Abstract

The quantification of the cloud frozen phase on a global basis is essential to fully capture and quantify the Earth energy budget and the Earth hydrological cycle. The estimation of frozen quantities from remote sensing, however, is still at a very early stage and remains one of the most important challenges for future satellite observations. The main reason for the difficulties encountered in detecting ice and snow signatures from space is the complex variability and lack of parameterizations of the microphysical properties, and thus radiative properties, of the frozen particles.

The work developed in this thesis aims at contributing to the scientific efforts needed in order to constrain such assumptions, by developing an understanding of the sensitivity of microwave and millimeter satellite observations to the microphysical properties of the frozen phase, specifically snow. Current microwave and millimeter observations are interpreted via radiative transfer simulations, mainly for passive observations, but active measurements are also considered. The Advanced Radiative Transfer Simulator (ARTS) is selected to solve the radiative transfer equation for a scattering medium, coupled with a number of tools that were developed during this thesis and allow the simulation of realistic scenes for passive and active microwave simulations. The development of such tools allowed two main studies to be pursued: (1) the analysis and interpretation of specific polarized scattering signatures over ice and snow clouds, and (2) the simulation of realistic passive and active microwave responses over ice and snow clouds, and their evaluation with satellite observations.

Polarized scattering signatures over ice and snow clouds are observed with conical imagers such as TMI and the recently launched MADRAS onboard Megha-Tropiques. Polarized observations are carefully analyzed with ancillary data and are interpreted with radiative transfer simulations. We show that this signal can be related to horizontally aligned mixed phase spheroids. Its sensitivity to changes in particle size, phase, shape and orientation, from solid ice to dry snow to melting snow, are assessed. The analysis of the first polarized passive observations at close-to-millimeter frequencies (157 GHz) with MADRAS and its interpretation with radiative transfer calculations, provides a unique opportunity to validate the importance of horizontally aligned mixed phase spheroids in the generation of polarized scattering signatures and the importance of higher frequency observations for the analysis of the frozen phase.

Finally, the radiative transfer ARTS code is coupled to a meso- scale cloud model (Meso-NH), to simulate consistently coincident active and passive observations of real atmospheric cases. The sensitivity of active and passive simulations to different microphysical parameters of the frozen phase are assessed. It is shown that hydrometeor

quantities simulated by Meso-NH can be used to simulate reasonable scattering in the presence of snow when using adequate microphysical hypothesis to calculate the single scattering properties. This is an important step towards building a robust database of simulated measurements to train a statistically base retrieval scheme.

Key words: remote sensing, radiative transfer, active/passive synergy, microwave radiometry, clouds

PUBLICATIONS

- V. S. Galligani, C. Prigent, E. Defer, C. Jimenez, and P. Eriksson. The impact of the melting layer on the passive microwave cloud scattering signal observed from satellites: A study using TRMM microwave passive and active measurements. *J. Geophys. Res. Atmos.*,118, 56675678, doi:10.1002/jgrd.50431.

- E. Defer, V. S. Galligani, C. Prigent, C. Jimenez. First observations of polarized scattering over ice clouds at close-to-millimeter frequencies (157GHz) with MADRAS on board Megha-Tropiques. *Submitted to J. Geophys. Res. Atmos. (Dec. 2013).*

- V. S. Galligani, C. Prigent, P. Eriksson, E. Defer, C. Jimenez, J.-P. Chaboureau, J.-P. Pinty. Meso-scale modeling and radiative transfer simulations of a snowfall event over France at microwave frequencies, both in passive and active modes, and their evaluation with satellite observations. *To be submitted.*

Contents

Acknowledgments

There aren't enough words to express my thanks to Catherine Prigent for her support, encouragement, and assistance in my research, but specially in the moments that life has chosen me to go through. I am forever grateful. I would also like to thank Carlos Jimenez and Eric Defer for their valuable time, advice and suggestions. Their help and discussions have greatly helped me throughout my PhD. Outside our group at LERMA, I would like to thank Patrick Eriksson who was always enthusiastic about scientific cooperation and for the valuable time he dedicated to my work. His help and inputs, specially concerning the Atmospheric Radiative Transfer Simulator, were very important for me. I would also like to thank Stefan Buehler for valuable advice, and the ARTS community for providing an open source software that I extensively used during my thesis. On a personal level, I wish to thank Jana with whom I shared the PhD 'student experience'.

En esta etapa Parisina conocí a gente muy valiosa y solo quería agradecerles genuinamente por lo vivido juntos. *"Todos soltamos un hilo, como los gusanos de seda. Roemos y nos disputamos las hojas de la morera pero ese hilo, si se entrecruza con otros, si se entrelaza, puede hacer un hermoso tapiz, una tela inolvidable"*. A Rafael Andreotti. A Marian, Manu, Virgi, Olivier, Diego, Gabo, Elide, Javi, Magdalena, Candela, Sergio, Shazline, y al Fuji team. A mi amiga Gabi. A Bruna y los discos de Beach House escuchados.

Pero ante todo a mi familia. A mis abuelos Mario y Ester, a mis hermanos Guido y Sofia, a mi mamá, a quien admiro profundamente por su grandeza y fortaleza, y a mi papá, por todo lo tuyo que trasciende en mi. Te dedico modestamente este trabajo, por todos los esfuerzos que hiciste con mamá, siempre pensando en nosotros, y que jamás pesaron como un esfuerzo para ustedes.

Chapter 1

Introduction

1.1 Satellite Remote Sensing

Atmospheric *satellite remote sensing* has evolved into an essential tool to probe the Earth's atmosphere, ocean and land surfaces. In the past decades, satellite remote sensing has greatly improved weather forecasting and our understanding of many atmospheric processes thanks to the continuous monitoring of the Earth's system that satellite measurements offer. Remote sensing involves observing objects indirectly. This means that the quantity measured is some function of the parameter that is actually required. In atmospheric remote sensing the electromagnetic radiation emerging from the atmosphere can be measured to obtain different meteorological quantities. This is very important for Numerical Weather Prediction (NWP) models because they need an accurate description of atmospheric constituents and surface parameters continuously and on a global basis. Satellite observations can also be used to evaluate and validate climate model outputs.

Measurements of the atmosphere can be performed by both in situ and remote sensing techniques. These two approaches are, to a large extent, complementary. While in situ data normally have high accuracy and fine spatial resolution, the temporal and geographical coverage is poor. For example, in situ measurements with radiosondes or with aircraft-borne sensors provide the most detailed information, but the validation of NWP and climate models requires global data with long time coverage. For economical and practical reasons, this cannot be achieved with in situ measurements. Satellite-borne instruments, in contrast, can provide frequent global measurements of the atmosphere on a long-term basis. There are two types of observations: passive observations where the natural radiation emitted or reflected by the ensemble Earth/Earth's atmosphere is measured, or active observations where energy is emitted from the satellite in order to measure the radiation reflected or backscattered by the target. Most remote sensing instruments operate in the visible, near infrared, infrared or microwave band (Figure 1.1). Their response depends both on the parameters of the instrument and on the properties of what is being observed.

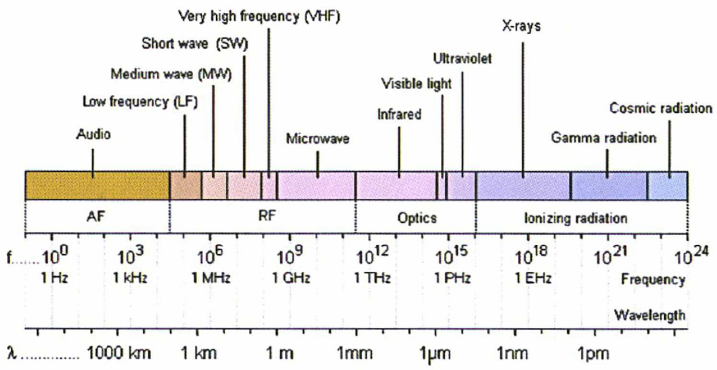

Figure 1.1: The electromagnetic spectrum with wavelength and frequency on a logarithmic scale from 0.1 Hz to 10^{24} GHz. From Kuphaldt (2007).

Since remote sensing is an indirect technique, i.e. meteorological quantities are not obtained directly from the measurements, an inversion is necessary. An inversion, or retrieval, is

the conversion of measurements to geophysical quantities. Retrievals are said to be an ill-posed problem, meaning that the solutions are not unique. Retrievals are therefore a question of finding the best representation of the required parameter given the measurements made, together with any appropriate prior information that may be available about the Earth system and the measuring device. Retrievals of geophysical quantities are accomplished by developing physically or statistically based algorithms. Such retrieval schemes are often developed from datasets consisting of simulated observations via a forward model, and their corresponding atmospheric parameters. The quality of the statistical dataset is essential: the variability described in the dataset should represent as correctly as possible the different atmospheric states of the region of interest. The different parameters can then be inferred from retrieval algorithms applied to a set of observations. In short, a complete forward model and a correct retrieval method are essential to estimate atmospheric parameters from satellite observations.

1.2 The Importance of Detecting and Estimating Frozen Hydrometeors from Microwave Remote Sensing

Remote sensing of clouds is of interest because they play a crucial role in both weather and climate through their impact on the Earth's energy budget and on the Earth's precipitation and hydrological cycle.

Pure ice clouds play a significant role in the extra-tropical hydrological cycle with at least 20% of the globe covered by these type of clouds (Buehler et al., 2007a). Snow constitutes a large percentage of surface precipitation in these areas, and is also commonly found in higher altitudes closer to the equator (Leinonen et al., 2012). This is evident from Figure 1.2 which shows the precipitation rate category as derived from a climatology based on oceanic surface observations. Furthermore, snowfall is a driver for many processes that have a direct impact on human activities, and is thus of socio-economic importance. Misrepresentations of upper atmospheric ice and snow clouds (hereafter frozen hydrometeors) lead to uncertainties in weather and climate forecasts, and in climate change projections. Cloud feedbacks remain the largest source of uncertainty in determining Earth's climate sensitivity, especially to a doubling of carbon dioxide, as published in the Intergovernmental Panel on Climate Change (IPCC) Fourth Assessment Report (IPCC AR4) (IPCC, 2007).

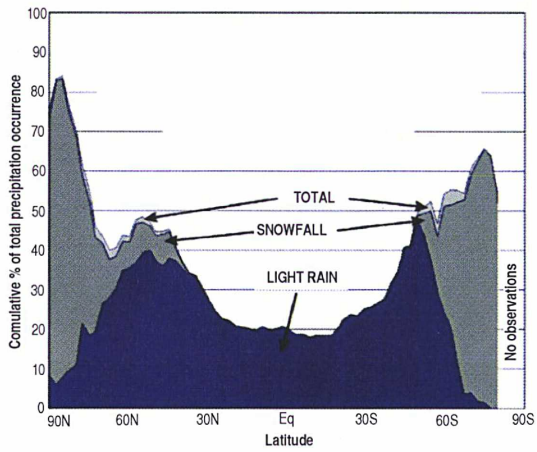

Figure 1.2: Precipitation rate category as a function of latitude as illustrated by Mugnai et al. (2007).

Ice and snow species have a large impact on the atmospheric radiation budget since they cool the atmosphere by reflecting incoming solar radiation, but also heat the atmosphere by absorbing and re-emitting outgoing terrestrial radiation. Their net radiative impact depends on factors such as cloud top temperature, vertical and horizontal extent, cloud optical thickness,

effective radius, and particle shapes (Eliasson et al., 2011).

While satellite-based rain rate retrievals are at a rather mature stage (e.g. Kummerow et al., 2000; Kawanishi et al., 2003; Ferraro et al., 2005), the measurement of snowfall rates from space is a relatively new field. Visible and IR techniques are not able to penetrate deeply within *thick* cloud structures and are sensitive only to the cloud top, but rainfall can roughly be inferred from this information. IR techniques are used only for relatively thin cirrus clouds, but such clouds constitute approximately half of all high clouds. In contrast, microwave radiometry has shown a promising ability in ice and snow cloud observations as it is able to penetrate and provide insight into the vertical profiles of most clouds. Microwave instruments, however, became available later than IR and visible observations. Figure 1.3 illustrates the sensitivity of infrared and microwave techniques to cloud structures.

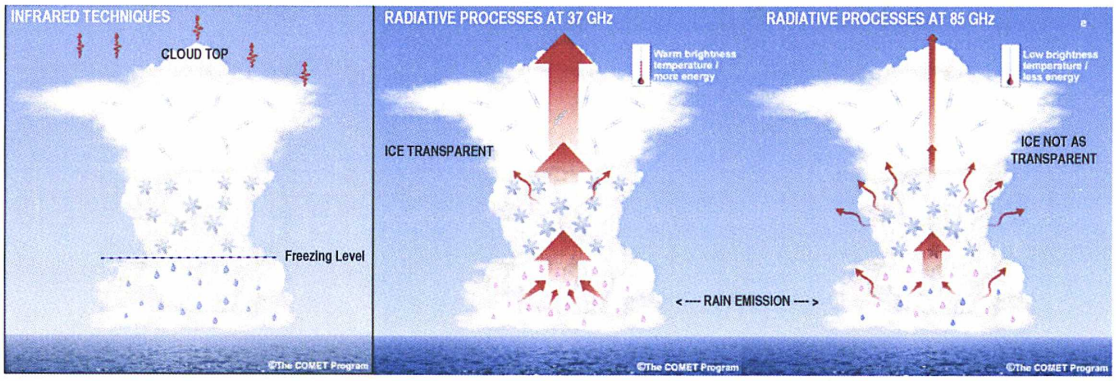

Figure 1.3: Schematic of infrared and microwave remote sensing of clouds (adapter from The COMET Program).

At low microwave frequencies (roughly below 60 GHz) microwave radiation is essentially sensitive to the emission from clouds. At higher frequencies, scattering processes also take place and can provide additional information on the cloud ice phase. Passive microwave observations are dependent on (1) gaseous absorption and emission; (2) absorption, emission and scattering from hydrometeors; and (3) surface reflection and scattering. Changing the observation frequency will change the observed upwelling radiation via changes in the sensitivity of the interaction mechanisms as shown in Figure 1.3. At high microwave frequencies frozen hydrometeors scatter the upwelling thermal radiation and this reduces the observed radiation. This reduction in the observed signal is used to detect and quantify ice and snow clouds in the microwave. For this reason, recent studies have shown the interest of microwave and the higher frequency millimeter and sub-millimeter observations for cloud and precipitation characterization (Buehler et al., 2007b; Jiménez et al., 2007; Defer et al., 2008). It is very important to have a good understanding of the interaction between microwave radiation and cloud and precipitating particles that are observed to fully, and correctly, exploit the observational power that current missions have and future missions will further add. Adding an ice clouds and snowfall retrieval capability for such sensors will enhance their remote sensing performance and provide a more complete characterization of the vertical atmospheric column. Properly characterizing the frozen phase is also essential for effectively incorporating microwave radiances

under cloudy and precipitating conditions in operational weather prediction. Its detection and quantification, however, is far from evident due to the variable structure of frozen hydrometeors in time and space. Measuring snow and snowfall from space is a major challenge in present climate studies, and has become a hot topic in the light of future missions. Despite recent efforts, frozen hydrometeor measurements are still difficult to obtain owing to the challenges involved in remotely sensing ice water vertical profile.

1.3 Uncertainties of the Frozen Phase in Numerical Weather Prediction, Climate Models and Satellite Retrievals

Most NWP models and climate models contain liquid and ice water content (LWC and IWC) as prognostic variables [1]. However, these models contain considerable uncertainties and over simplifications. These are largely introduced by assumptions on the microphysical properties that directly influence ice fall velocity, e.g., ice particle size, mass, and cross-sectional area (Buehler et al., 2007a; Heymsfield and Iaquinta, 2000). These uncertainties lead to misrepresentations of upper tropospheric ice and snow clouds (Kim et al., 2008; Protat et al., 2010).

Reitter et al. (2011) evaluated the microphysical assumptions in the global NWP model of the German Wether Service (GME) with respect to CloudSat data and showed that the low parameterised fall speed of snow directly overestimated the vertically integrated IWC, the ice water path (IWP), and also the snow water path (SWP). Figure 1.4 shows the IWP and SWP zonal averages for three different fall speed parameterisations. As expected, the faster falling snow leads to a reduction of SWC. Globally averaged, this amounts to a reduction of mean SWP from 81 gm^{-2} to 62 gm^{-2} using a density correction of the fall speed, and a further reduction to 40 gm^{-2} using an increased and more realistic fall speed based on previous studies.

Another approach to evidence the importance of constraining the assumptions in NWP models and climate models are inter-comparison studies on the climatologies of IWP outputs from different climate models. In a comparison of the climatologies of 10 years of the IPCC AR4 climate model outputs, John and Soden (2006) showed that the zonal annual mean IWP varies by up to an order of magnitude. Large differences in IWP model outputs are illustrated in Figure 1.5, from a similar study by Eliasson et al. (2011). The discrepancies in the model-predicted IWP response to a CO_2 doubling are even more striking as even the sign of the response is uncertain, i.e., some models predict an increase of IWP at certain latitudes where others predict a decrease. Similarly, Waliser et al. (2009) presents a comparisons of the global averaged, annual mean values of different physical climate quantities, including IWP. In this paper, quantities such as precipitation and water vapour are shown to be fairly in agreement between models. These quantities have had relatively robust long-standing observational constraints. In contrast, Waliser et al. (2009) shows that the globally averaged, annual mean IWP

[1] The term *prognostic* is given to variables that are directly predicted by the model by integration of a physical equation, in contrast to *diagnostic variables* that are obtained from the model's prognostic variables.

currently deviates by a factor of 20.

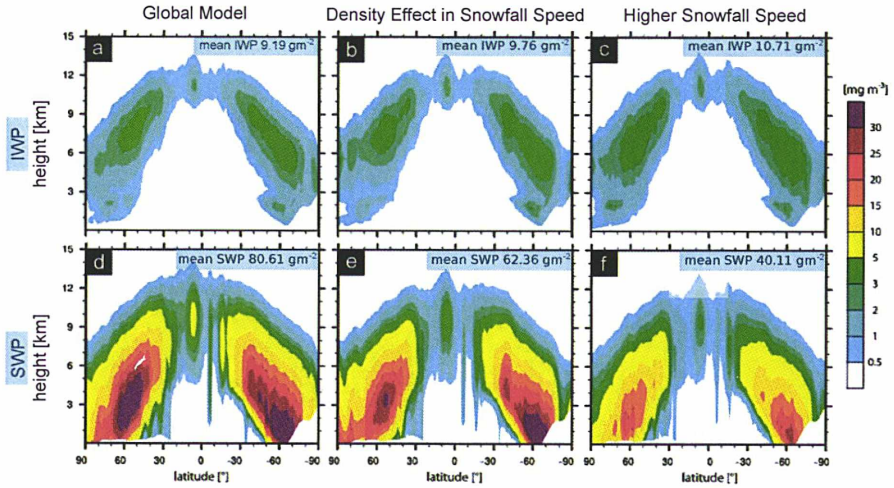

Figure 1.4: IWC and IWP zonal averages from the global NWP model of the German Wether Service (GME) for a 25 day period. Left Column: GME control simulation, middle column: GME simulations with a density correction to the fall speed correction, right column: GME simulations with an increased more realistic fall speed. From Reitter et al. (2011).

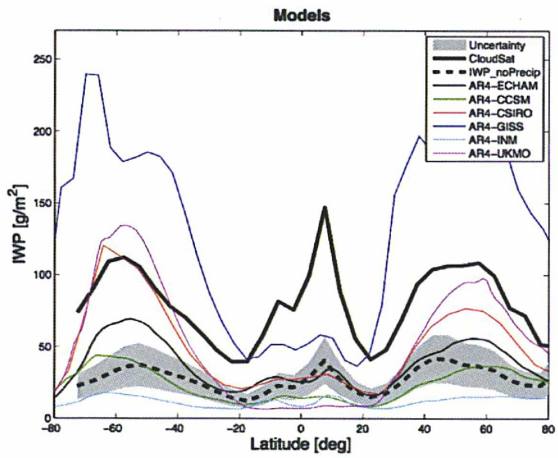

Figure 1.5: Ocean-only IWP zonal averages for climate models calculated from 100 years of monthly mean data. A factor 0.5 is applied to AR4-GISS in order to visualise it better (from Eliasson et al. (2011)). Note that two CloudSat products (CloudSat and IWP_noPrecip on the legend) are shown for reference. CloudSat represents CloudSat's IWP 2B-CWC-RO dataset and IWP_noPrecip represents CloudSats IWP product without profiles flagged to contain precipitation at the surface.

The most valuable source of information that can be used to potentially constrain NWP and climate models is global satellite data, but the satellite datasets also have large differences. There are many satellite datasets available, both active and passive, that provide an IWP retrieved product with a temporal coverage as long as 25 years. The instruments in these datasets cover a frequency range extending from the microwaves to the visible. Such frequency range provides different sensitivities to different parts of the vertical cloud structure as seen in Figure 1.6. The retrieval accuracy is usually limited by the uncertainties made in the cloud microphysical assumptions (Ekström et al., 2008). Even the definition of IWP itself is problematic. Some NWP and climate models make a clear distinction between precipitating ice particles and suspended cloud ice particles, whereas satellite retrieved IWP products are usually a mixture of both (Eliasson et al., 2011). Waliser et al. (2009) illustrated qualitatively the large level of disagreement between global datasets of satellite retrieved cloud properties. This study was extended by Eliasson et al. (2011) who provided a more quantitative approach, as shown in Figure 1.7 where the zonal mean IWP for the satellite datasets are compared on a common period. Figure 1.7 illustrates the large differences in the IWP between the satellite datasets. The lack of adequate cloud property measurements with which to constrain models is also a problem for retrievals.

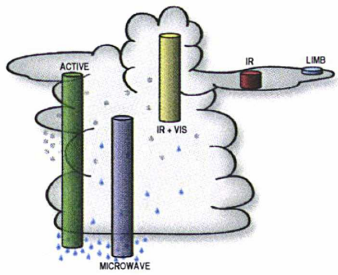

Figure 1.6: The columns indicate approximately where in the vertical cloud the different measurement techniques are sensitive (Eliasson et al., 2011).

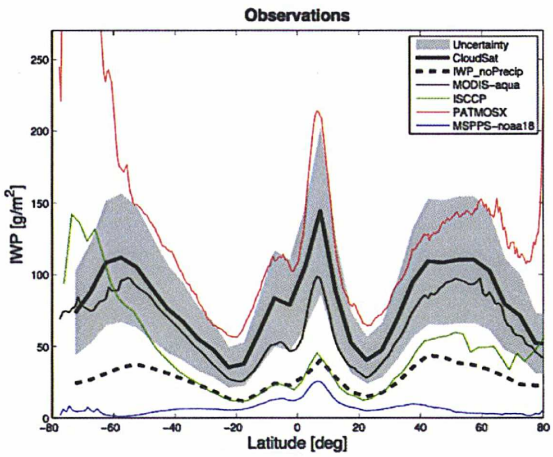

Figure 1.7: IWP ocean-only zonal averages of IWP from satellite datasets. The grey shaded area is the uncertainty interval.The averages are for the period July 2006 to April 2008 (Eliasson et al., 2011). Note that CloudSat and IWP_noPrecip in the legend are as described in Figure 1.5.

1.4 Microwave Remote Sensing of Ice Clouds and Snowfall

1.4.1 Instrument Timeline

Figure 1.1 illustrates the region of the electromagnetic radiation of interest for atmospheric remote sensing (in GHz and wavelengths in mm) together with the region of interest for this thesis with frequencies. This is the microwave to mm region. The advent of microwave atmospheric remote sensing can be tracked back to the early 1970's with the polar orbiting Nimbus-5 satellite. Nimbus-5 was equipped with the Electrically Scanning Microwave Radiometer (ESMR) with a sensor at 19.35 GHz. This sensor allowed measuring cloud-top temperatures as well as the water vapor content of the atmosphere, and was sensitive to the atmospheric liquid water column. The first precipitation retrievals showed promising results. The following Nimbus satellite and its successor instrument, the Scanning Multichannel Microwave Radiometer (SMMR), carried the first dual polarizing sensors at 18 and 37 GHz.

The next step was the launch of the Special Microwave Imager (SSM/I) which became operational in 1987. SSM/I operates at the frequencies of 19.35 (V+H), 22.23 (V), 37 (V+H) and 85.5 GHz (V+H), where V and H represent the vertical and horizontal polarizations of these channels. SSM/I provided the basis for retrieving quantities such as water vapor, sea surface temperature, ocean surface wind speed, and precipitation. The high sensitivity of the channel at 85.5 GHz to scattering by frozen particles allowed the retrieval of precipitation over land.

To improve the understanding of precipitation and to retrieve precipitation characteristics, the Tropical Rain Measuring Mission (TRMM) was launched in 1997. TRMM carries a microwave radiometer (TMI) operating at 10 (V+H), 19 (V+H), 21 (V), 37 (V+H) and 85 (V+H) GHz, and the Profiling Radar (PR) operating at 13.8 GHz. The PR was the first active space borne instrument and proved to be very useful to investigate the vertical structure of precipitation while the radiometer can discern liquid and ice quantities using a multifrequency retrieval algorithm. Active satellite-based observations are still extremely limited.

Higher microwave frequencies (>100 GHz) became available fairly recently with SSM/T-2 since 1991, AMSU since 1998, and MHS since 2005. These are all instruments carrying channels around the strong water vapor absorption line at 183.310 GHz. AMSU-A (with 15 frequencies up to 90 GHz) and AMSU-B (89, 150 and 176.31, 180.31, 182.31 GHz) are sensors primarily aimed at temperature and humidity profiling. The availability of these higher frequency channels motivated over the past few years focused efforts on passive microwave techniques for the observation of the atmospheric frozen phase. Microwave radiometry has been recognized as one of the most efficient and important approaches to observe ice and snow clouds (i.e. Wang et al. (2001); Skofronick-Jackson et al. (2004). Moreover, the launch of CloudSat and its 94 GHz nadir-looking Cloud Profiling Radar (CPR) in 2006 has provided global snowfall measurements. The observations from CloudSat provide important information for retrieving the microphysical properties of ice clouds (e.g. Delanoë and Hogan, 2010a).

The main future international project in the field of precipitation is the Global Precipitation Measurement (GPM) mission (Smith et al., 2007). GPM is scheduled to be launched in 2014 and will provide the next-generation of global observations of rain and snow. The GPM instruments are sought to extend the capabilities of the TRMM sensors to detect falling snow, measure light rain, and provide, for the first time, quantitative estimates of microphysi-

cal properties of precipitation particles. GPM will carry a Dual Frequency Precipitation Radar (DPR) with frequencies in the Ku-band (13 GHz) and the Ka-band (37 GHz), and a Microwave Imager (GMI) with channels as in TRMM TMI (10 to 89 GHz) plus new channels at 166, 183 ± 3 and 183 ± 8 GHz.

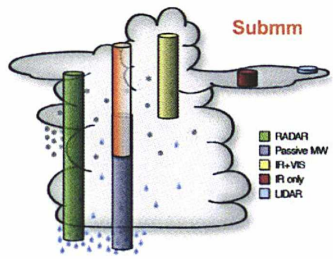

Figure 1.8: Same as Figure 1.6 but with the added sub-millimeter spectral range.

In terms of millimeter and sub-millimeter frequencies, no down-looking satellite instrument has been launched yet. The technology needed is frequently used in astronomy and, for atmospheric observation there are already three sub-millimeter limb sounders that have been launched (Odin-SMR, Aura-MLS and SMILES). Limb sounders measure the thermal emission from the limb of the Earth's upper atmosphere - tangential observations. These limb sounders only detect relatively high clouds with very poor spatial resolution. Although limb sounders only detect relatively high clouds with poor spatial resolution, their observation have also been exploited to study ice clouds (e.g. Eriksson et al., 2010). In 2005, the down-looking Cloud Ice Water Path Submillimeter Imaging Radiometer (CIWSIR) was presented to the ESA Earth Explorer call (Buehler et al., 2007a). This mission was not selected directly for a pre-phase-A study, but there was a strong recommendation to continue preparatory activities including the collection of more data from aircraft prototypes. Two airborne instruments (CoSSIR and PSR) are available in the US to perform studies in preparation for satellite based instruments. A third instrument is in preparation: ISMAR. ISMAR is a demonstrator partially supported by ESA and the UK Met-Office that should fly for the first time in December 2013 onboard the UK Met Office BAe 146-301 FAAM aircraft. Its current channels are at 118 (V), 243 (V+H), 325 (V), 448 (V) and 664 GHz (V+H). Complementary channels at 424 (V) and 874 GHz (V+H) have been presented to different technical calls from funding agencies, such as the EUFAR JRA Proposal. The Ice Cloud Imager (ICI), the heir of the CIWSIR proposal, has been accepted by EUMETSAT as an instrument for the European Meteorological Polar System Second Generation (MetOp-SG). The ICI sub-millimeter channels will fill the observational gap between IR and passive microwave observations as seen in Figure 1.8. Active microwave observations offer poor horizontal spatial coverage and infrared techniques only sense small ice water paths. On the contrary, the ICI sub-millimeter channels are more sensitive to the scattering signal by the frozen phase and will be capable of sensing different cloud altitudes depending on the wavelength and estimating ice mass and the mean ice particle size. The ICI channels will provide novel insight into cloud interior and frozen precipitation. They will improve NWP initial conditions, support cloud microphysical development, monitor ice clouds and snow, and asses cloud radiative effects.

1.4.2 State of the Art

This section aims at making a brief overview of the current state of the art of microwave remote sensing to characterise and retrieve the cloud frozen phase and falling snow. The readers are encouraged to refer to the cited literature for a more detailed account on specific points.

The primary signature in the microwave spectrum from the frozen phase is its scattering sig-

nal. In passive observations from high enough frequencies, this reduces the upwelling radiation emitted from the surface and the lower atmosphere, and in active observations it backscatters the signal to the radar. For this reason, many efforts have focused on passive and active microwave remote sensing techniques for the characterisation and observation of ice and snow clouds. Figure 1.9 presents the active and passive microwave instruments used in this study and illustrates the frozen phase scattering signal.

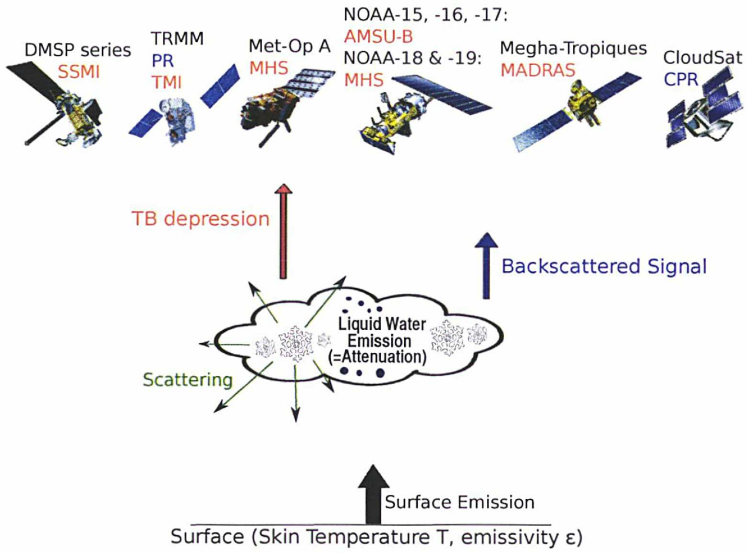

Figure 1.9: The effects of frozen hydrometeors and liquid water on microwave active (blue) and passive instruments (red) onboard the various platforms used in this thesis.

Any snowfall or ice cloud retrieval based on passive, active, or combined sensors is dependent on the assumptions made about hydrometeor microphysics. These assumptions have a large impact on the radiative properties, and hence the quality of the retrievals. A detailed and validated description of the cloud microphysics is not only needed, but the microphysical characteristics have to be converted into the electromagnetic properties accurately. The latter allows to relate the physical quantities to the measured variables like radar reflectivity or brightness temperature.

The passive signal response is related to the vertically integrated scattering properties of the atmospheric column. Thick ice and snow clouds have been found to significantly reduce the thermal radiation signal at frequencies greater than 80 GHz (e.g. Katsumata et al., 2000; Bennartz and Petty, 2001; Bennartz and Bauer, 2003). After analysing observations by an airborne radiometer over ocean, for example, Katsumata et al. (2000) reported that snow clouds can reduce upwelling brightness temperatures at 89 GHz by up to 15 K while being hardly detectable by radiometers at frequencies lower than 40 GHz. Bennartz and Bauer (2003) indicated that the 150 GHz channel in AMSU-B exhibits the most influence by ice particle scattering compared to the other AMSU-B channels. Different studies that followed confirmed these results: the effective sensitivity of frequencies around 150 GHz, possibly in combination with channels at 85 and 183±7 GHz, for the detection and retrieval of precipitation properties

at middle and high latitudes is suggested.

The scattering effect in passive observations can be used to derive the integrated snow water path (e.g. Noh et al., 2006), especially for moderate to heavy snowfall events under unfrozen or no-snow covered surfaces, but it is not able to provide any information about the vertical ice distribution. Passive only retrievals suffer from large uncertainties, exceeding 60% according to Kulie et al. (2010), mainly related to uncertainties in the microphysical properties of the hydrometeors.

From the active observations point-of-view, the Cloud Profiling Radar (CPR) onboard CloudSat (Stephens et al., 2002) currently offers one of the most advanced possibilities for deriving the distribution of global snowfall (Liu, 2008). Space-borne active sensors, capable of estimating the horizontal and vertical distribution of snowfall, had not been available prior to CloudSat. The PR on board TRMM carries a space-borne active sensors since 1997, but it is operating at a much lower frequency than CloudSat (13 GHz compared to 94 GHz), and measures the power reflected back by rain particles and the Earth's surface. Cloud particles measured in non precipitating water and ice clouds are rather weak scatterers at the PR frequency. The CPR onboard CloudSat makes it possible to sense the vertical structure of both clouds and rain. The advantage of CloudSat is that one can derive information on the vertical distribution of small cloud ice and snow particles. However, this is done through empirical relations between the equivalent radar reflectivity factor Z_e and the snowfall rate, which are in turn a function of particle fall velocity and thus particle habit and particle size distribution. Kulie and Bennartz (2009), Liu (2008), Matrosov et al. (2008) and Turk et al. (2011), to name but a few, have presented snowfall studies based on the measured radar reflectivity. Snowfall Z_e-S relations generally exhibit more variability in their coefficients than rainfall (Z_e-R), due to the larger uncertainties in snowflake habits and fall velocities relative to those in raindrops (Matrosov et al., 2008), and without additional measurements it is difficult to verify which, if any, of these parameters are physically correct. Furthermore, the CPR only measures a 1.5 km wide strip on the Earth surface for each orbit, which limits its utility for weather monitoring and climate data collection.

Radar and passive microwave observations have been combined in several studies. Noh et al. (2009) and Liu and Seo (2013) applied different Z_e-S relations based on single-frequency radar data to ground-based and airborne datasets. The resulting SWC profiles were used to build realistic a priori datasets with which to develop a snowfall retrieval algorithm based on passive microwave observations between 89 and 220 GHz. Other efforts derive snowfall over land from AMSU-B observations using empirical formulas (e.g. Kongoli et al., 2003). Kneifel et al. (2011) used CloudSat data and a comprehensive set of snow particle habits to simulate passive observations between 36 and 157 GHz. The simulated brightness temperatures have been compared to collocated satellite observations which allows excluding particles habits with systematic higher/lower scattering properties. In Kneifel et al. (2011), however, only one particle size distribution was applied and the influence of potential errors introduced by the particle size distribution itself could not be evaluated. Combined retrieval algorithms of SWC and snow particle size have been derived based on airborne radar and passive observations by Skofronick-Jackson et al. (2004) for snowfall over land and by Grecu and Olson (2008) for snowstorms over the ocean. A clear result common to these studies is that a significant improvement of snow retrievals can be obtained by combining passive and active microwave observations and using multiple frequencies.

Although empirical relationships and statistical techniques may be operationally useful,

physical radiative transfer models are still needed to understand how the measured brightness temperatures depend on various atmospheric and surface parameters. In order to develop accurate snow and ice retrievals, it is critical to run the forward model with detailed single scattering parameters and particle size distributions of the frozen particles in question. Among the difficulties encountered in this task are the unknown distributions of sizes, composition, densities, shapes, and orientations of these hydrometeors. All these parameters affect the scattering signal that is observed. The inverse problem in snow and ice studies is a difficult one to formulate, especially given the limited amount of independent information contained in a set of microwave observations. Theoretical studies on the sensitivity of passive microwave radiation to the scattering properties of ice and snow particles, and their size distributions have been conducted (e.g. Skofronick-Jackson and Johnson, 2011; Kneifel et al., 2010; Liu, 2008; Bennartz and Bauer, 2003) using radiative transfer simulations. Numerous studies have attempted to find both realistic and computationally inexpensive methods to perform this challenging task. Despite the significant progress made over the past years in understanding the single scattering properties of individual snow particles, determining the microphysical characteristics of frozen precipitation remains the most elusive step to properly characterize the scattering properties of frozen particles and to accurately quantify atmospheric ice and snow through remote sensing.

Another important source of information to help constrain the microphysical properties is the polarized scattering signal generated by frozen and mixed phase hydrometers. It is known that frozen hydrometeors with preferential orientation produce significant polarization differences between the horizontal and vertical polarizations (e.g. Evans and Stephens, 1995; Miao et al., 2003a; Eriksson et al., 2011b; Prigent et al., 2001, 2005b; Troitsky et al., 2001). These studies conducted radiative transfer simulations to investigate the potential of polarized observations from space for ice and snow characterization. The dielectric properties of mixed phase hydrometeors directly impact the emitted polarization signals. The analysis of polarized observations could add valuable information for the retrievals of ice clouds and snowfall.

1.5 Thesis Motivation and Objectives

The quantification of the frozen phase on a global basis is important to capture and quantify the full Earth energy budget and the Earth hydrological cycle. In reality, the estimation of frozen phase quantities form the present suite of satellite observations, limited to 190 GHz in the passive and 94 GHz in the active, is still at a very early stage. The sensitivity to scattering from frozen hydrometeors at microwave frequencies delivers, in principle, potential for snowfall characterization from space, the sensitivity to the scattering signal depending on a large degree on the size and phase of the hydrometeor with respect to the observing wavelength. The main difficulties encountered in this task are (a) the complex variability and lack of parameterizations of the microphysical properties, and thus radiative properties, of frozen particles (e.g. size, composition, density, the related dielectric properties, and shape), (b) the weak signal from snow with respect to the background emission from the snow covered land; and (c) separating the signal related to the emission/scattering from other cloud hydrometeors from the snow signal.

This thesis is developed in the context of the pressing need to constrain such microphysical properties from remote sensing in order to reduce the large uncertainties associated with frozen quantities in Numerical Weather Prediction and climate models. Furthermore, in the preparation of the upcoming NASA Global Precipitation Measurement (GPM) mission and ESA

MetOp-SG satellites with sub-mm frequency channels, an understanding of the bulk properties of frozen hydrometeors is also essential. This study seeks to improve the understanding of the relationship between the physical properties of frozen hydrometers, especially snow, and the radiative properties measured by active and passive instruments at microwave and millimeter waves, by exploiting the observational power of current observations, to better constrain the microphysical properties of the hydrometeors.

In this work, three main objectives will be pursued:

1. Developing the tools to simulate realistic scenes, as observed with passive and active microwave and millimeter wave instruments over ice/snow clouds.

   Simulating active and passive measurements over ice/snow clouds strongly depends on correctly characterizing the scattering signal of the frozen hydrometeors. Accurate radiative transfer calculations in a scattering medium are necessary. The Advanced Radiative Transfer Simulator (ARTS) is selected: it is a well documented and well validated community code. ARTS has provided the methods for rigorous simulations of limb sounding and near-nadir measurements involving mostly cirrus clouds at high frequencies (millimeter and sub- millimeter wavelengths). In this thesis, ARTS will be used to solve the radiative transfer equation at lower frequencies, mainly the microwave region from 20 up to 200 GHz. In this spectral region, larger mixed phase frozen particles are involved since observations have higher sensitivity to the lower atmosphere, and there is a significant sensitivity to the surface contribution, when the atmosphere is not too opaque. In order to use ARTS to simulate real microwave observations in the presence of ice and snow, a significant effort is required first to describe the microphysical properties of frozen particles, to calculate the scattering properties at these frequencies, and then to evaluate the ARTS calculations. In addition, calculation of the active response has to be added to complement ARTS passive simulations. Finally, the surface contribution has to be taken into account and the necessary surface emissivity calculation tools needs to be interfaced with ARTS.

2. Analyzing and interpreting specific polarized scattering signatures over ice/snow clouds.

   Polarized scattering signatures have been observed up to 100 GHz with conical imagers such as SSM/I, TMI, or AMSR-E. These signatures have already been partly analyzed and interpreted. However, their large occurrence and their potential to characterize the frozen phase microphysics deserve additional studies. In this thesis, we will jointly analyze passive and active observations from the TRMM mission, to better understand these signatures and possibly use them to infer cloud information. In addition, the French-Indian Megha-Tropique mission recently launched carries for the first time an instrument that measures polarized observations up to 157 GHz. This is a great opportunity to further test our understanding of the scattering signals from the frozen phase, using the ARTS radiative transfer solver.

3. Simulating realistic passive and active microwave responses over ice/snow clouds, and evaluating them with satellite observations.

   To prepare the next generation of millimeter and sub-millimeter observations, robust methods have to be developed to retrieve the ice/snow parameters from the satellite measurements. These methods are often based on large data sets of simulated observations. In this thesis, the ARTS code will be coupled to a meso-scale cloud model (Meso-NH),

to be able to generate a large data set of realistic simulations. For real atmospheric cases ARTS will be fed with the inputs from Meso-NH, and the results will be compared with coincident satellite observations, at close-to-millimeter frequencies, for both passive and active. The objective is to assess our capacity to simulate observations with adequate microphysical parameters and the radiative transfer model, and assess the accuracy of the coupling radiative transfer simulation/meso-scale cloud model.

This thesis is structured in seven chapters: Chapter 2 presents the microwave satellite instruments that will be used together with information on their operating frequencies, observation geometry and resolution. Chapter 3 summarizes radiative transfer theory and introduces the ARTS model selected to solve the radiative transfer equation. Chapter 4 follows with a description of the important parameters that need consideration when preparing for realistic simulations of large frozen hydrometeors in the microwave region with ARTS. This chapter also describes tools that were developed/coupled to ARTS in this thesis. Chapters 5 presents work conducted in this thesis to analyze the microwave polarized scattering signal over clouds. This involved interpreting satellite observations with radiative transfer simulations. Chapter 6 presents a study where coherent simulations of passive and active observations of a real case scenarios are conducted to help constrain the microphysical properties of snow in the radiative transfer model. Finally, chapter 7 draws conclusions and suggests the scientific perspectives.

Chapter 2

Analyzed Microwave Satellite Observations

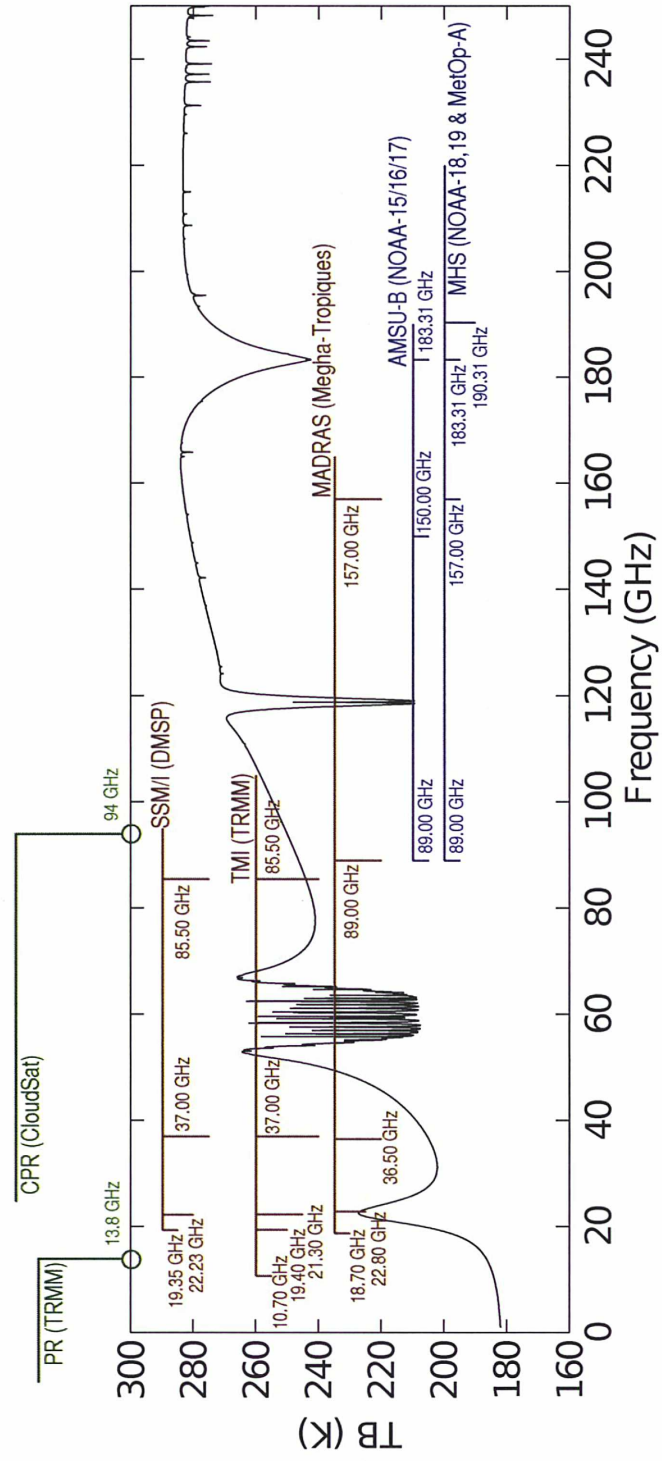

Figure 2.1: The brightness temperatures simulated by ARTS, as observed at nadir over ocean for a typical Tropical atmosphere under clear sky conditions. The central frequency bands of the passive instruments used in this study are shown: conical scanners in red and profilers in blue. The frequency bands of the active instruments used in this study are also shown in green for reference. Table 2.1 lists the central frequency bands.

This chapter introduces the microwave (10-200 GHz) instruments onboard satellites used in this thesis. Table 2.1 lists the central frequency bands at which all these instruments operate and divides them between active/passive instruments. For the microwave passive instruments, Table 2.1 further divides them into their scanning geometry (conical scanners or profilers). Figure 2.1 shows the simulated brightness temperature for a nadir-looking radiometer calculated using ARTS on a 1 MHz resolution under clear sky conditions, for a typical Tropical atmosphere, together with the position of central bands of all the instruments used. The locations of the frequency bands of the radars used in this thesis are also shown for reference. The following sections describe the characteristics of these instruments.

Passive Microwaves					Active Microwaves	
Conical Scanners			Profilers		Radars	
SSM/I (DMSP)	TMI (TRMM)	MADRAS (Megha-Tropiques)	AMSU-B (NOAA-15 16/17)	MHS (NOAA-18/19 MetOp-A)	CPR (CloudSat)	PR (TRMM)
–	10.70 GHz	–	–	–	–	13.8 GHz
19.35 GHz	19.40 GHz	18.70 GHz	–	–	–	–
22.23 GHz	21.30 GHz	22.80 GHz	–	–	–	–
37.00 GHz	37.00 GHz	36.50 GHz	–	–	–	–
85.50 GHz	85.50 GHz	89.00 GHz	89.00 GHz	89.00 GHz	94 GHz	–
–	–	157.00 GHz	150.00 GHz	157.00 GHz	–	–
–	–	–	183.31 GHz	183.31 GHz	–	–
–	–	–	–	190.31 GHz	–	–

Table 2.1: The central frequency bands of the different sensors used in this study. More details about the profilers are given in the text that follows.

2.1 Passive Microwave Instruments

2.1.1 The conical scanners: SSM/I, TMI, and MADRAS

The Special Sensor Microwave/Imager (SSM/I) onboard the Defense Meteorological Satellite Program (DMSP) satellites provides vertical and horizontal polarizations at 19.35, 22.235 (only vertical polarization), 37.0, 85.5 GHz (Hollinger et al., 1990). The DMSP satellites have an almost complete coverage of the Earth twice daily from their near-polar, circular, Sun-synchronous orbit. SSM/I is a conical scanning instrument with a constant scan angle of $\theta_s = 45^o$ from nadir that corresponds to a local zenith angle of $\theta_z = 53^o$ (it intersects the surface of the Earth at an incidence angle defined as the local zenith angle). The elliptical field of view decreases in size proportionally with frequency, from 43 x 69 km at 19 GHz, 40 x 50 km at 22 GHz, 28 x 37 km at 37 GH to 13 x 15 km at 85 GHz. Figure 2.2 illustrates the SSM/I viewing geometry.

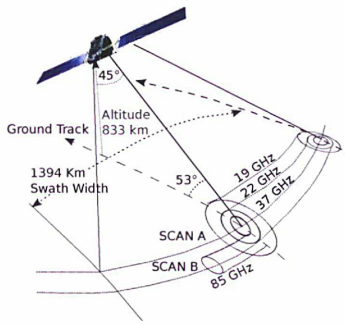

Figure 2.2: SSM/I scan geometry.

SSM/I channel selection has become a standard for passive microwave imagers, like the TRMM Microwave Imager (TMI) (see Figure 2.1). TMI is a similar conical imager onboard the Tropical Rainfall Measuring Mission (TRMM) and observes the Earth since 1997 (Kummerow et al., 1998a). Unlike SSM/I, TMI is not Sun-synchronous. The TRMM satellite carries a suite of instruments designed for precipitation studies of the Tropics (latitude coverage of approximately $\pm$ 40^o). TMI measures radiation at frequencies between 10 and 85 GHz, similarly to SSM/I but with an extra channel at 10 GHz, in both the vertical and horizontal polarizations (Table 2.1). In contrast to SSM/I, TMI provides measurements with a higher resolution (37 x 67 km at 10 GHz, 30 x 18 km at 19 GHz, 18 x 27 km at 22 GH, 9 x 16 km at 37 GHz and 5 x 7 km at 85 GHz). TMI operates with an observation geometry similar to SSM/I (scan angle of 49^o).

The Multi-frequency Microwave Scanning Radiometer (MADRAS) is a microwave radiometer onboard Megha-Tropiques, a collaborative effort between the Indian Space Research Organization (ISRO) and the French Centre National d' Etudes Spatiales (CNES) (Desbois et al., 2003). The Megha-Tropiques satellite was launched in 2011 and, as its name suggests, covers the Tropics (latitude coverage of approximately $\pm$ 23^o). MADRAS is a conical scanner similar to SSM/I and TMI with $\theta_z = 53.5^o$. MADRAS is not Sun-synchronous and provides vertical and horizontal polarized observations at 18.7, 23.8 (V polarization only), 36.5, 89, and 157 GHz. MADRAS is the first satellite instrument to measure polarized signals at high microwave frequencies, 157 GHz. MADRAS has a resolution of 40 km for all the low frequency channels, 10 km for the 89 GHz channel and 6 km for the 157 GHz channel.

2.1.2 The profilers: AMSU-B and MHS

The Advanced Microwave Sounding Unit (AMSU-B) (Saunders et al., 1995) and its successor the Microwave Humidity Sounder (MHS) (Bonsignori, 2007) are microwave Sun-synchronous radiometers designed for atmospheric sounding of humidity. AMSU-B is carried onboard the operational satellites NOAA-15, NOAA-16, and NOAA-17, while MHS is carried onboard NOAA-18, NOAA-19, and MetOp-A. Their main channels are located in the H_2O water vapor line at

183.31 GHz. Figure 2.3 shows the location of AMSU-B and MHS frequency bands in reference to the brightness temperature spectrum of a typical clear sky Tropical atmosphere as simulated with ARTS. Note that MHS is similar to AMSU-B but channels 1 and 2 are composed of only one passband, channel 2 is at 157 GHz (instead of 150 GHz) and channel 5 has only one passband at 190 GHz (instead of 183.31 ± 7 GHz).

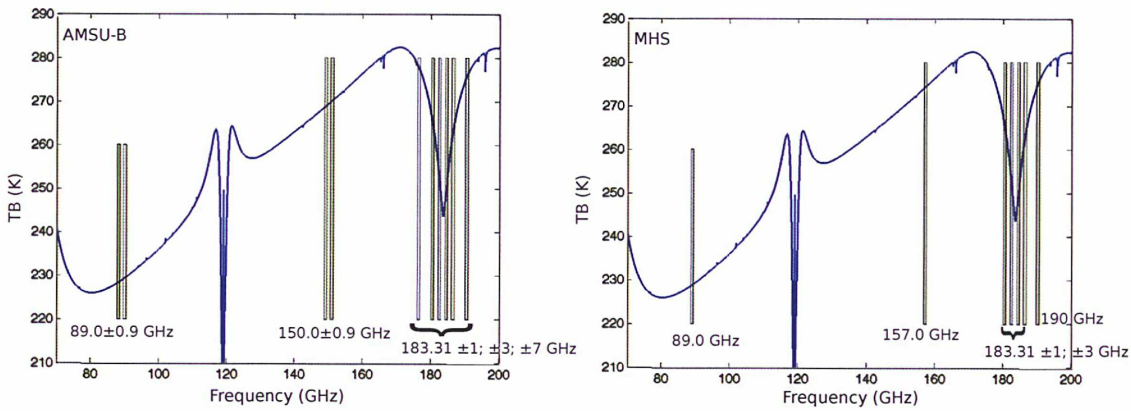

Figure 2.3: The brightness temperatures simulated by ARTS, as observed at nadir over ocean for a typical Tropical atmosphere under clear sky conditions. The frequency bands of AMSU-B and MHS are shown.

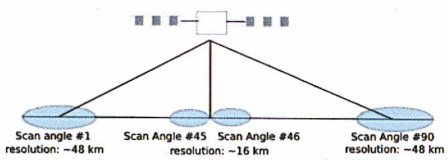

Figure 2.4: The AMSU-B scan-line.

AMSU-B and MHS are both cross-track scanners and are very similar in their scan characteristics and their antenna spatial response. AMSU-B has 90 positions at 1.1^o intervals from -44.5 x 1.1^o to $+44.5$ x 1.1^o, which translate into local zenith angles θ_z up to 48.5^o. The near-nadir scan angle footprint resolution is approximately 16 km, increasing to approximately 48 km at the swath edges as seen in Figure 2.4.

The polarization measured by AMSU-B and MHS rotates with scan angle due to the rotating-reflector/fixed feed type of antenna design. If θ_s is the scan angle and θ_z is the local zenith angle, then the measured signal TB(θ_z) seen for a local zenith angle (θ_z) is given by

$$TB(\theta_z) = TB_p(\theta_z)\cos^2(\theta_s) + TB_q(\theta_z)\sin^2(\theta_s) \tag{2.1}$$

where $\mathrm{TB}_p(\theta_z)$ and $\mathrm{TB}_q(\theta_z)$ are the two orthogonal polarized signals (expressed here in terms of the brightness temperature TB) at θ_z local zenith angle. Depending on the channels, p will represent the vertical or the horizontal polarization. The polarization p seen when the incidence is close to nadir (i.e. $\theta_z = \theta_s$ very close to 0^o) is always V for AMSU-B, while for MHS it is V for all channels but H for the two bands around 183.31 GHz.

2.2 Active Microwave Instruments

2.2.1 The Precipitation Radar onboard TRMM

The Precipitation Radar (PR) accompanies TMI onboard TRMM. As already mentioned TRMM observations are limited to the Tropics (latitude coverage of approximately $\pm$ 40^o). The PR observes the Earth around nadir ($\pm$17^o) at 13.8 GHz with a 4 km resolution and a swath of 215 km located at the centre of the TMI swath as seen in Figure 2.5. The PR has a pulse range corresponding to a 250 m vertical resolution and a minimum detectable signal of approximately 17 dBZ. The PR and TMI instruments onboard TRMM allow the exploitation of their active/passive synergy.

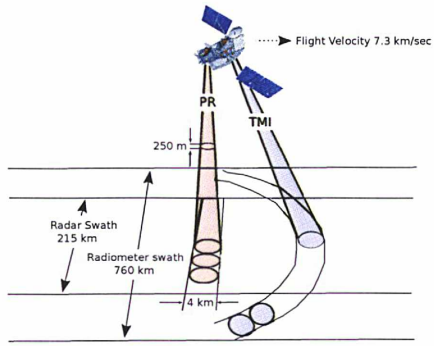

Figure 2.5: Observation geometry of the PR and TMI onboard TRMM. Adapted from Kummerow et al. (1998b).

The PR was the first space borne radar designed to provide 3D maps of storm structures. PR raw observations and derived products yield information on the intensity and distribution of rain, on the rain type, on the storm depth and on the height at which snow melts into rain. They provide vertical profiles of rain and snow from the surface up to a height of about 20 km, and makes it possible to detect the presence of the melting layer. Since the signal at 13.8 GHz suffers from attenuation, in order to obtain an accurate three-dimensional rain structure, it is necessary to correct for the attenuation effects before radar reflectivities are converted into rainfall rates.

2.2.2 The Cloud Profiling Radar onboard CloudSat

The Cloud Profiling Radar (CPR) is carried onboard CloudSat (Stephens et al., 2002). CloudSat is a polar-orbiting, sun-synchronous satellite, observing the Earth since 2006. CloudSat provides a unique opportunity to monitor atmospheric clouds at a global scale since it operates at a frequency of 94 GHz (nadir-looking). This frequency is capable of retrieving quantitative precipitation information. Moreover, it is part of the A-Train constellation of research satellites: Aura, Cloud Aerosol Lidar, CALIPSO, CloudSat, and Aqua (see Figure 2.6). The advantage of the A-Train is that its satellites share a nearly equal orbiting track allowing numerous synergies.

CloudSat has the spatial resolutions of approximately 1.4 km across-track, 1.8 km along-track and 500 m vertically (Stephens et al., 2002). The CPR minimum detectable signal is about -30 dBZ. CloudSat provides a good opportunity to evaluate NWP due to its high resolution, near-global coverage, and its capability to penetrate clouds and assess the occurrence of multi level clouds (Mace et al., 2009). CloudSat provided the first opportunity to survey the horizontal and vertical snowfall structures at a global scale (Liu, 2008; Kulie et al., 2010). Even with CloudSat single frequency and nadir only sampling, much has been learned about the global distribution of frozen precipitation (Kneifel et al., 2011; Liu, 2008). At 94 GHz, the attenuation by gases (essentially water vapor), liquid water droplets, and precipitation-size particles have to be taken into account to achieve accurate cloud and rain profiles.

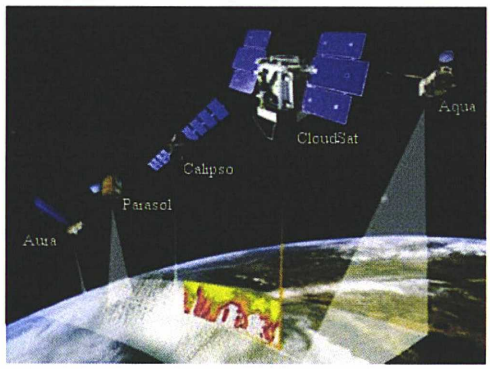

Figure 2.6: Illustration of the A-train constellation of satellites.

Chapter 3

Microwave Radiative Transfer in a Scattering Atmosphere

3.1 Theoretical Considerations

The estimation of physical parameters from passive satellite remote sensing techniques involves a thorough understanding of the radiative transfer of electromagnetic (EM) waves through the atmosphere. The following section introduces the basic theories of EM radiation: the plane wave solution of Maxwell's equations, how wave propagation relates to the intensity and the polarization state of radiation, and how EM fields interact with hydrometeors in the atmosphere.

3.1.1 Electromagnetic Theory

The behaviour of EM waves is described by Maxwell's equations:

$$\begin{aligned} \nabla \cdot \mathbf{D} &= \rho, \\ \nabla \times \mathbf{E} &= -\frac{\partial \mathbf{B}}{\partial t}, \\ \nabla \cdot \mathbf{B} &= 0, \\ \nabla \times \mathbf{H} &= \mathbf{J} + \frac{\partial \mathbf{D}}{\partial t}, \end{aligned} \tag{3.1}$$

where the electric and magnetic fields are denoted as $\mathbf{E}$ and $\mathbf{H}$ respectively, time as t, the magnetic induction as $\mathbf{B}$, and the electric displacement as $\mathbf{D}$. The free macroscopic charge density and the current density are denoted as ρ and $\mathbf{J}$ respectively. From these equations, the electric and magnetic field vectors under the plane wave solution, meaning the solution for a monochromatic parallel beam of light propagating in a homogeneous medium without sources, can be expressed as

$$\begin{aligned} \mathbf{E}(\mathbf{r}, t) &= \mathbf{E}_0 \exp(i\mathbf{k} \cdot \mathbf{r} - i\omega t), \\ \mathbf{H}(\mathbf{r}, t) &= \mathbf{H}_0 \exp(i\mathbf{k} \cdot \mathbf{r} - i\omega t), \end{aligned} \tag{3.2}$$

where $\mathbf{E}_0$ and $\mathbf{H}_0$ are constant complex vectors, $\mathbf{r}$ is the position vector, ω is the angular frequency of the wave and $\mathbf{k}$ is the complex wave vector $\mathbf{k}_R + i\mathbf{k}_I$, which describes the propagation properties of the wave. The complex wave vector $\mathbf{k}$ is equal to $\omega\sqrt{\mu_o \epsilon} = \frac{\omega n}{c}$ where n is the complex refractive index of the medium, c is the speed of light, μ_o is the magnetic permeability of free space, and ϵ is the electric permittivity of the medium. Since the magnetic field $\mathbf{H}$ can be expressed in terms of the electric field $\mathbf{E}$, it is sufficient to describe the electromagnetic wave considering only $\mathbf{E}$, where the first term, $\mathbf{E}_0 \exp(-\mathbf{k}_I \cdot \mathbf{r})$, is the amplitude and $(i\mathbf{k}_R \cdot \mathbf{r} - i\omega t)$ is the phase of the electric wave.

Figure 3.1 shows the coordinate system used to describe the direction of propagation of the unit vector $\mathbf{n}$ and the polarization state of a plane EM wave. In the case of a non-absorbing medium, the wave vector $\mathbf{k} = k\mathbf{n}$ is real and the electric field vector $\mathbf{E}$, perpendicular to the direction of propagation, reduces to a linear combination of components parallel to the direction of travel:

$$\mathbf{E}(\mathbf{r}, t) = \mathbf{E}_0 \exp(ik\mathbf{n} \cdot \mathbf{r} - i\omega t) = \mathbf{E}_v(\mathbf{r}, t) + \mathbf{E}_h(\mathbf{r}, t) \tag{3.3}$$

where the subscripts v- and h- indicate vertical and horizontal polarizations.

Considering a wave traveling in the positive z-direction,

$$\mathbf{E}(\mathbf{z}, t) = \begin{pmatrix} E_v(\mathbf{z}, t) \\ E_h(\mathbf{z}, t) \end{pmatrix} = \begin{pmatrix} E_v^0 \\ E_h^0 \end{pmatrix} \exp(ik\mathbf{z} - i\omega t) = \begin{pmatrix} a_v \exp(i\phi_v) \\ a_h \exp(i\phi_h) \end{pmatrix} \exp(ik\mathbf{z} - i\omega t), \tag{3.4}$$

where a_v and a_h are the amplitudes, and ϕ_v and ϕ_h are the phases, of the complex constants E_v^0 and E_h^0.

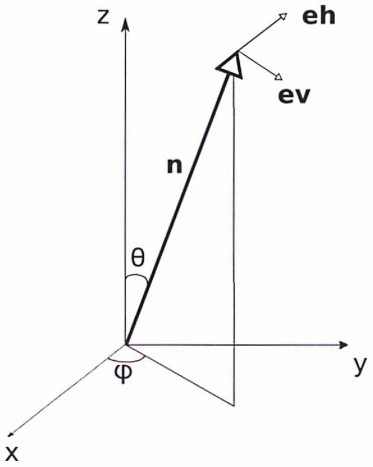

Figure 3.1: The unit vector and the coordinate system defining the direction of propagation and polatization of an EM wave.

3.1.2 The Stokes Vector

The electric field vectors of EM waves introduced in the previous section are not measured by instruments, but their time averaged intensities are. Such measurable parameters are the so-called Stokes parameters (I, Q, U, V) which denote the intensity and polarization of EM radiation. The Stokes parameters are the elements of the Stokes vector, **I**, which is defined as

$$\mathbf{I} = \begin{pmatrix} I \\ Q \\ U \\ V \end{pmatrix} = \frac{1}{2}\sqrt{\frac{\epsilon}{\mu}} \begin{pmatrix} < E_v^0 E_v^{0*} > + < E_h^0 E_h^{0*} > \\ < E_v^0 E_v^{0*} > - < E_h^0 E_h^{0*} > \\ < -E_v^0 E_h^{0*} > - < E_h^0 E_v^{0*} > \\ i < E_h^0 E_v^{0*} > -i < E_v^0 E_h^{0*} > \end{pmatrix}, \tag{3.5}$$

where $E_{v,h}^o$ are the complex constants in Equation 3.4, <> denotes time averages and the subscript * denotes the complex conjugate.

The Stokes parameters are real valued dimensions of monochromatic energy flux and characterize any plane EM wave. To get a physical sense of what each of the Stokes parameters represent, it is useful to rewrite Equation 3.5 as

$$\mathbf{I} = \begin{pmatrix} I \\ Q \\ U \\ V \end{pmatrix} = \frac{1}{2}\sqrt{\frac{\epsilon}{\mu}} \begin{pmatrix} < a_v^2 > + < a_h^2 > \\ < a_v^2 > - < a_h^2 > \\ - < 2a_v a_h \cos(\phi) > \\ - < 2a_v a_h \sin(\phi) > \end{pmatrix} = \begin{pmatrix} I_v + I_h \\ I_v - I_h \\ I_{-45} - I_{45} \\ I_{rcp} - I_{lcp} \end{pmatrix}, \tag{3.6}$$

where $\phi = \phi_v - \phi_h$ is the difference in the v- and h- phases. The first Stokes parameter I describes the total intensity and the other parameters describe the polarization state. The second Stokes component Q is the difference between vertical and horizontal polarizations, the third component U is the difference for $\pm 45^o$ polarizations and the last Stokes component V is the difference between left and right circular polarizations. The last three components of the Stokes vector can be thought of as preferences of the EM wave for vertical linear, -45^o linear or right circular polarization. I is always positive, and Q, U, and V are between +I and −I. Under Equation 3.5, the following quadratic equation holds,

$$I^2 \geq Q^2 + U^2 + V^2 \tag{3.7}$$

If the beam of light is said to be completely polarized, the equality in Equation 3.7 holds. This is the ideal case of a monochromatic plane wave where the amplitudes a_v and a_h and the phases ϕ_v and ϕ_h are fixed and do not vary with time. This means that the plane wave is emitted by one coherent source. In reality, i.e. in the case of natural radiation, the amplitudes and phases fluctuate, since radiation originates from several sources that do not emit radiation coherently. This means that there is a superposition of radiation from several incoherent sources, and that the polarization state of the radiation from each source fluctuates too. If the fluctuations are random for all the sources and if the different sources emit incoherently and are not in any way oriented, then there is no preferred orientation, which is called unpolarized. This is the case of radiation from the Sun. For unpolarized radiation, the equality does not hold because Q = U = V = 0.

3.1.3 Planck Emission

Any particle at a temperature above 0 K emits radiation. It is common to relate the radiation from objects at certain temperatures to the radiation that a blackbody of the same temperature would have. A blackbody is an idealized object that absorbs all incoming radiation and emits as a function of frequency as described by Planck's law

$$I_\nu = B(\nu, T) = \frac{2h\nu^3}{c^2(\exp(h\nu/k_B T) - 1)}, \tag{3.8}$$

where ν is the frequency of radiation, h = 6.629 x 10^{-34} Js is the Planck constant and k_B = 1.381 x 10^{-23} J/K is the Boltzmann constant.

In general, when dealing with radiative transfer in the atmosphere, radiation is expressed by the spectral radiance $I(\nu)$ in units of $[\frac{W}{m^2 sr Hz}]$. To illustrate Planck emission, Figure 3.2 shows the normalised blackbody curves for the Sun and the Earth (with effective surface temperatures of 5778 K and 287 K respectively).

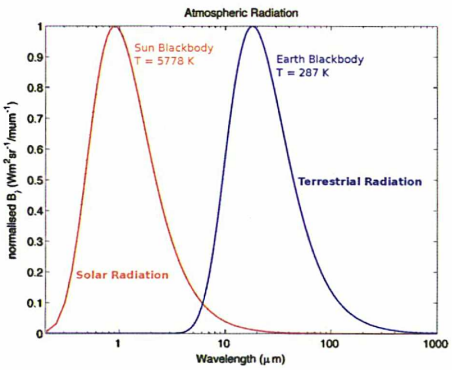

Figure 3.2: The normalised blackbody curves for typical solar and terrestrial emission temperatures. A clear distinction between shortwave radiation from the Sun, and the longwave radiation emitted by the Earth is seen. Although negligible in terms of energy (hidden here due to normalisation), the radiation emitted from the Earth's surface and atmosphere in the microwave is very valuable in remote sensing.

Radiation emitted by the Sun and then reflected by Earth is referred to as shortwave or solar radiation, whereas radiation emitted by Earth is known as longwave, thermal, or terrestrial radiation. Earth observation satellites measure both. At certain frequencies, terrestrial radiation is not significantly absorbed by greenhouse gases and reaches space if no clouds are present. These frequency regions of the EM spectrum are called window regions. Note that, although small energy-wise compared to the infrared, microwave radiation as emitted from the Earth's surface and atmosphere is very valuable for the purposes of remote sensing.

It is very common to transform radiant intensities into the more intuitive brightness temperature T_B. Note that this is not a real physical temperature, but a definition for a unit of intensity. Since real bodies never emit like blackbodies (they emit at a certain emissivity ϵ: $I = \epsilon(\nu)I_\nu$), the Planck brightness temperature T_B is defined as the temperature at which a blackbody in thermal equilibrium with its surroundings would have to be at, to generate the observed intensity I at a particular wavelength,

$$T_b = \frac{h\nu}{k_B \ln\left(1 + \frac{1}{\epsilon}(\exp\left(h\nu/k_B T\right) - 1\right)} \tag{3.9}$$

Another definition often used is the Rayleigh-Jeans brightness temperature for frequencies below the Rayleigh-Jeans limit $h\nu << k_b T$, where the brightness temperature can be approximated as a linear function of temperature

$$B(\nu, T) = \frac{2\nu^2 k_B T}{c^2} \tag{3.10}$$

This condition is valid in almost the whole microwave region with typical temperatures in the Earth atmosphere.

3.1.4 Basic Radiative Transfer

Radiation propagating through a medium where there is no absorption (i.e. the refractive index n is real) and no scattering would remain constant. However, radiation will be weakened and intensified due to its interaction with the medium if absorption, and consequently emission due to Kirchoff's law stating that the emissivity of a medium is equal to its absorptivity under local thermodynamic equilibrium, has to be taken into account. The reduction of the spectral radiance I_ν over an infinitesimal step ds is

$$\frac{dI(\nu)}{ds} = -k(\nu, s)I_\nu(s), \tag{3.11}$$

where k is the total absorption coefficient.

By applying Kirchoff's under local thermodynamic equilibrium, the intensification of the spectral radiance I_ν over an infinitesimal step ds is

$$\frac{dI(\nu)}{ds} = k(\nu, s)B(\nu, s), \tag{3.12}$$

where B_ν is the normalized Planck function defined in Equation 3.8. The emitted spectral radiance defined through B_ν is dependent on the physical temperature $T(s)$. By combining Equation 3.11 and Equation 3.12 and using the Rayleigh-Jeans approximation introduced in

the previous section, the radiative transfer equation for absorption and emission in terms of brightness temperature T_b is expressed:

$$\frac{dT_b}{ds} = k(\nu, s)(T(s) - T_b(s)), \tag{3.13}$$

This is the most common form used in microwave radiometry.

3.1.5 Gas Absorption

When calculating radiative transfer in the atmosphere, the local absorption coefficient at each point in the atmosphere has to be known. This section focuses on molecular absorption rather than on the absorption as a result of the presence of hydrometers in the atmosphere.

At a molecular level, three mechanisms of absorption exist: electronic transitions, vibration, and rotation. Molecules (in this context atmospheric constituents) gain energy by absorbing photons and lose energy by emitting photons. Since absorption (and emission) can only occur at discrete wavelengths according to quantum mechanics, absorption (and emission) should be monochromatic and these discrete wavelengths are often referred to as emission lines. However, due to different processes, these lines are broadened and acquire a line width. Line broadening in the microwave occurs principally in the lower atmosphere due to pressure broadening as a result of molecular collisions, and Doppler broadening in the upper atmosphere as a result of the thermal velocities of molecules. Note that gas absorption does not affect polarization, except for the Zeeman effect on the O_2 molecules very close to absorption line centers. In this study dedicated to the lower atmosphere with frequencies rather far from line centers, the Zeeman effect contribution to the polarization state will not be considered.

An absorption line is described by its corresponding absorption coefficient as a function of frequency $k(\nu)$ as given by;

$$k(\nu) = nL(T)F(\nu) \tag{3.14}$$

where L(T) is known as the line strength, T is the temperature, F(ν) is called the line shape function, and n is the number density of the absorbing species. The values of L(T) at a reference temperature T_0 are contained in spectroscopic databases (for example the HITRAN database (Rothman et al., 2003) used in this thesis) and the conversion to different temperatures can be calculated. The absorption discussed so far is known as resonant absorption, and does not explain the totality of the measured atmospheric absorption. Some molecules show a continuum absorption spectrum. The main qualitative difference is that continuum absorption has a smooth dependence on frequency. In the microwave region, continuum absorption for water vapour (H_2O), oxygen (O_2) and nitrogen (N_2) need to be taken into account.

The integral of the total absorption coefficient and summing over all species yields the optical depth. The optical depth expresses the quantity of radiation removed during its path through a medium, in this case the atmosphere. Figure 3.3 shows the optical depth, τ, at nadir for an average tropical atmosphere and another often used term, the optical transmittance ($= e^{-\tau}$) under the same conditions. The transmittance expresses the fraction of the incident radiation that passes through the atmosphere.

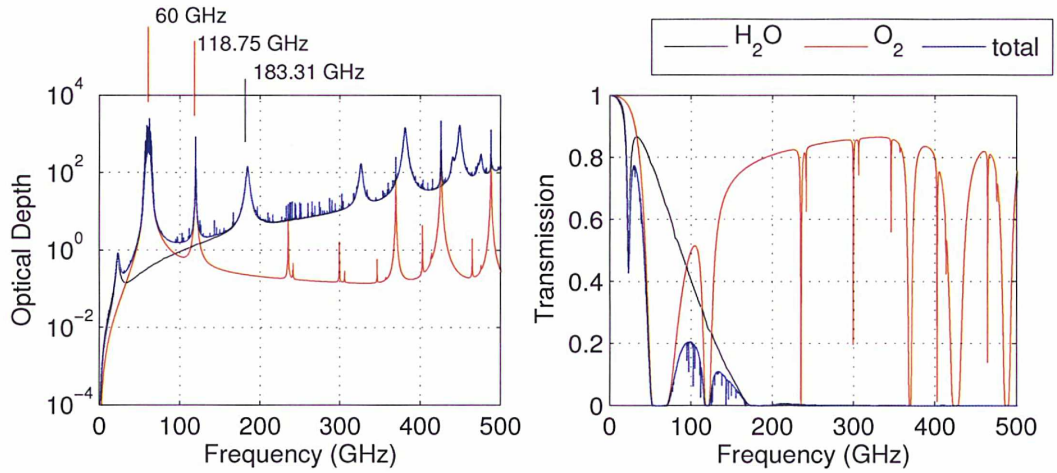

Figure 3.3: The optical thickness (left) and the transmittance (right) in a typical tropical atmosphere populated by H_2O only, O_2 only and by the main atmospheric constituents (H_2O, O_2, N_2 and O_3) labeled as total, as observed by a space-born instrument in the microwave region, at nadir.

Figure 3.3 shows the main absorption lines and the continuum spectrum in the region of interest for this thesis (1-500 GHz). The main absorption lines for microwave instruments are the 183.31 GHz water vapour line and the oxygen lines at 60 and 118.75 GHz. For example, the 183.31 GHz water vapour line is used by many instruments for humidity profiling. Frequencies above 200 GHz exhibit a strong absorption continuum by water vapour resulting in low transmittance down to the surface.

3.1.6 Single-Particle Interaction with EM Radiation

Like molecules, particles emit and absorb electromagnetic radiation too. In remote sensing of clouds and rain, the scattering, absorption, and emission by hydrometeors in clouds are all relevant depending on the cloud phase, hydrometeor particle size, and frequency.

In EM terms, a single hydrometeor in the atmosphere can be described as a collection of electric charges. A monochromatic oscillating EM field incident on this particle excites the charges and induces them to oscillate at its frequency and to radiate secondary EM waves through what is known as elastic scattering (where the frequency does not change)[1]. The total scattered field is the vector sum of the incident and scattered waves. In the case that the charges oscillate out of phase with the incident field, some of the incident energy is dissipated through absorption. At the same time, the particles themselves emit radiation in all directions due to internal energy state transitions in a process known as thermal emission.

This section lays the necessary mathematical foundations to describe scattering, absorption and emission processes that occur when an EM plane wave traveling through an infinite, homogenous, non-absorbing, linear, isotropic medium, interacts with a particle with a refractive

[1]It is assumed that electromagnetic scattering occurs at the same frequency of the incident radiation. This assumption excludes certain scattering phenomena that are not relevant to this thesis such as fluorescence.

index different from that of the medium. The refractive index is defined as

$$n = n_R + in_I = c\sqrt{\epsilon\mu} \tag{3.15}$$

where ϵ and μ are the dielectric permittivity and the magnetic permeability of the medium respectively. Note that for remote sensing of the atmosphere, μ is approximately constant and equal to the magnetic permeability of vacuum, μ_0 ($\mu_0 = 1$). In addition to the refractive index of the particle, the scattering and absorption properties depend on its size, shape, orientation, and the frequency of radiation.

The scattering of radiation is a conservative process where radiation is re-directed from its original trajectory. The nature of scattering depends on the wavelength of radiation, the size of the object, its shape, and its refractive index. In the microwave region, the scattering generated by the molecules of atmospheric constituents is negligible and thus neglected. It is the scattering due to hydrometeors that is of interest to study in the microwave, sub-millimeter and millimeter regions.

Solving Maxwell's equations it can be shown that the scattered EM field (E^s) is related to the incident EM field ($E^i = E^{i0} \exp ik_1 r$) by the complex scattering amplitude matrix **S**:

$$\begin{pmatrix} E_v^s(r\mathbf{n}) \\ E_h^s(r\mathbf{n}) \end{pmatrix} = \frac{\exp ik_1 r}{r} \begin{pmatrix} S_{11} & S_{12} \\ S_{21} & S_{22} \end{pmatrix} \begin{pmatrix} E_v^{i0} \\ E_h^{i0} \end{pmatrix} \tag{3.16}$$

The 2 x 2 amplitude scattering matrix accounts for the transformation of the h- and v-components of the incident plane wave (E_v^i, E_h^i) to those of the scattered spherical wave (E_v^s, E_h^s). In terms of the Stokes parameters Equation 3.16 can be rewritten as

$$\mathbf{I}^{\mathrm{S}}(r\mathbf{n}^{\mathrm{S}}) = \frac{\mathbf{Z}(\mathbf{n}^{\mathrm{S}}, \mathbf{n}^{\mathrm{i}})}{r^2}\mathbf{I}^{\mathrm{i}} \tag{3.17}$$

where the phase matrix **Z** (4 x 4 matrix) gives the transformation between the scattered Stokes vector and the incident Stokes vector for $\mathbf{n^S} \neq \mathbf{n^i}$. The phase matrix **Z** is also known as the scattering phase function and it represents the distribution of radiation after a beam of radiation is scattered (or, equivalently, the probability density function for a single scattering event). Only 7 of the 16 elements of the scattering phase function are independent, and elements Z_{ij} are real values with dimension of area.

Extinction is defined as a change of the EM wave in the exact forward direction and it can be described by a 4 x 4 extinction matrix, **K**.

It is useful to characterize the efficiency of particles to scatter, absorb, or emit. This can be done via the optical cross sections. Cross sections are real values and have dimensions of area. They depend on the properties of incident radiation, i.e., direction, frequency and state of polarization, and also on the microphysical properties of the particle in question, i.e., shape, refractive index (which in turn is a function of temperature), orientation. The product of the incident monochromatic energy flux and the scattering cross section (absorption cross section) gives the total monochromatic power removed from the incident wave as a result of the scattering into all directions (absorption). The total extinction cross section $\mathrm{C}_{\mathrm{ext}}$ is the sum of the absorption and scattering cross sections:

$$C_{\mathrm{ext}} = C_{\mathrm{abs}} + C_{\mathrm{sca}} \tag{3.18}$$

One can express the extinction cross section in terms of the extinction matrix elements and the incident Stokes vector. Similarly, the scattering cross section can be expressed in terms of the phase matrix elements and the incident Stokes vector.

3.1.7 Multiple Particles: Single Scattering Approximation

The previous equations describe the scattering, absorption and emission of an individual particle. It is important to consider a large number of particles, but solving Maxwell's equations for a large number of particles becomes computationally very expensive. It is possible to simplify the problem and consider a large group of scattering particles as a single medium. This approximation is valid under the following assumptions:

1. Each of the particle is placed in the far-field of the others and of the observation point.
2. Individual particle scattering is incoherent.

As a consequence of the second assumption, the Stokes parameters of the partial waves can be added disregarding phase. Applying the single scattering approximation means summing up the fields generated by the individual particles in response to the external field in isolation from all other particles.

Consider a volume element containing N particles and assume that N is small such that the mean distance between the particles is much greater than either the average particle size or the incident radiation wavelength. Under this assumptions, the extinction, absorption and scattering cross sections can be expressed as:

$$C_{\text{ext}} = \sum_{n=1}^{N} (C_{\text{ext}})_n = N < C_{\text{ext}} > \tag{3.19}$$

$$C_{\text{sca}} = \sum_{n=1}^{N} (C_{\text{sca}})_n = N < C_{\text{sca}} > \tag{3.20}$$

$$C_{\text{abs}} = \sum_{n=1}^{N} (C_{\text{abs}})_n = N < C_{\text{abs}} > \tag{3.21}$$

The extinction matrix $\mathbf{K}$, the Stokes phase matrix $\mathbf{Z}$ and the emission vector $\mathbf{a}$ can similarly be expressed

$$\mathbf{K} = \sum_{n=1}^{N} \mathbf{K}_n = N < \mathbf{K} > \tag{3.22}$$

$$\mathbf{Z} = \sum_{n=1}^{N} \mathbf{Z}_n = N < \mathbf{Z} > \tag{3.23}$$

$$\mathbf{a} = \sum_{n=1}^{N} \mathbf{a}_n = N < \mathbf{a} > \tag{3.24}$$

An accurate and computationally affordable calculation of the single scattering properties, i.e. the extinction, absorption and scattering properties of an individual particle, is the first

step in radiative transfer calculations for remote sensing of clouds where scattering, absorption, and emission can all be relevant, depending on cloud phase, particle size, and frequency.

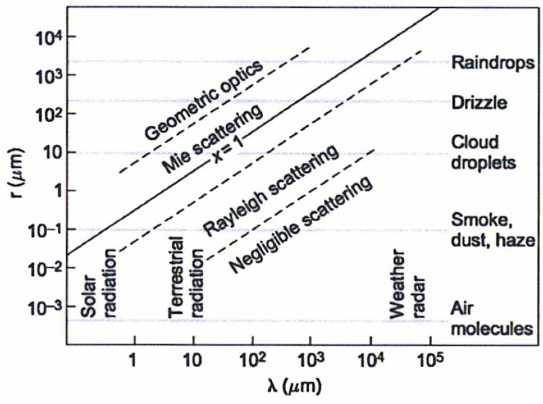

Figure 3.4: The scattering regime as a function of wavelength and particle radii. From Wallace and Hobbs (2006).

Several regimes can be identified to calculate the single scattering properties of particles at a given wavelength (λ) as seen in Figure 3.4. Their validity depends on the dimensionless size parameter

$$x = \frac{2\pi r}{\lambda} \tag{3.25}$$

of the given particle of size r. Here, the characteristic size r may be the radius of a spherical particle or the volume equivalent radius of a non-spherical particle. Table 3.1.7 presents a quick overview of the orders of magnitude of the size parameter for the atmospheric species of relevance for this thesis project. Note that frozen phase particles relevant for this work scatter in the Mie regime.

Type	Characteristic radius (μm)	Size Parameter $x = 2\pi r/\lambda$ 20 GHz (15 mm)	90 GHz (3.4 mm)	190 GHz (1.6 mm)	300 GHz (1.0 mm)
Cloud droplets	20	8×10^{-3}	4×10^{-2}	8×10^{-2}	1×10^{-1}
Rain droplets	200	8×10^{-2}	4×10^{-1}	8×10^{-1}	1
Ice	50	2×10^{-2}	9×10^{-2}	2×10^{-1}	3×10^{-1}
Snowflakes	500	2×10^{-1}	1	2	3

Table 3.1: Size parameters for typical hydrometeors in the atmosphere.

The single-scattering properties depend on the wavelength of observation, the size, shape and orientation of the particles in question. The main difficulties in computing single scattering properties arise from the lack of knowledge of accurate information on the refractive properties of the particles, their size distribution and their shape. Below is a short description of the most commonly used methods relevant in the microwave region to tackle calculate the scattering properties.

Lorentz-Mie Method: For spherical particles, the classical approach is to calculate the scattering and absorption coefficients using the Lorentz-Mie equations. This is the least complex and least computationally expensive method because the single scattering properties of homogenous spheres can be described analytically by a series of spherical harmonics. The expansion coefficients to these series are only dependent on the refractive index of the sphere in question and on the size parameter $\frac{2\pi r}{\lambda}$.

T-Matrix Method: Spherical solutions as an approximation are useful for example when polarization effects are insignificant or ignored, but these assumptions may lead to large errors since large atmospheric hydrometeors tend to have non-spherical shapes. In this case, it is key to turn to more adequate methods like the T-Matrix that allows a more complex treatment of the particles. It can be easily applied to spheroids and cylinders, and to randomly and horizontally aligned particles. The T-matrix approach is based on solving Maxwell's equations numerically. The T-matrix code used in this thesis was developed by Mishchenko (2000). The readers are referred to Mishchenko (2000) for details. The T-matrix code requires information on the complex dielectric properties of the particle, its equivalent volume radius, its shape (spheroid or cylinder), its aspect ratio and the frequency of radiation. The aspect ratio is defined as the ratio of the diameter of the particle to its length.

Figure 3.5 shows examples of the single scattering properties as calculated by the T-matrix method for two typical atmospheric spherical particles: pure ice particles (top panels) and pure liquid spheres (bottom panels). Liquid clouds have small droplets compared to microwave wavelengths and consequently have a low scattering cross section but a very high absorption cross section resulting from the dielectric properties of water drops. Ice cloud particles do not absorb much compared to liquid particles, but they can scatter strongly as the radius of the particle increases with respect to the wavelength of observation. The larger the particles, the larger their scattering influence. As it can be seen, for liquid water the dominant process is absorption, while for ice crystals it is scattering above a certain frequency threshold which varies with particle size. This is the main reason for which lower microwave frequencies are mostly sensitive to water emission while higher frequencies are sensitive to frozen hydrometeors. Note that higher frequencies are sensitive to both liquid and frozen hydrometeors. However, from instruments onboard satellites, the ice phase upper in the atmosphere is seen first and its optical opacity masks the liquid phase lower in the atmosphere. Consequently, the higher frequencies are essentially affected by the frozen phase when present.

3.1.8 Vector Radiative transfer equation (VRTE)

The radiative transfer equation under local thermodynamic equilibrium can be written in its general expression:

$$\begin{aligned}\frac{d\mathbf{I}(\mathbf{n},\nu)}{ds} = &- < \mathbf{K}(\mathbf{n},\nu,T) > \mathbf{I}(\mathbf{n},\nu) + < \mathbf{a}(\mathbf{n},\nu,T) > B(\nu,T) \\ &+ \int_{4\pi} d\mathbf{n}' < \mathbf{Z}(\mathbf{n},\mathbf{n}',\nu,T) > \mathbf{I}(\mathbf{n}',\nu)\end{aligned} \tag{3.26}$$

where **I** is the radiation intensity per unit area, <**K**> is the ensemble-averaged extinction matrix, <**a**> is the ensemble-averaged absorption vector, B is the Planck function, <**Z**> is the ensemble-averaged phase matrix, ν is the frequency, T is the temperature, and ds is an element of the propagation path and **n** is the propagation direction. Over the distance of the propagation path, radiation is attenuated through extinction as described by the first term in Equation 3.26. Thermal emission by gas and particles in the atmosphere is described by the second term in Equation 3.26 and the last term is the scattering source term, adding the amount of radiation which is scattered from all directions **n'** into the propagation direction **n**.

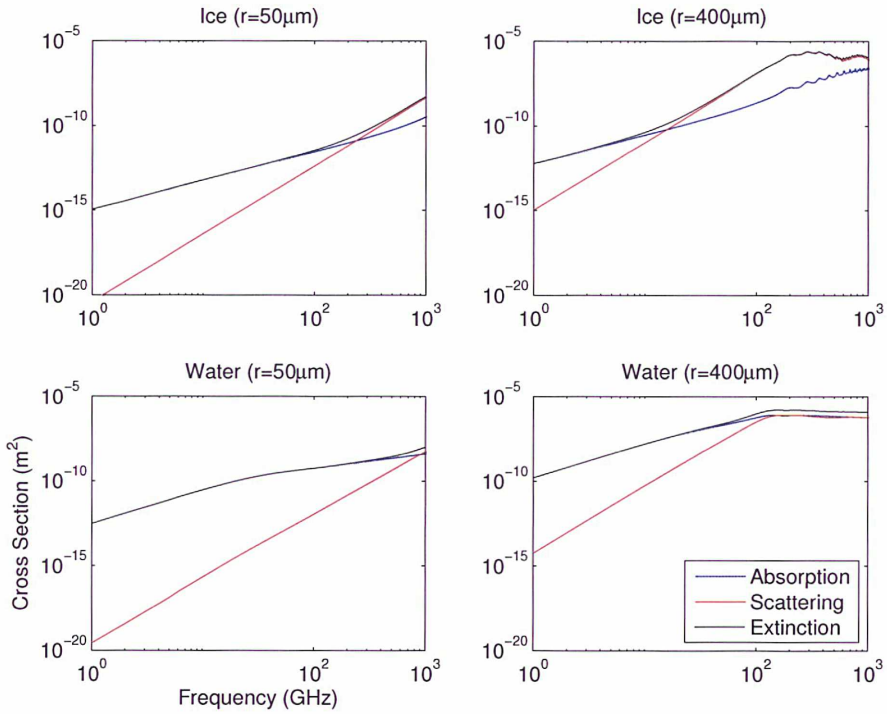

Figure 3.5: The scattering, absorption and extinction cross sections as calculated for pure ice and pure liquid spheres by the T-matrix for frequencies between 1 and 1000 GHz.

3.2 The Atmospheric Radiative Transfer Simulator (ARTS)

In remote sensing applications a solution to the VRTE (Equation 3.26) needs to be found. The solution for the VRTE for a non-scattering atmosphere can be found analytically, but when scatterers are present, a numerical approach needs to be applied to find a solution. Radiative transfer simulations performed in this thesis were conducted with the Atmospheric Radiative Transfer Simulator (ARTS). ARTS is a very flexible tool, capable of modelling different atmospheric conditions and different sensor configurations. Its development places emphasis on modularity, extendibility and generality (Eriksson et al., 2011a). It is a community code primarily developed and maintained between Chalmers University of Technology and Lulea University of Technology. ARTS is publicly available, along with extensive documentation.

ARTS is well validated (Melsheimer et al., 2005; Buehler et al., 2006a; Saunders et al., 2007) and used primarily for the analysis of ground-based and satellite-based measurements in the millimeter/sub-millimeter spectral range (Urban et al., 2005; John and Buehler, 2005, 2004; Buehler et al., 2007a). Historically, ARTS was developed in the context of the treatment of cloud-affected data from limb sounders such as ODIN (Frisk et al., 2003) and the ESA mission proposal CIWSIR (Buehler et al., 2007a), a sub millimeter instrument introduced in Section 1.4.2 for the characterization of ice clouds. A radiative transfer model that could simulate the scattering by ice particles was needed for these missions. ARTS has also been used

in the infrared spectral range (Buehler et al., 2006b; John et al., 2006).

Before this thesis, ARTS had not been used for the simulation of detailed realistic scenes with a large variety of hydrometeor species. It was essentially limited to the simulations of cirrus clouds. During this thesis, intensive tests have been performed for simulations with large hydrometeors frozen and liquid, talking also into account the surface parameters for down-looking satellite geometry. Significant improvements have been made with the ARTS team to extend its capabilities.

This section aims at introducing some basic concepts and definitions used in ARTS. The key features in ARTS are:

- **Atmosphere:** the main vertical coordinate with which atmospheric quantities are defined is pressure, but another vertical coordinate is needed from a geometrical perspective (e.g. to determine the propagation paths through the atmosphere). This other vertical coordinate is the geometrical altitude. ARTS allows the treatment of 1-D, 2-D and 3-D atmospheres, where 1-D and 2-D can be seen as special cases of 3-D. Concerning this thesis, simulations were conducted in 1-D and 3-D. The 3-D case is the most general case, where atmospheric grids vary in all three spatial coordinates of a spherical coordinate system, as in a true atmosphere (radius, latitude and longitude). The term 1-D is used here for simplicity, but it is not a true 1-D atmosphere that extends indefinitely along a line, rather it is a spherically symmetric atmosphere as shown in Figure 3.6. This means that the atmospheric fields and the surface extend in all three dimensions, but have no latitude or longitude variation, i.e. the radius of the geoid, the surface and all the pressure levels are constant around the globe.

- **Observation geometry:** ARTS flexible sensor positioning allows the simulation of sensors mounted on any kind of platform (satellites, aircrafts, or ground based measurements). In this thesis down-looking sensors either at nadir, or at an angle off nadir are simulated. The sensor is described with its position (altitude above the surface, latitude and longitude) and zenith angle.

- **Polarization:** ARTS allows the computation of the full Stokes vector. If polarization is ignored only the intensity, I, of the Stokes vector is calculated and the radiative transfer equation becomes scalar.

- **Gas Absorption:** ARTS provides an interface between radiative transfer calculations and the needed absorption matrix at each point in the atmosphere. ARTS can calculate the absorption coefficients of atmospheric matter in two different ways: on-the-fly absorption within the radiative transfer calculation or preparing a gas absorption lookup table. On-the-fly line-by-line calculations are very computationally expensive as the contributions of many absorption lines are read from line catalogues, e.g. the HITRAN database, and summed up to calculate the gas absorption at each atmospheric grid point along the propagation path. The other approach is the absorption lookup table. Gas absorption coefficients do not depend directly on the position but on the atmospheric state variables: pressure, temperature and trace gas concentrations. The idea is for absorption to be pre-calculated for a discrete combination of state variables, stored in a lookup table, and then interpolated to the actual atmospheric state variables. Since the pressure dependence of the calculation is the most important dependence, the calculated absorption cross sections are stored in a pressure grid for a reference temperature and interpolated

in pressure for intermediate values. A set of temperature perturbations for each pressure level can also be stored.

- **Scattering:** In ARTS, a cloudy atmosphere can be defined by what is referred as a "Cloudbox". Everything outside the Cloudbox is handled as clear sky. Clear sky is defined as an atmosphere free of any kind of scattering particle. On the contrary, the Cloudbox does have scattering particles. This approach saves computational time as scattering calculations are limited to the part of the atmosphere containing hydrometeors. The Cloudbox is defined to have its limits at the involved grids, e.g. the vertical limits are two pressure levels. Figure 3.6 shows schematically a 1-D atmosphere including a Cloudbox. It is possible to define several particle types - a particle type being either a specified particle or a specified particle size distribution. For each particle type, a data file containing the single scattering properties, calculated externally (by the T-matrix in this thesis: see Section 3.1.7), and the appropriate particle number density field is required.

- **Surface properties:** In window channels particularly, it is very important to define the surface properties below the modelled atmosphere, as it emits and reflects radiation where the propagation path intersects with it. ARTS is very flexible in this matter and one can select to represent the surface by a blackbody, a specular reflecting surface, or a Lambertian surface. In this thesis, a more accurate description of the model surface has been incorporated to ARTS as an external tool for both ocean and land (see Section 4.5).

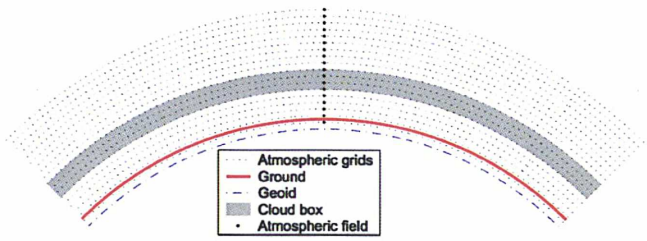

Figure 3.6: Schematic of a 1-D atmosphere with a Cloudbox. The atmosphere is spherically symmetric, meaning that the radius of the geoid, the surface and all the pressure levels are constant around the globe. In this case the Cloudbox is between two pressure levels (from The ARTS User Guide).

The sections below, discuss radiative transfer in ARTS more closely. Radiative transfer in ARTS calculates monochromatic radiances by solving the VRTE (Equation 3.26). For each specified frequency, monochromatic calculations are performed along the path of the electromagnetic wave through the atmosphere. This propagation path is defined by the sensor position and its viewing direction to the point where the beam actually starts from. At each intersection with the atmospheric grid, the VRTE is solved using the atmospheric composition that is averaged between the current grid values and the ones at the next intersection point. Figure 3.7 shows a schematic of the basic ARTS inputs relevant to this thesis. Everything shown outside

the blue dashed lines are inputs needed for ARTS. A large amount of the work conducted during this thesis involved studying this inputs.

Two radiative transfer domains can be identified from Figure 3.7, clear sky radiative transfer and cloudy sky (scattering) radiative transfer.

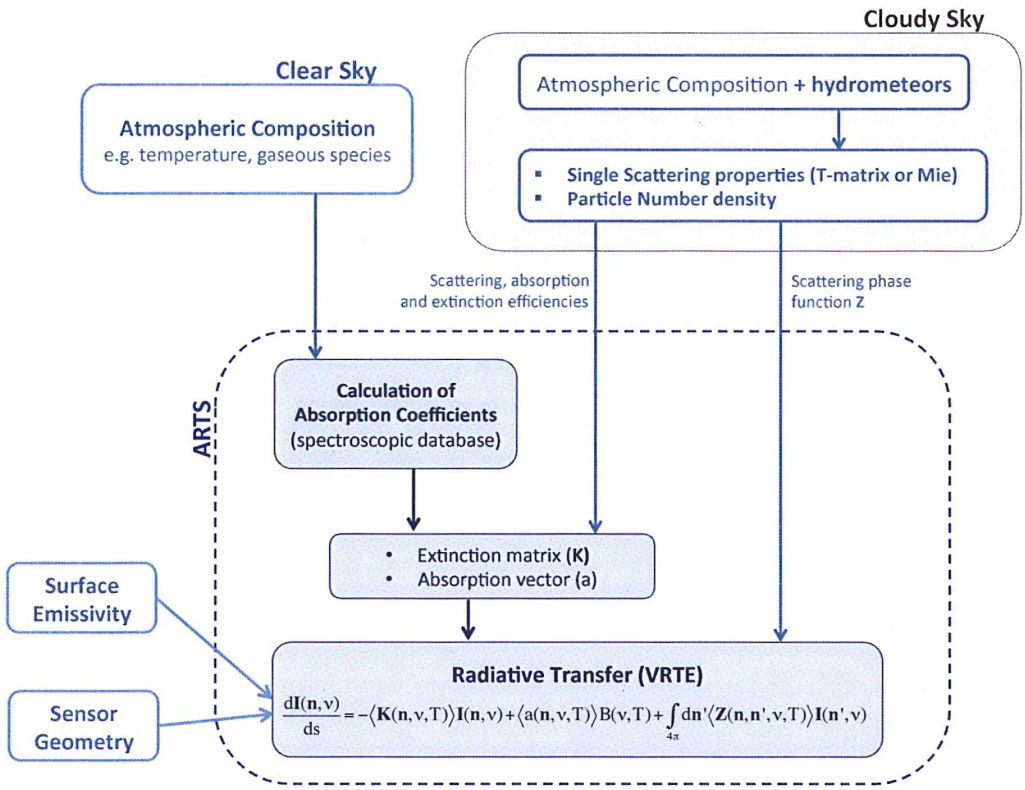

Figure 3.7: Schematic diagram of the basic inputs that were coupled to ARTS in this thesis for radiative transfer calculations under clear sky and cloudy sky conditions.

3.2.1 Clear Sky Radiative Transfer

ARTS sets the Stokes components for all frequencies to equal the radiative background and then solves the radiative transfer equation from one point of the propagation path to the next, until the end point is reached. In clear sky calculations, the general VRTE (Equation 3.26) needs to be solved while omitting the scattering integral and particle contributions to the extinction matrix and the absorption vector. The VRTE is solved for each specified frequency at each intersection of the propagation path with the atmospheric grid. In the context of this thesis, realistic surface emissivities, the sensor geometry and a correct description of the atmospheric composition are key in reference to the inputs described in Figure 3.7.

3.2.2 Cloudy Sky Radiative Transfer

Two different approaches are implemented within ARTS to solve the VRTE and determine the outgoing radiation field at the boundary of the Cloudbox. The role of the scattering calculations is to determine the outgoing intensity field of the Cloudbox. The outgoing intensity field is then used as the radiative background. Since there is no analytical solution to the VRTE under the scattering scheme, numerical methods are required. Two different approaches are implemented within ARTS: the backward Monte Carlo scheme and the Discrete Ordinate Iterative (DOIT) approach. Both schemes are described below.

The Polarized Discrete Ordinate Iterative Method (DOIT)

The DOIT module can be implemented in 1D and 3D atmospheres (Sreerekha et al., 2006), but it is strongly recommended to be used only in 1D atmospheres, the Monte Carlo method being a much more efficient tool for 3D calculations. DOIT yields the whole radiation field, meaning that a full account of the polarization signal is given. A description of the method is given in this section and for more information please refer to the ARTS User Guide, Emde et al. (2004) and Emde (2005):

DOIT applies an iterative method to solve the monochromatic vector radiative transfer equation (VRTE) shown in Equation (3.26). The scattering integral in the VRTE is solved with a first guess field, $\mathbf{I}^{(0)}$ (defined here to be the *old radiation field*), determined by the boundary conditions as given by the radiation coming from the clear sky part of the atmosphere and traveling into the cloud box. Inside the Cloudbox an arbitrary field can be chosen as a first guess. The closer the first guess field is to the solution field, the less the number of necessary iterations. The scattering integral in Equation (3.26) (i.e. $\int_{4\pi} d\mathbf{n}' < \mathbf{Z}(\mathbf{n}, \mathbf{n}', \nu, T) > \mathbf{I}(\mathbf{n}', \nu)$) is solved using the first guess field to obtain the first guess scattering integral field $< \mathbf{S}^{(0)} >$. The integration is performed over all incident directions $\mathbf{n}$' for each propagation direction $\mathbf{n}$. The evaluation of the scattering integral is done for all grid points inside the cloud box. Figure 3.8(a) gives a schematic approach to the iterative method described below. Figure 3.8(b) shows radiation arriving at a grid point $\mathbf{P}$ from the direction $\mathbf{n}$' and propagating into direction $\mathbf{n}$. The radiation arriving at $\mathbf{P}$ from $\mathbf{n}$' can be obtained by solving the linear differential equation

$$\frac{d\mathbf{I}^{(1)}}{ds} = - < \overline{\mathbf{K}} > \mathbf{I}^{(1)} + < \overline{\mathbf{a}} > \overline{B} + < \overline{\mathbf{S}^{(0)}} > \tag{3.27}$$

where $< \overline{\mathbf{K}} >$, $< \overline{\mathbf{a}} >$, $\overline{B}$ and $< \overline{\mathbf{S}^{(0)}} >$ are averaged quantities of the extinction matrix, the absorption vector, the Planck function, and the first guess scattering integral respectively. These are averaged quantities because to calculate the radiative transfer from $\mathbf{P}$' towards $\mathbf{P}$ all quantities are approximated by taking the averages between the values at $\mathbf{P}$' and $\mathbf{P}$. The average value of the temperature is used to get the averaged Planck function $\overline{B}$. Equation 3.27 can be solved analytically for constant coefficients. The solution to equation 3.27 is found analytically using a matrix exponential approach (for further details on how the solution to the linear differential equation is found using this approach please refer to the ARTS User Guide and Emde et al. (2004); Emde (2005):

$$\mathbf{I}^{(1)} = \exp^{-<\overline{\mathbf{K}}>s} \mathbf{I}^{(0)} + (1 - \exp^{-<\overline{\mathbf{K}}>s}) < \overline{\mathbf{K}} >^{-1} (< \overline{\mathbf{a}} > \overline{B} + < \overline{\mathbf{S}^{(0)}} >) \tag{3.28}$$

where $\mathbf{I}^{(0)}$ is the initial Stokes vector and $\mathbf{I}^{(1)}$ is the first iteration scalar intensity field. The radiative transfer step from $\mathbf{P}'$ to $\mathbf{P}$ is calculated, therefore $\mathbf{I}^{(0)}$ is the incoming radiation at

$\mathbf{P}'$ into direction (θ'_l, ϕ'_m), which is the first guess field interpolated on $\mathbf{P}'$. This is done for all points inside the cloud box in all directions. The resulting set of Stokes vectors ($\mathbf{I}^{(0)}$ for all points in all directions) is the first order iteration field, $\mathbf{I}^{(1)}_{ijlm}$ (the new radiation field). After each iteration a convergence test is performed where the new radiation field is compared to the old radiation field. If the absolute difference for all successive Stokes vectors is smaller than a requested accuracy limit (the accuracy limit being set by the user and containing convergence limits for all Stokes components), the convergence test is fulfilled and a solution to the VRTE equation is found. If the convergence test is not fulfilled, the first order iteration field is copied to the variable holding the old radiation field, and it is used to evaluate again the scattering integral at all cloud box points. As long as the convergence test is not fulfilled the scattering integral field and higher order iteration fields are calculated.

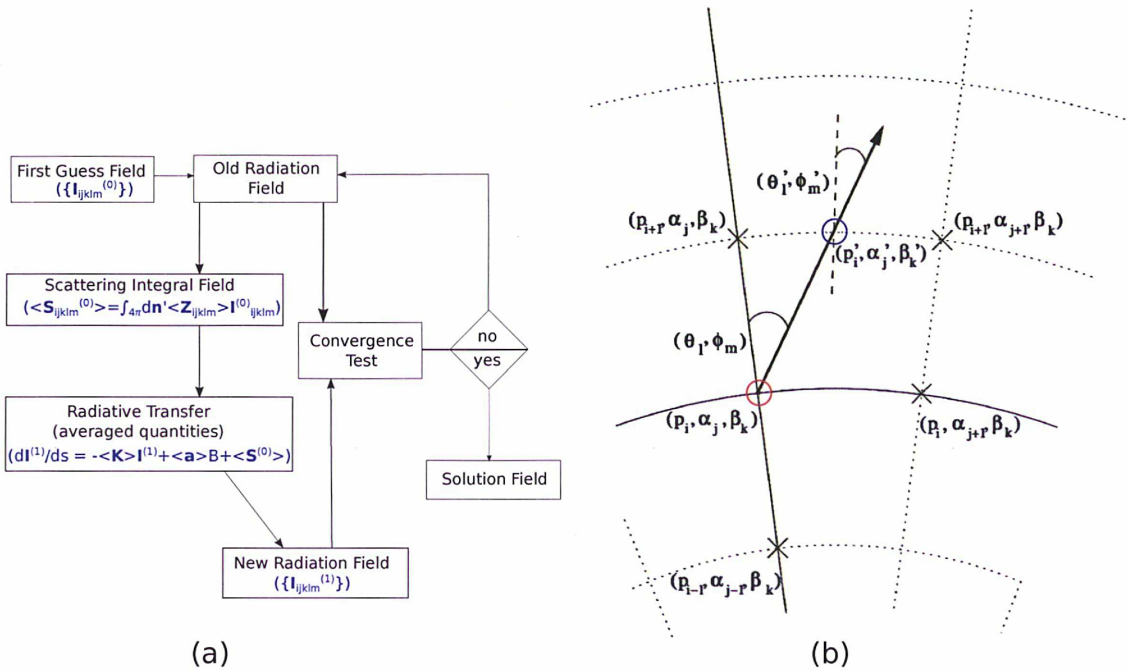

Figure 3.8: (a) Schematic of the iterative method to solve the VRTE in the Cloudbox (adapted from the ARTS User Guide). (b) Path from a grid point (defined by pressure p, latitude α, and longitude β) (p_i, α_j, β_k) (denoted o in the figure) to the intersection point $(p'_i, \alpha'_j, \beta'_k)$ (denoted o in the figure) with the next grid cell boundary. The viewing direction is specified by (θ_l, ϕ_m) at o or by (θ'_l, ϕ'_m) at o. Adapted from Emde (2005).

The Monte Carlo Method

The ARTS Monte Carlo scattering module (ARTS-MC) offers an efficient method for polarized radiative transfer calculations in 3D atmospheres. The idea here is to give the reader a general

idea about ARTS-MC. For more detail, please refer to the extensive literature on Monte Carlo methods, the ARTS User Guide, and to Davis et al. (2007) where the ARTS-MC method is presented.
A reference for the development of the Monte Carlo method used in ARTS (ARTS-MC) is the Backward-Forward Monte Carlo (BFMC) model described in Liu et al. (1996). In BFMC, photon paths are traced backwards from the sensor, with scattering angles and path lengths randomly chosen from probability density functions determined by the scattering phase function, and a scalar extinction coefficient respectively. The phase matrices for every scattering event and scalar extinction are then sequentially applied to the source Stokes vector to give the Stokes vector contribution for each photon. The difference between the ARTS-MC and the BFMC model is that BFMC can not handle a non-diagonal extinction matrix, which means it does not consider polarization fully. The ARTS-MC can.

Davis et al. (2007) gives a full mathematical account of the algorithm and of the probability density functions used to determine the necessary propagation paths.

The estimated error of the Cloudbox exit Stokes vector is strongly dependent on the optical thickness in the line of sight (i.e. ice water path of the scattering domain), and relatively independent on particle type and orientation (Davis et al., 2007). Although the absolute error in polarization difference is generally lower than that of total radiance, the relative error is much higher. It is suggested that where accurate Q determination is needed, the number of photons used in the simulations be increased. CPU time is strongly dependent on the optical thickness in the light of sight too (Davis et al., 2007). Additional CPU time is also necessary when dealing with horizontally aligned particle orientations.

Chapter 4

Preparing for Realistic Radiative Transfer Simulations of Complex Scenes in the Microwave Region with ARTS

This section describes the tools that were coupled with ARTS in this thesis in order to run simulations of realistic scenes observed by the instruments described in Chapter 2. Specifically, the realistic scenes of interest for this thesis are characterized by the presence of large frozen particles and the simulations include surface sensitive channels. As discussed in Section 3.2, ARTS has been mostly used so far for clear sky and cirrus cloud simulations (i.e. very small ice particles) at sub-millimetre and millimetre channels where the surface contribution needs not to be taken into account realistically. In this thesis, and as shown schematically in Figure 4.1, ARTS is coupled with the necessary tools to evaluate its radiative transfer methods for a large range of meteorological situations. A brief summary of the main points listed in Figure 4.1 that will be explored throughout this chapter, is given below.

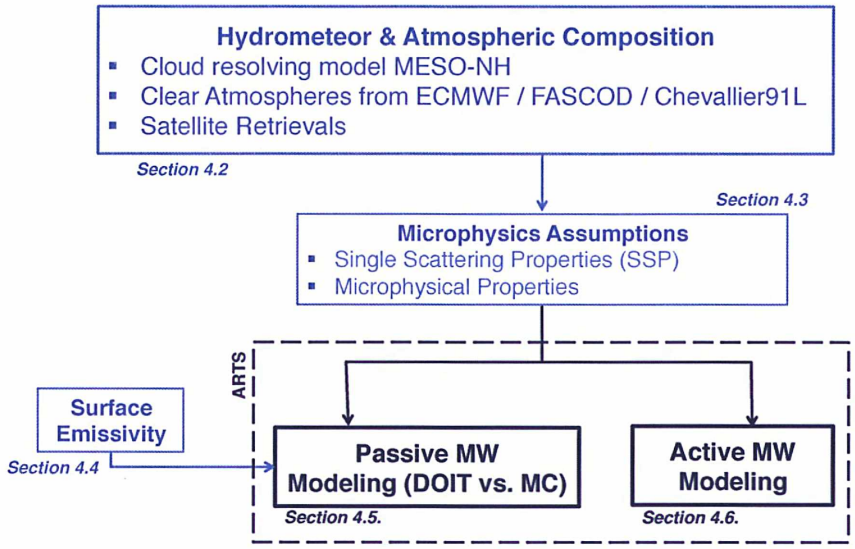

Figure 4.1: Schematic diagram showing the main tools that were coupled to ARTS in this thesis.

Atmospheric and hydrometeor profiles describing the state of the atmosphere are the main inputs to simulations. In this thesis, the following realistic atmospheric descriptions are used:

- **Cloud mesoscale model Meso-NH:** Atmospheric variables, together with information on the population of hydrometeor species in the atmosphere, can be taken from a cloud mesoscale model output. Outputs from the cloud mesoscale model Meso-NH are selected in this thesis to perform realistic simulations of coincident satellite observations. Meso-NH simulates the atmospheric state and the evolution of the mixing ratios of six water species (water vapor, cloud droplets and rain droplets, pristine ice, snow aggregates and graupel). Refer to Section 4.1 for more detail.

- **Atmospheric composition from databases:** One dimensional atmospheric data profiles describing the state of the atmosphere (pressure, temperature, gas vertical concentrations) are also taken from a number of different databases in this work: (1) the Fast Atmosphere Signature Code (FASCOD) profiles for typical tropical, midlatitude and arctic atmospheres (Anderson et al., 1986), (2) the Chevallier91L database (Chevallier et al., 2006), and (3) ancillary data from the European Center for Medium-Range Weather Forecasts (ECMWF) interpolated to each CloudSat CPR bin, i.e. the CloudSat-AUX product (Niu and Li, 2011). The term one dimensional profile is used here because the variability of the atmospheric variables is described only on a vertical grid, with pressure as a single coordinate.

As illustrated in Figure 4.1, assumptions on the microphysical properties are needed to describe the hydrometeor species populating the atmosphere and calculate their interaction with the radiation:

- **Hydrometeor Microphysical Properties:** Assumptions on the microphysical parameters are needed to calculate the Single Scattering Properties (SSP) of the simulated hydrometer profiles. Parameters such as the dielectric properties, the density, the shape, the orientation and the particle size distribution are key. These parameters are discussed in detail in Section 4.2. Note that some of these parameters, such as the particle size distribution, are indirectly provided by Meso-NH as detailed in Section 4.1.

A realistic description of the radiative properties of the surface is important for surface sensitive channels in the microwave region:

- **Surface Emissivity:** Section 4.5 describes the emissivity modules coupled with ARTS in this thesis: (1) FASTEM for ocean emissivities (English and Hewison, 1998), and (2) TELSEM for continental land (Aires et al., 2011).

Active microwave simulations are important to analyse the observations from the active sensors. Section 4.4 presents the recent developments made with the ARTS team to simulate the active and passive signals consistently and better benefit from potential synergy . The work performed in this thesis uses this new internal module for the first time to exploit the active/passive synergy.

4.1 Real Case Atmospheric Scenarios

4.1.1 The Cloud Mesoscale Model Meso-NH

The non-hydrostatic mesoscale cloud model Meso-NH (Lafore et al., 1998), jointly developed by Météo-France and the Centre National de la Recherche Scientifique (CNRS), is a research model. The motivation for coupling Meso-NH with ARTS is to perform realistic simulations for different scenes, and to evaluate them with satellite observations in the microwave region.

Meso-NH can provide the first steps for radiative transfer simulations by offering hydrometeor and atmospheric profiles of real scenes. Its microphysical scheme predicts the evolution of the mixing ratios (mass of water per mass of dry air) of five hydrometeor categories: cloud droplets, rain drops, pristine ice crystals, snowflakes, and graupel. Meso-NH outputs include a full description of the atmospheric parameters (pressure, temperature, and mixing rations for the water vapor, and the five hydrometer categories). The multiple interactions operating between the different water species are accounted for through the parameterization of 35 microphysical processes including nucleation, conversion, riming and sedimentation. Meso-NH performance has been assessed in the past using space-borne sensors at various wavelengths (Chaboureau et al., 2000; Chaboureau et al., 2008; Wiedner et al., 2004; Meirold-Mautner et al., 2007) showing that neither strong nor systematic deficiencies are present in the microphysical scheme and in the prediction of the precipitating hydrometeor contents.

The physical properties of hydrometeors are described in terms of the particle size distribution (PSD). The assumptions made on the PSD of each of the individual species in Meso-NH is described in detail in Lafore et al. (1998) and Pinty and Jabouille (1998). All species are assumed to be spheres of diameter D, although the respective mass-size relations implicitly assume non-sphericity. The concentration of the PSD is parametrized with a total number concentration N given by

$$N_h = C\lambda_h^x \tag{4.1}$$

where C and x are empirical constants derived from ground and in-situ measurements (see Table 4.1), λ_h is known as the slope parameter of the size distribution, and the subscript h denotes the hydrometeor category. Two special cases are drawn from Equation 4.1: (a) for $x = 0$ the total number concentration is held fixed, and (b) for $x = -1$ the total number concentration follows a simpler two-parameter exponential size distribution, also known as the Marshall-Palmer distribution (Equation 4.5 introduced below).

Another important relation is the mass-size relation:

$$m(D) = aD^b, \tag{4.2}$$

and the velocity-size relation:

$$v = cD^d \tag{4.3}$$

where the diameter D is in [m] and the speed v is in [ms^{-1}]. Table 4.1 describes the constants a, b, c, and d for each of the hydrometeor species.

The size distribution of the hydrometeors is assumed to follow the generalized Gamma distribution,

$$n(D)dD = N_h g(D)dD = N_h \frac{\alpha}{\Gamma(\nu)} \lambda_h^{\alpha\nu} D^{\alpha\nu-1} \exp\left(-(\lambda_h D)^\alpha\right) dD, \tag{4.4}$$

where g(D) is the normalized distribution and both α and ν are parameters as described in Table 4.1. For $\alpha = \nu = 1$, Equation 4.4 reduces to a simple exponential size distribution:

$$n(D)dD = N_{0h} \exp -(\lambda_h D)dD, \tag{4.5}$$

where N_{0h} is the intercept parameter ($N_{0h} = N_h \lambda_h$). Particle size distributions are discussed in more detail in Section 4.2.2.

The different hydrometeor mixing ratios q_h can be defined according to:

$$\rho_h q_h = \int_0^\infty m(D)n(D)dD = aN_h M_h(b), \tag{4.6}$$

where ρ_h is the density and $M_h(b)$ is given by the moment formula of the p^{th} moment of the size distribution,

$$M(p) = \frac{G(p)}{\lambda_h^p} = \frac{1}{\lambda_h^p} \frac{\Gamma(\nu + p/\alpha)}{\Gamma(\nu)}, \tag{4.7}$$

where G(p) is the generalized Gamma size distribution. The slope parameter can be deduced from Equation 4.6 together with Equations 4.1 and 4.7,

$$\lambda_h = \left(\frac{\rho q_h}{aCG(b)} \right)^{\frac{1}{x-b}} \tag{4.8}$$

Table 4.1: Parameters of the Meso-NH microphysical scheme. Equations are given in mks units

Category	α	ν	a	b	c	d	C	x
q_c (cloud)	3	3	524	3	3.2 x 10^7	2		
q_i (ice)	3	3	0.82	2.5	800	1		
q_s (snow)	1	1	0.02	1.9	5.1	0.27	5	1
q_g (graupel)	1	1	19.6	2.8	124	0.66	5 x 10^5	-0.5
q_r (rain)	1	1	524	3	824	0.8	10^7	-1

4.1.2 Case Studies

In this thesis two specific midlatitude scenes are simulated. The two cases correspond to real meteorological conditions, allowing an evaluation of the quality of the simulations by comparison to coincident satellite observations. The two cases occurred during winter in Europe and covered both land and sea. The two cases are (1) a frontal case with light precipitation over the Rhine area (10 February 2000, see Figure 4.2) already analyzed with the Atmospheric Transmission at Microwaves (ATM) radiative transfer code and compared with the available AMSU-B and SSM/I satellite observations by Meirold-Mautner et al. (2007), and (2) a heavy snowfall case over France (8 December 2010) that provides the unique opportunity to compare simulations with coincident active (CloudSat) and passive (MHS and AMSR-E) satellite observations. This two case scenarios are described in detail and analyzed in Chapter 6.

Table 4.2: Overview of the Meso-NH simulation cases

Name	Event	Date	Available Satellite Observations
RHINE	Light Precipitation over Rhine	10 Feb. 2000	AMSU-B / SMM/I
FRANCE	Heavy Snowfall over France	8 Dec. 2010	MHS / CloudSat / AMSR-E

This section has introduced the mixing ratios of the different species as modeled by Meso-NH. The following section introduces the microphysical assumptions needed in conjunction with such profiles.

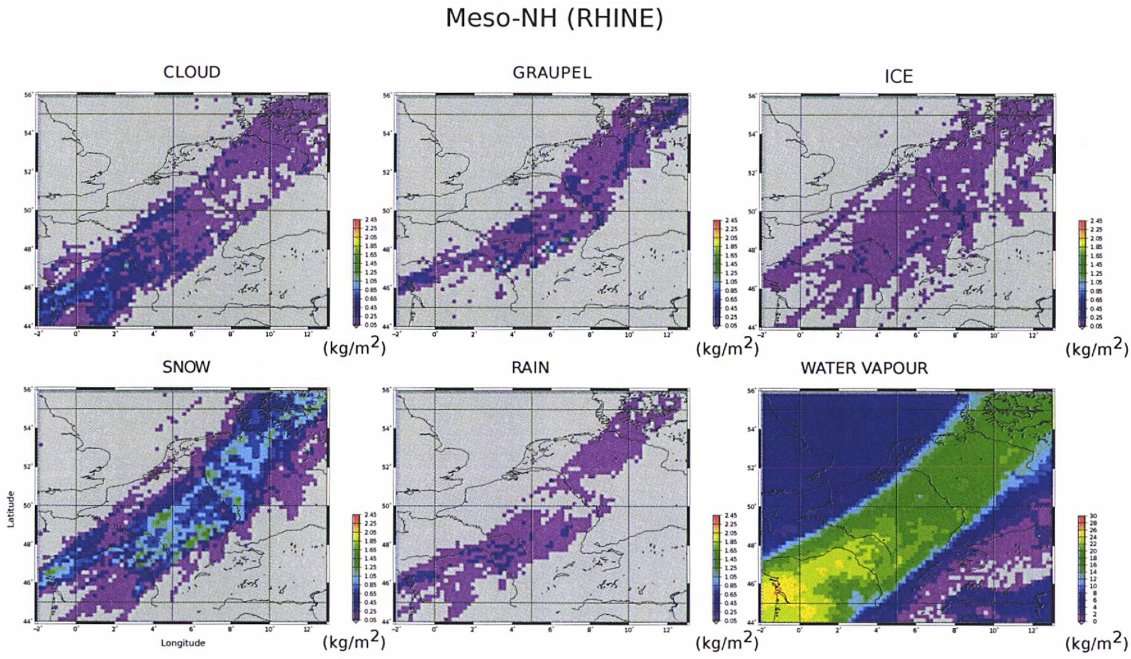

Figure 4.2: Total integrated columns (kg/m^2) of cloud, rain, ice, graupel, snow, and water vapour as simulated by Meso-NH. This simulation is a real scene where light precipitation was related to a cold front passing West Germany on the 10 February 2000 at 18:00 UTC.

4.2 Hydrometeor Microphysical Properties

Whether simulating the radiative signal from Meso-NH model outputs (see Section 4.1) or simplified cloud populations using atmospheric profiles from a database, determining the microphysical properties of the hydrometeor populations is the most important and most complex step. Realistic microphysical assumptions allow accurate single scattering properties. At microwave frequencies, ice, liquid water and mixed-phase hydrometeors have very different scattering properties due to differences in their microphysical properties (dielectric properties, density, size, shape). A detailed account of the mentioned microphysical properties follows.

4.2.1 Dielectric Properties of Hydrometeors

As discussed in Section 3.1.6, the complex dielectric properties ($\epsilon = \epsilon' + i\epsilon''$) are key parameters when calculating the scattering properties of a given particle. For example, the absorption coefficient is derived from the imaginary part of the refractive index n, which as already discussed follows simply from $n = \sqrt{\epsilon}$. The accuracy of radiative transfer computations is often limited by insufficient knowledge of the dielectric properties of the hydrometeors in question.

The dielectric properties of a substance depend both upon the incoming electromagnetic field (the frequency ν) and upon the physical properties of the substance itself (i.e., bulk properties such as composition and temperature). A brief description of the accepted models to compute the dielectric properties for pure liquid water, pure ice and and mixed phase hydrometeors (i.e. snow) is given below for the microwave frequency range.

Pure Liquid Water

Pure liquid water is the substance for which we have the most experimental permittivity data both in frequency and in temperature. The microwave region, up to approximately 20 GHz, has been fairly well explored but there are less independent experimental data in the frequency range starting at approximately 50 GHz and going up to the far infrared (25 THz).

In this work, the dielectric properties from Liebe et al. (1991) that allow calculations above 100 GHz are used. Liebe et al. (1991) provided an interpolation function for the permittivity of liquid water for frequencies between 100 GHz and 30 THz at atmospheric temperatures. This interpolation function has been used extensively by the remote sensing community and is shown in Figure 4.3 as a function of frequency for a temperature of 10^{o}C.

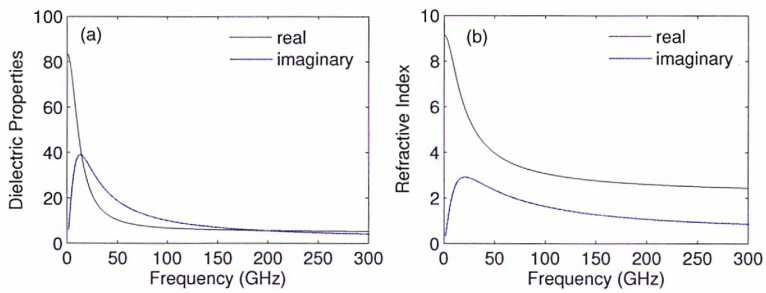

Figure 4.3: The real and imaginary parts of (a) the dielectric properties of pure liquid water according to Liebe et al. (1991) at 10^{o}C and (b) the corresponding refractive index.

Pristine Ice

Ice on the other hand is very transparent at microwave frequencies due to its very low dielectric loss. In this thesis, the dielectric properties of pure ice are calculated according to Mätzler and Melsheimer (2006) where all the available dielectric data were used to improve and test the existing dielectric models. This function is valid for frequencies between 0.01 and 3000 GHz, and for temperatures between 20.0 to 273.15 K. Figure 4.4 shows the computed dielectric properites as a function of frequency for pure ice at 0 ^{o}C, - 10^{o}C and - 20^{o}C. Ice, in contrast

with pure liquid water, has a very small imaginary component to the dielectric properties and thus much smaller absorption coefficients. Xie et al. (2009) studied the effect of ice permittivity uncertainties on the emerging brightness temperatures for AMSU-B frequencies and found that the absolute error is no more than 2 K at a zenith angle of 53^o.

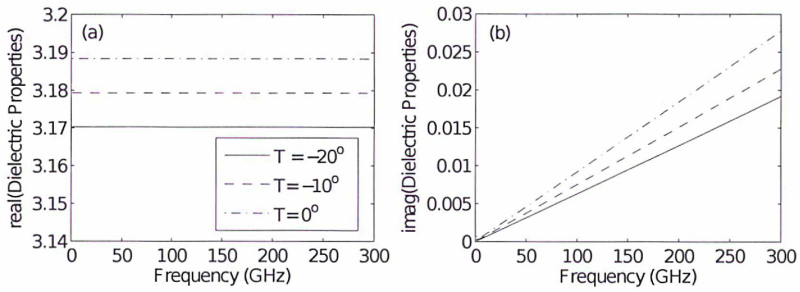

Figure 4.4: The real (a) and imaginary (b) components of the dielectric properties of pure ice as calculated using Mätzler and Melsheimer (2006) for different temperatures.

Heterogenous hydrometeors: Snowflakes and Melting Snowflakes

Natural media are heterogenous materials that can be treated as being homogenous by describing them in terms of an effective dielectric constant. In this way, frozen and melting hydrometeors can be represented by a single effective medium composed of different mixtures (ice and air for snowflakes; ice, water and air for melting snowflakes). As seen in Figure 4.5, spherical inclusions (dielectric constant ϵ_i) are embedded in a background medium (dielectric constant ϵ_e). Mixing rules are capable of calculating effective dielectric properties as a function of the constituent permittivities (ϵ_i and ϵ_e) and their fractional volumes. The aim is that this macroscopic effective permittivity describes realistically the behavior of the heterogenous material.

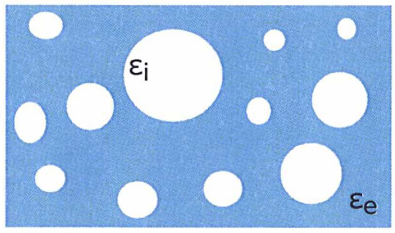

Figure 4.5: Spherical inclusions (ϵ_i) in a homogenous environment (ϵ_e).

There is a large number of mixing formulas available to compute the effective dielectric constants of mixed phase hydrometeors and their results vary to a great extent when defining the order of the inclusions. It is physically unclear how to select among these various formulas. Furthermore, questions remain as to which of these mixing formulas can be applied to

computations for non-spherical melting particles. In summary, there are many ways to model the dielectric properties of mixtures which can directly lead to variabilities in radiative transfer calculations and radar simulations (Liao and Meneghini, 2005). Uncertainties in the scattering properties of mixed phase hydrometeors are one of the major sources of error in radiative transfer simulations of the cloud snow melting layer and snowfall.

A review of the effective dielectric constants of mixed phase hydrometeors is proposed by Meneghini and Liao (2000). They investigated their effect on extinction and backscattering coefficients at radar wavelengths, concluding that the Maxwell Garnett (MG) mixing rule for an air-ice mixture in a water matrix compares best to the Fast Fourier Transform numerical method (a derived expression of ϵ_{eff} that depends on the mean internal electric fields within each of the components of the mixture). The MG formulation has been commonly used since (e.g. Battaglia et al. (2003); Olson et al. (2001b,a)). The MG formula is written:

$$\epsilon_{eff} = \epsilon_e + 3f\epsilon_e \frac{\epsilon_i - \epsilon_e}{\epsilon_i + 2\epsilon_e - f(\epsilon_i - \epsilon_e)}, \tag{4.9}$$

where $f = nV$ is the dimensionless volume fraction of the inclusions in the mixture with $0 \leq \mathrm{f} \leq 1$ (V is the volume of spherical inclusions and n their number density). In the limit where the inclusion phase vanishes ($\mathrm{f} \to 0$), the MG formula gives $\epsilon_{eff} \to \epsilon_e$. Similarly, in the limit where the environment vanishes ($\mathrm{f} \to 1$), the resultant $\epsilon_{eff} \to \epsilon_i$, satisfying its physical sense.

Under the MG formulation, snow is often divided between a two-phase mixture of air and ice (dry snow) and a two phase mixture of dry snow and water (melting snow). However, questions still remain as to how these three phase mixtures are composed. Since the choice of which component is the matrix and which is the inclusion will affect the result, a variety of different models arises depending on how the inclusion phases are defined (described in Fabry and Szyrmer (1999) and Brown and Ruf (2007). When defining snow as a three-component mixture (air, ice, and water), the MG formula must be applied twice.

Snow Density

Density is a key parameter directly related to the dielectric properties and thus the scattering properties of mixed phase hydrometeors. The volume fraction in the MG formula is closely linked with density. For example, the density ρ_m of wet snow (dry snow and water mixture) varies with the melted fraction f_m, i.e. the volume fraction of water in the mixture, as

$$\rho_m = \frac{\rho_s \rho_w}{f_m \rho_s + (1 - f_m)\rho_w} \tag{4.10}$$

where ρ_s and ρ_s are the densities of dry snow and water respectively. The equivalent is seen for the volume fraction of dry snow (air-ice mixture) which is closely linked with the density of dry snow $f = \frac{\rho_s}{\rho_{ice}}$.

It has been recognized since Magono (1965) and many later studies, that a size-independent density is not a physically sound assumption for snowflakes because of the rigidity of ice and the nature of the snow formation processes (Leinonen et al., 2012). Snow density has shown a considerable variability in measurements. This is due to a combination of many crystal habits of ice and the method of growth (e.g. accretion vs. aggregation) which varies with temperature (Fabry and Szyrmer, 1999). The only consensus reached is that on average snow has a density of 0.1 g/cm^3 and that there is a decrease of density with snowflake size. It is important to

mention that such measurements are also difficult to make and may be one of the reasons for the observed variability on its own.

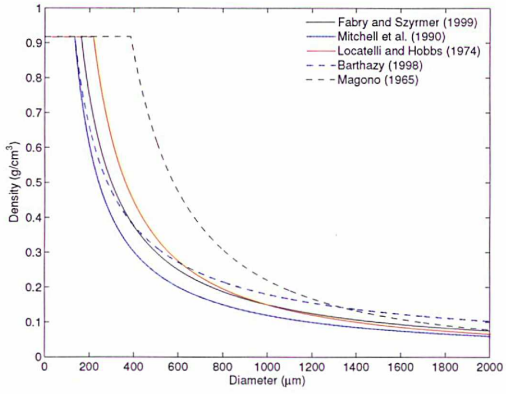

Figure 4.6: Different snow density parameterizations.

Parameterization	Details
$\rho_s = 0.015 D_s^{-1}$	Fabry and Szyrmer (1999).
$\rho_s = 0.012 D_s^{-1}$	Mitchell et al. (1990).
$\rho_s = 0.015 D_s^{-1.18}$	Locatelli and Hobbs (1974).
$\rho_s = 0.018 D_s^{-0.8}$	Barthazy (1998).
$\rho_s = 0.022 D_s^{-1.5}$	Magono (1965).

Table 4.3: Density $\rho_s(D)$ parameterizations of snow from the literature. Equations are given in cgs units.

Different relationships are seen in the literature where the upper limit is the density of pure ice (0.917 g/cm^3) and the lower limit is 0.005 g/cm^3 (Klaassen, 1988). A lower density snowflake will melt faster than a higher density snowflake of the same diameter. Therefore, dense snowflakes will produce a deeper melting layer as compared to fluffy aggregates. In Table 4.3, a number of snow density parameterizations found in the literature are listed, and shown in Figure 4.6. Another number agreed on throughout the literature is the density of graupel at 0.4 g/cm^3.

Figure 4.7 illustrates the impact of density on the dielectric properties of dry snow (air inclusions in an ice matrix) as calculated with the Maxwell Garnett mixing formula under different snow densities. As shown, the frequency dependence of the dielectric properties of snow are similar to the one of pure ice but with smaller magnitudes due the host material air.

4.2.2 Particle Size Distributions

Particle size has a very important impact on the scattering and absorption properties. Since clouds contain a whole range of different particle sizes, it is important to describe the correct size distribution of a population of hydrometeors. A particle size distribution relates the radius r of a particle to the particles number density $n(r)$, i.e. the number of particles per cubic meter. This section briefly lists the particle size distributions (PSDs) parameterizations which are relevant to the simulations conducted in this study.

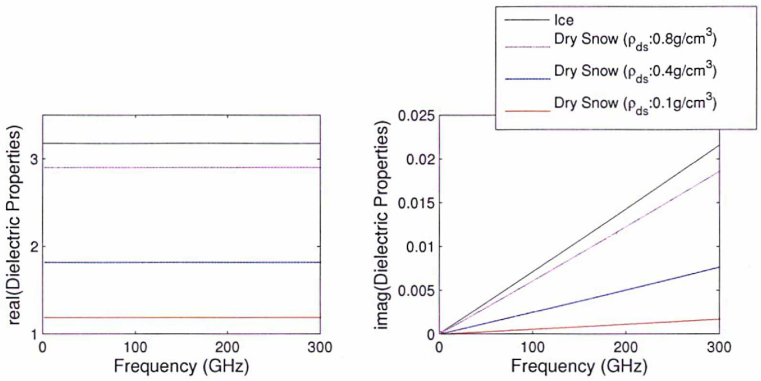

Figure 4.7: Real (left) and imaginary (right) part of the dielectric properties for dry snow (air inclusions in an ice matrix) with different densities as a function of frequency as calculated with the Maxwell Garnett mixing rule.

Mono-disperse Particle Size Distribution

The mono-disperse size distribution is the most simple assumption one can make: all the particles in the cloud have the same size. This assumption is very useful to analyze effects such as the influence of particle shape or orientation, because the effect from the particle size distribution itself is neglected.

Assuming a mono-disperse particle size distribution, the particle number density n is given by

$$n(IWC, r) = \frac{3\text{IWC}}{4\pi\rho r^3} \tag{4.11}$$

where IWC is the Ice Water Content (kg/m^3), ρ is the hydrometeor density (kg/m^3) and r is the radius of the hydrometeor.

Particle Size Distributions for liquid and frozen species

The gamma size distribution is commonly used in remote sensing of hydrometeors and follows as,

$$n(r) = n_0 r^{\mu} \exp\left(-\lambda r^{\gamma}\right), \tag{4.12}$$

where the particle number density in a given particle size range $n(r)$ (1/m^4) is parameterized by the intercept parameter n_0 (m^{-4}), the slope parameter λ (m^{-1}) and the dimensionless parameters μ and γ. The particle number density for PSDs like the gamma size distribution is obtained by integrating the PSD over all sizes ($n = \int_0^{\infty} n(r)dr$).

Setting $\mu = 0$ and $\lambda = 1$ is the simpler two-parameter exponential size distribution and parameterizations found in the literature are often expressed in terms of the particle diameter, D, by the general form:

$$n(D) = n_0 \exp\left(-\lambda D\right) \tag{4.13}$$

Note that the definition of the diameter D can be ambiguous for non-spherical particles. Most particle size distributions use the maximum dimension, D_{max}, to characterize the size.

Another definition is the diameter of the smallest circle that completely circumscribes the particle.

Cloud meso scale model schemes explicitly define the parameters in equation 4.12. The exponential size distribution used in the Meso-NH microphysical scheme has already been introduced in Section 4.1 where the values of n_0 and λ depend on the hydrometeor category. The rest of this thesis follows this notation. Exponential PSDs are used to parameterize both rainfall and snowfall. Table 4.4 below lists some of the parameterizations found in the literature. The parameters n_0 and λ may be expressed either as constants or functions of rainfall rate R. The Sekhon and Srivastava (1970) (SS) PSD is commonly used in snowfall studies (e.g. Skofronick-Jackson et al., 2002; Noh et al., 2006; Brown and Ruf, 2007; Liu, 2004; Noh et al., 2009).

Table 4.4: Particle size distribution (PSD) parameterizations, where R and S are the rainfall and snowfall rate respectively in [mm hr^{-1}].

Details	n_0	λ
Marshall and Palmer (1948) (MP)	8.0×10^3 (m^{-3}mm^{-1})	$4.1\mathrm{R}^{-0.21}$ (mm^{-1})
The Sekhon and Srivastava (1970) (SS)	$2.5 \times 10^3\ S^{-0.94}$ (m^{-3}mm^{-1})	$2.29S^{-0.45}$ (mm^{-1})

There is a number of different parameterizations describing the particle size distributions of pure ice particles. The McFarquhar and Heymsfield (1997) (MH97) size distribution is a realistic size distribution for tropical cirrus ice crystals as a function of IWC and temperature. This parametrization is based on observations during the Central Equatorial Pacific Experiment (CEPEX). Smaller ice crystals (equal volume sphere radius $< 50\mu$m) are represented with a gamma function and larger ice crystals are represented by a log-normal function. Different parameterizations are also available for midlatitude cirrus clouds (e.g. Donovan, 2003; Ivanova et al., 2001; Mitchell et al., 1999). These are bi-modal gamma distributions based on measurements from different field campaigns, and are functions of temperature, IWC, and maximum size dimension.

4.2.3 Particle Shape and Orientation

Particle shape is a complicated function of temperature, humidity, individual particle history, and geographical particularities of the region. For example, Figure 4.8 shows images of particle size and shape as a function of ambient temperature for sub-topical deep clouds, and illustrates well the complexity of modeling the shape of the frozen phase.

However, a common approach in both active and passive simulations is not to describe the precise individual particle shapes, but to determine the overall shape of the particles as determined by the aspect ratio (Dungey and Bohren, 1993a; Matrosov et al., 2005a; Hogan et al., 2012). From multiple aircraft observations, Heymsfield (personal communication) confirms the importance of the bulk shape of particles as characterized by its aspect ratio, neglecting the microwave passive simulation of individual complicated particle shapes. Aspect ratios (longest/shortest axis of ellipse) of the order of 1.6 close to the 0° isotherm are selected, as suggested in Korolev and Isaac (2003); Hanesch (2009); Matrosov et al. (2005a) and Heymsfield (personal communication). Unfortunately, aircraft observations cannot be used to infer

the orientation of particles, since turbulence around the measuring probe inlets and the flow around them tends to reorient them. However, it has been confirmed through different studies using differential reflectivity observations that particles fall with their largest dimension in the horizontal plane, and the deviation from the horizontal orientation is small enough to be neglected in scattering calculations (e.g. Matrosov et al., 2001, 2005b).

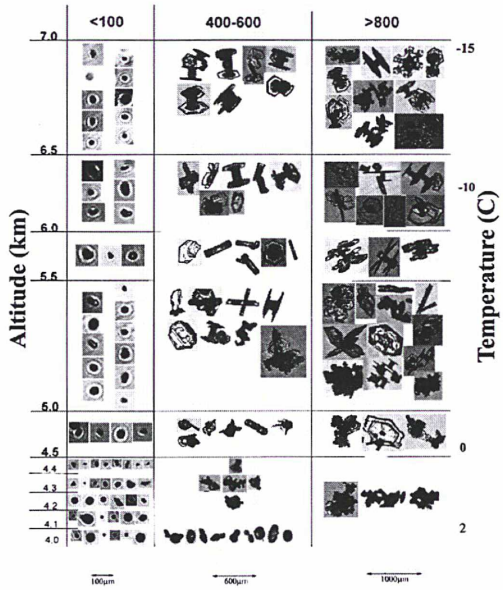

Figure 4.8: Particle shapes as a function of altitude and temperature as measured in a field campaign in three size ranges (< 100, 400 − 600, > 1000 μm) (Heymsfield et al., 2002).

4.3 Calculating the Single Scattering Properties

As briefly discussed in Section 3.1.7, the T-matrix approach is used in this thesis. The T-matrix code is powerful and widely used for the computation of scattering properties for non-spherical particles. It has been developed by Mishchenko (2000) and can calculate the scattering properties of both random and oriented particles. The main driving parameters of the T-matrix code are frequency and the dielectric properties, with the latter dependent on the phase, density and temperature of the hydrometeors. The size, shape and orientation of particles is also important in the T-matrix. Figure 4.9 shows the single scattering properties as calculated with the T-matrix code for a randomly oriented pure ice spheroid of aspect ratio (longest/shortest axis of ellipse) 1.6. Note that the scattering of a particle is highly dependent on the size parameter $2\pi r/\lambda$ (see Section 3.1.7).

Liu approximation

Another method often used to calculate the single scattering properties of spherical and non-spherical particles is the discrete-dipole approximation (DDA) (Purcell and Pennypacker, 1973).

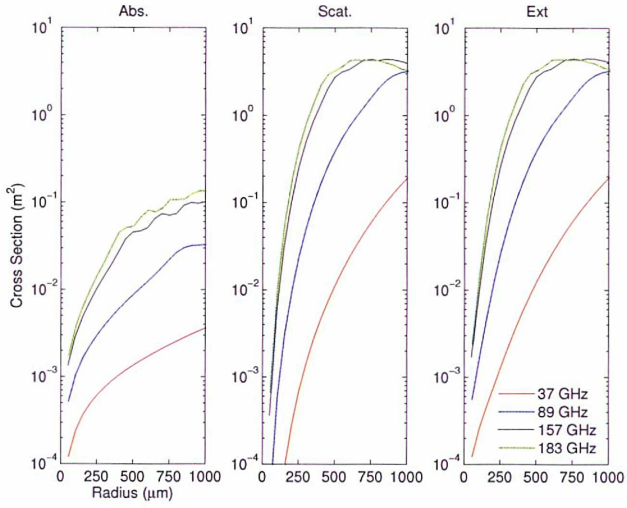

Figure 4.9: The absorption, scattering and extinction efficiency for spheroid ice particles (aspect ratio of 1.6) in the microwave region as calculated by the T-matrix.

The DDA method can be used to calculate the single scattering properties of arbitrary sized, shaped and oriented particles. However, T-matrix calculations are much more time efficient. An approach often used in order to use the T-matrix, is to approximate the single scattering properties of non-spherical particles by those of sphere where the particles *non-sphericity* is described by the density and/or size. One such approach is described by Liu (2004).

Liu (2004) presents an approximation to calculate the single scattering properties of species based on results of DDA modeling. Liu (2004) notes that snow particles have scattering and absorption properties between those of a solid ice equal-mass sphere of diameter D_0 and an ice-air mixed sphere with a diameter equal to the maximum dimension of the particle D_{max}. The dielectric properties of snow are then described by the Maxwell-Garnett mixing formula and its diameter by a softness parameter $SP = (D - D_0)/(D_{max} - D_0)$. The frequency dependent softness parameter (SP) gives the diameter of the best-fit equal-mass sphere, i.e., a frequency dependent effective density and a modified diameter is used to calculate the single scattering properties with the T-matrix. Table 4.5 gives the SP averaged over different snowflake shapes at different frequencies.

Table 4.5: The frequency dependent softness parameters (SP) derived by Liu (2004) to calculate the single scattering properties of snow, averaged over different snowflake shapes.

Frequency	Softness Parameter (SP)
85 GHz	0.33
150 GHz	0.27
220 GHz	0.22

4.4 Simulations of the Radar Response

The equivalent radar reflectivity factor Z_e is the main quantitive parameter measured by radar instruments. In the absence of attenuation, the equivalent radar reflectivity factor Z_e is given by integrating the backscatter cross sections of the individual particles over their size distribution:

$$Z_e = \frac{\lambda^4}{\pi^5 |K_w|^2} \int_0^\infty \sigma_b(D) n(D) dD, \tag{4.14}$$

where λ is the radar wavelength, $|K_w|^2$ is the reference dielectric factor, σ_b is the backscatter cross section and $n(D)$ is the particle size distribution.The backscatter cross section is the scattering in the exact backward direction, expressed as

$$\sigma_b = \sigma_s P(\Theta)|_{\Theta=\pi}, \tag{4.15}$$

where $P(\Theta)$ is the scattering phase function.

One of the motivations of this thesis is analysing the consistency of microphysical assumptions in reproducing real passive and active observations. A method capable of extracting the backscattering signal in equation 4.14 from the microphysical properties used to solve the radiative transfer equation was incorporated in cooperation with the ARTS team. In this method, only the two-way attenuation by gases and the targeted backscattering (i.e. no multiple scattering) are considered, ignoring surface scattering. Note that the single scattering assumption is a frequently accepted simplification for precipitation and cloud radar observations, although at high microwave frequencies Battaglia et al. (2008) has shown that multiple scattering can significantly enhance the reflectivity profiles as observed at 94 GHz with CloudSat.

It is important to emphasise that for the interest of this study, the T-matrix used to calculate the single scattering properties needed in the radiative transfer simulations also calculates σ_b. Further using the same particle size distribution in passive and active simulations allows passive and active calculations performed in this thesis to be consistent in terms of the microphysical properties. This is essential to simulate in a consistent manner active and passive observations, as done in Chapter 6.

ARTS can output the equivalent radar reflectivity factor Z_e from Equation 4.14, where $|K_w|$ is calculated using the complex refractive index of water n at a user specified temperature,

$$K = \frac{n^2 - 1}{n^2 + 2}. \tag{4.16}$$

Note that for CloudSat, a value of 0.75 for K is generally accepted. Figure 4.10 shows the backscattering cross section of pure ice spheres at CloudSat 94 GHz as a function of particle radius, according to T-matrix calculations. For comparison, cross sections at the PR 37 GHz are shown, together with cross sections under the Raleigh approximation. As expected, ice crystals have higher backscattering cross sections at 94 GHz rather than at 37 GHz, and at larger particle sizes. Figure 4.11 shows how these backscattering cross sections translate to Z_e. Figure 4.11(a) shows an IWC profile, which together with a midlatitude winter atmosphere, is used to run a very simple example of the ARTS radar method. Figure 4.11(b) shows the resulting Z_e under three different assumptions, i.e., describing the IWC profile with the McFarquhar and Heymsfield (1997) (MH97) particle size distribution (Figure 4.11(c)), or via a mono disperse size distribution of ice spheres with diameter $50\mu m$ or $400\mu m$.

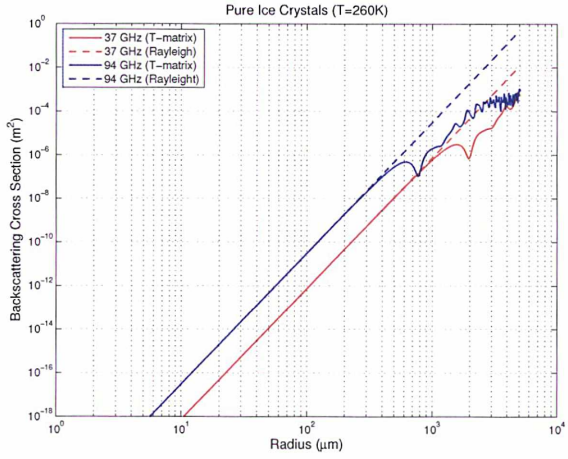

Figure 4.10: The backscattering cross-sections for pure ice spheres (at T=260 K) at 37 and 94 GHz as calculated with the T-matrix. For comparison, cross sections in the Rayleigh regime are shown.

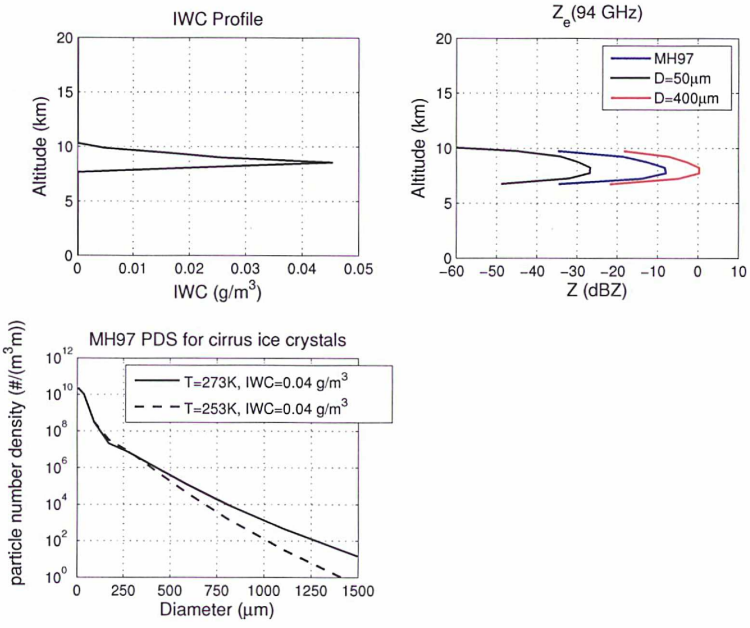

Figure 4.11: (a) Ice Water Content (IWC) profile in altitude as derived from the Chevallier91L database (Chevallier et al., 2006), (b) the equivalent radar reflectivity factor (Z_e) as calculated with the ARTS radar method under different particle size distribution assumptions, and (c) illustrates the realistic McFarquhar and Heymsfield (1997) particle size distribution used.

4.5 Surface Emissivity

The purpose of this section is to provide an introduction to surface emission in the microwaves and the methods used in this thesis to incorporate realistic surface emissivities to the simulations performed with ARTS.

ARTS considers the emission and scattering by the surface when the propagation path intercepts it. It includes methods for blackbody surfaces, specular surfaces and a basic treatment of Lambertian surfaces (an ideal scattering rough surface). In the microwave region, channels with frequencies away from absorption lines are not only sensitive to emission from the atmosphere, but they are also affected by the Earth's surface emission because atmospheric opacity is limited. For this reason it is important to understand and quantify the contribution of the Earth's surface emission to the observations. Even for AMSU-B water vapour channels, Wang and Chang (1990) showed that the impact of the sea surface response on the retrieval of the water vapour content is far from negligible. In a very rough approximation, at a window frequency, a 0.05 change in surface emissivity leads to a change of approximately 15 K ($\Delta T_B \sim T_S \Delta e$ with a surface temperature, T_s, of 300 K). To accurately simulate real scenes observed by a number of instruments with the help of cloud mesoscale model outputs, a correct description of the surface properties is important. Incorporating tools able to calculate realistic surface reflectivities to ARTS is a necessary step to make. In the following sections a brief theory of surface emission is given, followed by a description of the approaches taken in this thesis. These tools are ready to be incorporated into the ARTS distribution.

4.5.1 Surface Emission and Reflection

Natural surfaces can be assumed to be in thermodynamic equilibrium. Reflection from a smooth surface takes the name of specular reflection and following Kirchoff's law, the emissivity ϵ can be expressed as ϵ=1-r, where r is the reflectivity of the surface. Specular reflection is assumed when the surface is sufficiently smooth that radiation will be reflected and scattered only in the complementary angle as seen in Figure 4.12.

Assuming specular reflection is not always possible. In the cases of very dry sand, vegetation and snow cover, volume scattering is involved because radiation does not emanate from a thin surface layer, but can arise from below or within the canopy or snow layer. Furthermore, radiation incident on rough surfaces is partly reflected in the specular direction but also partly scattered into all directions (surface scattering in this case). The specular assumption is valid for flat surfaces when there is no surface or volume scattering. Note that a surface may appear very rough to an optical wave, and very smooth in the microwaves. A more detailed discussion of the validity of the specular approximation is given below.

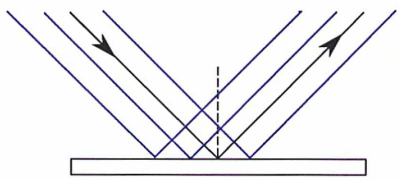

Figure 4.12: In specular reflection radiation will be reflected and scattered only in the complementary angle.

The complex intensity reflection coefficient, describing the amplitude of the reflected EM wave for the vertical (R_v) and the horizontal (R_h) polarizations, is given for a specular reflection by the Fresnel equations:

$$R_v = \frac{n_2 \cos\theta_1 - n_1 \cos\theta_2}{n_2 \cos\theta_1 + n_1 \cos\theta_2} \tag{4.17}$$

$$R_h = \frac{n_1 \cos\theta_1 - n_2 \cos\theta_2}{n_1 \cos\theta_1 + n_2 \cos\theta_2} \tag{4.18}$$

where n_1 is the refractive index of the propagation medium, θ_1 is the incident angle and n_2 is the refractive index of the reflecting medium. The angle θ_2 is the angle of propagation of the transmitted radiation and is given by Snell's law,

$$\mathbb{R}(n_1)\sin\theta_1 = \mathbb{R}(n_2)\sin\theta_2 \tag{4.19}$$

The power reflection coefficients can be converted to the reflectivity according to,

$$r = |R|^2 \tag{4.20}$$

The transformation matrix for specular surface reflection is then

$$\mathbf{R} = \begin{pmatrix} \frac{r_v+r_h}{2} & \frac{r_v-r_h}{2} & 0 & 0 \\ \frac{r_v-r_h}{2} & \frac{r_v+r_h}{2} & 0 & 0 \\ 0 & 0 & \frac{R_h R_v^* + R_v R_h^*}{2} & i\frac{R_h R_v^* - R_v R_h^*}{2} \\ 0 & 0 & i\frac{R_v R_h^* - R_h R_v^*}{2} & \frac{R_h R_v^* + R_v R_h^*}{2} \end{pmatrix} \tag{4.21}$$

If the downwelling radiation is unpolarised, then the reflected part of the upwelling radiation is given by

$$\mathbf{R}\begin{bmatrix} I \\ 0 \\ 0 \\ 0 \end{bmatrix} = \begin{bmatrix} \frac{I(r_v+r_h)}{2} \\ \frac{I(r_v-r_h)}{2} \\ 0 \\ 0 \end{bmatrix} \tag{4.22}$$

In this context, the integral to the scalar radiative transfer equation can be expressed as

$$I^{up} = I^{down} r + (1-r)B, \tag{4.23}$$

where I^{up} is the upwelling radiation, I^{down} is downwelling radiation and B is the magnitude of blackbody radiation. Assuming specular reflection, ARTS needs to be given the reflectivity transformation matrix as described in Equation (4.21).

4.5.2 Incorporating Realistic Ocean Emissivities into ARTS

The low emissivity of the ocean in the microwave region reduces the surface radiative contributions and makes it easier to observe the atmospheric phenomena against the oceanic cold background.

The thermal emission and scattering properties of the ocean in the microwave domain are mainly related to the wind-driven surface roughness, with or without accompanying foam, and to its dielectric properties (Guillou et al., 1996). The microwave radiative properties of the ocean have been the object of several studies in the past, from model developments and airborne measurements, to satellite observations. Despite uncertainties in dielectric property

models, foam emissivity parameterizations and the nature of the wind-surface geometry relationship, sea surface emissivity is now fairly well understood (Boukabara and Weng, 2008). The dielectric properties are dependent on the water temperature and salinity, but at high microwave frequency channels this dependence is negligible.

Most meteorological operational centers use a microwave emissivity model in the assimilation process of surface-sensitive channels. The Fast Microwave Emissivity Model (FASTEM) is widely used.

FASTEM calculates the sea surface emissivities from wind, sea surface temperature, and viewing angle assuming a constant salinity of 38%. The current version, FASTEM-4 (Liu et al., 2011), has been improved for more than 10 years since FASTEM-1 (English and Hewison, 1998) was first developed. FASTEM includes an accurate permittivity model, a foam model, takes into account the treatment of non-specular reflection and the dependence of the ocean surface emissivity on the azimuth angle between the wind direction and the line of sight of the instrument. It is also able to model the behaviour of the 3rd and 4th elements of the Stokes vector as a function of wind speed and wind direction. FASTEM follows the permittivity formulation of Ellison et al. (2003), a double Debye model with coefficients determined from the fitting of permittivity measurements. For further details, please refer to Liu et al. (2011).

Since FASTEM can be used for frequencies between 10 and 400 GHz and for all zenith angle configurations, it is very adequate as a tool to provide ocean emissivity estimates to ARTS users. FASTEM was re-coded in this thesis and used with ARTS as an external tool. The outputs from this model are then easily used together with the ARTS specular surface reflection method. Figure 4.13 below shows the ocean emissivity outputs as calculated by FASTEM at 89, 150 and 183 GHz for the RHINE Meso-NH simulations presented in Section 4.1 at an incidence angle of 53^o. Note that as expected, there is a higher variability on the horizontal polarized emissivity and that the vertical component is always higher than the horizontal component. Figure 4.13 also shows the signatures of high wind speeds in the North Sea causing higher ocean emissivities.

4.5.3 Incorporating Realistic Land Emissivities into ARTS

Microwave land surface emissivities are usually much higher that ocean emissivities, making the surface contribution to microwave observations larger. This is one of the factors for which assimilation of microwave observations is more difficult over land than over ocean. Land surface emissivities, ranging from arid surfaces to dense vegetation to snow, have shorter spatial correlation scales. Surface emissivities are hard to model because they are dependent on a large number of highly variable parameters. Even if the perfect land surface emissivity model existed, the inputs required (e.g. soil texture and humidity, vegetation characteristics, percentage of vegetation coverage within a field of view, snow density) would need to be available on a global basis with the required resolution and accuracy which is not the case (Prigent et al., 2005a). The alternative is to derive them form satellite observations.

Global land surface emissivity maps were first produced at SSM/I frequencies by removing the contribution of the atmosphere, clouds and rain using ancillary data, and assuming specular reflection (Prigent et al., 1997, 1998). Such emissivities are estimated for SSM/I conditions, that is, for a 53^o zenith angle at 19.35, 22.235, 37.0 and 85.5 GHz for both vertical and horizontal polarizations with the exception of 22 GHz, which has vertical polarization only. The emissivities are available on a 0.25^o x 0.25^o grid. Prigent et al. (2008) presented a parameterization of the land surface emissivities between 19 and 100 GHz under all observing conditions

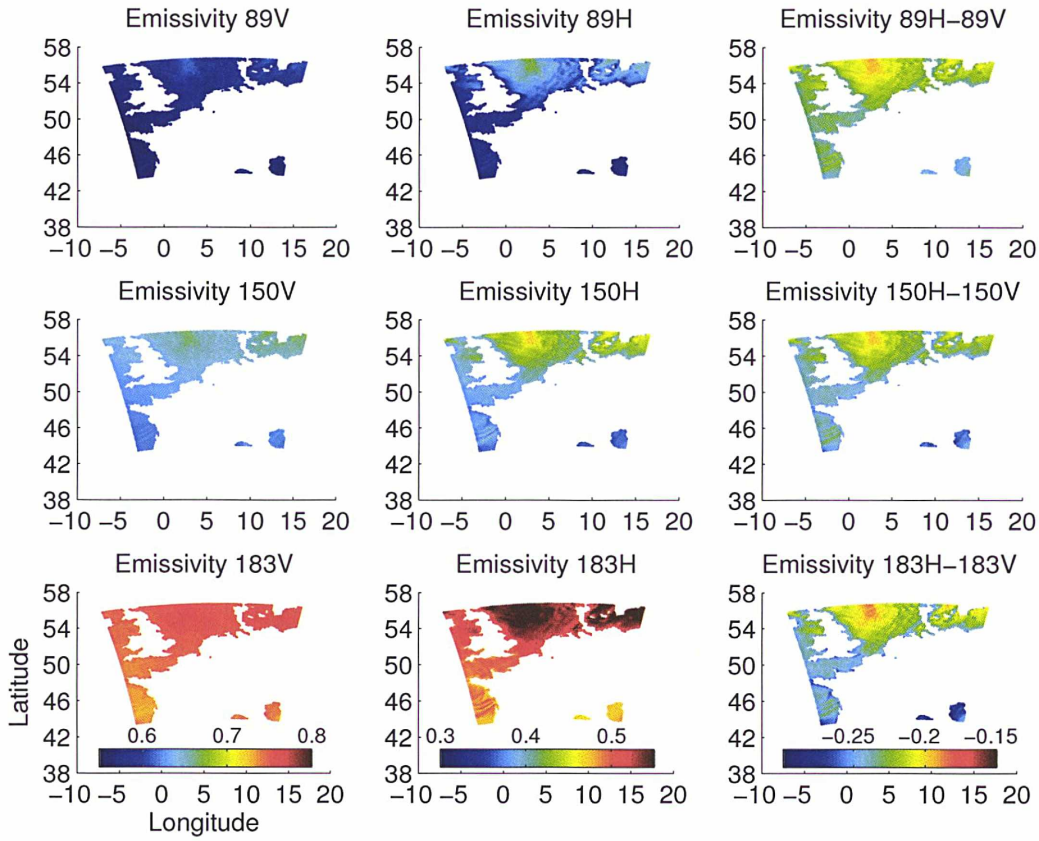

Figure 4.13: Ocean polarized emissivity as calculated by FASTEM at 89 (top), 150 (middle) and 183 GHz (bottom), for the Meso-NH RHINE scene introduced in Section 4.1 over Western Europe at an incidence angle of 53°, on the 10 February of 2000.

derived from this global SSM/I emissivity atlas. It is based on an analysis of the frequency, angular, and polarization dependence of the emissivities calculated from SSM/I observations, but also from TMI and AMSU-A. This parameterizations were used to develop the Tool to estimate Land Surface Emissivites at Microwave Frequencies (TELSEM) (Aires et al., 2011), which can be used to provide a first guess emissivity for each location over the globe, for any month of the year, for any incidence angle and polarization configuration.

TELSEM provides realistic emissivity uncertainties, estimated to be lower than 0.02 in snow-free regions (Aires et al., 2011). TELSEM works as shown in Figure 4.14 and is adapted in conjunction with ARTS. The latitude, longitude and month of the year of the desired emissivity estimates are used to search the SSM/I atlas of emissivities. This gives the SSM/I emissivity at 53^o, $\epsilon_{SSM/I}V(53^o)$ and $\epsilon_{SSM/I}H(53^o)$ for all SSM/I frequencies. TELSEM is then capable of calculating the corresponding vertical and horizontal emissivities for each SSM/I frequency at nadir with a multilinear regression of $\epsilon_{SSM/I}V(53^o)$ and $\epsilon_{SSM/I}H(53^o)$. The next step involves a pre-computed polynomial function that describes the angular dependence for each polarization and each SSM/I frequency to deduce $\epsilon V(\theta)$ and $\epsilon H(\theta)$ at the desired incidence angle, θ. Finally, a linear interpolation in frequency is applied to derive $\epsilon V(\theta, f)$ and $\epsilon H(\theta, f)$ at the desired frequency.

The validity of this regression is optimal for 19-85 GHz (Aires et al., 2011). For frequencies lower than 19 GHz, the 19 GHz emissivities are adopted as evaluated down to 6 GHz in (Aires et al., 2011). For frequencies higher than 85 GHz, the 85 GHz emissivities are used up to 190 GHz (Aires et al., 2011). The spatial resolution of the emissivity estimates is 0.25^o x 0.25^o but other spatial resolutions (degraded) can be specified and TELSEM can either use the closest climatology-derived emissivity, or it will perform spatial averaging. Note, that over snow, the emissivities have larger standard deviations (Prigent et al., 2005a); interaction of the microwave radiation with snow involves volume scattering, specially for dry snow at high frequencies. This means that TELSEM estimates must be used with care in snow/freezing regions. Note that TELSEM also estimates the full covariance matrix for this new set of frequency channels.

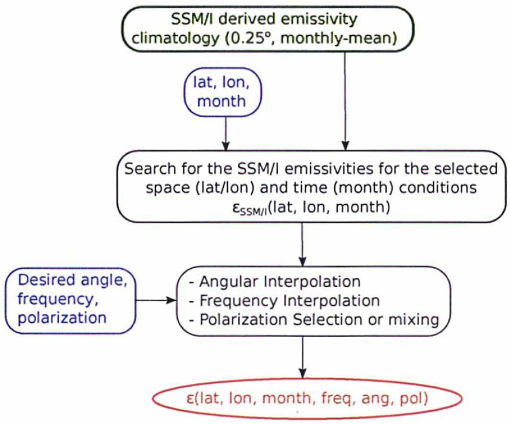

Figure 4.14: Flow chart describing TELSEM. Adapted from Aires et al. (2011).

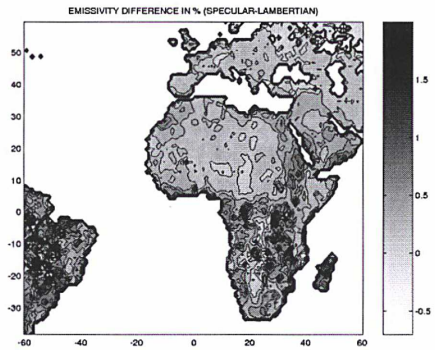

Figure 4.15: Mean emissivity difference (in percentage) map between the specular and the Lambertian cases using data near nadir from AMSU-A at 23 GHz during February 2000. From Karbou and Prigent (2005).

The validity of the specular approximation has been evaluated by Karbou and Prigent (2005) where the obtained emissivity differences between specular and rough surfaces are small, even for high observation angles where the errors related to the specular approximation are within 1% for all channels. Figure 4.15 shows that in most cases, differences associated to the specular and Lambertian approximations are very limited.

Figure 4.16 compares the observed and simulated brightness temperatures for clear sky conditions using TELSEM, and was used as a form of evaluation of the performance of TELSEM in Aires et al. (2011). Figure 4.16 shows that results are clearly better with TELSEM land surface emissivities. Note that at 157 GHz, the 85 GHz emissivity is adopted in TELSEM and that the effect is not large compared to stand-alone RTTOV or the Weng model, but it is still

positive, howing that this rather crude extrapolation is still beneficial.

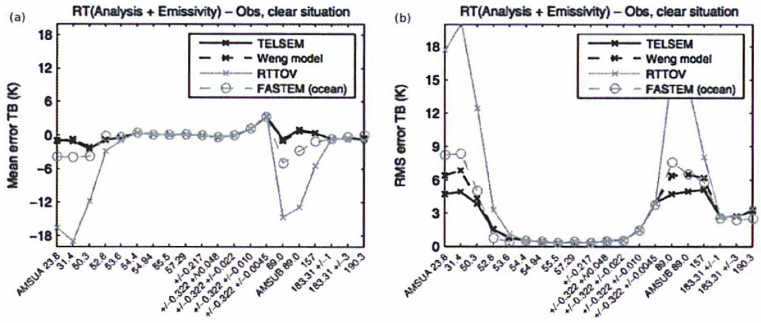

Figure 4.16: RMS errors between simulated and observed brightness temperatures from AMSU-A and AMSU-B onboard NOAA-17, for two months (July 2002 and January 2003). High latitudes ($\pm 60^o$ in latitude) and precipitating scenes have been excluded from the statistics. (a) Bias for cloud free situations, (b) RMS for cloud free situations. The continous black line denotes the simulations with TELSEM emissivities, the continuous gray lines the original RTTOV simulations using a fixed emissivity and the dashed black emissivities from a model known as the Weng model. Similar statistics are shown over the ocean using FASTEM as the dashed/circle grey line. Figure from Aires et al. (2011).

TELSEM is thus incorporated into ARTS simulations, as FASTEM was for the oceans. Figure 4.17 below shows the land surface emissivity outputs as calculated by TELSEM during February for 19, 37 and 89 GHz assuming that each pixel is being observed at 53^o. The latitude and longitude grids corresponds to the Meso-NH simulations presented in Section 4.1. Emissivities are shown to be high over land, but rather low in certain regions like the Alps that are snow covered at this time of the year. Snow is particularly difficult to estimate due to its high variability in space and time. In terms of frequency dependence, the higher the frequency, the lower the emissivities, with the H polarized component being considerably lower than the V component. As expected, the H polarized component is also a lot more variable than the H component.

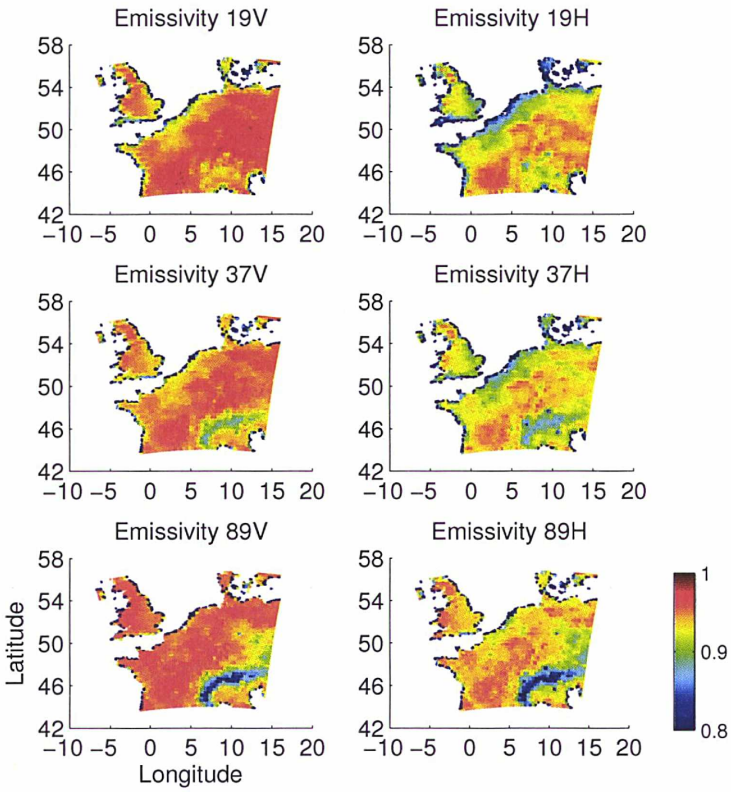

Figure 4.17: Land surface polarized emissivity as calculated by TELSEM during February for 19 (top), 37 (middle) and 89 GHz (bottom), for the RHINE Meso-NH scene introduced in Section 4.1 over Western Europe at an incidence angle of 53°, on the 10 February 2000.

Chapter 5

Analysis of the Microwave Polarized Scattering Signal over Clouds: Satellite Observations and Radiative Transfer Interpretations

5.1 Introduction

The polarization of electromagnetic radiation, introduced in Section 3.1.2, is determined by the elements of the Stokes vector $\mathbf{I} = [I, Q, U, V]^T$, where I is the total intensity of the EM wave and the other three Stokes parameters Q, U and V specify the polarization state of the wave. The second Stokes component Q is the difference in intensities between the vertical and horizontal linearly polarized components of the EM wave, the third Stokes component U is the difference in intensities between the linearly polarized components oriented at -45^o and $+45^o$, and the fourth Stokes component V is the difference in intensities between the left-hand and right-hand circularly polarized components. This section focuses on the second Stokes vector Q, as a result of the presence of frozen and melting hydrometeors in the atmosphere.[1]

The brightness temperature difference measured by a radiometer at two orthogonally polarized channels, i.e., the vertical brightness temperature TBV minus the horizontal brightness temperature TBH, represents the second Stokes parameter Q, hereafter TBV−TBH, or TBVH. Accurate measurements of TBVH in the microwave range are provided by SSMI, AMSR-E and TMI up to 89 GHz. The MADRAS instrument onboard Megha-Tropiques, recently added to this list of available instruments, further extends polarized observations to a higher frequency at 157 GHz.

Scattering signatures have been observed to be associated with significant polarized signatures in cloud structures from satellites as early as 1989 by Spencer et al. (1989), where TBVH observations by SSM/I at 85 GHz in stratiform regions were attributed to non-spherical particles with non-random orientations. Model studies confirmed that spherical particles or non-oriented particles do not generate polarization, but that oriented non-spherical hydrometeors are necessary to generate large polarized scattering signatures in the microwave, and that the magnitude of TBVH is strongly influenced by particle shape and orientation (e.g. Miao et al., 2003b; Troitsky et al., 2001; Prigent et al., 2005b, 2001; Czekala, 1998).

Figure 5.1 presents an example of the polarized cloud scattering signatures observed from satellites at 85 GHz, in this case with TMI, over land. Figure 5.1 shows that at 85 GHz, regions of low TBV where scattering is important are associated with TBVH values of the order of 7 K.

In this thesis, the polarized scattering signals from TMI are analyzed and interpreted with the help of realistic radiative transfer simulations to confirm the role of non-spherical oriented mixed phase species and to analyze the sensitivity of the scattering polarized signal to the microphysical properties of mixed phase hydrometeors. The recently available close-to-millimeter (157 GHz) observations from MADRAS are also exploited in this study. MADRAS observations provide a unique opportunity to evaluate the conclusions drawn from radiative transfer simulations up to 90 GHz as the higher frequency 157 GHz channel is expected to be much more sensitive to cloud scattering.

This chapter is structured as follows: Section 5.2 describes the setup chosen for the radiative transfer simulations. Section 5.3 presents a general analysis of the sensitivity studies to changes in different microphysical parameterizations. Section 5.4 presents a published study using TRMM passive and active observations assessing the use of the polarized signal as a tool to identify the melting layer, that is the change in particle composition from ice (more realistically

[1]The U and V components are not discussed as they are not observed yet from the satellites at frequencies where scattering is strong. Limited circular polarization should be observed, unless the particles have a preferred azimuthal orientation (Troitsky et al., 2003).

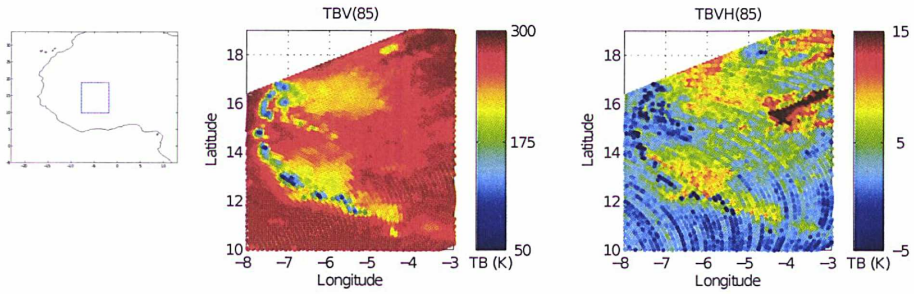

Figure 5.1: Maps of TBV (left) and TBVH (right) as observed by TMI over Africa on 19/08/2006, to illustrate the magnitude of the observed polarized scattering signatures. At 85 GHz, cloud structures appear cold over the highly emitting land surface (down to 50 K here) due to the scattering effect of the frozen phase. Regions of low TBV are associated with TBVH values of the order of 7 K. Note that the large observed polarized signatures of the order of 15 K located around -4^oE and 15^oN do not correspond to cloud structures, but to standing water at the surface (the Inner Niger Delta).

a mixture of ice and air) to water, often observed in stratiform rain. This publication focused on analyzing qualitatively how changes in hydrometeor dielectric properties impact the polarized scattering signal observed at 85 GHz to investigate on the possible link between polarized scattering on the microwave and the dielectric properties in the melting layer. Section 5.5 presents the higher frequency polarized observations recently available onboard Megha-Tropiques at close-to-millimeter frequencies (157 GHz). Radiative transfer simulations of MADRAS observations provide a unique opportunity to validate the role of non-spherical oriented mixed phase particles in the observed scattering polarized signal.

5.2 Polarized Radiative Transfer Simulation Setup

This section describes the setup of the polarized radiative transfer simulations performed with ARTS. Since cloud polarized scattering signals are measured from conical scanners such as SSM/I, TMI or AMSR-E up to 89 GHz, radiative transfer simulations were first performed with the observational parameters of these instruments: incidence angle at 53^o. Radiative transfer simulations were then extended to 157 GHz to exploit the observational data from the conical scanner MADRAS onboard Megha-Tropiques.

The following simulations were done using the DOIT method since the DOIT algorithm is recommended for one dimensional simulations. Standard clear-sky atmospheric data were extracted from the FASCOD dataset (Anderson et al., 1986) for typical tropical and mid-latitude-winter atmospheres. Figure 5.2 summarizes (a) the temperature profiles, and (b) the water vapor profiles of these atmospheres. The opacity of an average clear sky atmosphere at 157 GHz is roughly twice as that at 37 GHz. For specific simulations, ECMWF atmospheric profiles were obtained in spatial and temporal coincidence with satellite observations. In terms of surface emissivity, unless otherwise stated, it is fixed at 0.9 for both V and H polarizations to eliminate any surface contributions to the polarized signatures and to focus only on atmospheric sources of polarization.

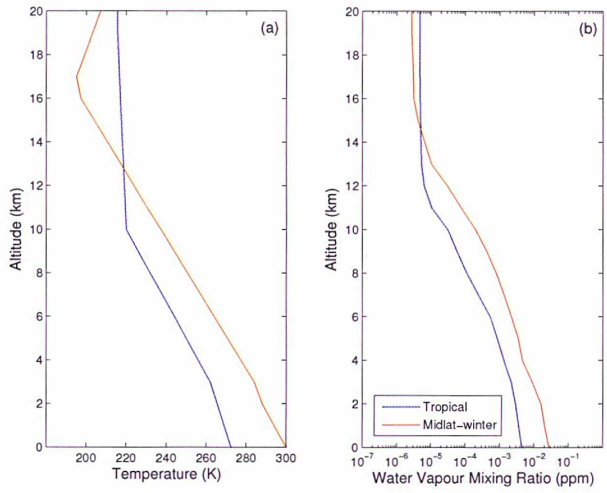

Figure 5.2: Tropical (blue) and Midlatitude-winter (red) atmospheres taken from the FASCOD as a function of altitude.

Key to the simulations are the profiles of hydrometeor species and the microphysical assumptions characterizing them: size, density, refractive index, shape and orientation. The following list enumerates how some of these parameters were parameterized in the simulations:

1. Size: Defining the size for non-spherical particles can be ambiguous. In this study, the term radius used for non-spherical particles is defined according to the effective radius, i.e., the equal volume of a sphere with the same radius.

2. Density: This is an important parameter for snow as discussed in Section 4.2.1. For liquid, pure ice and graupel species there is no or limited uncertainty, but for snow species, the density is an open parameter. The density of snowflakes are well known to decrease rapidly with size. Different relationships are seen in the literature where the upper limit is the density of pure ice (0.917 gcm^{-3}). Here a number of parameterizations found in the literature (see Table 4.3) are used to define ρ_s (dry snow). In the case of a melting snowflake, i.e. a two phase mixture of dry snow and water, its overall effective density (ρ_m) varies with the melted volume fraction of water, f_m, as

$$\rho_m = \frac{\rho_s \rho_w}{f_m \rho_s + (1 - f_m)\rho_w} \tag{5.1}$$

   where ρ_s and ρ_w are the density of dry snow and water, respectively.

3. Refractive Index: The dielectric properties of various mixed phase hydrometeors were used in order to study its impact on microwave passive simulations. The dielectric properties were calculated for either (a) pure ice using Mätzler and Melsheimer (2006), (b) a two phase mixture composed of ice inclusions in an air mixture (defined as dry snow), and (c) a two phase mixture composed of dry snow and water, as described in Section 4.2.1 by applying the Maxwell Garnett formula twice: once to calculate dry snow and a second time to mix dry snow and water (water inclusions of melted volume fraction f_m in a

dry snow environment). This model has shown to agree with the average characteristics of the melting layer in longterm observations (Fabry and Szyrmer (1999); Olson et al. (2001b,a); Battaglia et al. (2003); Zawadzki et al. (2005)).

4. Shape: The particle shapes are here defined to be either perfectly spherical or spheroids with a given aspect ratio as discussed in Section 4.2.3. The approach taken is to focus on the bulk aspect of particles as characterised by its aspect ratio, neglecting the simulation of individual complicated particle shapes: aspect ratios of the order of 1.6 close to the 0°C isotherm are selected for non-spherical particles.

5. Orientation: Considered in this study are randomly oriented and perfectly horizontally aligned particles, i.e., azimuthally symmetric. In the case of horizontally aligned particles, most particles are likely to suffer particle tumbling related to turbulence. The effect of tumbling has already been evaluated in Prigent et al. (2001). Xie et al. (2012) showed that perfectly horizontally aligned particles behave similarly to horizontally aligned particles with a preferred zenith angles orientation of standard deviation of 10^o, with TBs and polarization differences deviating by less than 0.2 K compared to the perfect horizontal case. In this study, we will concentrate on perfectly horizontally aligned particles for practical reasons.

These inputs allow a detailed calculation of the scattering properties of hydrometers using the T-matrix (Mishchenko, 2000).

5.3 Sensitivity of the Simulated Polarized Scattering Signals to Frozen Hydrometeors

The following simulations provide a sensitivity study to analyze the potential polarization difference of various particle types. This serves as an introduction to the studies presented later in this chapter.

The sensitivity of the scattering polarization signal to shape and orientation is here assessed for various particle species (different dielectric properties). In order to do so, a number of different simulations were run with different shapes (i.e. perfect spheres vs. spheroids of varying aspect ratios) and orientations (randomly vs. perfectly horizontally aligned). To neglect any effects of the particle size distribution itself, a mono-disperse size distribution is chosen. Simulations are performed as described in Section 5.2 using atmospheric data from a mid-latitude FASCOD atmosphere and a surface emissivity fixed at 0.9 for both V and H polarizations. The dielectric properties for dry snow were calculated using ice inclusions in an air matrix. The volume fraction of ice inclusions was determined by applying the density parameterization from Mitchell et al. (1999) (see Table 4.3).

Figure 5.3 shows the sensitivity of the simulated vertical polarization, TBV, and polarization difference, TBVH, of pure ice (black) and dry snow (blue) horizontally aligned species, to particle aspect ratio as a function of radius for a mono-disperse distribution of hydrometeors with fixed IWP of 0.2 kg/m^2. Concentrating on the sensitivity of the three frequency bands of interest (37, 89 and 157 GHz) and ignoring for now any differences in the signals between the different species, it can be easily seen from Figure 5.3 that the sensitivity to the frozen phase increases with frequency. This behavior is expected. For all frequency bands, TBV

decreases with increasing particle size since the larger particles scatter more efficiently. The higher frequency 157 GHz results in TBV values of the order of 150 K for dry snow particles of 500 μm radius, while the lower frequency 85 GHz band only produces TBV values of the order of 225 K for the same particle radius. Note that at 37 GHz brightness temperature depressions are very limited, specially for ice. The TBV signal is shown to be very different for dry snow and pure ice species, with dry snow species having a larger impact on TBV than pure ice particles. In terms of the polarization difference TBVH, a similar trend is observed. However, the TBVH scattering signal is a lot more sensitive to particle shape and orientation than the TBV signal. Figure 5.3 evidences that only at 157 GHz the TBV signal is *slightly* sensitive to particle shape, where particles with larger aspect ratios scatter the most. Perfect spheres do not produce significant TBVH differences as expected (not shown). Note that at 157 GHz a saturation of the polarization scattering signal is observed and is discussed later in this section.

The sensitivity analysis here shows that TBVH at 157 GHz is approximately twice as that observed at 85 GHz. This further feeds into the spirit of the work of this thesis to emphasize the importance of high microwave frequency channels for frozen phase studies, and in the light of the next generation of sub-mm and mm instruments. The aspects discussed so far are not surprising and give confidence on the conducted ARTS simulations and chosen set-ups.

An evaluation of the sensitivity of the scattering signal to particle composition needs to be done with care for mono-disperse distributions. It is important to keep in mind that a comparison between ice and dry snow equal size particles needs to take into account a decrease in density of dry snow particles: this decrease in density translates into an increase in the particle number concentration. Clearly, for a give particle size, the increase of particle number concentration increases the scattering effect, as well as the polarization difference. Due to this effect, Figure 5.3 shows how important density can be as a parameter, especially at 85 and 157 GHz.

Figure 5.4 through Figure 5.5, further shows the sensitivity of pure ice and dry snow spheroids with an aspect ratio of 1.6 as a function of not only size, but also IWP. Figure 5.6 also explores the effect of wetness in the snow by including a melted fraction in the ice-air mixture. These figures show that the larger the IWP, the lower the TBV simulated due to a larger scattering effect. The TBVH signal at 89 GHz and 157 GHz also increases with increasing particle size and with increasing IWP.

The saturation effect mentioned above is easily seen in the TBVH maps of Figure 5.4 through Figure 5.6, especially 157 GHz. At 157 GHz, TBVH reaches a maximum and then decreases to zero. This saturation has been reported before in radiative transfer simulation studies (e.g., Troitsky et al. (2001); Miao et al. (2003b)) and is explained by the fact that the H and V components of radiation are not two independent radiation streams, when radiation is polarized at a scattering event, some V radiation is converted to H, and vice-versa. This means that with a very large number of scattering events, the values of H and V tend to a similar value, and TBVH reaches zero. As seen in Figure 5.3 the saturation shows no sensitivity to particle shape, meaning that saturation occurs for the same size regardless of the particle shape. As seen in Figure 5.4 through Figure 5.6, the larger the IWP, the smaller the particle size needs to be for TBVH saturation to occur. It is also seen that since dry snow appears to scatter more efficiently when compared to other species, it has a higher polarization signal for smaller sizes and lower IWP contents. This also means that dry snow polarization saturates at lower sizes and lower IWPs when compared to other species.

Assessing the effect of dry snow and snow wetness in comparison with pure ice species

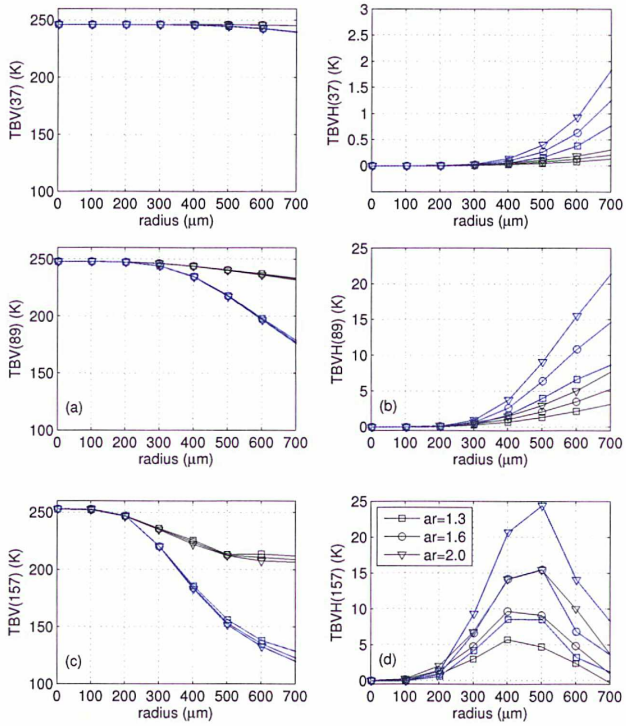

Figure 5.3: The sensitivity of the simulated vertical polarization TBV and polarization difference TBVH for ice (black) and dry snow (blue) species to the particle's aspect ratio as a function of radius for a mono disperse distribution of horizontally aligned hydrometeors with fixed IWP (0.2 kg/m^2).

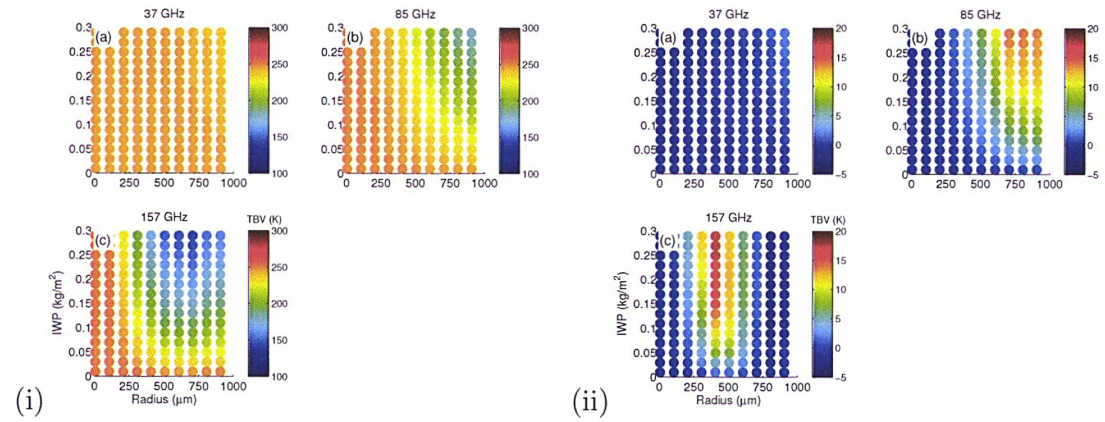

Figure 5.4: The sensitivity of the simulated (i) TBV and (ii) TBVH for horizontally distributed particles of pure ice (aspect ratio 1.6) as a function of radius and IWP.

needs to be done with care too. Since the IWP is maintained constant and for a given particle size of dry snow the density is smaller than for pure ice (and for wet snow an increase in

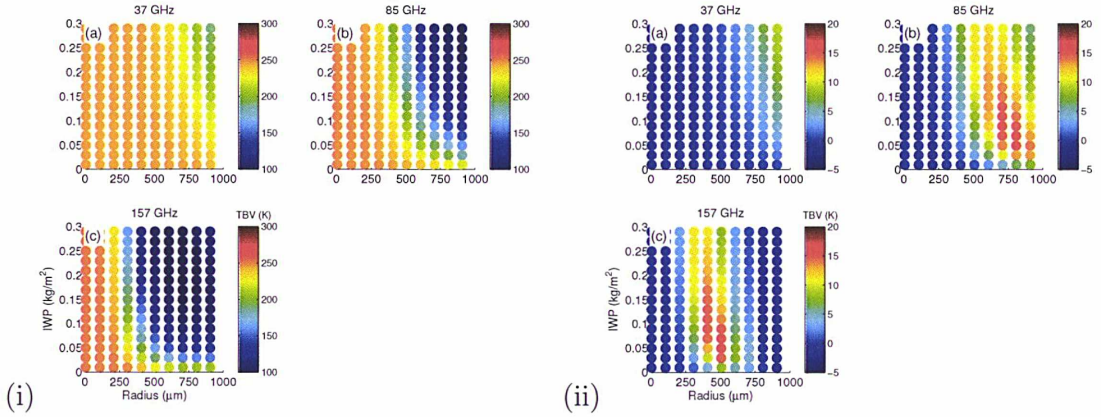

Figure 5.5: Same as above but for dry snow.

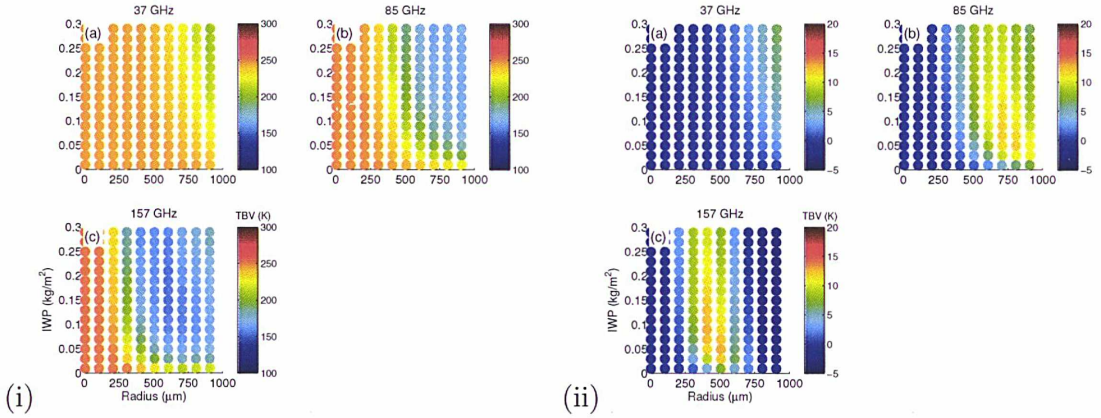

Figure 5.6: Same as above but for wet snow (f_m =0.05)

melting fraction leads to an increase in density), the particle number density is affected. A decrease (increase for wet snow) in density leads to an increase (decrease) in particle number concentration. For realistically large particle sizes, when the melted fraction increases, the simulated TBV depressions and polarization differences are more limited than for dry snow. Density proves to be a very important parameter. Further analyzes follow to assess if the large differences observed between ice and snow come from changes in the dielectric properties, or from changes in the particle number density.

Using a mono-disperse distribution of horizontally aligned spheroids of aspect ratio 1.6, Figure 5.7 below shows TBV and TBVH for pure ice (solid black curve) and dry snow (solid blue curve) with a given IWP of 0.2 kg/m^2 (just like in Figure 5.3 but for 89 and 157 GHz only). Overlaid in the Figure are similar simulations where the particle number densities for pure ice (dashed black curve) and dry snow (dashed blue curve) are kept fixed at a value corresponding to the particle number density of pure ice particles of radius of 400μm. Clearly in this case the IWP is not fixed.

The impact of using a fixed particle number density for dry snow species is smaller than using it for ice species. This is simply a consequence of running simulations where the total

mass is no longer fixed. For dry snow, the change in mass as a result of a fixed particle number density is very small because its density also decreases with size, counteracting the effect. In comparison, ice species have a constant density and consequently the mass with a fixed particle number density is much larger than the fixed mass simulations (solid curves). For this reason, TBV (TBVH) is low (high) for ice particles with a fixed particle number density. In terms of snow species, TBV(solid curve) is lower than TBV(dashed) because the fixed particle number density forces the total mass to decrease. Despite this, the TBVH is very similar for both dry snow simulations, indicating the importance of the dielectric properties in generating polarized scattering signatures.

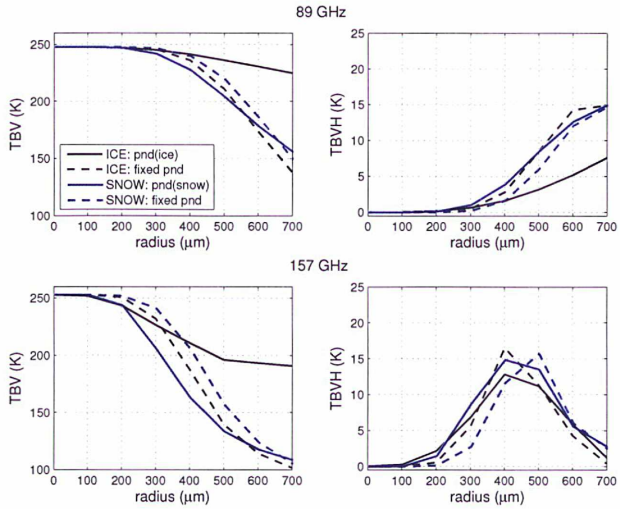

Figure 5.7: The sensitivity of the simulated vertical polarization TBV and polarization difference TBVH for ice (solid black line) and dry snow (solid blue line) to particle radius for a mono disperse distribution of horizontally aligned hydrometeors with fixed IWP (0.2 kg/m^2) and for a fixed particle number density (dashed lines). The simulations were performed for a tropical atmosphere over land (fixed emissivity of 0.9). See the text for more details.

5.4 The impact of the melting layer on the passive microwave cloud scattering signal observed from satellites: A study using TRMM microwave active and passive measurements

5.4.1 Introduction

In the stratiform regions of clouds, particles undergo complex melting processes as they fall through the freezing level. These processes have been described through aircraft microphysical measurements (e.g. Willis and Heymsfield, 1989), tunnel experiments (e.g. Mitra et al., 1990) and modelling studies (e.g. Zawadzki et al., 2005). Around the 0°C isotherm, the aggregation of snow particles of different sizes and fall velocities forms larger flakes of similar velocity, leading to a large increase in the maximum-sized particles and a decrease in the total number concentration. The low density flakes start to melt and turn into a mixture of water, ice, and air. Snow flakes typically melt within 100 to 500 m, and ice particles can be present at temperatures as high as 5°C. The melting of hydrometeors is a very complex process with impacts on the particle size, number concentration, and possibly shape and orientation.

An increase in the radar backscattered signal close to the freezing level in stratified clouds, the so-called bright band, has been observed by ground based weather radars as early as the 1940's, and it was interpreted in terms of the melting of snow flakes (Cunningham, 1947). Since the dielectric constant of water is greater than that of ice, the scattering caused by raindrops is greater than the one caused by ice particles of the same size. In the melting layer, wet snow flakes behave like large water drops, enhancing the backscattering whereas in the melted layer below, the decrease in number concentration and in particle size acts to reduce the radar reflectivity. The contrast between the higher reflectivity in the melting layer and the lower reflectivity below produces a bright band in the radar response, especially at low frequencies where attenuation by rain is not significant. The Precipitation Radar (PR) onboard TRMM operating at 13 GHz is sensitive to the signatures of the melting layer. Furthermore, when the bright band is detected with the PR at 13 GHz, its effect on the reflectivity profile is taken into account in rain retrieval algorithms. At CloudSat higher frequency, 94 GHz, only a sharp increase in the backscattering is observed at the melting layer: the decrease in the backscattering measured by TRMM at 13 GHz is not observed at 94 GHz due to the significant attenuation by rain (Di Girolamo et al., 2003; Kollias and Albrecht, 2005; Sassen et al., 2007).

The impact of the melting layer on passive microwave observations has been explored, mainly through modeling studies (Bauer et al., 1999, 2000; Olson et al., 2001b,a). Rather detailed melting processes have been implemented in cloud resolving models to produce realistic hydrometeor profiles, later used in radiative transfer simulations along with various dielectric models, size and density distributions. The advanced melting scheme developed by Olson et al. (2001a) includes melting, evaporation, particle interaction and the effect of changing particle density within a three-dimensional cloud model over the radiatively cold ocean. Other simulation studies have also focused on the modelling of the dielectric properties of the mixed-phase melting particles (e.g. Meneghini and Liao (1996, 2000). All these studies result in an increase of the brightness temperatures (TBs) when the bright band is present. Olson et al. (2001b) found an increase of the TBs up to 15, 12 and 9 K at 19, 37, and 85 GHz respectively. From observations around a North Atlantic cyclone with SSM/I along with aircraft microphysical

measurements, Schols et al. (1999) concluded that melting snow aggregates generate rather high TBs at 85 GHz compared to the regions where dense ice particles are present. Battaglia et al. (2003) conducted the first systematic analysis of observations to explore the effect of the melting layer on the passive microwave signal by looking at coincident radar and passive microwave observations during 5 years in TRMM data from December, January and February over the East Pacific. They focus on frequencies below 40 GHz and conclude that the bright band has a significant impact on the microwave signal. At 10 and 19 GHz, at constant rain rate, the average TBs are always higher in the presence of a bright band suggesting the significant role of emission at those frequencies. The average TB difference between presence and absence of the bright band decreases with increasing rain rate at 19 and 37 GHz, but at 85 GHz TBs are lower in presence of a bright band, contradicting previous results (essentially from simulations) and suggesting the importance of the scattering effect above the melting layer. This scattering signal at 85GHz has been used, for example, by Mohr et al. (1999) to estimate precipitation over ocean and land.

Work presented in Galligani et al. (2013) (published version found in the Appendix B *PAPER A* of this thesis and described in the following sections) explores the impact of particle phase changes around the melting layer on passive microwave observations using combined passive and active observations from TRMM. The focus is on the radiometric signatures of the TRMM Microwave Imager (TMI) at 37 and 85 GHz in bright band cloud regions based on TRMM Precipitation Radar (PR) measurements. The TRMM instruments have been presented in Chapter 2. The methodology and the data are described in Section 5.4.2. Section 5.4.3 presents the observational results that suggest that polarized scattering at 85 GHz coincides with the presence of a melting layer. Section 5.4.4 uses radiative transfer simulations to examine the link between polaraized scattering in the microwave and the properties of the hydrometeors, essentially their phase and density. Section 5.4.5 concludes this study, insisting on the interest of the analysis of the polarized signal at 85 GHz for more accurate precipitation retrievals.

5.4.2 The TRMM Observations

TMI and PR observations, together with its derived products, have been merged together on a regular 0.2° x 0.2° grid mesh for two years (2006 and 2007). Each grid box contains, when available, the TMI 1B11 brightness temperatures (TBs) located within the box, the TMI 2A12 derived rain parameters (not used in the analysis), and the PR level 2A products 2A23 and 2A25. Precipitation properties such as near surface rain rate, convective/stratiform rain and bright band properties, are determined by the PR products 2A23 and 2A25. The analysis of the database is performed over sea and land separately based on the 2A12 surface flag. In order to avoid contamination of the radiometric signal by snow on the ground, snow-covered pixels are filtered out using the National Snow and Ice Data Center (NSIDC) data (Armstrong and Brodzik, 2005).

Here, the PR observations are considered as valid and accurate enough to describe the properties of the precipitation (e.g. geographical distribution, rain rate type and rain rate). The algorithm 2A25 uses a Z-R relationship based on a particle size distribution model and retrieves profiles of the radar reflectivity factor with rain attenuation correction and rain rate for each radar beam (Iguchi et al., 2000). The algorithm 2A23 verifies if a bright band exists in rain echoes and determines the bright band height and intensity when it exists (Awaka et al., 1997). The rain type is classified into stratiform, convective and others, based on the detection

of BB and the properties of the horizontal structure of the reflectivity field. The PR minimum detectable rain is usually considered to be 0.5 mm h^{-1}. Schumacher and Houze (2000) derive maps of rainfall rate and convective/stratiform classification for oceanic cases that compare well between PR and S-band validation radar records during the Kwajex experiment. Schumacher and Houze (2000) also report a tendency of the PR to under sample weaker echoes associated with stratiform rain near the surface and ice particles aloft, but the PR is still able to record most of the near-surface precipitation accumulation. Liao and Meneghini (2009) showed a fairly good agreement between the PR and the Melbourne Weather Surveillance Radar-1988 Doppler (WSR-88D) derived rain rates for stratiform rain while during convective rain the PR seems to overestimate light rain, and underestimate moderate to heavy rain in comparison with the WSR data. However, different performances are expected worldwide according to variability in climate, surface background, and raindrop size distributions (Liao and Meneghini, 2009). More recently the analysis performed by Berg et al. (2010) reported a rather good agreement between PR and Cloud Profiling Radar (CPR) rain rates in the range 1 to 3 mm h^{-1} and for a total precipitable water (TPW) estimate above 40 mm.

5.4.3 Analysis of the Polarized Scattering Signatures of TMI data in the Presence of a Melting Layer

Figure 5.8 presents a case study at pixel level over land. It corresponds to a squall line in Africa as observed during the African Monsoon Multidisciplinary analyzes (AMMA) campaign (19/07/1998).

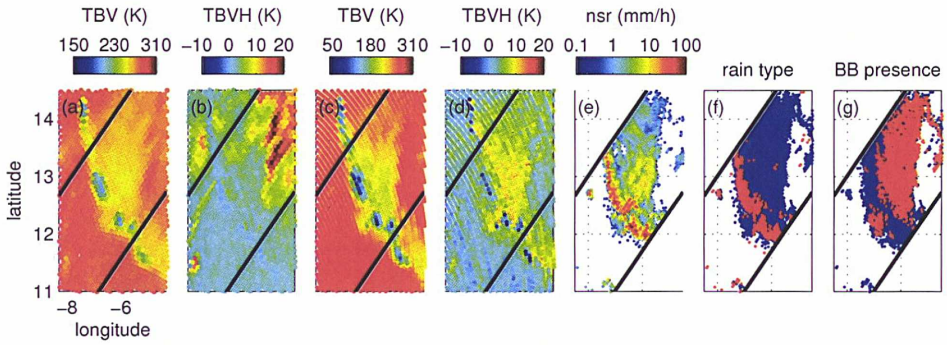

Figure 5.8: TRMM observations of a squall line in Africa during the AMMA campaign (19/08/2006) with (a) TBV(37 GHz), (b) TBVH(37 GHz), (c) TBV(85 GHz), (d) TBVH(85 GHz), (e) the near surface rain rate, (f) the PR rain type flag from the 2A23 PR product, convective in red and stratiform in blue, and (g) the presence of a BB in red.

In the convective phase of the cloud of Figure 5.8, strong scattering is evidenced by the observed low TBVs, which are lower than those of the stratiform phase both at 37 and 85 GHz. The convective phase shows little polarization difference. Less pronounced scattering is present at 37 GHz than at 85 GHz both in the stratiform and convective phases as expected. Figure 5.8 shows coincident TBVH(85 GHz) signals of the order of 8 K and TBV(85 GHz) signals of the order of 220 K when the PR detects stratiform rain and the presence of BB, as presented in the statistical analysis that follows. Irrespective of the presence or not of a BB, near surface

rain rates as provided by PR range over two orders of magnitude in the stratiform region. Furthermore, as shown in this case study at pixel level, and as follows in a statistical analsysis, regions of convective rain where there is no BB reported very low TBVs and negative, or negligible, polarization signals, high rain rate and lightning activity (not shown).

In order to assess the impact of the melting layer on TMI observations, cases of stratiform rain are first identified with the PR and further divided into cases with and without melting layers as detected by the PR bright band (BB). Stratiform rain boxes of 0.2° x 0.2° are identified as having at least 20 PR observations with 50% of them stratiform; considered in this study are only those boxes where the bright band is detected for 100% of stratiform observations or for 0% of them. Averaged vertical and horizontal brightness temperatures (TBV and TBH) and polarization differences (TBVH) at TMI frequencies are analyzed as a function of the stratiform near surface rain rate, with and without a melting layer. Figure 5.9 presents the variations as a function of stratiform rain rate of the TMI averaged brightness temperatures (TBH) and their polarization differences (TBVH) over ocean (top panels) and land (bottom panels), along with their standard deviations, computed over the 0.2° x 0.2° grid at 37 and 85 GHz for stratiform rain with a BB (blue curve) and without a BB (red curve).

The ocean has a rather low surface emissivity with large polarization differences. At low frequencies, emission by cloud and rain increases the TBs over the radiometrically cold background, and the polarization generated by the surface decreases with increasing cloud and rain attenuation. For all frequencies above 10 GHz, the presence of BB tends to decrease the TBs. At 85 GHz, two phenomena compete, namely the emission and the scattering by cloud and rain. The difference between the presence and absence of a bright band is evidenced clearly over land at 85 GHz for high rain rates. TBs are lower when a BB is detected, likely associated with the increasing number of frozen particles associated to the melting layer. In addition TBs decrease with increasing RR for BB cases. The difference between BB and no-BB polarization difference increases with increasing rain rate, i.e., increasing ice quantities. This is a clear evidence that the polarization difference (of the order of 7K) is generated by the presence of hydrometeors, not by the polarized surface of the ocean.

Land surface emissivities in the microwave region are usually very high (above 0.95) and have low polarization differences. Consequently, cloud and rain emission signatures are more difficult to detect due to the lack of contrast between the surface and the atmospheric contributions. At 37 and 85 GHz, the variation of the brightness temperatures in presence of BB decreases for an increasing rain rate while the average brightness temperature is more or less constant in stratiform rain without a melting layer. The scattering signal by frozen particles is not only observable at 85 GHz when a melting layer is detected, but also at 37 GHz. Note nevertheless that, as expected, the magnitude of the TB decrease at 37 GHz is much more limited than at 85 GHz. Similar to what is observed over ocean, the polarization difference increases with increasing rain rate. On average, a polarization difference of 4-5 K is observed for a rain rate of 5 mm/h between cases with and without melting layer.

A sensitivity study (not shown) of the different thresholds over ocean shows that decreasing the percentage of BB for a given rain rate at 85 GHz induces warmer TBs, a decrease of the polarization difference, and a larger standard deviation of both TBs and polarization difference. When one increases the percentage of stratiform pixels, the number of non-BB rain pixels decreases and the averaged brightness temperatures get warmer at 85 GHz.

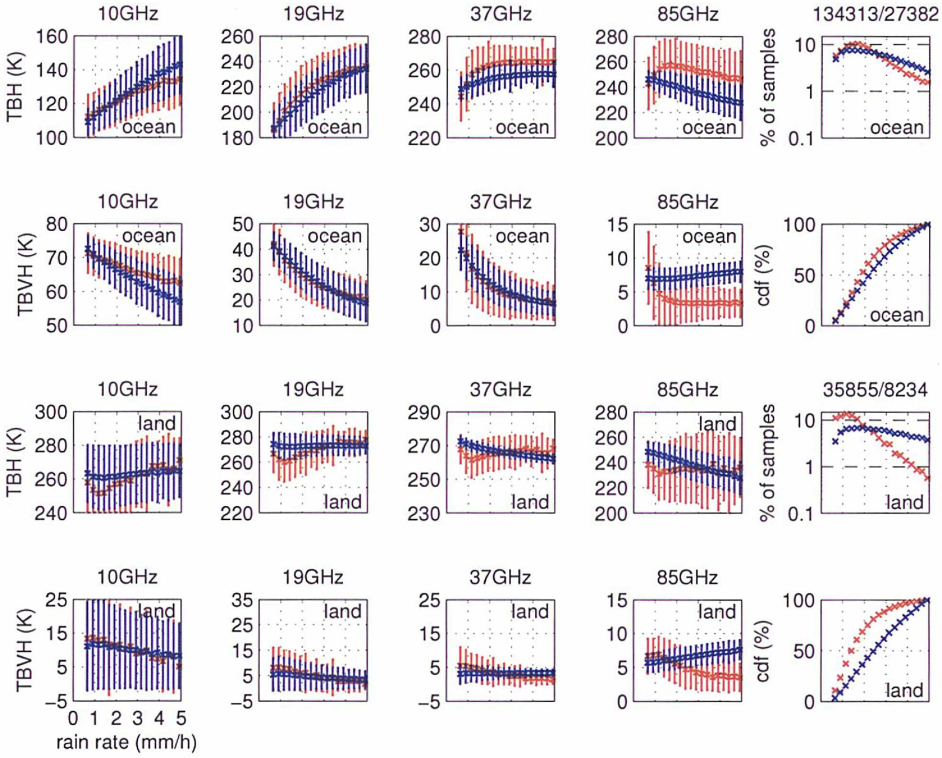

Figure 5.9: Variations of TMI averaged brightness temperatures (TBH) and averaged polarization differences (TBVH) along with their standard deviations as a function of the averaged rain rate as computed over a 0.2° × 0.2° grid over two years for the Tropical region. The 0.2° × 0.2° rain boxes are identified as having at least 20 PR observations with 50% of them being stratiform. Blue (red) represents grid boxes where the bright band (BB) was detected for 100% (0%) of stratiform observations. The top right panel (bottom third right panel) present the percentages of grid-boxes relative to the total number of grid-boxes (indicated at the top of the panel - with/without BB) that satisfy the selection criteria as a function of rain rate over ocean (land). Their respective cumulative distribution function as a function of rain rate for cases with a BB (blue) and without a BB (red) is shown on the second and fourth right panels for ocean and land respectively.

Figure 5.10 presents the probability of precipitation cases (precipitation, convective precipitation, stratiform precipitation and precipitation with BB) at 85 GHz as a function of vertical brightness temperatures (TBV) and polarization difference (TBVH) using two years of data over both ocean and land, for 1 K × 1 K pairs of TBVH versus TBH. The probability of precipitation is defined as the averaged value of the number of PR pixels identified as precipitation divided by the number of PR observations within the same box. Only cases at least partly precipitating are considered, representing approximately 5% of the total population over both surfaces. In the case of precipitation over ocean (Figure 5.10a), the vertical branch with large polarization differences corresponds to situations with partial transmission of the surface polarized signal despite the rain attenuation. The horizontal branch in the scatter plots corre-

sponds to the decreasing TBs associated with the scattering signal of clouds. As expected, the probability of rain increases when the brightness temperatures decrease, i.e. when the convection deepens. Figure 5.10b (ocean) and Figure 5.10f (land) further show the percentage of PR pixels identified as convective rain pixels divided by the number of PR observations within the same box. Colder brightness temperatures are more often observed over land than over ocean, which is consistent with the fact that continental convection is deeper than oceanic convection. Deeper convection induces more ice in the clouds and, consequently, more efficient scattering by large ice particles. Additionally, cold brightness temperatures associated with deep convection can exhibit negative polarization differences. Prigent et al. (2005b) explain such radiometric behavior by the presence of predominantly vertically oriented graupel located in the convective cores. Convective rain (Figure 5.10b and Figure 5.10f) and stratiform rain (Figure 5.10c and Figure 5.10g) are clearly reported in two different regions of the TBV / TBVH space over both ocean and land. Convective rain is basically expected where brightness temperatures (TBV) at 85 GHz are below 200 K with a negative or slightly positive polarization difference. Stratiform rain is statistically dominant for TBV ranging from 200 K to 260 K and a positive polarization difference (TBVH) above 5 K and below 12 K. Some basic threshold delimiting the specific regions of the TBVH space could be used as convective/stratiform classification for microwave-based retrieval schemes for TMI, but also for other space missions with similar frequencies and footprints after cross-calibration of the microwave sensors.

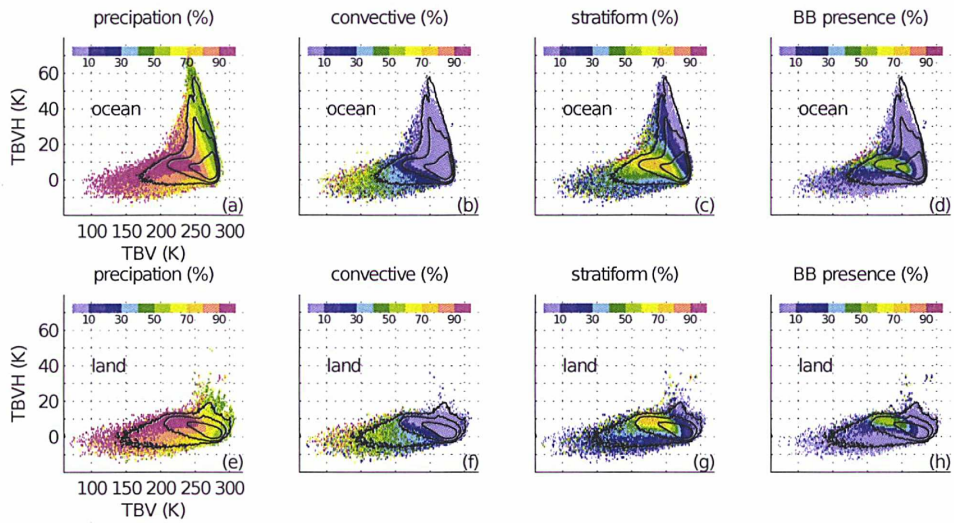

Figure 5.10: Scatter plot of the polarization difference (TBVH) versus the vertical polarization (TBV) at 85 GHz, for 2006 and 2007 data, over ocean (top) and over land (bottom), of the probability of precipitation (a and e), of convective rain (b and f), of stratiform rain (c and g), and of the presence of a BB (d and h). Black iso-lines delineate the population that represents 10^{-3}, 10^{-2} and 0.1% of the total number of samples.

For stratiform rain, one can expect a large spatial distribution of the rain field and a relatively homogeneous microwave signal within the box. Brightness temperatures with low

percentage of stratiform rain correspond to clouds where there is also convection sampled in the same grid box. Note also that the sum of convective rain probability and stratiform rain probability is not necessary equal to 100% because some of the PR pixels can be classified as non convective and non stratiform. Finally Figure 5.10d (and Figure 5.10h) presents how the signal at 85 GHz correlates with the presence of BB over ocean (and land). Interestingly, the high probability of BB presence spans over a relatively limited domain in the TBVH space around 7 K and, as expected, the high percentage of BB presence corresponds to regions where stratiform rain is also predominantly detected.

For comparison, Figure 5.11 presents similar plots to Figure 5.10 but at 37 GHz. Stratiform and convective rains are clearly reported in two separate regions of the TBVH space for both ocean and land. Convective rain is predominantly detected (>70%) for brightness temperatures below 250 K and polarization differences up to 10 K (Figure 5.11b). Colder brightness temperatures can be recorded over land, because of more intense and therefore deeper convection over surfaces that can undergo strong solar heating. Stratiform rain (Figure 5.11c) is recorded for a large range of brightness temperatures (220 to 280 K) and a positive polarization difference of up to 40 K. Over land the distribution peaks lie in a relative narrow area in the TBVH space.

The possible links between the polarized scattering signatures at 85 GHz, and the polarized observations in the visible (Noel and Chepfer, 2004; Bréon and Dubrulle, 2011) have also been investigated (see the appendix of the published paper in the Appendix B (*PAPER A*) of this thesis) but the relationship between the two phenomena was not conclusive.

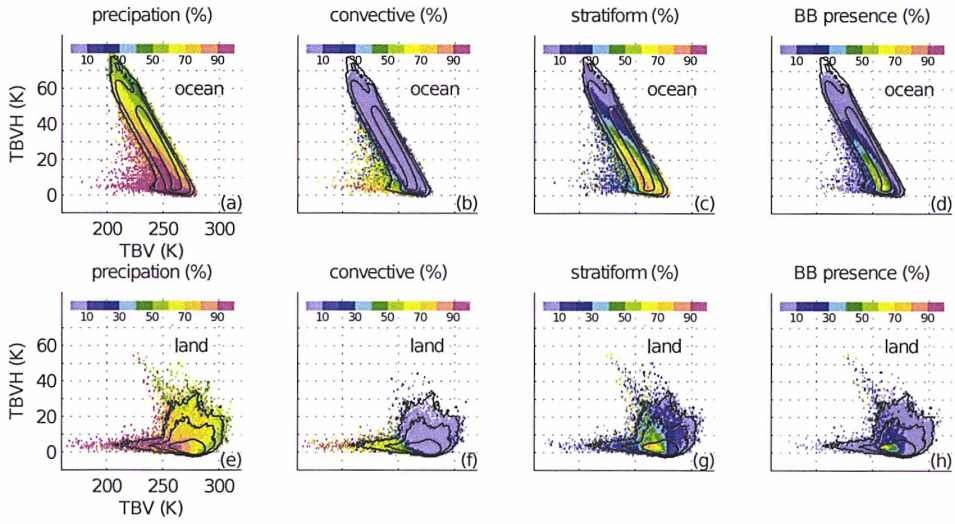

Figure 5.11: Same Figure 3 but for 37 GHz.

5.4.4 Modeling the Sensitivity of the Passive Microwave Signal to Changes in Hydrometeor Phases

As discussed, the melting layer is primarily characterized by a change in the particle composition from ice (more precisely a mixture of ice and air) to liquid water. This transformation has multiple impacts in terms of particle size, number concentration and, possibly, shape and orientation. Our objective here is to assess qualitatively how changes in hydrometeor dielectric properties impact the polarized scattering signal in passive observations via radiative transfer simulations to investigate on the possible link between polarized scattering in the microwave and the dielectric properoties in the BB melting layer. What causes the strongly polarized scattering signal observed at 85 GHz in stratiform situations? What is the role of frozen hydrometeors on the observed polarized scattering signal? How do pure ice and snow compare in terms of scattering at 85 GHz for realistic particle habits? Does the snow wetness enhance the scattering effect and compensate for the decrease in size a melting particle goes through?

Radiative properties of the melting layer are sensitive to a large number of parameters, such as the choice of dielectric models, density parameterization or the integrated water paths (IWP, defined as the hydrometeor, ice, snow or melting snow, column integrated water mass). Here we attempt to asses the sensitivity to such parameters for passive microwave observations. It is important to keep in mind that modeling the optical properties of frozen particles is problematic even for pristine frozen particles that are not undergoing melting. The particle size distribution, the dielectric properties of the material, and the shape of the particle are all subject to large uncertainties that can translate into significant differences in terms of simulated brightness temperatures (e.g. Surussavadee and Staelin, 2006; Meirold-Mautner et al., 2007; Kulie et al., 2010).

The radiative transfer simulations conducted are similar to those in Section 5.3 but in the physical context of a melting layer, using a given atmospheric profile of temperature, pressure, water vapor, ozone and height from the Chevallier et al. (2006) database (atmosphere of 8.3 kg/m^2 of water vapor). The land surface emissivity in the simulations is set to 0.9 for both polarizations and the nadir angle is set to 50°. A single layer (2 km thick) of hydrometeors populates the atmosphere around the 0° isotherm (4 km in altitude) with varying IWP (between 0.1 kg/m^2 and 2 kg/m^2). A mono-disperse particle size distribution of horizontally orientated spheroids was assumed and varied between 50 μm - 700 μm (size refers to the size of a mass equivalent sphere). The dielectric properties are as determined by the Maxwell Garnett mixing formula (discussed in Section 4.2.1 and 5.2). Literature has shown this model to be most in agreement with the average characteristics of the melting layer in longterm observations (Olson et al. (2001b,a); Battaglia et al. (2003); Fabry and Szyrmer (1999); Zawadzki et al. (2005)).

Simulations with hydrometeor profiles of more realistic characteristics (3 plane parallel hydrometeor layers) are also analyzed (not shown). The 3 layers were composed of (1) a layer of ice particles between 5 and 8 km with an equivalent ice water path of 0.4 kg/m^2 and single-size spheres of 150 μm radius; (2) a layer representing the melting layer between 3 and 5 km as described above; and (3) a rain layer of 4 mm/hr between 0 and 3 km containing liquid water single size spherical randomly orientated particles with a Marshall Palmer size distribution. Such hydrometeor profiles yield similar results in terms of polarization difference at 85 GHz than the melting layer alone. The ice cloud above only adds limited extinction to the signal (a decrease of the polarization difference smaller than 2 K), and the rain below is not observed as the melting layer is quite opaque. We focus thus on the parameters of the particles populating

the melting layer relevant to the observed polarized scattering signals described earlier in the presence of a BB, by simplifying the hydrometeor profiles to just the melting layer.

With respect to defining the shape of these hydrometeors for the purpose of modelling the radar bright band at TRMM frequencies, as already discussed in Section (5.2), the precise particle shapes are not very important and scattering properties depend mostly on the overall shape of the particles as determined by the aspect ratio (Dungey and Bohren, 1993b; Matrosov et al., 2005a).

Prigent et al. (2005b, 2001) explained the observed polarized scattering signal of pristine ice habits in terms of particle shape and orientation, where simulations with randomly oriented, large spheroidal particles cannot replicate the observed polarization differences at 85 GHz, but oriented non-spherical particles can. Following these studies, Figure 5.12a and Figure 5.12b (Figure 5.12c and Figure 5.12d) show the vertical brightness temperature, TBV, and the polarization differences, TBVH, for 37 and 85 GHz as a function of particle size for pristine, horizontally distributed ice particles (ρ=0.917 kg/m^3) of aspect ratio 1.6. As expected, the TBVs decrease with increasing particle size, especially at 85 GHz: the larger the IWP, the larger the depression. The polarization differences at 85 GHz also increase with increasing particle size and with increasing IWP. To evaluate the sensitivity of the scattering signal to particle composition, Figure 5.12 also shows the TBV and TBVH for dry snow (i.e. a mixture of air and ice). The dielectric properties for dry snow were calculated using ice inclusions in an air matrix, but it is worth noting that using air inclusions in a matrix of ice yielded very similar results (not shown). The volume fraction of the ice inclusions was determined by applying the density parameterisation from Mitchell et al. (1990) (see Table 4.3) to the snowflake diameter (ρ_{ds}(D)). Using the other parameterisations listed in Table 4.3 yielded very similar results, with differences in TBVH of the order of 1 K and in TBV of the order of 2 K at 85 GHz. Figure 5.12 evidences that the scattering is much more important at 85 GHz than at 37 GHz for both pristine ice and dry snow hydrometeors, while comparing pristine ice with dry snow shows that dry snow has enhanced the scattering and the polarization differences. For large particles of dry snow that have a large scattering effect (TBVs lower than 160 K) TBVH reaches a limit where multiple scattering effects become significant and TBVH approaches a saturation limit and starts decreasing. For higher IWPs, the TBVH saturation limit is approached with smaller particle sizes. It is important to keep in mind, however, that a comparison between ice and dry snow equal size particles takes into account a decrease in density in the dry snow particles: this decrease in density translates into an increase in the particle number concentration. Clearly, for a given particle size, the increase of particle number increases the scattering effect, as well as the polarization difference. Due to this effect, Figure 5.12 evidences how important density can be as a parameter, specially at 85 GHz. Note that in Figure 5.12d TBVH for dry snow particles (IWP=0.2 kg/m^2) of aspect ratios of 1, 1.2 and 1.4 are also shown for comparison. Reminder that an aspect ratio of 1 corresponds to spheres, and they generate very limited polarisation differences.

Figure 5.13 explores the effect of snow wetness by including different melted fractions (f_m) in the ice-air-water mixture for an IWP of 0.4 kg/m^2. Note that when discussing wet snow species, the term IWP is used and represents the total column mass. In the case of wet snow, since the IWP is maintained constant for a given particle size, an increase in melting fraction leads to an increase in density and to a decrease in particle number concentration. For realistically large particle sizes, when the melted fraction increases, the simulated TBV depressions and polarization differences are more limited. Tests were also run to evaluate the sensitivity of wet

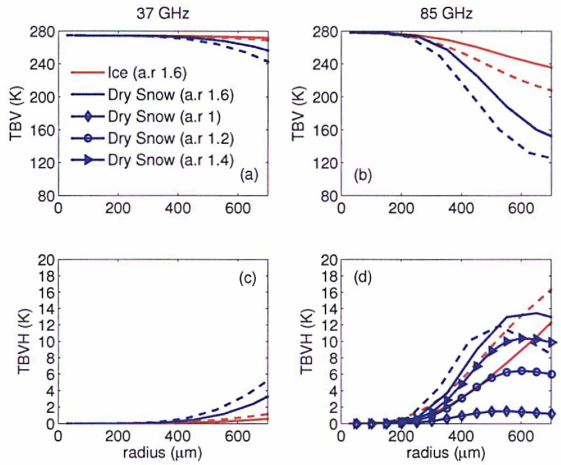

Figure 5.12: The sensitivity of the vertical brightness temperature (TBV) and the polarization difference (TBVH) at 37 GHz and 85 GHz to the particle size (effective radius) of horizontally aligned pure ice and dry snow spheroids of aspect ratio 1.6, under different IWPs (solid lines for 0.2 kg/m^2 and dashed lines for 0.4 kg/m^2). Additionally, the simulated polarization difference at 85 GHz for dry snow (0.2 kg/m^2) of different aspect ratios were added in (d).

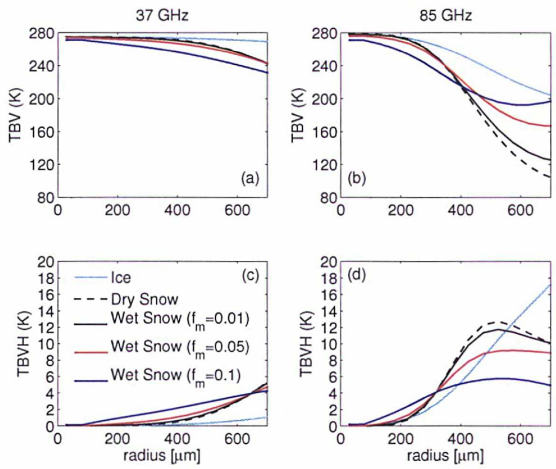

Figure 5.13: The simulated vertical polarization and polarization difference at 37 and 85 GHz for pure ice and wet snow hydrometeors (air-ice-water mixture). Different melted fractions (f_m) are shown. The IWP is 0.4 kg/m^2.

snow to the choice of $\rho_s(D)$ when calculating the dielectric properties of its dry snow matrix. This sensitivity was observed in the simulations to be not larger than 2 K for both TBVH and TBV at 85 GHz. In a cloud during the melting process, the transition from dry snow to melting snow does not induce a change of particle number concentration but a change in particle size, with the melting particle being smaller than the dry snow particle of the same mass. Figure 5.14 tests the effect of the melting fraction (f_m) for a given IWP, when conserving

the particle number concentration. For each value of IWP and each hydrometeor phase, the particle number concentration is calculated for dry snow particles of 400 μm effective radius. For the wet hydrometeors simulated, in order to conserve IWP with the number concentration fixed to that of dry snow, their size is allowed to decrease. Figure 5.14 illustrates that for a given value of IWP and for a given particle number concentration, the change in dielectric properties from dry to wet snow does not compensate for the reduction in particle size that occurs in the melting layer.

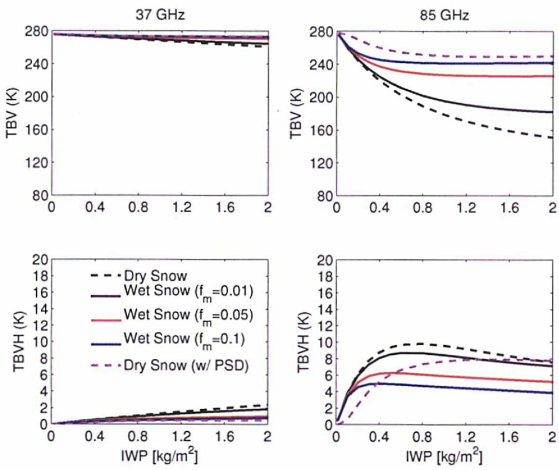

Figure 5.14: The simulated vertical polarization and polarization differences at 37 and 85 GHz for dry snow as a function of IWP for particles of 400 μm radius. The radiative properties of the wet snow hydrometeors under different melted fractions (f_m) were simulated for the particle number concentration calculated for dry snow and their size allowed to decrease to conserve the IWP. The simulated vertical polarization and polarization differences for dry snow with the Sekhon and Srivastava (1970) (SS) PSD applied is also shown.

The simulations discussed so far with a mono-disperse particle size distribution assess qualitatively the impact of hydrometeor dielectric properties on the polarization signal. The step to make to assess the polarization signal of realistic clouds is to apply a particle size distribution. For this, we used an exponential particle size distribution (PSD), or number density of particles within the diameter range D to $D + dD$, which is one of the most commonly applied particle size distribution for snowflakes:

$$N(D) = N_0 \exp(-\lambda D) \qquad [cm^{-4}] \tag{5.2}$$

We used values for the parameters N_0 and λ from the Sekhon and Srivastava (1970) (SS) size distribution for dry snow. In the SS size distribution for dry snow aggregates: $N_0 = 6.4 \times 10^{-3} M^{-1.09}$ (cm^{-4}), $\lambda = 11.9 \times M^{-0.52}$ (cm^{-1}) and M is the mass content (g/cm^3). Calculations using this PSD were done for horizontally aligned dry snow aggregates only (and shown in Figure 5.14), the idea being to show that under realistic cloud settings, the magnitude of the depolarization generated by radiative transfer modeling is comparable to that observed. The maximum depolarization signal generated by horizontally aligned ice particles (not shown)

as calculated with the McFarquhar and Heymsfield (1997) PSD parameterization for the same IWP range as dry snow aggregates was approximately 3 K at 85 GHz.

These simulations show that horizontally oriented oblate dry snow particles can generate the scattering signatures observed at 85 GHz, with polarization differences of the order of 5 K and higher. For a given IWP and particle size, dry snow is more efficient than pure ice at scattering and at generating polarized scattering at 85 GHz: the decrease in the real part of the refractive index from pure ice to dry snow, a mixture of ice and air, is largely compensated by the increase in particle number as a result of the lower density of dry snow. Melting of the snow does not enhance the brightness temperature depression nor the polarization difference. The changes in the real part of the refractive index from dry snow to melting snow do not compensate for the decrease in particle size that occurs with the melting of the particle.

5.4.5 Conclusion

Scattering at 85 GHz over clouds is often associated with significant polarization differences (TBVH $>$ 5 K), both over land and ocean. Coincident passive and active observations from TRMM show that a large portion of polarized scattering tends to occur when the radar observes a bright band, i.e., in the presence of a melting layer. The scattering signal by frozen particles is not only observable at 85 GHz when a melting layer is detected, but also at 37 GHz. Note nevertheless that, as expected, the magnitude of the TB decrease at 37 GHz is much more limited than at 85 GHz. Aggregation of snow particles around the 0°C isotherm produces large flakes that can significantly scatter the microwave. The simulations show that the observations with TMI that coincide with a detected bright band on the PR can be interpreted in terms of dry snow particles of oblate bulk shapes with aspect ratios of the order of 1.6, and with horizontal orientation. The melting of the large snow flakes does not appear to increase the scattering effects.

The sensitivity of passive microwave polarized scattering to the shape and orientation of the hydrometeors is unique among the current observations: it is an unexpected tool to gain understanding in complex microphysical processes in clouds.

The presence of a melting layer can be deduced from the analysis of the polarized scattering signal, as shown in this study, with a rather stable relationship in the TBV and TBVH space when a radar bright band is observed. Neglecting the effect of the melting layer in the retrieval has been shown to lead to an overestimation of the precipitation for light stratiform rain (Brown and Ruf, 2007), a key issue in mid-latitude regions where the majority of the precipitation has a low freezing level. The Global Precipitation Measuring (GPM) mission will extend the TRMM capacity outside the Tropics to global and more frequent observations. Outside the regions where both passive and active observations from GPM will be available, the polarized scattering signal around 85 GHz can indicate the presence of the melting layer and will allow to re-direct the retrieval scheme towards a more realistic precipitation scheme over land and ocean.

The French-Indian Megha-Tropiques mission, launched in October 2011, carries a passive microwave conical scanner with polarized measurements at 18.7, 23.8, 36.5, 89 and 157 GHz. The polarized scattering signal at 157 GHz provides a novel and unique opportunity to study further the microphysics of frozen hydrometeors. The following section concerns the analysis of these novel observations at close-to-millimeter frequencies.

5.5 First Satellite Based Observations of the Cloud Polarized Scattering Signal at close-to-millimeter Frequencies (157 GHz) with MADRAS

5.5.1 Introduction

The French-Indian Megha-Tropique satellite, launched in 2011, carries several instruments including the conical microwave scanner MADRAS. MADRAS has frequency channels between 10 and 157 GHz capable of measuring both orthogonal polarizations (the 23.8 GHz channel only measures the V component). This includes the 157 GHz channel which provides the first satellite based polarized observations at close-to-millimeter frequencies. So far, passive satellite observations were available up to 190 GHz, but with no orthogonal polarizations measurements.

The interaction of millimeter radiation with frozen hydrometeors, as discussed throughout this thesis project, is complex and involves not only the ice quantities but also the size distribution of the particles, their dielectric properties, their shapes, and their orientation. Understanding and quantifying the scattering signals from the frozen phase at millimeter waves is of importance for a full exploitation of the observational capabilities in the next generation of satellite instruments (e.g., the Ice Cloud Imager at frequencies between 160 GHz to 660 GHz onboard the next generation of European operational satellites MetOp-SG).

This section explores the impact on the microwave signal of variations in the microphysical parameters of the cloud frozen phase at 157 GHz, that are expected to have a higher effect than at 89 GHz. This section is structured as follows: Section 5.5.2 analyzes the polarized cloud scattering observations available from MADRAS. Section 5.5.3 presents two different sets of realistic radiative transfer simulations performed to explore and interpret the observed polarized scattering up to 157 GHz. Section 5.5.4 concludes this study.

5.5.2 Analysis of MADRAS Cloud Polarized Scattering Signatures

Figure 5.15 shows almost time-coincident vertical brightness temperature (TBV) observations from MADRAS (left) and TMI (right). The region of interest covers observations over both land and ocean in the south east coast of Africa, covering the north of Madagascar, Mozambique, Tanzania and a small fraction of the Indian Ocean. For comparison, the TRMM VIRS observations at 10.8 μm are also plotted. Similarly, Figure 5.16 presents the corresponding polarization difference TBVH observations from MADRAS and TMI. Despite different spatial resolutions and a small time difference, the observations of the two radiometers are quite similar in terms of the radiometric range, the sensitivity over land and sea, as well as in pinpointing convective regions. Note the differences in spatial resolution between 36 GHz (with rather blurred structures at this frequency) and 157 GHz, and the spatial resolution difference at 37 GHz between MADRAS and TMI (with TMI having a better spatial resolution).

The behavior of TBV and TBVH is as expected. While at 36 and 89 GHz the radiometric signal at the observed latitude range can be sensitive to the surface, the 157 GHz channel appears not contaminated by the surface (continent and ocean). This is also the case for TBVH maps. The ocean surface emissivities are rather low and polarized, contrarily to the land that usually has a high emissivity with very limited polarization. For low atmospheric

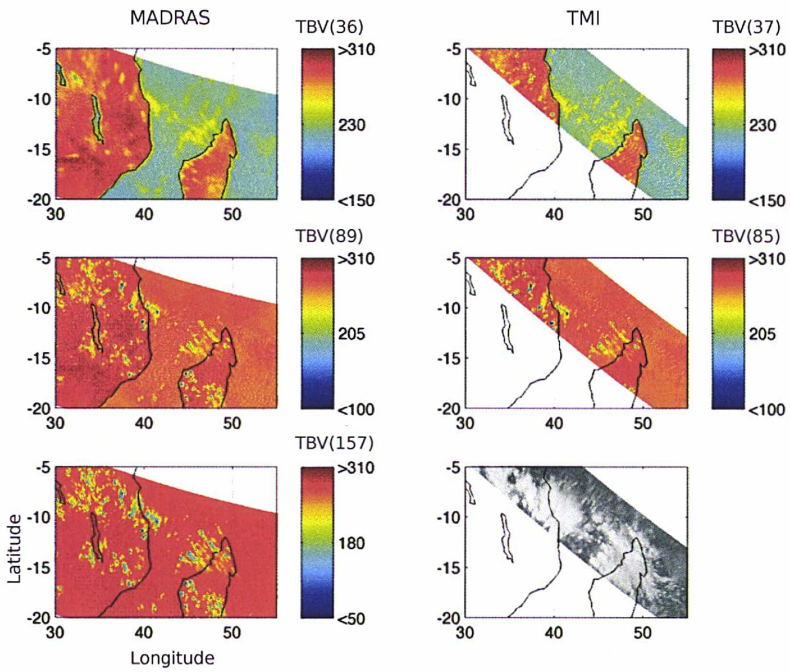

Figure 5.15: Maps of almost time-coincident MADRAS (left) and TMI (right) TBV observations from the 9th of December 2011. MADRAS (TMI) data was recorded between 12:05 and 12:12 TU (12:10 and 12:18 TU). TRMM VIRS 10.8 μm data is also shown for reference.

opacity at the lower frequencies, the contrast between ocean and land is larger. At 157 GHz, the atmospheric opacity in these tropical regions completely masks the surface signal. At 36 GHz, liquid water emission in clouds induces an increase in TBV over ocean but a decrease over the highly emitting land. Liquid water emission also induces a decrease of the polarized surface emissions over ocean. Note that the observed polarized signature over land at 35^oE between -15^o and -10^oN for 37 and 89 GHz does not correspond to cloud structures, but to standing water at the surfaces (Lake Malawi). At 157 GHz, cloud structures appear cold over both ocean and land due to the scattering of the cloud ice phase, with rather low TBVs (down to almost 50 K on this case study) associated to an increase in the TBVH signal. These large TBVH observations cannot be due to the surface as the cloud free areas do not show any polarization.

For all the available MADRAS measurements (the MADRAS V05 84-day dataset), Figure 5.17 presents scatterplots of TBVH versus TBV for 14 days that satisfied additional in-house verification related to calibration errors. The ocean and land cases are treated separately, and for each 1 K x 1 K box the color indicates the relative number of pixels with respect to the total. Clear sky and cloudy sky in the scattering regime can be easily distinguished, especially over ocean. At 36, 89, and 157 GHz, clear sky and thin clouds have low TBV with large polarization differences caused by the ocean surface, but as cloud opacity increases, TBV increases and the polarization difference decreases. Over land, the maximum density of pixels is located at high TBV and close to 0 K polarization for all frequencies. This is expected: the land emissivity is only weakly polarized in average, and atmospheric gaseous emission and absorption processes are not polarized. At 157 GHz, even under clear sky condition and over

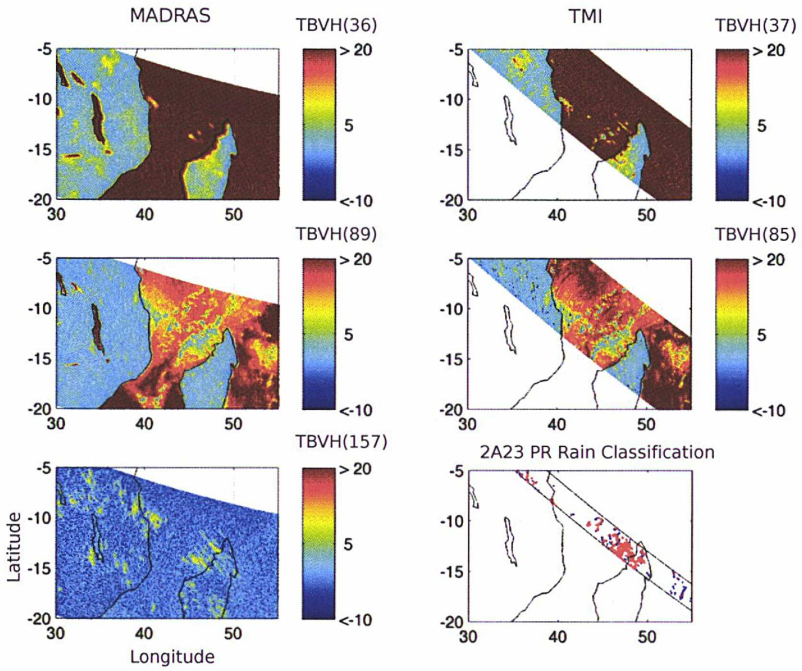

Figure 5.16: Same as Figure 5.15 above but for TBVH observations as well as 2A23 PR rain classification (red = Stratiform; blue = Convective) within the PR swath

ocean, the opacity related to the water vapor is often very high (large TBV) and masks the polarized surface signal (low TBVH). In the scattering regime, most often observed for clouds with colder top temperatures, TBV decreases due to the scattering of large ice particles and can reach very low values, especially over land where convection is deeper. As previously discussed with TMI in Section 5.4.3, deeper convection induces more ice in the clouds and, consequently, more efficient scattering by large ice particles. The relative population of pixels with TBVs lower than 200 K is larger over land than over ocean (at 85 and even larger at 157 GHz). This general trend is expected, as the higher frequency 157 GHz channel is more sensitive to the ice phase. These types of scatter plots are similar to those presented in Prigent et al. (2001, 2005b) for SSM/I, TMI, and Galligani et al. (2013) for TMI.

As shown in Figure 5.17, the maximum of the 2D cumulative distribution over land is located at high TBV and close to 0 K polarization for all frequencies. This is expected as the land emissivity is only weakly polarized in average, and atmospheric emission processes are not polarized. At 157 GHz a significant number of pixels corresponding to high TBV show negative polarization difference. We argue that the distribution of the polarization difference at the maximum density of points for high TBV over land can provide an estimate of the instrument noise on the polarization difference (using $\sigma^2_{V-H} = \sigma^2_V + \sigma^2_H$ and assuming $\sigma_V = \sigma_H$). The derived estimates are above the values announced by the instrumental documents but they are in agreement with the required instrumental especifications and follow the same trend where values are higher at 157 GHz (deduced 2.4 / instrumental specification 2.2), than at 89 GHz (deduced 1.2 / instrumental specification 0.76).

In order to perform a quick inter-comparison of TMI and MADRAS channels at 37 and

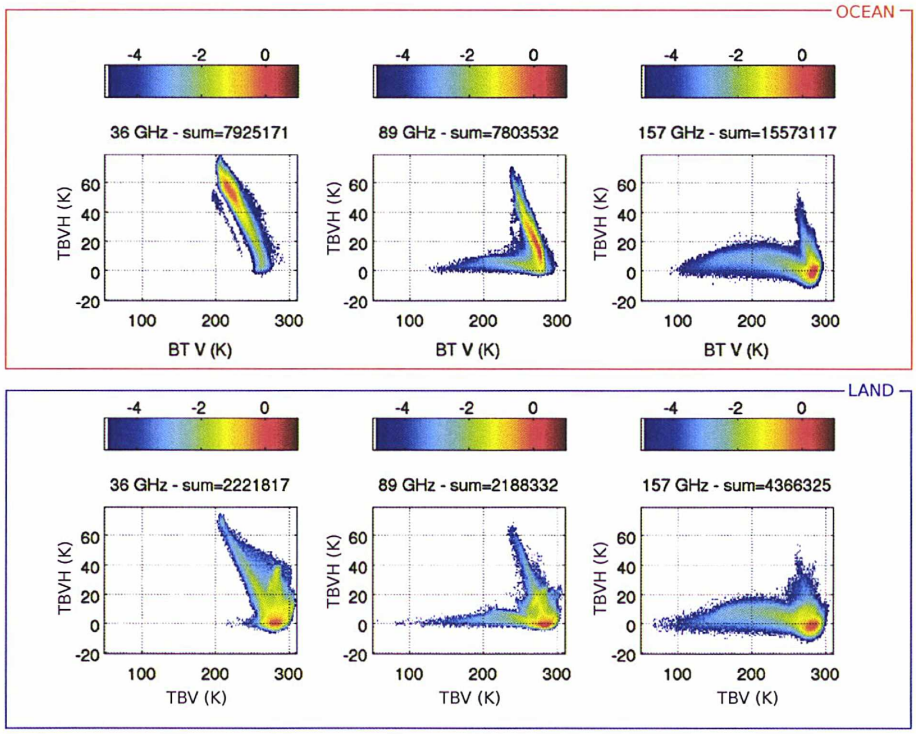

Figure 5.17: Scatter plots of polarization difference TBVH versus the vertical brightness temperature TBV, for ocean (top) and land (bottom), at 36, 89, and 157 GHz from left to right. For each 1 K × 1 K box, the color indicates the relative number of pixels, with respect to the total number of pixels indicated at the top of each panel (logarithmic scale).

89 GHz, Figure 5.18 presents a comparison of TBV-TBVH scatter plots for MADRAS and TMI for the almost time-coincident observations shown in Figure 5.15 and Figure 5.16. Note that the 157 GHz channel in MADRAS is shown for comparison. Figure 5.18 shows that while the TBV-TBVH maps from MADRAS and TMI observations at 37 GHz are rather similar, spanning over the same domain, some differences are observed at 85 GHz: TMI observes null to negative polarization differences while MADRAS observations of TBVH are rarely below 0^oK. Lower values of TBVH are also observed by MADRAS around 270 K TBV. In order to analyze the differences seen, Figure 5.19 presents the histograms and the cumulative distributions of the two orthogonal brightness temperatures, TBV and TBH, and the polarization differences, TBVH, over land and ocean together, for the radiometric bands in common between TMI and MADRAS. These histograms were derived from Figure 5.18. At 37 GHz, both radiometers provide rather similar histograms at both sides of the distributions, i.e. in clear sky over sea and in likely clear sky conditions over land. A difference exists in the mid brightness temperature range, i.e. mainly for beams located over water. At 85 GHz, at both polarizations, differences exist at cold brightness temperatures, i.e. for convective clouds. The discrepancies observed in Figure 5.18 and Figure 5.19 can be explained by the different spatial resolutions between the two radiometers, the viewing geometry of the convective clouds depending on the orientation of the TMI/MADRAS beams relative to the cloud structure, and the natural evolution of the

sampled clouds between the two 6-min delayed overpasses. Also by the noisier measurements of TMI in this temperature range, as discussed in the Annex of Paper B (Appendix B).

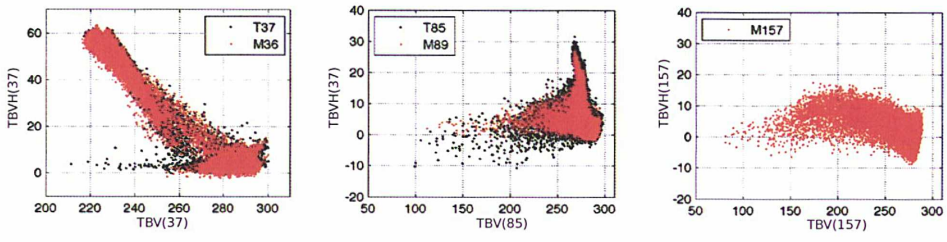

Figure 5.18: Scatter plots of TBV and TBVH at 37, 85, and 157 GHz for TMI (T) and MADRAS (M) from observations shown in Figure 5.15 and Figure 5.16. Only pixels located within the common area defined by the intersections of the overpasses of the two swaths were used to produce the plot.

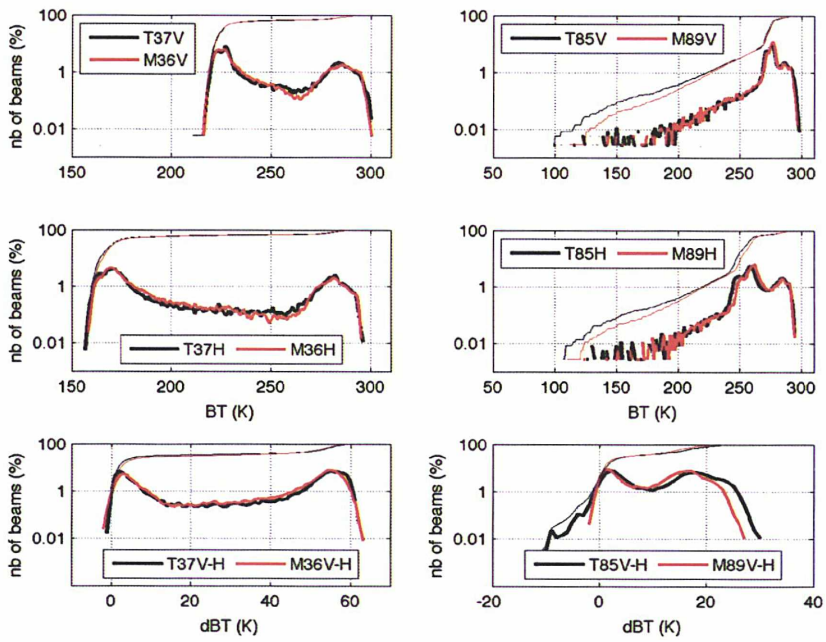

Figure 5.19: Histograms (in solid lines) and cumulative distributions (in thin lines) of the brightness temperatures mapped in Figure 5.18. Note that the horizontal brightness temperature, TBH, is also shown. Only pixels located within the common area defined by the intersections of the overpasses of the two swaths were used to produce the plot.

5.5.3 Assessment of the Role of Frozen Hydrometeors in the Observed Polarized Scattering Signals using Realistic Radiative Transfer Simulations

The sensitivity of the polarized brightness temperatures to particle characteristics such as size, phase, shapes, and orientation have been explored throughout this chapter using mainly a simplified approach where mono-disperse hydrometeor size distributions as used. This is important to analyze the influence of microphysical assumptions without the effect of the particle size distribution itself. In this section, however, polarized radiative transfer simulations are performed with realistic hydrometeor profiles. For a transect on the scene presented in Figure 5.15, the profiles of water and ice contents retrieved from TMI (the 2A12 TMI product) are adopted along with coincident ECMWF re-analysis products, for more realistic simulations of the polarized signals observed by MADRAS. The focus is still on exploring the impact of variations in the microphysical parameters of the cloud frozen phase on the microwave signal. This is relevant in confirming the role of frozen hydrometeors in the cloud polarized scattering signatures observed, as discussed throughout this chapter and more specifically as observed by MADRAS.

RT Simulation Setup

With the motivation of performing simulations of more realistic characteristics and performing simulations/observations direct comparisons, the TMI/MADRAS observed scene presented in Figure 5.15 and Figure 5.16 is exploited. Specifically, we focus on the stratiform system off the coast of Madagascar by using a transect corresponding to the PR nadir footprint as depicted in Figure 5.20. The TBV and TBVH maps are reproduced in Figure 5.21 with a zoom on the region of interest. The PR 2A23 and the TMI 2A12 products were used to perform more realistic simulations.

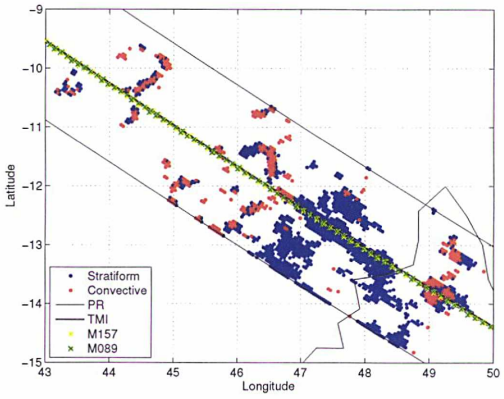

Figure 5.20: Transect corresponding to the PR nadir footprint.

The PR 2A23 algorithm, already presented and used in Section 5.4.2, provides information on the presence and location of the BB, on the rain type (i.e. stratiform, convective, or other), on the freezing height and on the cloud top height, as measured by the PR. The TMI 2A12 algorithm generates surface rainfall and vertical hydrometeor profiles of 5 species (snow cloud water, cloud liquid water, ice, graupel and rain) from the TMI brightness temperatures. It is derived from a Bayesian retrieval and it gives the most probable structure of the hydrometeor profiles, given the TMI observations.

Figure 5.22 shows the cloud liquid water content (CLWC), the rain water content (RWC), the cloud ice water content (CIWC), the snow water content (SWC), the graupel water content (GWC), and their integrated contents, as retrieved from the TMI 2A12 product for the transect of interest. The PR bright band height (black circles) and the cloud top height as measured by the PR (solid red curve) are overlaid. The PR cloud top product fails to detect the frozen phase as expected. Note that the region around 45^o in longitude has no retrieved values and

that the species are populating the atmosphere, most generally, above the freezing level height. The key step in these RT simulations is defining the microphysical assumptions to describe this TMI 2A12 hydrometeor profiles.

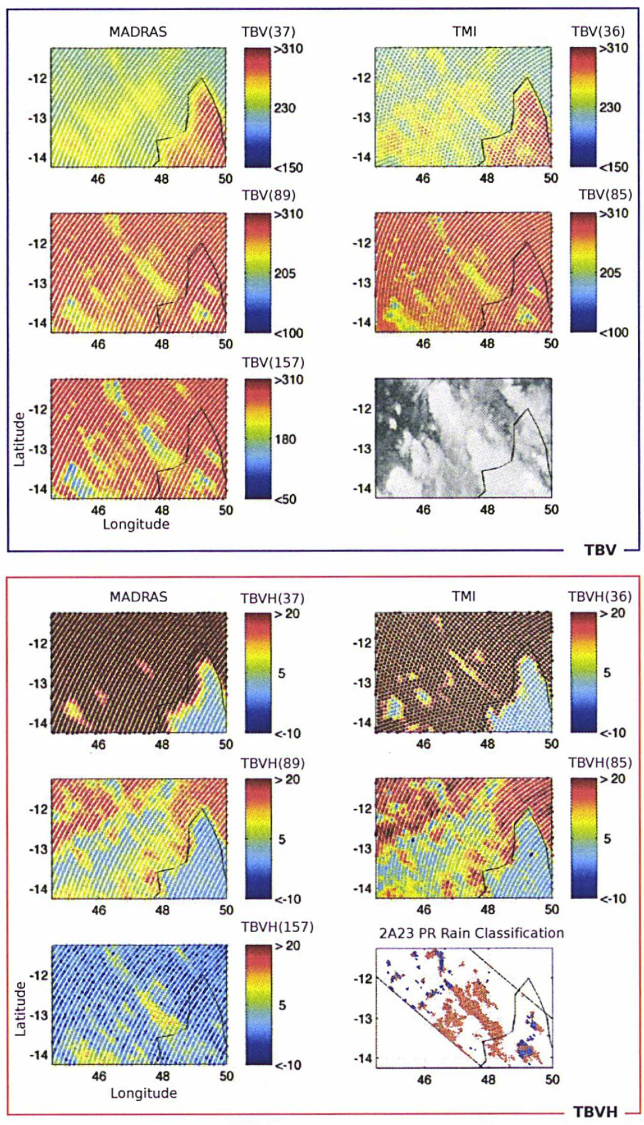

Figure 5.21: Same as Figure 5.16 but zoomed on a specific region. Note the 2A23 PR rain classification (red = Stratiform; blue = Convective) within the PR swath.

Figure 5.23 shows schematically the simulations, with the TMI 2A12 products used together with ECMWF re-analsysis products (atmospheric and surface variables) in order to simulate the MADRAS observational records of interest with ARTS. Since the TMI 2A12 algorithm only retrieves hydrometeor profiles over ocean, the RT simulations were conducted with FASTEM

ocean emissivities as calculated using information on surface wind and surface skin temperature (Tskn) as provided by ECMWF re-analysis.

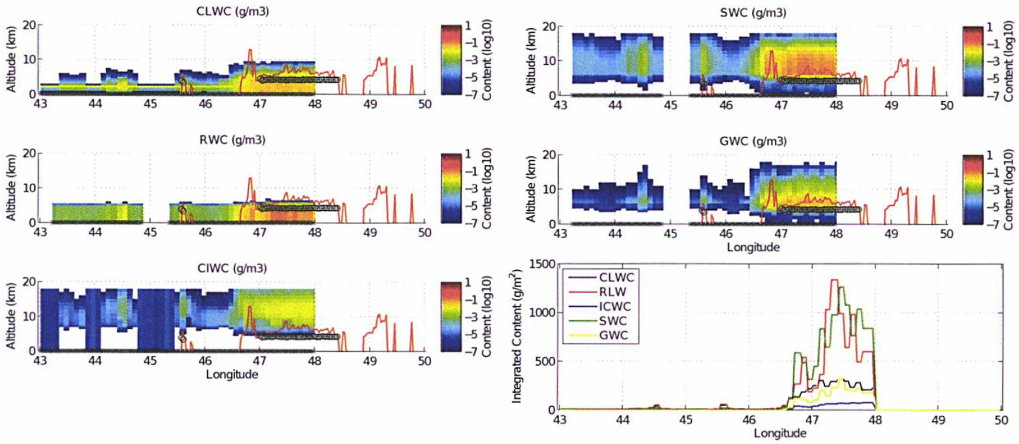

Figure 5.22: The retrieved TMI 2A12 hydrometeor profiles in the transect of interest; (a) the cloud liquid water content (CLWC), (b) the rain water content (RWC), (c) the cloud ice water content (CIWC), (d) the snow water content (SWC), (e) the graupel water content (GWC), and (f) their integrated contents. Note that the PR bright band height (black circles) and the PR cloud top height (solid red curve) are overlaid. Note that East of 48° W, TMI is no longer over ocean and the TMI 2A12 algorithm cannot retrieve hydrometeor profiles over land.

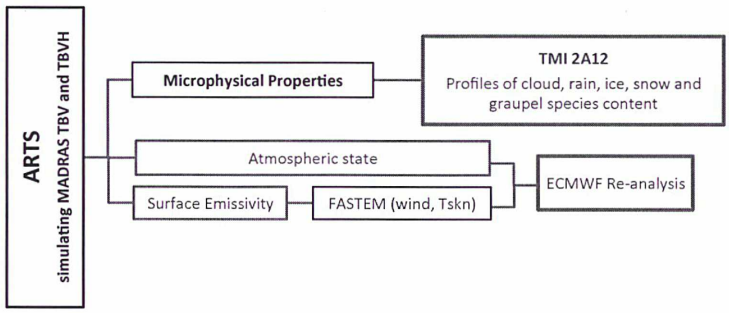

Figure 5.23: Schematic diagram summarizing the inputs used to conduct realistic simulations of the transect of interest.

In the RT simulations, the retrieved profiles of cloud water species are considered to be single sized spherical particles of 20 μm radius and the retrieved profiles of rain water species are considered with a Marshall-Palmer drop size distribution. The relevant parameters describing the microphysical properties of the frozen phase (the retrieved profiles of ice, graupel and snow) are mainly the dielectric properties (as a function of density essentially) and the particle size distribution. Pure ice species in this specific transect have a negligible impact on the simulations

due to their low IWP, but they are included for compeleteness. Thus, we concentrate on the microphysical properties of graupel and snow.

Sensitivity of the Polarized Simulations to the hydrometeor characteristics

Figure 5.24 shows the observations from MADRAS (left) and the corresponding simulations (right) for the transect of interest for TBV and TBVH at 85 and 157 GHz. Note that the observations from MADRAS correspond to coincident pixels with the nadir-PR footprint. Through the 37 GHz channel simulations, the surface emissivities used and the general set-up of the atmospheric state was shown in reasonable consistency with observations. The first simulation (solid blue curve) corresponds to the initially selected parameter for snow and graupel species where the particle size distribution and the intrinsic mass of the particles are defined as specified by the cloud mesoscale model Meso-NH. For each layer of the atmosphere and each hydrometeor type, i.e., cloud water, rain water, pure ice, snow and graupel, Meso-NH provides the mass content (kg/m^3) and the size distribution of the maximum dimension of the particle (Section 4.1). The mass of each hydrometer category is specified by the microphysical scheme implemented in Meso-NH ($m = aD^b$). Since the shape of the species and their density are not explicitly provided by the microphysical scheme of the mesoscale model, they are open parameters. However, they are crucial parameters for the single scattering properties. In terms of shape, graupel and small pure ice crystals are not strictly perfect spheres, but are approximated to spheres in this analysis to simplify the problem and to avoid using more complicated shapes with no real justification. For example, graupel species are rimmed particles for which it is reasonable to assume a spherical shape. Snow species, however, are not spherical (e.g. Meso-NH parameterizes $m \propto D^{1.9}$). In this analysis two shape approximations are used: perfect spheres and oblate spheroids. The justification for favoring such shapes has been discussed throughout this chapter. Oblate spheroids are favored from aircraft observations (Heymsfield personal communication). The dielectric properties of the snow and graupel species retrieved from TMI are calculated using the Maxwell Garnett mixing formula for dry snow with an ice volume fraction, $f = \rho_s/\rho_{ice}$, where ρ_s is the density of snow and graupel as deduced from the Meso-NH parameterization on the mass of these species. These initial conditions (solid blue curve) with perfect snow spheres, result in limited scattering and no polarization. In fact TBV(clear)−TBV(snow) is of the order of 80 (50) K for 157 (89) GHz, which does not compare with the observed brightness temperature depressions by MADRAS of the order of 120(70) K at 157 (89) GHz. Note that a simulation where only the liquid phase is taken into account is also shown to emphasize the importance of the higher frequency 157 GHz channel to the sensitivity of the ice phase when compared to the 89 GHz channel (dashed blue curve).

West of 47^{o}W, TBVH simulations are observed to peak at 85 GHz to values of 13 K, in disagreement with MADRAS observations. In fact, the simulated TBVHs and TBVs are similar to MADRAS observations at clear sky conditions (west of 46.5^{o}W). These RT simulations are clear evidence that the retrieved species content are underestimated in this region. Otherwise, the atmosphere would be opaque enough to mask the surface emissivity polarization that is simulated at 85 GHz for TBVH for example.

Note that the dielectric properties are calculated for dry snow, and not for wet snow, as it is considered that the temperatures of the snow profiles are too low to consider a wetness degree [W(%) = 0 for T < 258.15 K; W(%) = T - 258.15 for T < 258.15K; W(%) = 15 for T > 273.15 K from Skofronick-Jackson et al. (2002). The melting layer region spans approximately

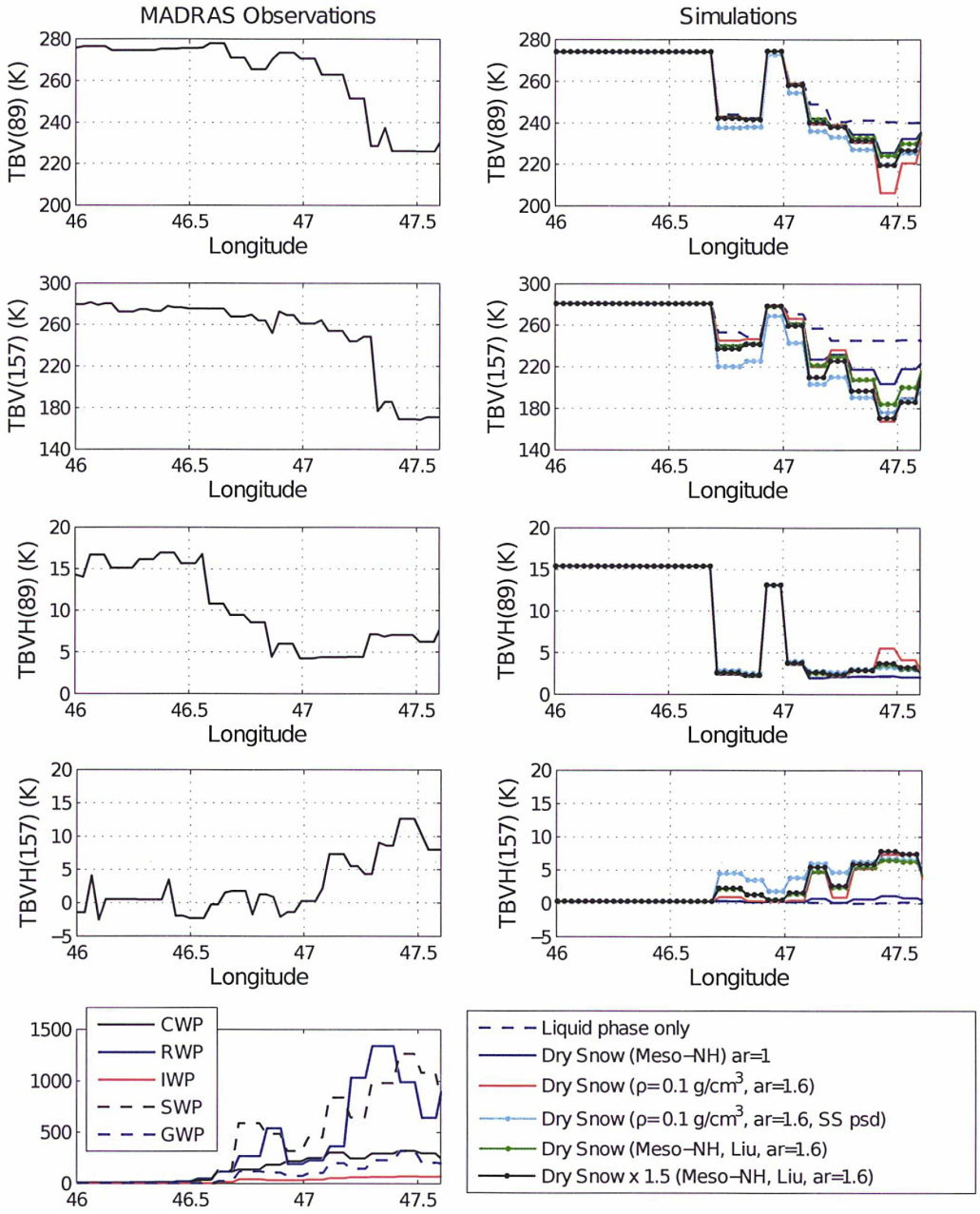

Figure 5.24: The TBV and TBVH signals at 89 and 157 GHz observed by MADRAS (left) and simulated with ARTS (right) under different microphysical properties of snow and graupel species, for the transect of interest. See the text for more detail.

500 m around the freezing level height, and as shown in Galligani et al. (2013), the passive polarization signal appears to originate from the dry snow layer above the melting layer.

Changing the aspect ratio, the orientation or the PSD (to that of the Meso-NH PSD param-

eterization for graupel) of the dry snow particles, but using the same density parameterization has a limited effect on TBV (and TBVH) (not shown). Multiplying the snow content by 1.5 in each layer changes the result by less than 5 K at 157 GHz, far from the observed TBV. Snow particle sizes that are likely to scatter and polarize radiation at 89 and 157 GHz have very low density under this parameterization, affecting the dielectric properties via the ice volume fraction, and are transparent to the microwaves (already seen in e.g Meirold-Mautner et al. (2007)). In fact, the following assumptions show that the too-low density of the largest flakes in the $m(D)$ parameterization is responsible for the underestimation of the scattering.

Assuming the Meso-NH particle size distribution for snow species but calculating the dielectric properties for dry snow particles with a fixed density of 0.1 g/cm^3 (a value that is often selected for snow) has an important impact on the single scattering properties via the ice volume fraction, $f = \rho_s/\rho_{ice}$, and thus on the TBVs. Randomly oriented spheres show similar TBVs to those observed (not shown) but do not polarize the scattering signal. Oblate horizontally oriented snow particles with aspect ratios 1.6 (solid red curve) and 2 (not shown) lead to observed TBVs and polarization signals of the order of those observed by MADRAS at both 157 and 89 GHz. Furthermore, the polarized scattering signals simulated for 157 GHz (9-12 K) are approximately twice those at 89 GHz (4-6 K) as expected and observed in Figure 5.17. Note also that oriented particles of aspect ratio 2 polarize radiation significantly more than particles of aspect ratio 1.6.

The following sensitivity tests were run for the configuration that shows good consistency with the simulations and reasonable physical assumptions (snow horizontally aligned spheroids with a fixed density of 0.1 g/cm^3 and graupel species as parameterized with Meso-NH). The sensitivity to the snow content is analyzed by running additional simulations and multiplying the snow content by 1.5 in each atmospheric layer. Under these simulations, TBV is significantly depressed for both frequencies and TBVH increased by approximately 3 K (not shown), evidencing the efficiency of the parameterized microphysical properties in producing a polarized scattering signal. Changing the properties of graupel such that the particles are spheres with a fixed density of 0.4 g/cm^3 (not shown) yields lower TBVs and lower polarization differences with respect to those observed by MADRAS.

To assess the impact of the PSD on the radiometric signals, the Meso-NH snow PSD was replaced by the Sekhon and Srivastava (1970) (SS) PSD (cyan circled curve). The SS distribution leads to smaller size particles and consequently, the TBV are increased by approximately 10 K and the TBVH are limited at 89 GHz. At 157 GHz, however, this is not the case, further evidencing the importances of higher microwave frequency window channels for the detection and characterization of the frozen phase.

Finally, the approach suggested by Liu (2004) to approximate the single scattering properties of snow species, introduced in Section 4.3, is analyzed. For 85 and 157 GHz, a softness parameter $SP = (D - D_0)/(D_{max} - D_0)$, is derived for different particle shapes. The frequency dependent softness parameter SP gives the diameter of the best-fit equal-mass sphere, i.e., a frequency dependent effective density and a modified diameter is used to calculate the single scattering properties with the T-matrix. As shown in Figure 5.24 (dotted green line), the results are very encouraging in accordance with the observed TBV and TBVH. Analyzing the sensitivity of these assumptions to the snow content by multiplying by 1.5 in each atmospheric layer shows that the scattering effect is significant. Especially in terms of TB depression and polarization difference at 157 GHz. The snow quantities provided by the TMI inversion are realistic, and adding more snow does not improve the agreement between simulations and observations. The

proportional increase in polarization difference observed in MADRAS observations between 89 and 157 GHz, is reproduced in the simulations. With realistic atmospheric profiles, it is thus possible to reproduce consistently the polarized scattering signals observed at 89 and 157 GHz. This confirms the validity of our previous interpretation of the signals up to 90 GHz, with additional stringent constraints imposed by the higher frequency.

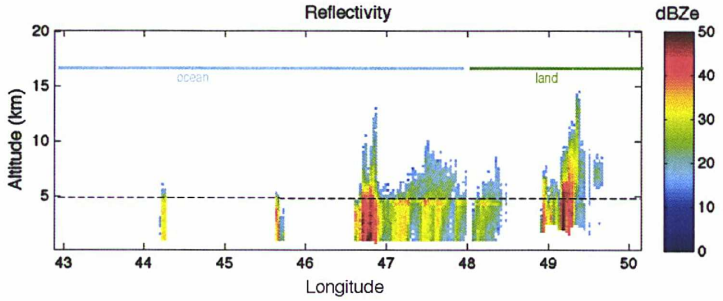

Figure 5.25: The observed radar reflectivity (in dBZ) at nadir by the PR (13.8 GHz). Note the indicated freezing level height.

The fairly poor performance of the TMI 2A12 hydrometeor retrievals west of 47°W has already been mentioned. It is important to emphasize that this region is characterized by a higher cloud top than the rest of the transect (see Figure 5.22) and convective rain classification (see Figure 5.20). The cloud top is derived from the radar reflectivies, shown in Figure 5.25. We concentrate on the PR reflectivities west of 49°W which correspond to the TMI 2A12 retrievals. The system observed from 49°W is over land and as already mentioned, the TMI 2A12 only works over ocean. In the region over the ocean, the convective cells are easily distinguished from the PR vertical profiles. The convective cells, however, do not show any distinctive signatures in the MADRAS TBV observations of Figure 5.24. This is because MADRAS has a much larger footprint than the PR and its radiometric signal covers many PR pixels. The number of convective pixels here are not enough to have an impact on the radiometric TBV signal (deduced from Figure 5.20). MADRAS TBVH observations, however, do show a distinct polarization signature at 157 GHz with large polarization differences associated with the PR stratiform pixels in the presence of a bright band as shown statistically for TMI channels in Galligani et al. (2013). The TBVH signatures could be used by retrievals such as the TMI 2A12 to re-direct the retrieval scheme towards a more realistic precipitation scheme.

5.5.4 Conclusion

Cloud scattering signals had been observed to be associated with significant polarization differences with conical scanners such as TMI up to 90 GHz. The recently available high microwave polarized channels onboard MADRAS confirm the occurrence of cloud polarized signatures. MADRAS provides the first satellite based close-to-millimeter polarized measurements. The polarized scattering signal at 157 GHz, shown to be more sensitive to scattering from the frozen phase, provides a unique opportunity to study further the microphysics of mixed phase hydrometeors. Simulations confirm that this is due to horizontally oriented oblate particles in the cloud

frozen phase. This polarized scattering signal at 157 GHz is consistent with the polarized signatures previously observed around 85 GHz, and as expected it is more common and stronger at higher frequencies. The large occurrence of the polarized scattering in the observations as well as the magnitude of the polarization tends to show that horizontally oriented oblate particles are very frequent in the cloud frozen phase.

Understanding the microphysical properties of the frozen phase and their scattering effects is crucial in estimating parameters of the precipitation from space-borne radar and microwave radiometers. In fact, the sensitivity of passive microwave polarized scattering to the shape and orientation of hydrometeors is unique among the current observations: it is an unexpected tool to gain understanding in complex microphysical processes in clouds. The polarized scattering signatures could be used to re-direct retrieval schemes towards more realistic precipitation schemes over land and ocean.

The analysis of MADRAS measurements contributes to the preparation for the next generation of millimeter and sub-millimeter radiometers. Understanding the microphysical properties of the frozen is also crucial for the development of precipitation and cloud property retrievals from the upcoming missions with higher microwave frequencies, such as the GPM algorithms that are presently under development, or the Ice Cloud Imager (ICE) with frequencies between 170 and 675 GHz on board the next generation of the European meteorological satellites (MetOp-SG) where quantifying the ice scattering is a key issue.

Chapter 6

Passive and Active Radiative Transfer Simulations for two Real Snow Scenes and their Evaluation with Satellite Observations

6.1 Introduction

Most retrieval algorithms for atmospheric parameters are based on radiative transfer simulations, with the accuracy of the retrieval largely related to the ability of the simulations to reproduce observations. For instance, statistically-based algorithms are constructed from large datasets of simulated observations, and the algorithms (i.e., multi-linear regression, neural network) are trained over these databases to reproduce the relationships between the simulations and the geophysical parameters. In variational assimilations as well, the radiative transfer is used iteratively to fit the measured observations, and the accuracy of the retrieval is linked to the quality of the radiative transfer scheme.

Coupling Meso-NH with ARTS will make it possible to simulate the reponses of microwave instruments for real scenes, in the passive but also in the active mode. In this chapter, Meso-NH simulations are selected for real situations, in coincidence with microwave satellite observations. The radiative transfer calculations are performed with ARTS using the Meso-NH outputs and the results are compared with the satellite measurements. This will allow a fine tuning of the radiative transfer parameters, and an evaluation of the accuracy of the radiative transfer simulations. In addition, these types of comparisons, also called model-to-satellite approach, are an efficient method to evaluate meso-scale cloud models. Different studies have already been carried out to evaluate the Meso-NH cloud model scheme, such as comparisons with observations from METEOSAT (Chaboureau et al., 2002), TRMM (Wiedner et al., 2004), SSMI and AMSU (Meirold-Mautner et al., 2007). They concluded that neither strong nor systematic deficiencies in the microphysical scheme are present in the prediction of the hydrometeor contents with Meso-NH. Our study emphasises on the simulations of the snow, both in the cloud and as precipitation, and for the selected cases, significant snow quantities are present (in the cloud for the first case and as falling snow for the second case).

In the context of this thesis, a collection of matlab functions were developed together with Patrick Eriksson (Chalmers University of Technology) in order to: (1) grid the Meso-NH outputs for ARTS 3D simulations, (2) incorporate realistic surface emissivities for ocean (using FASTEM) and land (using TELSEM), (3) configure the geometry of the simulation to replicate real passive observations and radar measurements, (4) prepare the necessary fields for users to describe the particle size distribution and the corresponding single scattering properties for the 5 hydrometeor species in the Meso-NH scheme, and finally (5) run 3D ARTS simulations with the ARTS-MC method for passive microwave simulations and the newly developed active microwave simulations. The ARTS-MC method, in comparison with the previously used method DOIT, treats 3D atmospheres accurately. This package, named ArtsMesoNH can be made available upon request.

In this Chapter, the sensitivity of radiative transfer calculations to the assumed microphysical properties is assessed. This task is undertaken for two different real case scenarios. Section 6.2 analyses the simulated brightness temperatures from a light precipitation case over the Rhine region as modelled by Meso-NH, and observed with AMSU-B and SSM/I. Similarly, Section 6.3 discusses a heavy snowfall scene over France, with an evaluation of both active and passive radiative transfer simulations, thanks to comparisons to coincident passive (MHS) and active (CloudSat) observations. Section 6.4 draws conclusions.

6.2 Microwave Passive Simulations: Rhine Case Study

6.2.1 Presentation of the Situation

The Rhine case corresponds to a precipitation event, 10 February 2000, related to a cold front passing over the Rhine region. For this scene, two Meso-NH model outputs are available in coincidence with SSM/I (at ~09:00UTC) and AMSU-B (at ~18:00UTC) observations respectively. Figure 6.1 presents the Meso-NH model outputs coincident with AMSU-B (the Meso-NH model outputs coincident with SSM/I can be found in Figure 7.2 of Appendix A). It can be seen that rather large quantities of snow are present in the clouds during this event.

Figure 6.2 (left) shows the corresponding AMSU-B observations. Note that for these observations in coincidence with Meso-NH simulations, AMSU-B viewing zenith angles vary between 0^o (on the east) and $\sim 58^o$ (on the west) (see Section 2.1.2 for more detail about the AMSU-B observations). In the window channels, the observations over the ocean present rather low brightness temperatures, due to the low ocean emissivity as compared to land. Low brightness temperatures are also observed over the Alps: the Alps are snow covered at this time of the year and snow has a very low emissivity in the microwave. With increasing atmospheric opacity in the H_2O water vapor line, the contrast between land and ocean disappears: the closer the channel is to the absorption line center, the more opaque the atmosphere and consequently, the lower the contribution from the surface. At 183.31 ± 1 and 183.31 ± 3 GHz, the sharp transition between the two distinct air masses is obvious. In the window channels at high frequencies, the scattering effect by the cloud frozen phase can be observed, especially at 150 GHz, with the brightness temperatures depressions. These brightness temperature depressions correspond well to the cloud structure simulated by Meso-NH and it is reasonable to say that they are essentially due to the scattering effect by the snow presence in the cloud.

In a first step, radiative transfer simulations are performed without taking into account the hydrometers (i.e., 'clear sky' simulations), with the objective of evaluating the cloud contribution to the observations (Figure 6.2 right). The simulations do take into account the scanning angles and the polarization mixture of AMSU-B observations. As expected, the largest differences correspond to the cloud structure over the Rhine region. The window channels at high frequencies are the most sensitive, in agreement with the expected higher scattering contribution from the frozen phase at these frequencies. In fact, a large amount of snow is modeled by the Meso-NH scheme as observed in Figure 6.1. The presence of snow is associated with brightness temperature depressions of up to 40 K at 150 GHz when the most intense scattering signal is observed. In the very opaque channels in the H_2O line, the water vapor absorption masks the cloud contribution.

Further comparisons between AMSU-B observations and Meso-NH model outputs show that a cloud system on the North Sea is observed by AMSU-B but not modeled by Meso-NH. In addition, the observed front is shifted by approximately 2^o to the west with respect to the Meso-NH outputs. This is most easily seen at 183 ± 1 GHz close to the coast of France.

Similar figures for clear sky radiative transfer simulations of the Meso-NH outputs coincident with SSM/I observations are presented in Appendix A. The SSM/I channel frequencies are lower and the observations are more sensitive to the surface emissivities, especially under clear sky conditions. A more quantitive comparison of the simulated and observed brightness temperatures follows by computing their statistical distribution. Analysis of the highly surface sensitive SSM/I channels allows an evaluation of the surface emissivity estimates used in the

simulations by incorporating TELSEM and FASTEM.

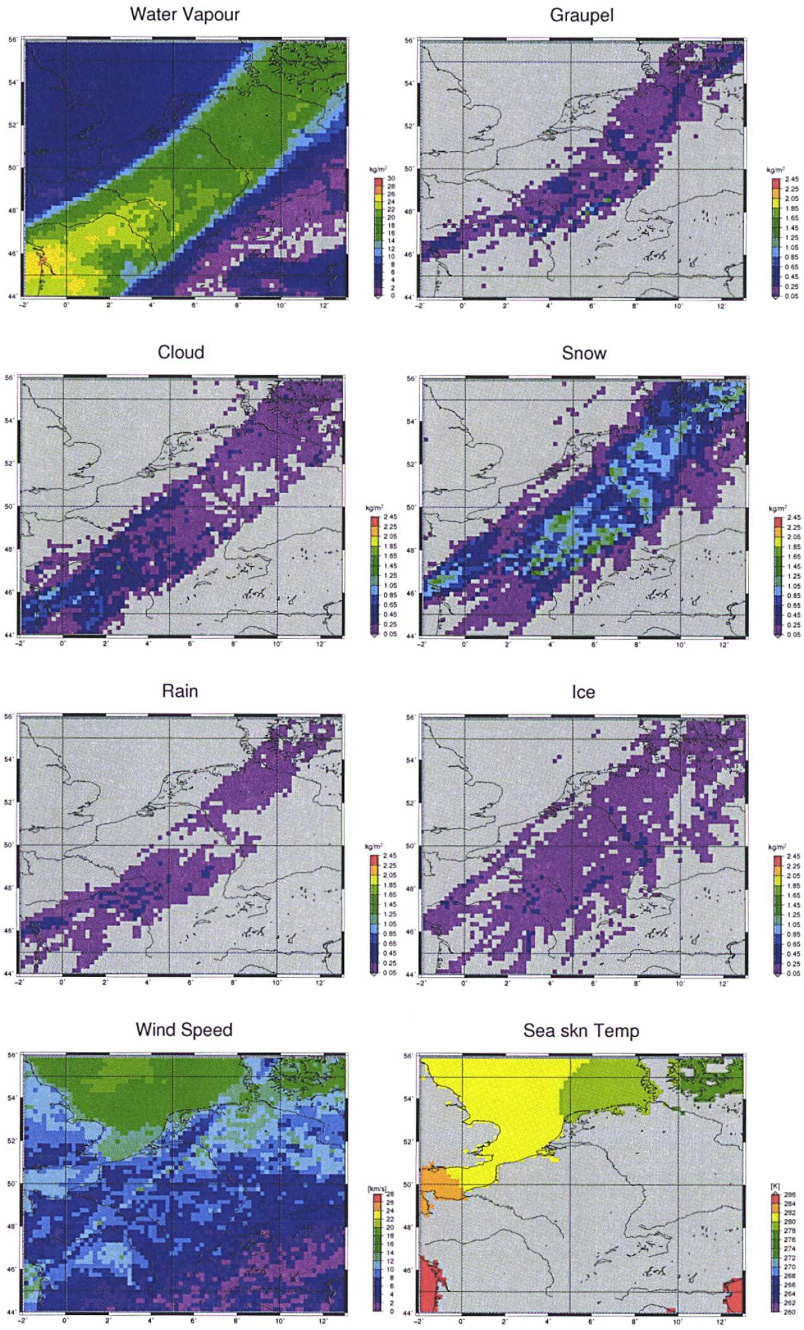

Figure 6.1: The Meso-NH fields of the RHINE scene on 10 February 2000 at AMSU-B over-pass time (18:00UTC).

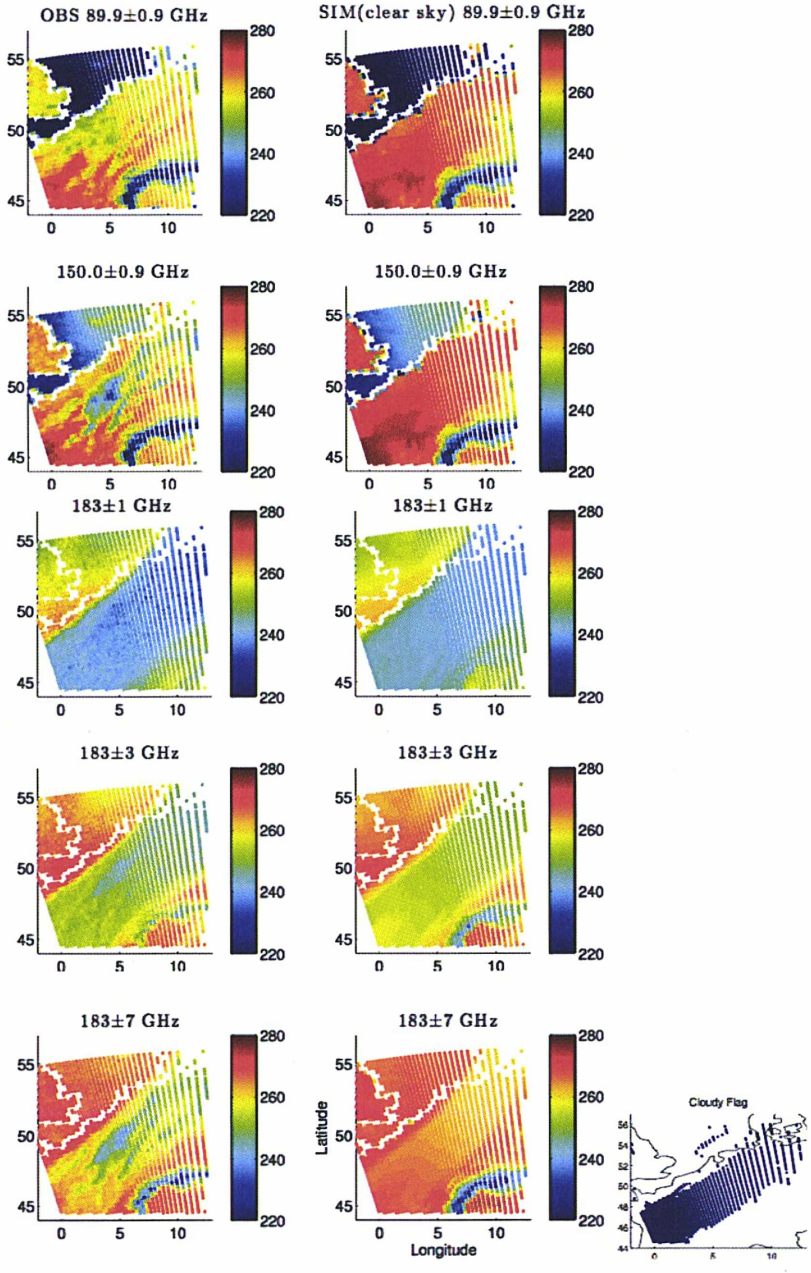

Figure 6.2: AMSU-B observations (left) for the Rhine case on the 10 February 2000, along with ARTS radiative transfer simulations with Meso-NH inputs, ignoring the cloud and rain components (right).

To calculate the statistical distribution of clear sky simulations, clear sky pixels are identified according to a cutoff ($< 0.05 \mathrm{kg/m^2}$) on the amount of the total hydrometeor column mass as specified by Meso-NH outputs (see Figure 6.2 bottom left). To assess the sensitivity of the simulations to the surface emissivities, simulations were conducted over land for both TELSEM and a fixed land surface emissivity (0.98 for both orthogonal polarizations), and over ocean for FASTEM and with the Fresnel equations for the ocean (assuming a perfectly flat surface). Figure 6.3 (Figure 6.4) shows the histograms of the differences between the observed and simulated brightness temperatures for AMSU-B (SSM/I) for clear sky pixels only, computed separately for the mentioned ocean and land emissivities (coastal regions are avoided). Note that for SSM/I, histograms are only shown over land as the precipitating front is over the ocean at that time. The histograms illustrate well the importance of using realistic surface emissivities for the window channels. FASTEM provides more realistic simulations of the ocean emissivity, as indicated by the decrease of the RMS at 89 GHz from 18.2 K with the Fresnel model to 10.1 K with FASTEM. This value is still large, but as already discussed, Meso-NH underestimates a cloudy region in the North Sea, and this is expected to translate into mismatches between the observations of this cloudy scene and the simulation of pixels flagged as clear sky by Meso-NH. Similarly, over land, the use of TELSEM improves the simulations compared to using fixed emissivities. With SSM/I observations, TELSEM gives RMS differences below 6.5 K at all frequencies, while with AMSU-B observations, the results are significantly better with TELSEM than with the fixed emissivity but with still rather large discrepancies (RMS of 11.4 and 9.1 at 89 and 150 GHz). This is largely due to the Alps that are snow covered in February. Snow has a very variable emissivity, in space and time, and is particularly difficult to estimate. Nevertheless, using TELSEM improves the overall simulations.

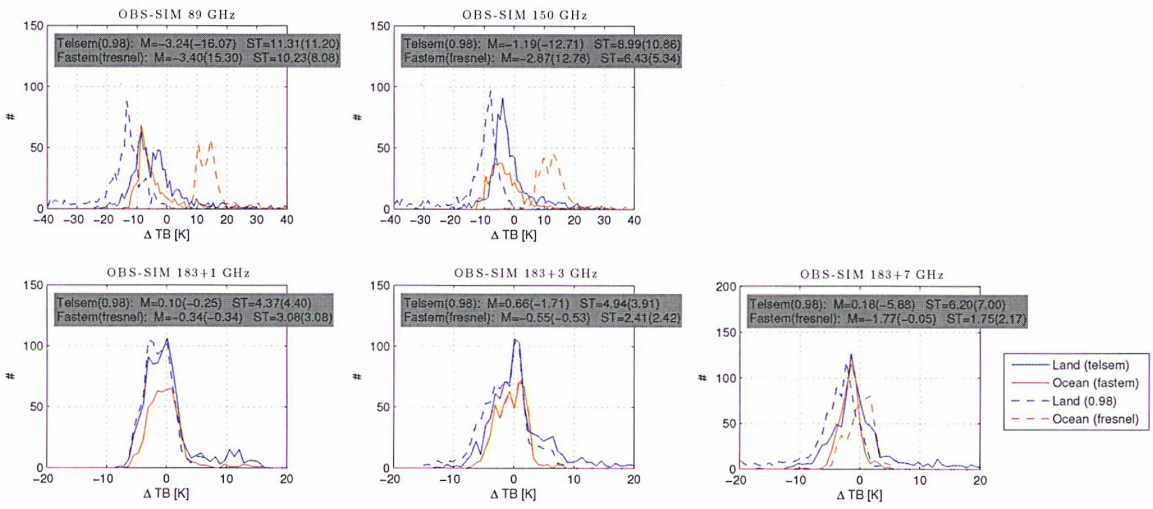

Figure 6.3: Histograms of the difference between the observed and the clear sky simulated brightness temperatures for AMSU-B over land (in blue) and ocean (in red) for a fixed unpolarized surface (dashed lines) and realistic surface emissivities (solid lines).

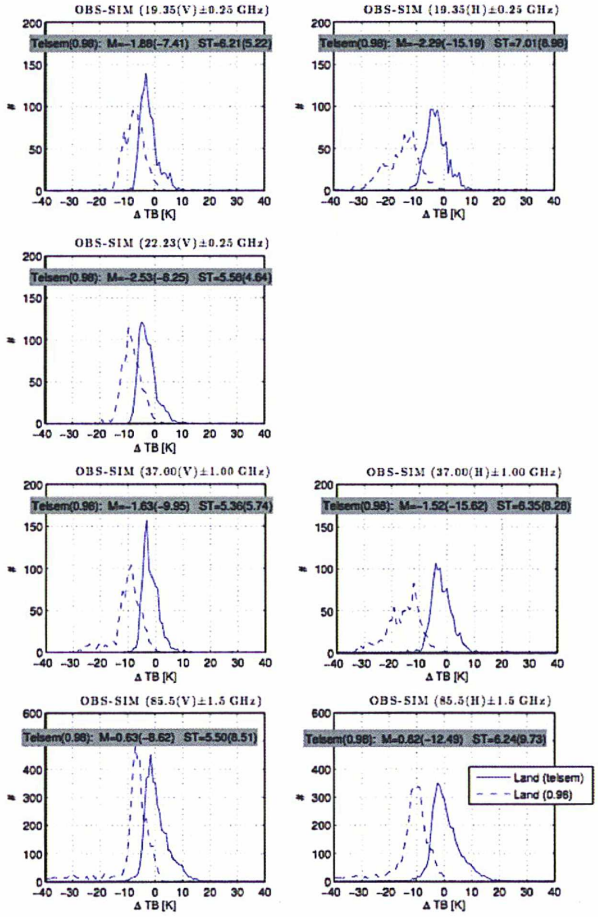

Figure 6.4: Histograms of the difference between the observed and the clear sky simulated brightness temperatures for SSM/I over land for a fixed unpolarized surface (dashed lines) and realistic surface emissivities (solid lines).

6.2.2 Sensitivity of the Microwave Simulations to the Hydrometeor Characteristics

We now concentrate on the simulations of the cloud contribution, and we will focus on the cloud structure over the Rhine area. First, the Meso-NH original microphysical scheme is selected to provide the inputs to ARTS. The mass-size relationships and the particle size distributions described in Section 4.1 are used for the 5 species provided by Meso-NH (rain, cloud, ice, snow, and graupel). All particles are considered to be spherical. The dielectric properties for dry snow and graupel are estimated from the Maxwell-Garnett mixing formula. The single scattering properties are calculated by the T-matrix. The Monte-Carlo version of the ARTS radiative transfer is selected to simulate the microwave responses at the observed frequencies and measurement conditions (incidence angles and polarization). As previously mentioned, the ARTS-MC method can handle 3D calculations accurately while the DOIT method is recom-

mended to be used for 1D atmospheres only. The resultant brightness temperatures from these microphysical assumptions are shown in Figure 6.5 (right) as compared with the corresponding AMSU-B observations (left). With these hypothesis, the global structure of the cloudy scene is fairly well modeled by Meso-NH in agreement with its location in the observations. The scattering signal however, appears less intense in the simulations under these assumptions and fail to reproduce the observed signal.

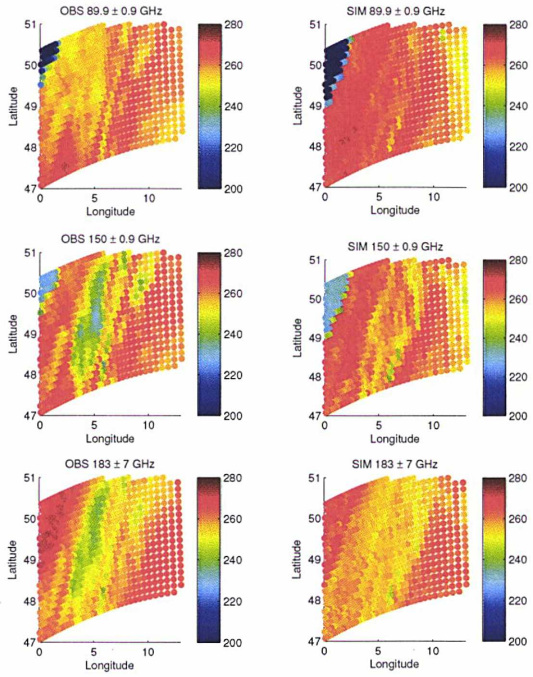

Figure 6.5: AMSU-B observations (left panels) as compared with ARTS-MC simulations (right panels) using the Meso-NH initial microphysical scheme.

A more quantitive approach is taken in Figure 6.6, with histograms of the observed and simulated pixels presented in Figure 6.5 above. The pixels taken into account to calculate the histograms are located over land and are identified as cloudy according to the Meso-NH cut-off flag previously introduced. The statistical distributions essentially show that for window channels, the distribution of simulated brightness temperatures is shifted towards higher brightness temperatures (i.e., failing to reproduce the intense scattering that translates into the observed brightness temperature depressions). Note that there is a non-negligible dispersion of the distributions that is expected due to the impossibly perfect coincidence between the modeled and observed atmospheric structures, and also the varying incidence angle of the AMSU-B observations. To evidence that the largest difference between observed and simulated brightness temperatures in window channels are located in regions where the scattering signatures are mis-calculated, Figure 6.7 shows histograms separating the cloudy pixels according to the amount of snow total column (always considering pixels over land only). Small snow concentrations, considered to be under the cut-off used for the cloudy Meso-NH flag (0.05 kg/m^2) result

in moderate ΔTBs (observed - simulated brightness temperatures) centered close to zero and with a reasonable narrow distribution even at window channels. For larger snow mass columns, the distributions are shifted towards larger negative values, further evidencing the failure of this simulations to reproduce the intense scattering signature. Figures 6.7 also evidences the sensitivity of the 89 and 150 GHz channels to the snow content. For this reason, in the remaining analysis of this scene, the focus is on these two frequency channels.

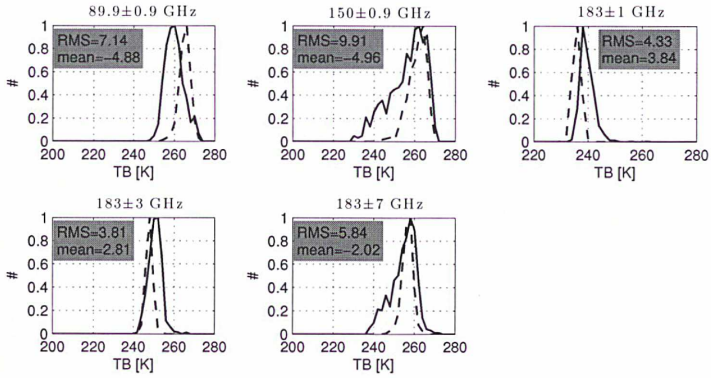

Figure 6.6: Histograms of the observed (solid line) and simulated (dashed line) AMSU-B brightness temperatures with the Meso-NH microphysical scheme. The data used to calculate these distributions corresponds to cloudy pixels (as determined my Meso-NH) over land as presented in Figure 6.6. The RMS and bias of the difference between the two is indicated for each frequency channel.

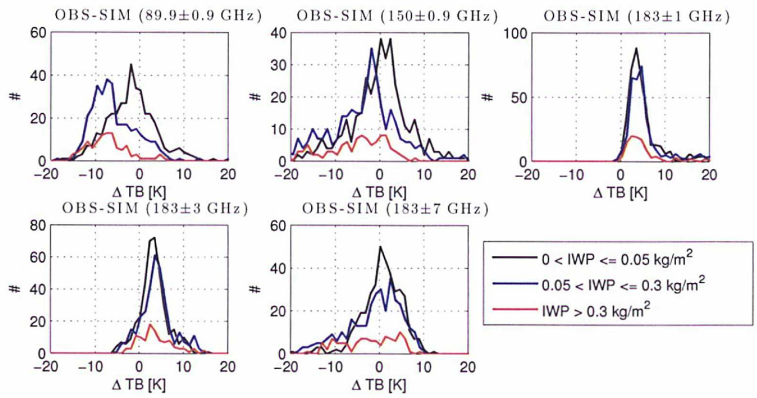

Figure 6.7: Histograms of the difference between the observed and simulated AMSU-B brightness temperatures (ΔTB), taking into account only the cloudy pixels over land presented in Figure 6.6, and for different ranges of snow total column.

The discussed misrepresentation in the scattering signatures leads to the following possible

explanations. There is either (1) a misrepresentation of the scattering properties of the frozen phase, more specifically of snow species, in the RT simulations in terms of dielectric properties, effective size, and shape, or (2) the amount of frozen particles produced by Meso-NH simulations is underestimated. As discussed throughout this thesis, the microphysical parameters describing snow particles are subject to many uncertainties, originating from the microphysical scheme of Meso-NH or on the interpretation of the Meso-NH information in terms of scattering efficiency.

The objective here is to analyze the sensitivity of the radiative transfer simulations to different microphysical assumptions of the frozen phase, focussing on a specific transect of the Rhine case study as described in Figure 6.8. This transect corresponds to a specific scan of AMSU-B from nadir to its outermost angle west and it is characterized by the dominance of snow species in the atmospheric column as modeled by Meso-NH (see middle panel Figure 6.8). Figure 6.9 shows simulations at 89, 150 and 89-150 GHz for this transect under various microphysical assumptions on the frozen phase properties (left), as compared to coincident AMSU-B observations (right). Note that the simulations are performed at different angles as illustrated in Figure 6.8. The idea is to successfully reproduce the brightness temperature depressions related to the frozen phase of the cloud. It is not to simulate the detailed spatial structure of the observations: differencies in time between the simulations and the observations (although small), added to the uncertainties in the detailed spatial structure of the front with Meso-NH would make this task unrealistic.

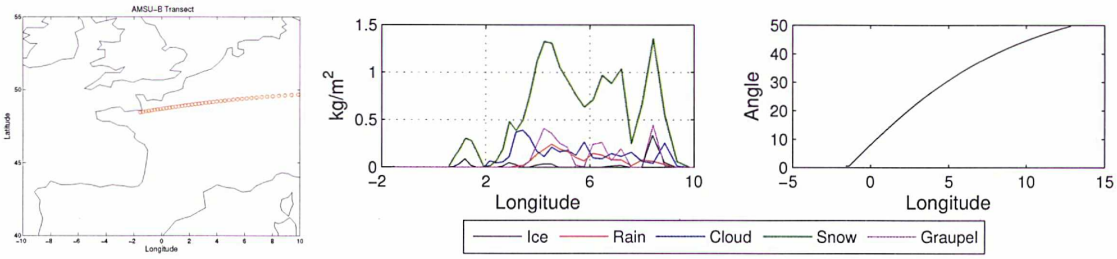

Figure 6.8: Selected transect on the Rhine case, for our sensitivity study. Left: the location of the transect; middle: the integrated content of the different Meso-NH hydrometeors along this transect; right: the incidence angle of the AMSU-B observations along the transect.

The starting point for this analysis is the radiative transfer simulations performed assuming the microphysical properties from the Meso-NH intrinsic microphysical scheme. This was shown to fail reproducing the intensity of the scattering signal observed by AMSU-B in Figure 6.5. Figure 6.9 shows this simulation (blue dashed line) for the specific transect, with its underestimation of the depression related to the clouds, especially at 150 GHz.

In a first attempt to reproduce more scattering, the snow content in Meso-NH has been multiplied by 1.4 in each layer. This does not change the results by more than 1 K along the transect. With these initially selected parameters, different configurations were run with different assumptions (not shown): (a) the snow size distribution was replaced by the particle size distribution of graupel, (b) perfect spheres were replaced by horizontally aligned spheroids of aspect ratio 1.6, (c) the dielectric properties of snow species were calculated with the Maxwell-Garnett mixing formula but with different wetness degrees. All these microphysical assumptions failed to change significantly the simulated brightness temperatures by more than 3 K along

the transect.

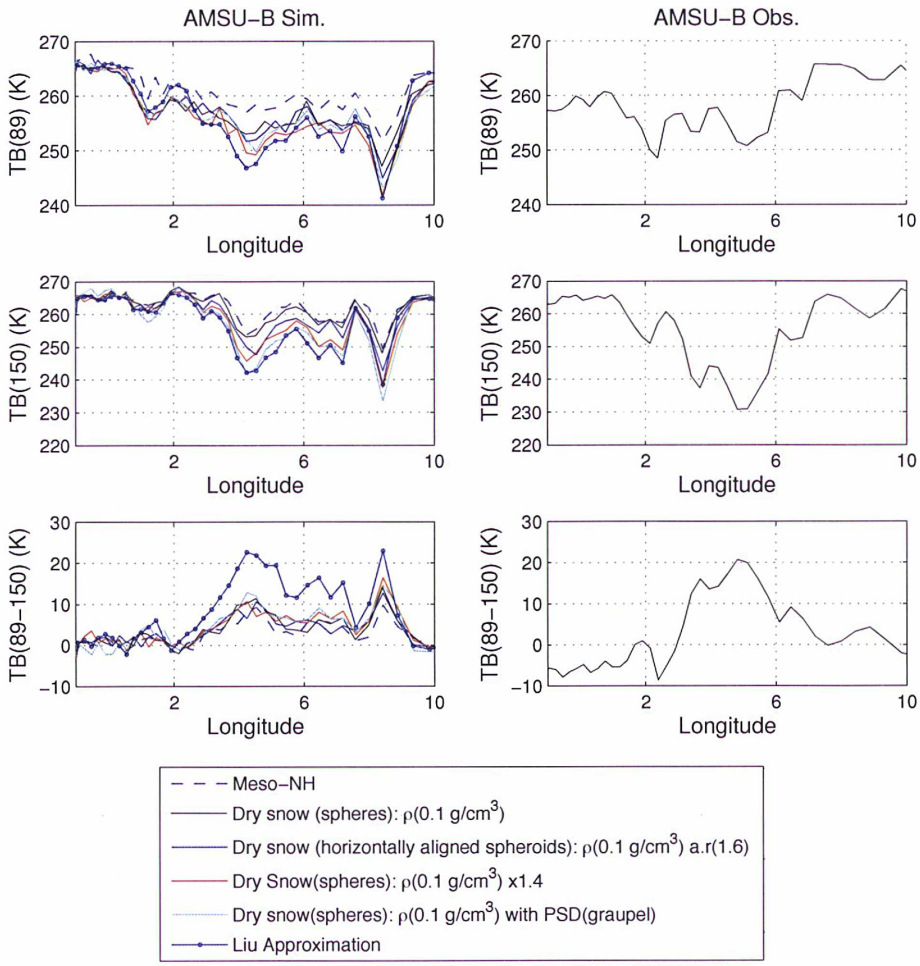

Figure 6.9: The simulated brightness temperatures (right) under different microphysical properties of snow of AMSU-B observations (right) at 89, 150 and 89-150 GHz for the transect of interest.

Similar weak scattering effects were also noted for the MADRAS transect analyzed in Section 5.5.3, with the intrinsic microphysical scheme of Meso-NH. The conclusion was that the large snow particles that are likely to scatter radiation more efficiently at 89 and 157 GHz have a very low density, and as a consequence, have a very limited impact on the signal. Changing the density of snow to a fix value of 0.1 g/cm^3, a value that is often used in the literature for snow, leads to a significant depression of the brightness temperatures (solid black line). Similar results are obtained with horizontally aligned spheroids of aspect ratio 1.6 (solid blue line). So far the density for graupel was parameterized according to Meso-NH (but with a minimum value of 0.1g/cm^3 for the simulations when the density of snow is fixed to 0.1 g/cm^3 in order to maintain a physical consistency). Setting the graupel density to a fixed value of 0.4 g/cm^3,

a value often used as well for graupel, yields brightness temperatures that are much lower than those observed by AMSU-B (not shown).

The sensitivity to the snow content modeled by Meso-NH under these last assumptions (horizontally aligned spheroids of aspect ratio 1.6) is analyzed by multiplying the snow content by 1.4 in each atmospheric layer (solid red line). The impact of the PSD is also assessed by replacing the particle size distribution of snow by that of graupel for spherical particles with fixed density (solid cyan lines). The particle size distribution of graupel assumes fewer larger particles, and more abundant smaller particles. This causes large brightness temperature depressions.

Finally, the Liu (2004) approximation (introduced in Section 5.5.3) is tested using the average parameters of 0.33 for 89 GHz and 0.27 for the higher frequency of AMSU-B. Results are very encouraging as this approximation is able to generate a scattering signal of the same order of magnitude as the observations. It is shown that with the hydrometeor quantities simulated by Meso-NH, it is possible to simulate reasonable scattering in the presence of snow. The microphysical assumptions in Meso-NH are realistic, provided that they are well interpreted for use in the scattering calculation. The Liu approximation is very effective in producing realistic scattering parameters for snow. This approach will be explored further in the next section, for both passive and active modeling.

6.3 Passive and Active Microwave Simulations: A heavy snowfall event over France

6.3.1 Presentation of the Situation

The second case study, presented in Figure 6.10, corresponds to a strong snowfall event over France, 8 December 2010, very early in the cold season. This meteorological event led to large disruptions in the transportation network over a large part of France, especially in the Paris area. Meso-NH model outputs are available every hour for this scene and the outputs corresponding to the over-pass of the A-train mission, with microwave observations from MHS (passive) and CloudSat (active), are selected for this study. CloudSat overflew France at 12:55 and MHS observed the scene approximately 20 minutes later (see Section 2.2.2 for more detail on the CPR instrument). This represents an interesting opportunity to analyze the responses of both active and passive instruments under snowfall conditions, and evaluate the Meso-NH/ARTS coupling under these circumstances.

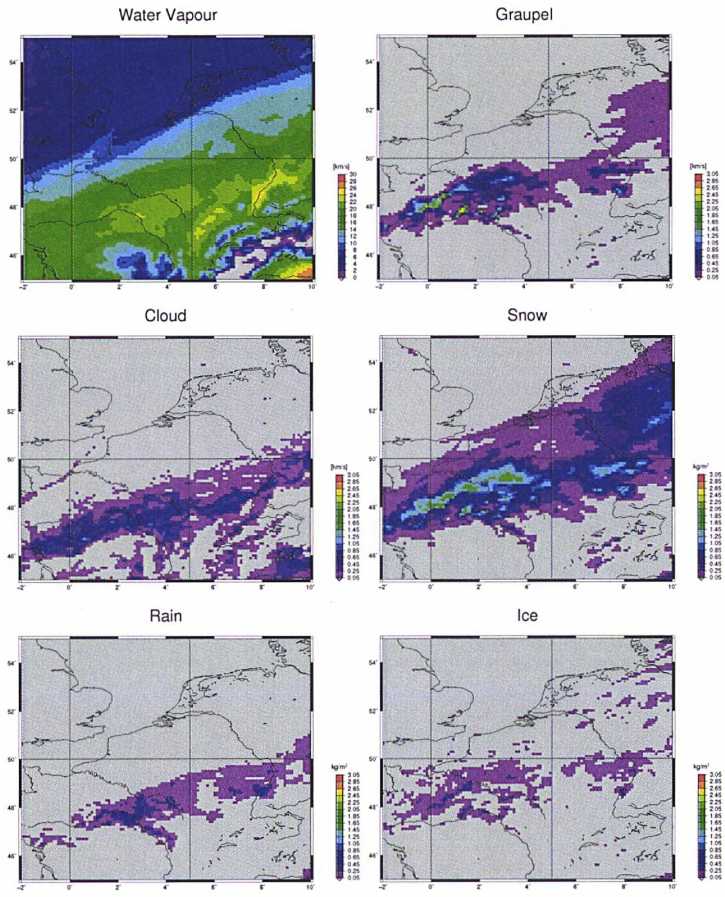

Figure 6.10: The Meso-NH fields of the heavy snowfall scene over France on 8 December 2010. The Meso-NH outputs are for 13:00 in coincidence with CloudSat and MHS observations.

Figure 6.11 presents the MHS observations at 89.0 (CH1), 157.0 (CH2), 183±1 (CH3), 183±3 (CH4) and 190.3 (CH5) GHz. MHS is a cross-track scanner similar to AMSU-B, with viewing zenith angles between 0^o and 58^o (see Section 2.1.2 for more detail). MHS observations show strong brightness temperature depressions between 0^oW and 6^oW and at approximately 50^oN associated with strong snow content modeled by Meso-NH (Figure 6.10). Overlaid in black in Figure 6.11 is the transect corresponding to the CloudSat footprint. Figure 6.11 also shows the CloudSat CPR reflectivity at 94 GHz.

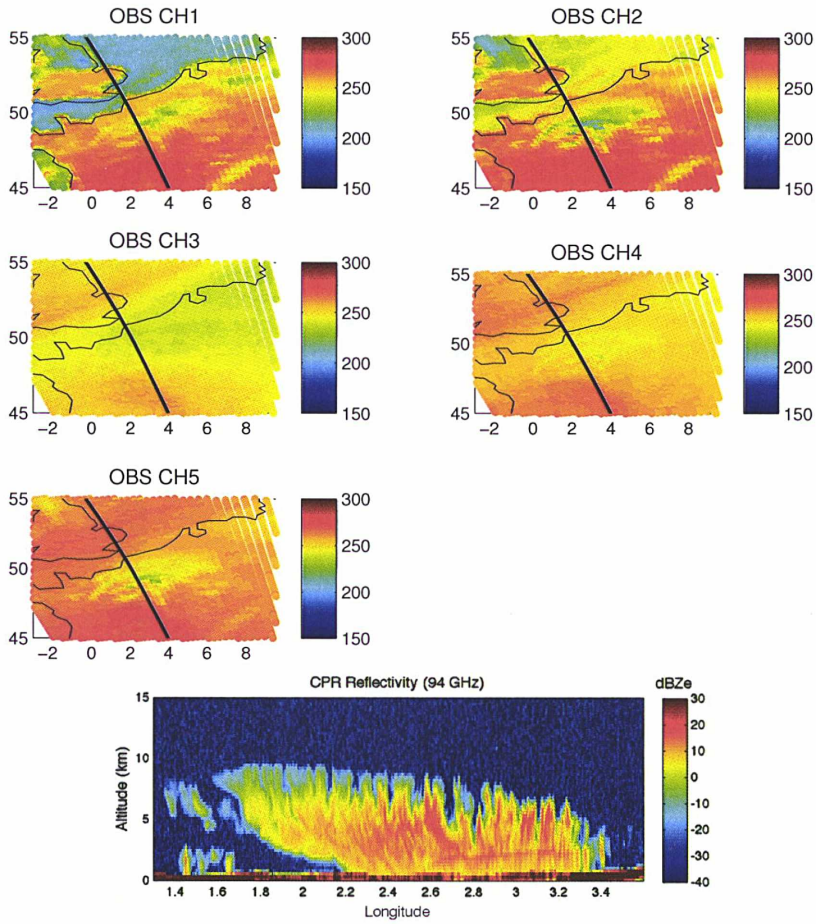

Figure 6.11: MHS observations at 89 (CH1), 157 (CH2), 183 ± 1 (CH3), 183 ± 3 (CH4) and 190 (CH5) GHz. The CloudSat overpass, approximately 20 minutes before, is shown by the black line crossing France southeast to northwest. CloudSat's CPR (94 GHz) radar reflectivity is also shown.

Closer examination of both MHS observations and Meso-NH outputs (and the hourly Meso-NH outputs not shown here) reveals that the cloud system modeled by Meso-NH is slightly time lagged with respect to the observations. This can easily be seen in Figure 6.12 which shows the observed brightness temperatures already presented in Figure 6.11 together with coincident

simulations resultant from radiative transfer simulations that assume the microphysical scheme intrinsic to Meso-NH previously introduced. Note that the observations and simulations are shown for pixels located over land only, and that the snow mass column modeled by Meso-NH is shown for reference. The difference between the observed and simulated brightness temperatures evidences the poor scattering signatures modeled under such microphysical assumptions (as observed with the Rhine case study). Analysis of Figure 6.12 also shows the agreement of the modeled and observed cloud structure located between the longitudes 0°E and 5°E, but the second cloud structure observed north east, is misplaced in the Meso-NH model outputs.

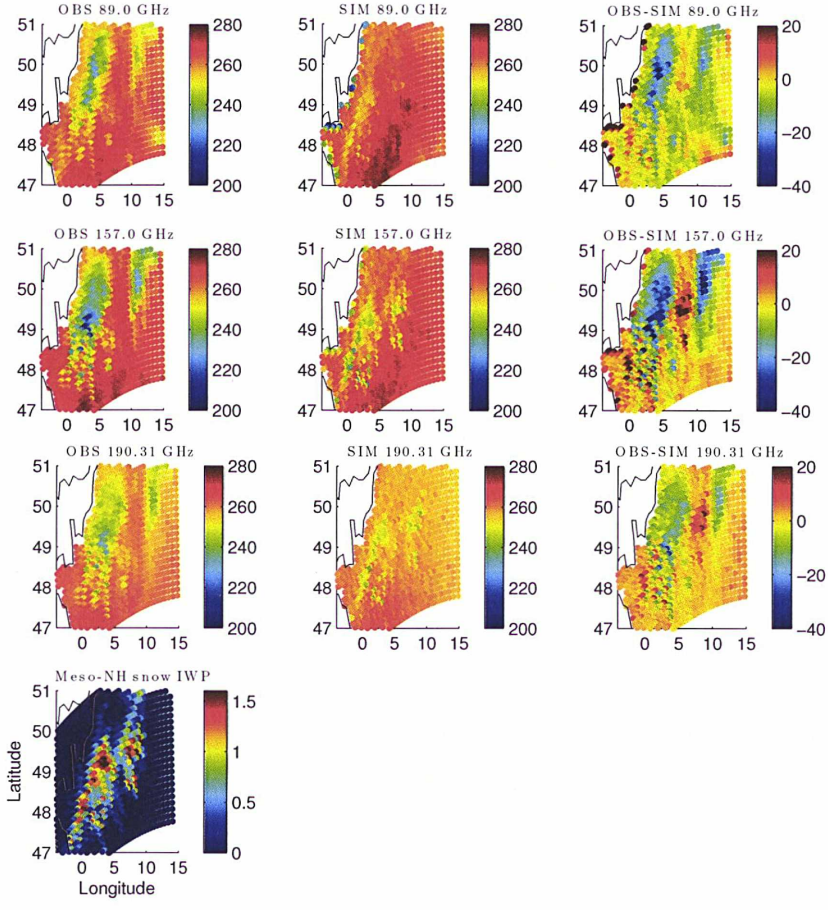

Figure 6.12: The MHS observations (left), as compared with the corresponding simulated brightness temperatures with the microphysical scheme intrinsic to Meso-NH (middle), and the difference between the observed and simulated brightness temperatures (right) for 89, 157 and 190 GHz. The Meso-NH modeled snow mass column is shown for reference on the bottom left.

Before proceeding to the analysis of the sensitivity of the active and passive observations to different microphysical assumptions, Figure 6.13 shows the distribution of the observed and simulated pixels presented in Figure 6.12. Note that only pixels over land and flagged

as cloudy according to the Meso-NH cut-off flag previously introduced are included in the distributions. As discussed with the Rhine scene, the statistical distributions show that for 89 and 157 GHz, observations are most sensitive to the snow mass column and the distribution of simulated brightness temperatures is shifted towards higher brightness temperatures (i.e., failing to reproduce the intense scattering that translates into the observed brightness temperature depressions).

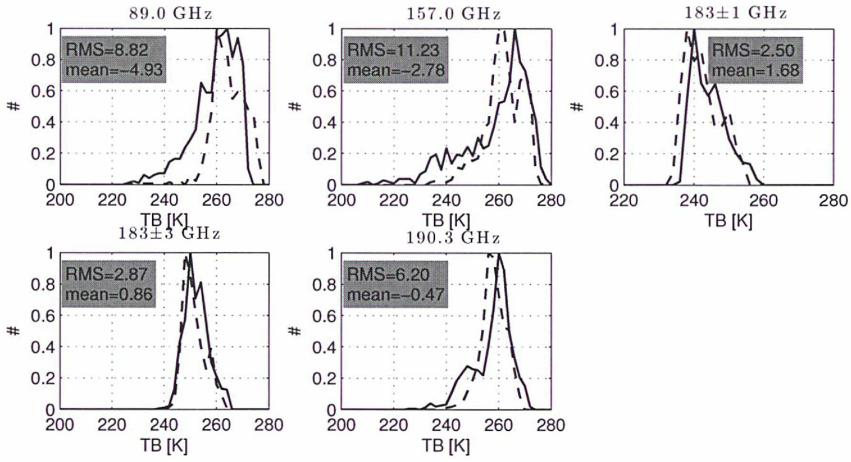

Figure 6.13: Histograms of the observed (solid line) and simulated (dashed line) MHS brightness temperatures with the Meso-NH microphysical scheme. The data used to calculate these distributions corresponds to cloudy pixels (as determined my Meso-NH) over land as presented in Figure 6.12. The RMS and bias of the difference between the two is indicated for each frequency channel.

6.3.2 Evaluation of the Passive and Active Simulations

Similar to the previous case studied, an MHS scan is selected along the cloud structure for a careful analysis of the sensitivity of the simulations to the hydrometeor properties. Figure 6.14 shows the Meso-NH hydrometeor integrated mass contents along this transect, with the corresponding incidence angles for MHS. From the experience gained with the previous case study and with the MADRAS analysis, we will concentrate on the simulations using the Meso-NH microphysics, coupled to the Liu (2004) approximation for soft spheres.

Figure 6.15 shows the simulated brightness temperatures at 89 and 157 GHz on the left, and the corresponding observations by MHS on the right. The integrated content of the different Meso-NH hydrometeors are displayed on the bottom right for reference. As already discussed with Figure 6.12, the high IWP modelled by Meso-NH between 6°E and 10°E is misplaced with respect to the observations from MHS. This analysis focuses on the overall magnitude of the simulated and observed fields west of 6°E, with MHS having brightness temperature depressions of the order of 50 K at 157 GHz. The 89 GHz channel, in contrast is less sensitive to the snow presence, with observed brightness temperature depressions of the order of 25 K.

In contrast to the Meso-NH microphysical scheme, simulations with a snow fixed density hypothesis once more improves the simulations, but still fails at reproducing the strong bright-

ness temperature depressions observed by MHS. The softness parameter from the Liu (2004) approximation, however, provides an accurate representation of the observed measurements. Horizontally aligned spheroids (aspect ratio 1.6) are only slightly more efficient scatterers than perfect spheres, though for a mixed polarized response as MHS, this is most likely due to the change in particle shape and its impact on the effective density approximated by Liu (2004). Finally, the sensitivity to the snow content is tested for this last microphysics assumptions by multiplying each layer of the modelled snow content by 1.25, with an important impact at 157 GHz where observations and simulations are of the same order of magnitude.

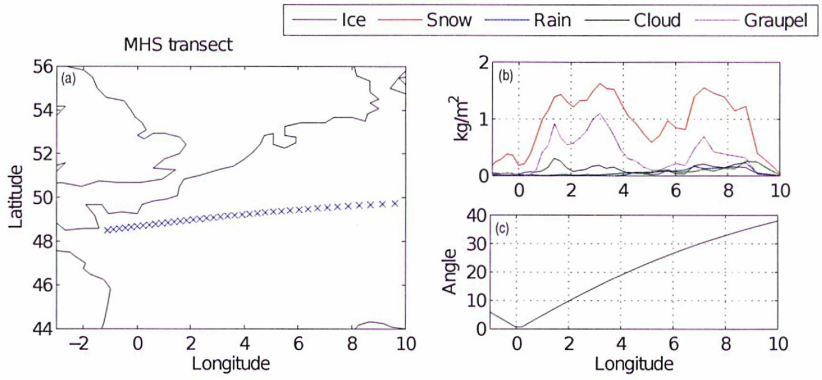

Figure 6.14: Selected transect for the heavy snowfall scene over France. Left: the location of the transect; top right: the integrated content of the different Meso-NH hydrometeors along this transect; bottom left: the incidence angle of the MHS observations along the transect

The CloudSat response is next simulated using the coincident Meso-NH species contents, presented in Figure 6.16. The first step is to simulate the active response assuming the initial microphysical properties from the Meso-NH scheme, which proved to underestimate the scattering efficiency for passive radiative transfer simulations. The results are shown in Figure 6.17(a) for perfect spheres. The overall 3D structure of the observed reflectivity, given the scales of the Meso-NH output, are captured reasonably well. It is evident, however, that such microphysical assumptions also underestimate the backscattering properties, for the same reason as with passive simulations. Figure 6.17(b) replaces the Meso-NH parameterization on mass by a fixed density of 0.1 g/cm^3 as done for passive simulations. There is only a slight improvement. Figure 6.17(c) shows, similarly, fixed density horizontally aligned spheroids of aspect ratio 1.6. Only a slight improvement is observed with higher reflectivities where the total ice content is higher (mainly around 2.4^{o}W and east of 3^{o}W). The Liu (2004) approximation is also tested for the active response (Figure 6.17(d) and (e)) for spheres and horizontally aligned spheroids of aspect ration 1.6 respectively. The reflectivity is still systematically underestimated, regardless

of the hypothesis.

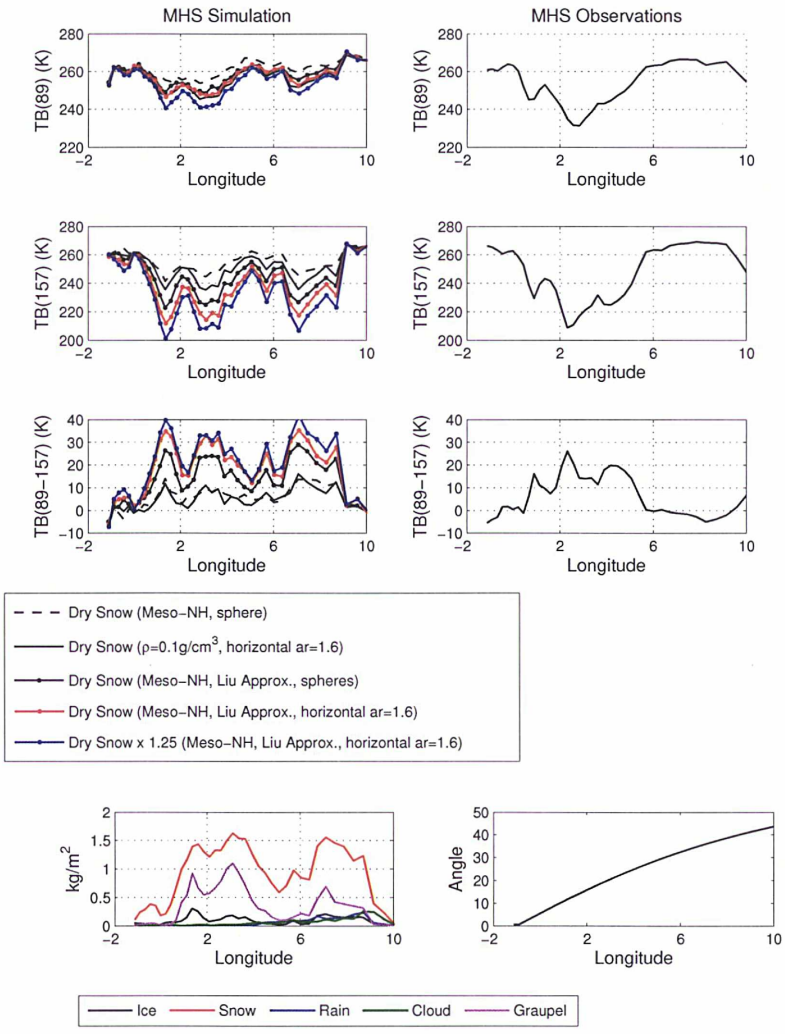

Figure 6.15: The observed (right) and simulated (left) brightness temperatures measurements from the MHS window channels along the chosen transect of the scene on the 8 Decemeber 2010.

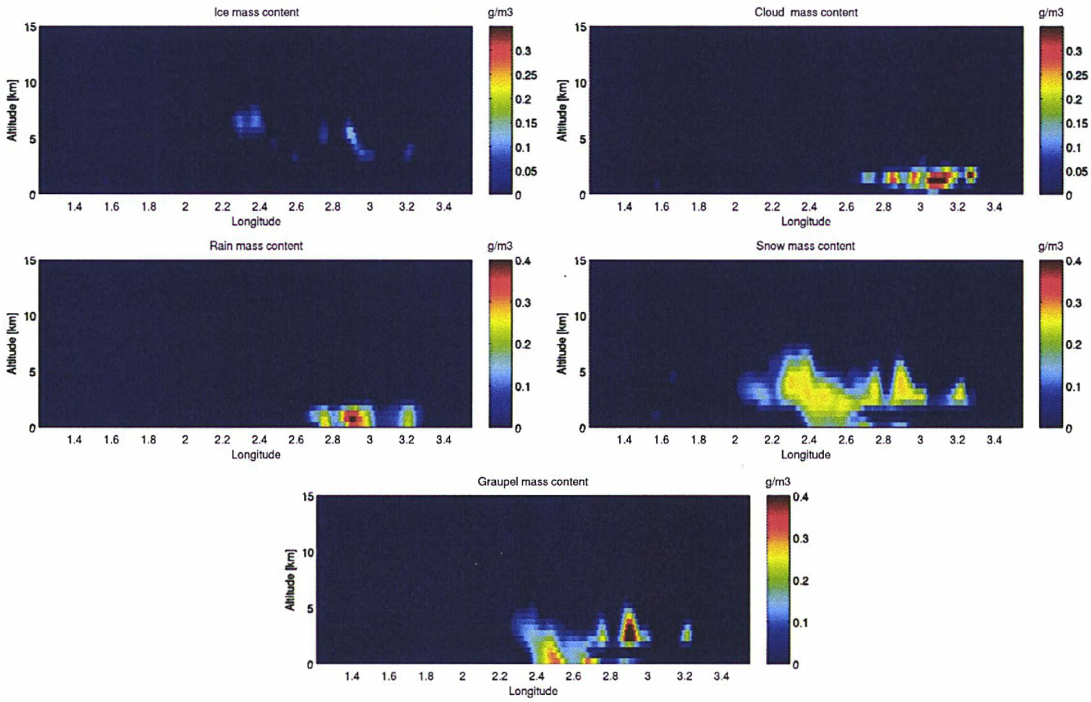

Figure 6.16: Meso-NH species mass content in g/m^3 for the CloudSat transect.

The availability of coincident CloudSat observations allows comparing its different retrieved ice water path (IWP) products with those modeled by Meso-NH. Figure 6.18 presents different ice water path products for the transect of interest. In order to carry out this comparison, the three frozen species from Meso-NH are summed (ice, graupel and snow) along this transect. The total Meso-NH frozen phase content is shown in Figure 6.18 (magenta line). The RO-IWP product (blue line) is one of CloudSat standard products and is available from the 2B-CWC-RO dataset. RO-IWP is the radar only (RO) retrieved value of IWP, obtained by assuming that the entire profile is ice, and zeroing out cases where all cloudy bins are warmer than 273 K (assumed to be liquid). The IO-RO-IWP (red line), similarly available from the 2B-CWC-RO dataset, assumes that the entire column is ice only. DARDAR exploits lidar/radar synergy onboard the A-Train. The CPR radar can penetrate thick systems of precipitating clouds, but is mainly sensitive to large particles and does not detect small ones. The CALIOP lidar, on the other hand, is sensitive to smaller particles, but gets attenuated quickly. Therefore radar/lidar DARDAR approach (Delanoë and Hogan, 2008, 2010b) is complementary. Despite retrieved IWP having large errors, reported by Austin et al. (2009) to be around 40%, this qualitative comparison gives an idea of the performance of the Meso-NH to simulate the high resolution footprint of CloudSat, with three different retrieved products including DARDAR. The Meso-NH outputs are observed to underestimate the total IWP estimated with CloudSat observations. This is not surprising given the difficulties in modeling the frozen phase, and the mentioned time lag between Meso-NH model outputs and the observations. Neglecting the fine structures of the CloudSat products, Meso-NH total IWP is comparable between 2.8°W and 2.9°W (mainly due to the strong presence of graupel as presented later). In the region between

2.3°W and 2.5°W, Meso-NH is comparable to the IROIWP retrieval. This is further evidenced in Figure 6.19 which shows the IWC cross-section of the transect as retrieved by DARDAR and the two CloudSat retrievals. The CPR reflectivity is shown for reference. Closer examination of the IWC cross-sections corresponding to CloudSat retrievals (Figure 6.19) and Meso-NH outputs (Figure 6.16) shows that the high IWC region at 2.6°W as reported by the retrieved IWC and the CPR high reflectivities (approximately 20 dBZ) is observed to be shifted to the west by Meso-NH by 0.2°. At 3.2°W Meso-NH is very similar to retrieved IWC as already shown in Figure 6.18.

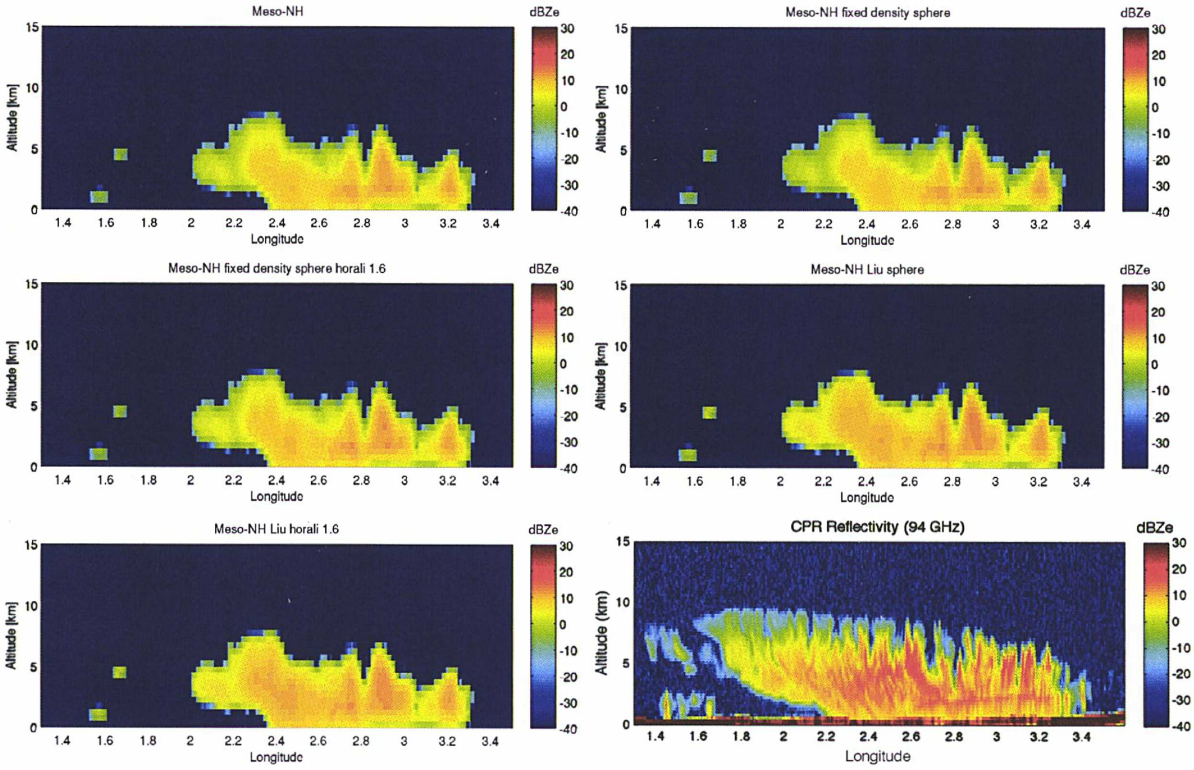

Figure 6.17: The simulated CPR (94 GHz) radar reflectivity. See individual figure titles for more information.

The previous simulations (Figure 6.17) are re-run, but multiplying the ice quantities systematically by 1.25 to account for the underestimation of the Meso-NH IWP noted above (Figure 6.20). The comparisons with the observations are not better in the case of the Meso-NH hypothesis, but they are significantly improved with the Liu (2004) approximation. As previously discussed, this same configuration was shown to work well with the passive simulations. This is very encouraging, and shows that we can reasonably simulate both passive and active observations, with careful and consistent assumptions about the parameters that determine the scattering properties.

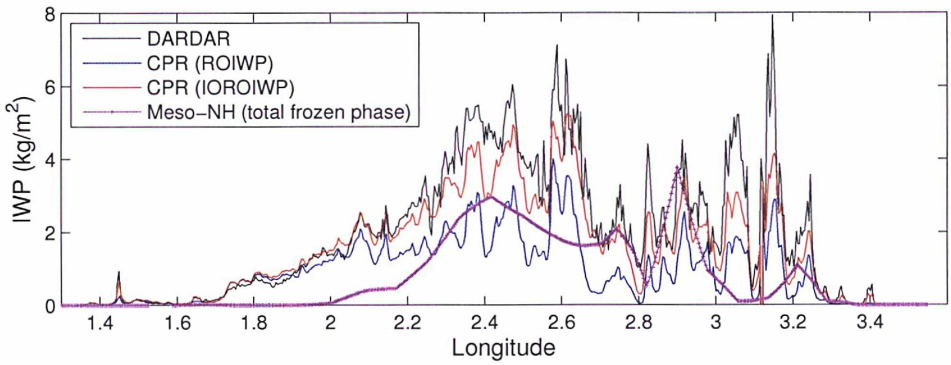

Figure 6.18: Comparison of the Meso-NH total ice water path with the ice water path retrieved from CloudSat.

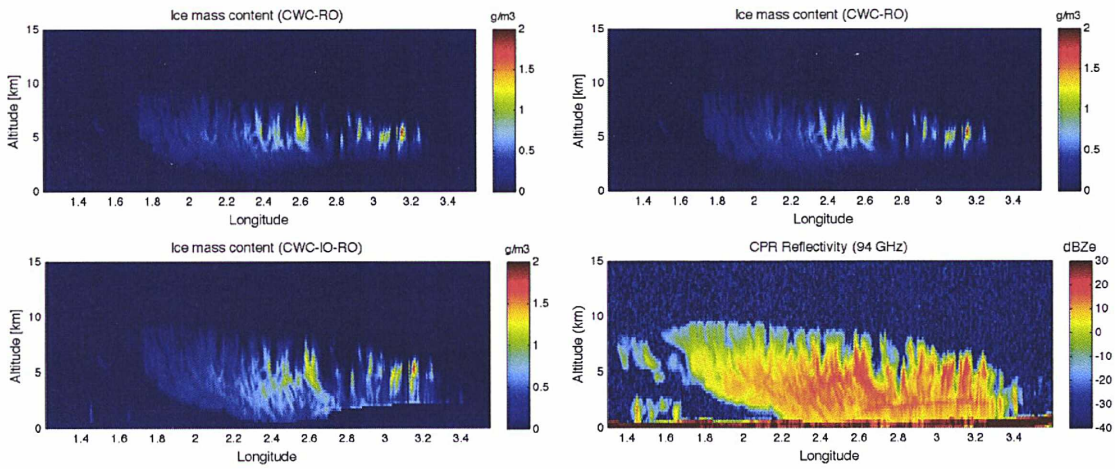

Figure 6.19: CloudSat CPR ice mass content as retrieved by, from top to bottom CWC-IO-RO, DARDAR and CWC-RO. The CPR reflectivity is shown for reference.

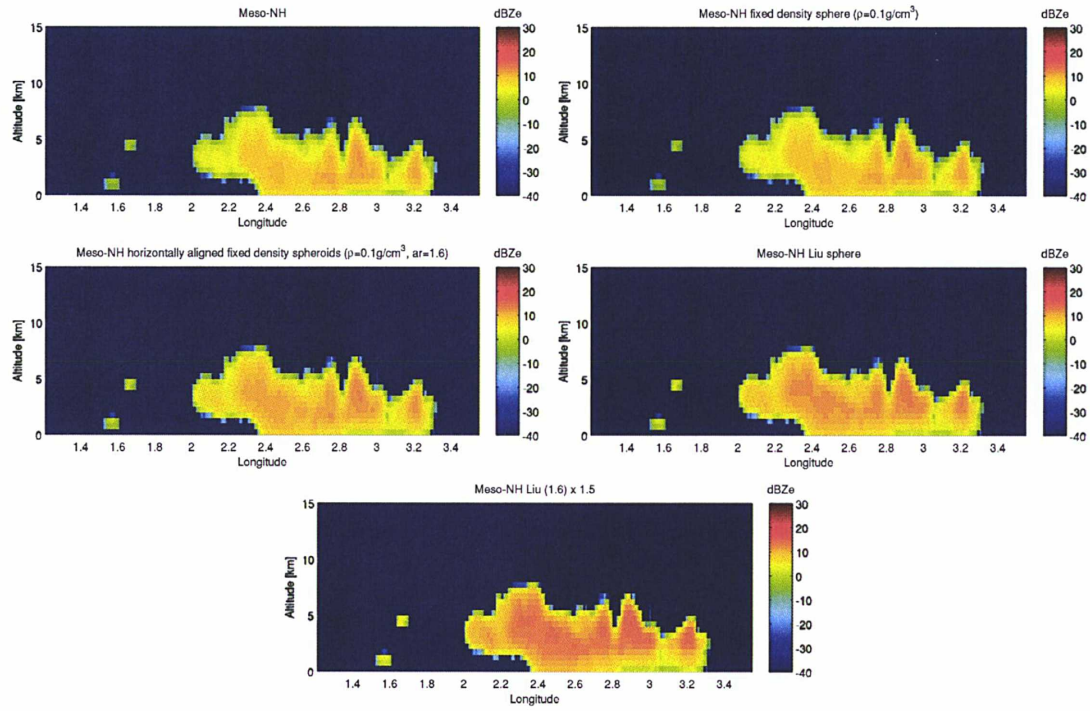

Figure 6.20: Same as Figure 6.17, but with the IWC multiplied by 1.25 at each layer for the snow profiles.

6.4 Conclusions

The observed brightness temperatures in two real case scenarios are simulated by coupling ARTS with the cloud meso-scale model Meso-NH. The first case scenario, corresponding to a light ptrecipitaion event over the Rhine area, is characterised by the presence of suspended snow. Coincident observations from SSM/I and AMSU-B are used to show the importance of setting realistic surface emissivities with TELSEM, a land surface emissivity atlas, and FASTEM, a wind-roughened ocean emissivity model. The second case scenario corresponds to a snowfall case over France with coincident passive (MHS and AMSR-E) and active (CloudSat) observations.

The sensitivity of radiative transfer simulations to the characteristics of the frozen particles (size, density, dielectric properties) is presented for the first case, and the approximation derived by Liu (2004) shows good agreement with the observations in contrast with the limited scattering signal generated when radiative transfer simulations are based on the microphysical properties intrinsic to Meso-NH. It is shown that the Meso-NH simulated hydrometeor quantities can be used to simulate reasonable scattering in the presence of snow. The availability of active observations from the second case, showed very encouraging results, as we can reasonably simulate both passive and active observations from consistent assumptions on the parameters that determine the scattering properties, specially with the Liu (2004) approximation. Hence, the microphysical assumptions in the Meso-NH scheme are realistic, provided that they are well

interpreted in the scattering calculation.

Further work is planned to be carried out to in order further exploit the active/passive synergy of this scene. This is important for building a robust database of simulated measurements to train a statistically base retrieval scheme, the final aim of the sensitivity analyses conducted. The Liu (2004) approximation is based on Discrete Dipole Approximation (DDA) modeling of complex shapes, and calculations are planned to be performed for the individual non-spherical shapes from which the approximation was derived. A comparison between radiative transfer simulations from Meso-NH outputs and other meso-scale cloud models, such as the Weather Research and Forecasting model (WRF), is also important to assess the variability in the modeling of the frozen phase by cloud meso-scale models.

Chapter 7

Conclusions and Perspectives

7.1 Conclusions

This thesis has been developed in the context of the pressing need to better characterize the frozen phase in clouds, for weather prediction and for climate studies. Climate models predict the ice phase with very large uncertainties, and the satellite-retrieved estimates also show significant errors. Additional studies had to be conducted to better constrain the microphysical properties of the frozen phase and reduce these large uncertainties. Furthermore, in the preparation of the upcoming NASA Global Precipitation Measurement (GPM) mission and the next generation of millimeter, sub-millimeter instruments onboard MetOp-SG, the operational European meteorological satellites, an understanding of the bulk properties of frozen hydrometeors is essential. The general theme of this thesis has been to work towards a better understanding of the microwave and millimeter responses of frozen hydrometeors, specifically snow, due to its strong scattering signal at these frequencies. This has been done for passive observations in priority, but active measurements have also been considered.

Correctly simulating microwave and millimeter observations over frozen clouds essentially depends on an accurate characterization of the scattering by the frozen hydrometeors. In order to do this, an important amount of time has been invested in understanding the radiative transfer calculations, and their limitations, and in developing necessary tools for realistic simulations. The Advanced Radiative Transfer Simulator (ARTS) has been adopted to provide the methods for rigorous calculation of radiative transfer in a scattering medium. During this thesis, ARTS has been thoroughly evaluated, in the presence of significant quantities of large hydrometeors (it had been mostly used before for the simulation of pristine small ice crystals that characterize cirrus clouds). The T-matrix code has been used to calculate the scattering properties of different hydrometeors under a number of different microphysical assumptions concerning the size, phase, shape and orientation. Tools have been coupled with ARTS, such as surface emissivity modules (TELSEM and FASTEM), in order to simulate the response of microwave instruments for real scenes. A module has been developed to calculate the active responses with ARTS. This makes it possible to have both passive and active simulations, with perfectly constant hypothesis. This has been made with the help of the ARTS community, and especially Chalmers University, where I spent a few weeks during this thesis.

An important part of this thesis focuses on studying and understanding the observed orthogonally polarized passive microwave signal with conical imagers such as TMI and the recently launched MADRAS onboard Megha-Tropiques. Cloud scattering signals had been observed to be associated with significant polarization differences. Analysis of concurrent passive and active microwave observations onboard TRMM has shown that under cloudy conditions, when a melting layer is detected by the precipitation radar, a fairly stable polarized scattering signal at 85 GHz in the passive mode is observed. Radiative transfer simulations have shown that this signal can be related to horizontally aligned mixed phase spheroids and its sensitivity to the effect of changes in particle size, shape, orientation and phase, from solid ice to dry snow to melting snow, has been assessed. MADRAS provides for the first time polarized measurements above 100 GHz. The instrument underwent some technical problems, but we showed that the data provided are of good quality. The analysis of the first polarized passive observations at close-to-millimeter frequencies (157 GHz) available from MADRAS and their interpretation with radiative transfer calculations, has provided a unique opportunity to validate the importance of horizontally aligned mixed phase spheroids in the generation of polarized scattering signatures and the importance of higher frequency observations for the analysis of the frozen

phase. The observed polarized scattering signal at 157 GHz has been shown to be consistent with the polarized scattering signatures observed at 85 GHz, and as expected these signatures have been found to be more common and stronger at the higher frequency. The sensitivity of the passive polarized scattering signal to the shape and orientation of hydrometers has been shown to be a unique tool to gain understanding on the complex microphysical processes in clouds. The potential to deduce the presence of a melting layer from the analysis of the polarized scattering signal has been shown by the rather stable relationship in the TBV and TBVH space from the analysis of TRMM observations. MADRAS observations have further validated our hypothesis for this stable relationship. Polarized scattering signatures are a unique set of observations that could be incorporated to re-direct rain and snow retrieval algorithm towards more realistic precipitation schemes over both land and ocean by detecting the melting layer. Re-directing retrieval schemes under the presence of the melting layer could address the overestimation of precipitation for light precipitating rain when retrievals neglect the melting layer.

In an effort to evaluate the representativity of the implemented cloud optical properties, large meteorological scenes have been simulated by coupling a cloud meso-scale model (Meso-NH) with the radiative transfer model (ARTS), in coincidence with real satellite observations. In this thesis, the focus has been centered on the simulations of snow events, both suspended in clouds and precipitating. Two different mid-latitude stratiform scenes modeled by Meso-NH are studied. The first real case scenario corresponds to a precipitating scene on the 10 February 2000 with coincident passive observations from AMSU-B and SSM/*I*. The second case study is an intense snowfall scene on the 8 December 2010 over France with coincident passive observations from MHS and AMSR-E and active observations form CloudSat. This last case has allowed a qualitative evaluation and assessment of the microphysical parameterizations under passive and active simulations since they were consistently simulated. The sensitivity analysis of active and passive responses to microphysical properties conducted in this thesis has provided confidence on the methods to develop a database with which to train statistical retrieval schemes for frozen species.

7.2 Perspectives

The advent of the next generation of high frequency instruments will provide the scientific community with access to data with a very high sensitivity to the scattering properties of frozen hydrometeors. The Ice Cloud Imager (ICI) is a conically scanning millimeter / sub-millimeter wave radiometer selected by EUMETSAT as an instrument for MetOp-SG, the next generation of European operational meteorological satellites. This instrument will complement the microwave sounder (MicroWave Sounder MWS) and imager (MicroWave Imager MWI) with frequencies up to 190 GHz, also on board the MetOp-SG platform. No down-looking sub-millimeter satellite instrument has been launched yet, despite the necessary technology being frequently used in astronomy and applied in limb sounders for atmospheric remote sensing. The ICI frequency coverage spans from 183 GHz up to 664 GHz, with two window channels (243 GHz and 664 GHz) measuring both V and H polarizations. Table 3 shows the ICI channels and their utilization. ICI will measure primarily ice clouds, and will provide cloud ice water path, cloud ice effective radius and cloud altitude. Information about snowfall is also expected. The launch of ICI opens new perspectives to detect, quantify and track cloud systems. However, the wide range of variability in the microphysics of clouds plays a crucial role in the detection of the frozen phase for both active and passive instruments, and specifically at the high ICI frequency channels. The studies conducted in this thesis will contribute to the preparation of this mission, with the tools that have been put in place (ARTS / Meso-NH coupling), and with the better understanding of the frozen phase derived from our analysis. However, there are still significant scientific efforts to be pursued, in preparation for this next generation of satellite instruments, both in the understanding of the physics and in the development of the retrieval algorithms.

Freq. (GHz)	Utilisation	Polarization
183.31 ± 7.0	Water vapour profile and snowfall	V
183.31 ± 3.4	Water vapour profile	V
183.31 ± 2.0	Water vapour profile	V
243.20 ± 2.5	Quasi-window, cloud ice retrieval, cirrus clouds	V, H
325.15 ± 9.5	Cloud ice effective radius	V
325.15 ± 3.5	Cloud ice effective radius	V
325.15 ± 1.5	Cloud ice effective radius	V
448.00 ± 3.0	Cloud ice water path and cirrus	V
448.00 ± 1.4	Cloud ice water path and cirrus	V
664.00 ± 4.2	Cirrus clouds, cloud ice water path	V, H

Table 7.1: The central frequency bands of the Ice Cloud Imager (ICI), a conically scanning millimeter / sub-millimeter wave radiometer that has been selected by EUMETSAT as an instrument for MetOp-SG.

Three airborne instruments are now available to perform the necessary scientific studies for the preparation of ICI. CoSSIR and PSR have been developed in the US and are operated on US aircrafts. They have already flown. The International Sub-Millimeter Airborne Radiometer (ISMAR) is a new aircraft instrument financed and built by the UK Met Office and by ESA. It is certified to operate on the UK Met Office BAe 146-301 FAAM aircraft (Figure 7.1),

which has a range of auxiliary instrumentation from microwave radiometers to infrared and visible spectrometers, as well as insitu cloud physics measurements. ISMAR will be used as a demonstrator for ICI, for scientific applications and ultimately for calibration / validation once ICI is launched. Table 7.2 describes the spectral response of the ISMAR channels. ISMAR channel combinations provide novel spectral synergy, and flexibility in viewing geometry: it is capable of down-looking and up-looking observations. Potentially, ISMAR can be placed on other platforms since it has been built as a modular and autonomous portable instrument. For example, it could fly on HALO, the high altitude and long range research aircraft of the German science community or even on the international space station, to overcome the altitude limitation of the FAAM aircraft.

Figure 7.1: The BAe FAAM aircraft showing the position of ISMAR.

Freq. (GHz)	Num. of Channels	Type	Polarization	Status	Support
118	5	O_2	V	Under Testing	ESA
243	1	window	V, H	Under Testing	ESA
325	3	H_2O	V	Under Testing	UKMO
448	4	H_2O	V	Under Testing	ESA
664	1	window	V, H	Under Testing	ESA
874	1	window	V, H	To build	ESA †

† Channels to be built by Omnisys Instruments.

Table 7.2: The central frequency bands of the International Sub-Millimeter Airborne Radiometer (ISMAR). The orthogonally polarized channel at 874 GHz has recently received funding from ESA and is currently under construction.

The millimeter and sub-millimeter spectral regions are new domain to explore for down-looking atmospheric remote sensing instruments and, as such, additional analysis has been undergoing. ISMAR will contribute to this effort. It will fly in aircraft field campaigns to test and improve radiative transfer algorithms. The Met Office is investing into campaigns with ISMAR with flight opportunities in December 2013 and January 2014. The first objective of these preliminary campaigns will be the technical evaluation of this new instrument, but scientific outcomes are nevertheless expected. The ISMAR measurements will be collected,

along with all the ancillary observations provided by the aircraft during these campaigns. First, the consistency of the observation will be tested, using radiative transfer simulations, under clear sky conditions. Then, the impact of the clouds on the observations will be analyzed. Finally, retrieval algorithms are planned to be derived from the data base collected during these campaigns. The sensitivity analyses conducted during this thesis will contribute to this work, with the improved understanding it provides on the frozen phase contributions.

Before ICI is available with observations above 200 GHz, the current microwave satellite observations can be used in synergy with other sensors, in an attempt to provide reasonable estimates of the frozen quantities. Multi-sensor retrieval schemes have proved the importance of exploiting the synergy of observations. A good example is the combined radar, lidar, and infrared radiometer data product DARDAR by Delanoë and Hogan (2008, 2010b). Coupling of the passive observations above 100 GHz (MHS for instance) with CloudSat radar can help constrain the problem and retrieve more accurate ice quantities. We showed in our work that consistent simulation of active and passive observations could be performed, and this approach is planned in the development of an adequate retrieval that would exploit this synergy.

References

Aires, F., Prigent, C., Bernardo, F., Jiménez, C., Saunders, R., Brunel, P., 2011. A tool to estimate land-surface emissivities at microwave frequencies (telsem) for use in numerical weather prediction. Quarterly Journal of the Royal Meteorological Society 137 (656), 690–699.

Anderson, G. P., Clough, S., Kneizys, F., Chetwynd, J., Shettle, E. P., 1986. Afgl atmospheric constituent profiles (0.120 km). Tech. rep., DTIC Document.

Armstrong, R., Brodzik, M., 2005. Northern hemisphere ease-grid weekly snow cover and sea ice extent version 3, boulder, co, usa: National snow and ice data center. Digital media 19826, 19852.

Austin, R. T., Heymsfield, A. J., Stephens, G. L., 2009. Retrieval of ice cloud microphysical parameters using the cloudsat millimeter-wave radar and temperature. Journal of Geophysical Research: Atmospheres (1984–2012) 114 (D8).

Awaka, J., Iguchi, T., Kumagai, H., Okamoto, K., 1997. Rain type classification algorithm for trmm precipitation radar. In: Geoscience and Remote Sensing, 1997. IGARSS'97. Remote Sensing-A Scientific Vision for Sustainable Development., 1997 IEEE International. Vol. 4. IEEE, pp. 1633–1635.

Barthazy, E., 1998. Microphysical properties of the melting layer. Ph.D. thesis, Ph. D. Thesis, ETH, Zürich.

Battaglia, A., Haynes, J., L'Ecuyer, T., Simmer, C., 2008. Identifying multiple-scattering-affected profiles in cloudsat observations over the oceans. Journal of Geophysical Research: Atmospheres (1984–2012) 113 (D8).

Battaglia, A., Kummerow, C., Shin, D.-B., Williams, C., Jun 2003. Constraining microwave brightness temperatures by radar brightband observations. Journal of Atmospheric and Oceanic Technology 20 (6), 856–871.

Bauer, P., Baptista, J. P. V. P., de Iulis, M., Mar 1999. The effect of the melting layer on the microwave emission of clouds over the ocean. Journal of the Atmospheric Sciences 56 (6), 852–867.

Bauer, P., Khain, A., Pokrovsky, A., Meneghini, R., Kummerow, C., Marzano, F., Baptista, J. P., 2000. Combined cloud-microwave radiative transfer modeling of stratiform rainfall. Journal of the atmospheric sciences 57 (8), 1082–1104.

Bennartz, R., Bauer, P., 2003. Sensitivity of microwave radiances at 85–183 ghz to precipitating ice particles. Radio Science 38 (4).

Bennartz, R., Petty, G. W., Mar 2001. The sensitivity of microwave remote sensing observations of precipitation to ice particle size distributions. Journal of Applied Meteorology 40 (3), 345–364.

Berg, W., L'Ecuyer, T., Haynes, J. M., 2010. The distribution of rainfall over oceans from spaceborne radars. Journal of Applied Meteorology and Climatology 49 (3), 535–543.

Bonsignori, R., 2007. The microwave humidity sounder (mhs): in-orbit performance assessment. In: Remote Sensing. International Society for Optics and Photonics, pp. 67440A–67440A.

Boukabara, S.-A., Weng, F., feb. 2008. Microwave emissivity over ocean in all-weather conditions: Validation using windsat and airborne gps dropsondes. Geoscience and Remote Sensing, IEEE Transactions on 46 (2), 376 –384.

Bréon, F.-M., Dubrulle, B., 2011. Horizontally oriented plates in clouds. J. Atmo. Sci.

Brown, S. T., Ruf, C. S., Apr 2007. Validation and development of melting layer models using constraints by active/passive microwave observations of rain and the wind-roughened ocean surface. Journal of Atmospheric and Oceanic Technology 24 (4), 543–563.

Buehler, S., Jimenez, C., Evans, K., Eriksson, P., Rydberg, B., Heymsfield, A., Stubenrauch, C., Lohmann, U., Emde, C., John, V., et al., 2007a. A concept for a satellite mission to measure cloud ice water path, ice particle size, and cloud altitude. Quarterly Journal of the Royal Meteorological Society 133 (S2), 109–128.

Buehler, S. A., Courcoux, N., John, V. O., 2006a. Radiative transfer calculations for a passive microwave satellite sensor: Comparing a fast model and a line-by-line model. J. Geophys. Res. 111.

Buehler, S. A., Jimenez, C., Evans, K. F., Eriksson, P., Rydberg, B., Heymsfield, A. J., Stubenrauch, C. J., Lohmann, U., Emde, C., John, V. O., Sreerekha, T. R., Davis, C. P., 2007b. A concept for a satellite mission to measure cloud ice water path, ice particle size, and cloud altitude. Quarterly Journal of the Royal Meteorological Society 133 (S2), 109–128.

Buehler, S. A., von Engeln, A., Brocard, E., John, V. O., Kuhn, T., Eriksson, P., 2006b. Recent developments in the line-by-line modeling of outgoing longwave radiation. J. Quant. Spectrosc. Radiat. Transfer 98 (3), 446–457.

Chaboureau, J.-P., Cammas, J.-P., Mascart, P., Pinty, J.-P., Claud, C., Roca, R., Morcrette, J.-J., 2000. Evaluation of a cloud system life-cycle simulated by the meso-nh model during fastex using meteosat radiances and tovs-3i cloud retrievals. Quarterly Journal of the Royal Meteorological Society 126 (566), 1735–1750.
URL http://dx.doi.org/10.1002/qj.49712656609

Chaboureau, J.-P., Cammas, J.-P., Mascart, P. J., Pinty, J.-P., Lafore, J.-P., 2002. Mesoscale model cloud scheme assessment using satellite observations. Journal of Geophysical Research: Atmospheres 107 (D16), AAC 8–1–AAC 8–20.
URL http://dx.doi.org/10.1029/2001JD000714

Chaboureau, J.-P., Söhne, N., Pinty, J.-P., Meirold-Mautner, I., Defer, E., Prigent, C., Pardo, J. R., Mech, M., Crewell, S., 2008. A Midlatitude Precipitating Cloud Database Validated with Satellite Observations. Journal of Applied Meteorology and Climatology 47, 1337.

Chevallier, F., Di Michele, S., McNally, A. P., 2006. Diverse profile datasets from the ECMWF 91-level short-range forecasts. European Centre for Medium-Range Weather Forecasts.

Cunningham, R. M., Oct 1947. A different explanation of the "bright line". Journal of Meteorology 4 (5), 163–163.

Czekala, H., 1998. Effects of particle shape and orientation on polarized microwave radiation for off-nadir problems. GRL 25, 1669–1672.

Davis, C., Evans, K., Buehler, S., Wu, D., Pumphrey, H., 2007. 3-d polarised simulations of space-borne passive mm/sub-mm midlatitude cirrus observations: a case study. Atmospheric Chemistry and Physics 7 (15), 4149–4158.

Defer, E., Prigent, C., Aires, F., Pardo, J., Walden, C., Zanifé, O.-Z., Chaboureau, J.-P., Pinty, J.-P., 2008. Development of precipitation retrievals at millimeter and sub-millimeter wavelengths for geostationary satellites. Journal of Geophysical Research 113 (D8), D08111.

Delanoë, J., Hogan, R. J., 2008. A variational scheme for retrieving ice cloud properties from combined radar, lidar, and infrared radiometer. Journal of Geophysical Research: Atmospheres (1984–2012) 113 (D7).

Delanoë, J., Hogan, R. J., 2010a. Combined cloudsat-calipso-modis retrievals of the properties of ice clouds. Journal of Geophysical Research: Atmospheres 115 (D4).
URL http://dx.doi.org/10.1029/2009JD012346

Delanoë, J., Hogan, R. J., 2010b. Combined cloudsat-calipso-modis retrievals of the properties of ice clouds. Journal of Geophysical Research: Atmospheres (1984–2012) 115 (D4).

Desbois, M., Eymard, R. R. L., Viltarda, N., Violliera, M., Srinivasanb, J., Narayananc, S., 2003. The megha-tropiques mission. In: Proc. of SPIE Vol. Vol. 4899. p. 173.

Di Girolamo, P., Demoz, B. B., Whiteman, D. N., 2003. Model simulations of melting hydrometeors: A new lidar bright band from melting frozen drops. Geophysical research letters 30 (12), 1626.

Donovan, D., 2003. Ice-cloud effective particle size parameterization based on combined lidar, radar reflectivity, and mean doppler velocity measurements. Journal of Geophysical Research: Atmospheres (1984–2012) 108 (D18).

Dungey, C., Bohren, 1993a. Backscattering by nonspherical hydrometeors as calculated by the coupled-dipole method- an application in radar meteorology. Journal of Atmospheric and Oceanic Technology 10 (4), 526–532.

Dungey, C. E., Bohren, C. F., Aug 1993b. Backscattering by nonspherical hydrometeors as calculated by the coupled-dipole method: An application in radar meteorology. Journal of Atmospheric and Oceanic Technology 10 (4), 526–532.

Ekström, M., Eriksson, P., Read, W., Milz, M., Murtagh, D. P., 2008. Comparison of satellite limb-sounding humidity climatologies of the uppermost tropical troposphere. Atmospheric Chemistry and Physics 8 (2), 309–320.

Eliasson, S., Buehler, S. A., Milz, M., Eriksson, P., John, V. O., 2011. Assessing observed and modelled spatial distributions of ice water path using satellite data. Atmospheric Chemistry and Physics 11 (1), 375–391.
URL http://www.atmos-chem-phys.net/11/375/2011/

Ellison, W. J., English, S. J., Lamkaouchi, K., Balana, A., Obligis, E., Deblonde, G., Hewison, T. J., Bauer, P., Kelly, G., Eymard, L., 2003. A comparison of ocean emissivity models using the advanced microwave sounding unit, the special sensor microwave imager, the trmm microwave imager, and airborne radiometer observations. Journal of Geophysical Research: Atmospheres 108 (D21).

Emde, C., January 2005. A polarized discrete ordinate scatterig model for radiative transfer simulations in spherical atmospheres with thermal source. Ph.D. thesis, University of Bremen, ISBN 3-8325-0885-4.

Emde, C., Buehler, S., Davis, C., Eriksson, P., Sreerekha, T., Teichmann, C., 2004. A polarized discrete ordinate scattering model for simulations of limb and nadir long-wave measurements in 1-d/3-d spherical atmospheres. Journal of Geophysical Research: Atmospheres (1984–2012) 109 (D24).

English, S. J., Hewison, T. J., 1998. Fast generic millimeter-wave emissivity model. In: Asia-Pacific Symposium on Remote Sensing of the Atmosphere, Environment, and Space. International Society for Optics and Photonics, pp. 288–300.

Eriksson, P., Buehler, S., Davis, C., Emde, C., Lemke, O., 2011a. Arts, the atmospheric radiative transfer simulator, version 2. Journal of Quantitative Spectroscopy and Radiative Transfer 112 (10), 1551 – 1558.

Eriksson, P., Rydberg, B., Buehler, S. A., 2011b. On cloud ice induced absorption and polarisation effects in microwave limb sounding. Atmospheric Measurement Techniques 4 (6), 1305–1318.
URL http://www.atmos-meas-tech.net/4/1305/2011/

Eriksson, P., Rydberg, B., Johnston, M., Murtagh, D. P., Struthers, H., Ferrachat, S., Lohmann, U., 2010. Diurnal variations of humidity and ice water content in the tropical upper troposphere. Atmospheric Chemistry and Physics 10 (23), 11519–11533.

Evans, K. F., Stephens, G. L., Jun 1995. Microwave radiative transfer through clouds composed of realistically shaped ice crystals. part i. single scattering properties. Journal of the Atmospheric Sciences 52 (11), 2041–2057.

Fabry, F., Szyrmer, W., Oct 1999. Modeling of the melting layer. part ii: Electromagnetic. Journal of the Atmospheric Sciences 56 (20), 3593–3600.

Ferraro, R., Weng, F., Grody, N., Zhao, L., Meng, H., Kongoli, C., Pellegrino, P., Qiu, S., Dean, C., 2005. Noaa operational hydrological products derived from the advanced microwave sounding unit. Geoscience and Remote Sensing, IEEE Transactions on 43 (5), 1036–1049.

Frisk, U., Hagström, M., Ala-Laurinaho, J., Andersson, S., Berges, J.-C., Chabaud, J.-P., Dahlgren, M., Emrich, A., Florén, H.-G., Florin, G., et al., 2003. The odin satellite. i. radiometer design and test. Astronomy and Astrophysics 402, L27–L34.

Galligani, V. S., Prigent, C., Defer, E., Jimenez, C., Eriksson, P., 2013. The impact of the melting layer on the passive microwave cloud scattering signal observed from satellites: A study using trmm microwave passive and active measurements. Journal of Geophysical Research: Atmospheres 118 (11), 5667–5678.
URL http://dx.doi.org/10.1002/jgrd.50431

Grecu, M., Olson, W. S., 2008. Precipitating snow retrievals from combined airborne cloud radar and millimeter-wave radiometer observations. Journal of Applied Meteorology and Climatology 47 (6), 1634–1650.

Guillou, C., English, S. J., Prigent, C., Jones, D. C., 1996. Passive microwave airborne measurements of the sea surface response at 89 and 157 ghz. Journal of Geophysical Research: Oceans 101 (C2), 3775–3788.

Hanesch, M., May 2009. Fall velocity and shape of snowflakes. Ph.D. thesis, Swiss Federal Institute of Technology.

Heymsfield, A. J., Bansemer, A., Field, P. R., Durden, S. L., Stith, J. L., Dye, J. E., Hall, W., Grainger, C. A., 2002. Observations and parameterizations of particle size distributions in deep tropical cirrus and stratiform precipitating clouds: Results from in situ observations in trmm field campaigns. Journal of the atmospheric sciences 59 (24), 3457–3491.

Heymsfield, A. J., Iaquinta, J., Apr 2000. Cirrus crystal terminal velocities. Journal of the Atmospheric Sciences 57 (7), 916–938.
URL http://dx.doi.org/10.1175/1520-0469(2000)057<0916:CCTV>2.0.CO;2

Hogan, R. J., Tian, L., Brown, P. R. A., Westbrook, C. D., Heymsfield, A. J., Eastment, J. D., Mar 2012. Radar scattering from ice aggregates using the horizontally aligned oblate spheroid approximation. Journal of Applied Meteorology and Climatology 51 (3), 655–671.
URL http://dx.doi.org/10.1175/JAMC-D-11-074.1

Hollinger, J. P., Peirce, J. L., Poe, G. A., 1990. Ssm/i instrument evaluation. Geoscience and Remote Sensing, IEEE Transactions on 28 (5), 781–790.

Iguchi, T., Kozu, T., Meneghini, R., Awaka, J., Okamoto, K., Dec 2000. Rain-profiling algorithm for the trmm precipitation radar. Journal of Applied Meteorology 39 (12), 2038–2052.

IPCC, 2007. Climate change 2007: Synthesis report. contribution of working groups i, ii and iii to the fourth assessment report of the intergovernmental panel on climate change. IPCC.

Ivanova, D., Mitchell, D. L., Arnott, W. P., Poellot, M., 2001. A gcm parameterization for bimodal size spectra and ice mass removal rates in mid-latitude cirrus clouds. Atmospheric research 59, 89–113.

Jiménez, C., Buehler, S., Rydberg, B., Eriksson, P., Evans, K., 2007. Performance simulations for a submillimetre-wave satellite instrument to measure cloud ice. Quarterly Journal of the Royal Meteorological Society 133 (S2), 129–149.

John, V., Soden, B., 2006. Does convectively-detrained cloud ice enhance water vapor feedback? Geophysical research letters 33 (20), L20701.

John, V. O., Buehler, S. A., 2004. The impact of ozone lines on AMSU-B radiances. Geophys. Res. Lett. 31.

John, V. O., Buehler, S. A., 2005. Comparison of microwave satellite humidity data and radiosonde profiles: A survey of European stations. Atm. Chem. Phys. 5, 1843–1853, sRefID:1680-7324/acp/2005-5-1843.

John, V. O., Buehler, S. A., von Engeln, A., Eriksson, P., Kuhn, T., Brocard, E., Koenig-Langlo, G., 2006. Understanding the variability of clear-sky outgoing long-wave radiation based on ship-based temperature and water vapor measurements. Q. J. R. Meteorol. Soc. 132 (621), 2675–2691.

Karbou, F., Prigent, C., july 2005. Calculation of microwave land surface emissivity from satellite observations: validity of the specular approximation over snow-free surfaces? Geoscience and Remote Sensing Letters, IEEE 2 (3), 311 – 314.

Katsumata, M., Uyeda, H., Iwanami, K., Liu, G., Dec 2000. The response of 36- and 89-ghz microwave channels to convective snow clouds over ocean: Observation and modeling. Journal of Applied Meteorology 39 (12), 2322–2335.

Kawanishi, T., Sezai, T., Ito, Y., Imaoka, K., Takeshima, T., Ishido, Y., Shibata, A., Miura, M., Inahata, H., Spencer, R. W., 2003. The advanced microwave scanning radiometer for the earth observing system (amsr-e), nasda's contribution to the eos for global energy and water cycle studies. Geoscience and Remote Sensing, IEEE Transactions on 41 (2), 184–194.

Kim, M.-J., Weinman, J. A., Olson, W. S., Chang, D.-E., Skofronick-Jackson, G., Wang, J. R., 2008. A physical model to estimate snowfall over land using amsu-b observations. Journal of Geophysical Research: Atmospheres 113 (D9).
URL http://dx.doi.org/10.1029/2007JD008589

Klaassen, W., Dec 1988. Radar observations and simulation of the melting layer of precipitation. Journal of the Atmospheric Sciences 45 (24), 3741–3753.

Kneifel, S., Kulie, M. S., Bennartz, R., 2011. A triple-frequency approach to retrieve microphysical snowfall parameters. Journal of Geophysical Research: Atmospheres 116 (D11).
URL http://dx.doi.org/10.1029/2010JD015430

Kneifel, S., Löhnert, U., Battaglia, A., Crewell, S., Siebler, D., 2010. Snow scattering signals in ground-based passive microwave radiometer measurements. Journal of Geophysical Research: Atmospheres (1984–2012) 115 (D16).

Kollias, P., Albrecht, B., 2005. Why the melting layer radar reflectivity is not bright at 94 ghz. Geophysical Research Letters 32 (24).
URL http://dx.doi.org/10.1029/2005GL024074

Kongoli, C., Pellegrino, P., Ferraro, R. R., Grody, N. C., Meng, H., 2003. A new snowfall detection algorithm over land using measurements from the advanced microwave sounding unit (amsu). Geophysical Research Letters 30 (14).
URL http://dx.doi.org/10.1029/2003GL017177

Korolev, A., Isaac, G., Aug 2003. Roundness and aspect ratio of particles in ice clouds. Journal of the Atmospheric Sciences 60 (15), 1795–1808.
URL http://dx.doi.org/10.1175/1520-0469(2003)060<1795:RAAROP>2.0.CO;2

Kulie, M. S., Bennartz, R., 2013/07/11 2009. Utilizing spaceborne radars to retrieve dry snowfall. Journal of Applied Meteorology and Climatology 48 (12), 2564–2580.
URL http://dx.doi.org/10.1175/2009JAMC2193.1

Kulie, M. S., Bennartz, R., Greenwald, T. J., Chen, Y., Weng, F., Nov 2010. Uncertainties in microwave properties of frozen precipitation: Implications for remote sensing and data assimilation. Journal of the Atmospheric Sciences 67 (11), 3471–3487.

Kummerow, C., Barnes, W., Kozu, T., Shiue, J., Simpson, J., Jun 1998a. The tropical rainfall measuring mission (trmm) sensor package. Journal of Atmospheric and Oceanic Technology 15 (3), 809–817.

Kummerow, C., Barnes, W., Kozu, T., Shiue, J., Simpson, J., 1998b. The tropical rainfall measuring mission (trmm) sensor package. Journal of Atmospheric and Oceanic Technology 15 (3), 809–817.

Kummerow, C., Simpson, J., Thiele, O., Barnes, W., Chang, A. T. C., Stocker, E., Adler, R. F., Hou, A., Kakar, R., Wentz, F., Ashcroft, P., Kozu, T., Hong, Y., Okamoto, K., Iguchi, T., Kuroiwa, H., Im, E., Haddad, Z., Huffman, G., Ferrier, B., Olson, W. S., Zipser, E., Smith, E. A., Wilheit, T. T., North, G., Krishnamurti, T., Nakamura, K., Dec 2000. The status of the tropical rainfall measuring mission (trmm) after two years in orbit. Journal of Applied Meteorology 39 (12), 1965–1982.
URL http://dx.doi.org/10.1175/1520-0450(2001)040<1965:TSOTTR>2.0.CO;2

Kuphaldt, T. R., 2007. Fundamentals of electrical engineering and electronics.
URL "www.vias.org/feee"

Lafore, J. P., Stein, J., Asencio, N., Bougeault, P., Ducrocq, V., Duron, J., Fischer, C., Héreil, P., Mascart, P., Masson, V., Pinty, J. P., Redelsperger, J. L., Richard, E., Vilà-Guerau de Arellano, J., 1998. The meso-nh atmospheric simulation system. part i: adiabatic formulation and control simulations. Annales Geophysicae 16 (1), 90–109.

Leinonen, J., Kneifel, S., Moisseev, D., Tyynelä, J., Tanelli, S., Nousiainen, T., 2012. Evidence of nonspheroidal behavior in millimeter-wavelength radar observations of snowfall. Journal of Geophysical Research: Atmospheres (1984–2012) 117 (D18).

Liao, L., Meneghini, R., dec. 2005. On modeling air/spaceborne radar returns in the melting layer. Geoscience and Remote Sensing, IEEE Transactions on 43 (12), 2799 – 2809.

Liao, L., Meneghini, R., 2009. Validation of trmm precipitation radar through comparison of its multiyear measurements with ground-based radar. Journal of Applied Meteorology and Climatology 48 (4), 804–817.

Liebe, H. J., Hufford, G. A., Manabe, T., 1991. A model for the complex permittivity of water at frequencies below 1 thz. International Journal of Infrared and Millimeter Waves 12 (7), 659–675.

Liu, G., 2004. Approximation of single scattering properties of ice and snow particles for high microwave frequencies. Journal of the atmospheric sciences 61 (20), 2441–2456.

Liu, G., 2008. Deriving snow cloud characteristics from cloudsat observations. Journal of Geophysical Research: Atmospheres (1984–2012) 113 (D8).

Liu, G., Seo, E.-K., 2013. Detecting snowfall over land by satellite high-frequency microwave observations: The lack of scattering signature and a statistical approach. Journal of Geophysical Research: Atmospheres 118 (3), 1376–1387.
URL http://dx.doi.org/10.1002/jgrd.50172

Liu, Q., Simmer, C., Ruprecht, E., 1996. Three-dimensional radiative transfer effects of clouds in the microwave spectral range. Journal of geophysical research 101 (D2), 4289–4298.

Liu, Q., Weng, F., English, S., april 2011. An improved fast microwave water emissivity model. Geoscience and Remote Sensing, IEEE Transactions on 49 (4), 1238 –1250.

Locatelli, J. D., Hobbs, P. V., 1974. Fall speeds and masses of solid precipitation particles. Journal of Geophysical Research 79 (15), 2185–2197.

Mace, G. G., Zhang, Q., Vaughan, M., Marchand, R., Stephens, G., Trepte, C., Winker, D., 2009. A description of hydrometeor layer occurrence statistics derived from the first year of merged cloudsat and calipso data. Journal of Geophysical Research: Atmospheres 114 (D8).
URL http://dx.doi.org/10.1029/2007JD009755

Magono, C., 1965. Aerodynamic studies of falling snowflakes. J. Meteorol. Soc. Japan 43, 139–147.

Marshall, J. S., Palmer, W. M. K., 1948. The distribution of raindrops with size. Journal of meteorology 5 (4), 165–166.

Matrosov, S. Y., Heymsfield, A. J., Wang, Z., 2005a. Dual-frequency radar ratio of nonspherical atmospheric hydrometeors. Geophysical Research Letters 32 (13).
URL http://dx.doi.org/10.1029/2005GL023210

Matrosov, S. Y., Reinking, R. F., Djalalova, I. V., 2005b. Inferring fall attitudes of pristine dendritic crystals from polarimetric radar data. Journal of the atmospheric sciences 62 (1), 241–250.

Matrosov, S. Y., Reinking, R. F., Kropfli, R. A., Martner, B. E., Bartram, B., 2001. On the use of radar depolarization ratios for estimating shapes of ice hydrometeors in winter clouds. Journal of Applied Meteorology 40 (3), 479–490.

Matrosov, S. Y., Shupe, M. D., Djalalova, I. V., Mar 2008. Snowfall retrievals using millimeter-wavelength cloud radars. Journal of Applied Meteorology and Climatology 47 (3), 769–777. URL http://dx.doi.org/10.1175/2007JAMC1768.1

Mätzler, C., Melsheimer, C., 2006. Radiative transfer and microwave radiometry. In: Mätzler, C. (Ed.), Thermal microwave radiation: Applications for remote sensing. The Institution of Engineering and Technolog, London, UK, pp. 1–23.

McFarquhar, G. M., Heymsfield, A. J., 1997. Parameterization of tropical cirrus ice crystal size distributions and implications for radiative transfer: Results from cepex. Journal of the atmospheric sciences 54 (17), 2187–2200.

Meirold-Mautner, I., Prigent, C., Defer, E., Pardo, J. R., Chaboureau, J.-P., Pinty, J.-P., Mech, M., Crewell, S., May 2007. Radiative transfer simulations using mesoscale cloud model outputs: Comparisons with passive microwave and infrared satellite observations for midlatitudes. Journal of the Atmospheric Sciences 64 (5), 1550–1568.
URL http://dx.doi.org/10.1175/JAS3896.1

Melsheimer, C., Verdes, C., Buehler, S. A., Emde, C., Eriksson, P., Feist, D. G., Ichizawa, S., John, V. O., Kasai, Y., Kopp, G., Koulev, N., Kuhn, T., Lemke, O., Ochiai, S., Schreier, F., Sreerekha, T. R., Suzuki, M., Takahashi, C., Tsujimaru, S., Urban, J., 2005. Intercomparison of general purpose clear sky atmospheric radiative transfer models for the millimeter/submillimeter spectral range. Radio Sci. 40, RS1007.

Meneghini, R., Liao, L., Oct 1996. Comparisons of cross sections for melting hydrometeors as derived from dielectric mixing formulas and a numerical method. Journal of Applied Meteorology 35 (10), 1658–1670.

Meneghini, R., Liao, L., May 2000. Effective dielectric constants of mixed-phase hydrometeors. Journal of Atmospheric and Oceanic Technology 17 (5), 628–640.
URL http://dx.doi.org/10.1175/1520-0426(2000)017<0628:EDCOMP>2.0.CO;2

Miao, J., Johnsen, K.-P., Buehler, S., Kokhanovsky, A., 2003a. The potential of polarization measurements from space at mm and sub-mm wavelengths for determining cirrus cloud parameters. Atmospheric Chemistry and Physics 3 (1), 39–48.
URL http://www.atmos-chem-phys.net/3/39/2003/

Miao, J., Johnsen, K.-P., Buehler, S., Kokhanovsky, A., 2003b. The potential of polarization measurements from space at mm and sub-mm wavelengths for determining cirrus cloud parameters. Atmospheric Chemistry and Physics 3 (1), 39–48.

Mishchenko, M. I., 2000. Calculation of the amplitude matrix for a nonspherical particle in a fixed orientation. Applied Optics 39 (6), 1026–1031.

Mitchell, D., Ivanova, D., Macke, A., McFarquhar, G., 1999. A gcm parameterization of bimodal size spectra for ice clouds. In: Proceedings of the 9th ARM Science Team Meeting.

Mitchell, D. L., Zhang, R., Pitter, R. L., Feb 1990. Mass-dimensional relationships for ice particles and the influence of riming on snowfall rates. Journal of Applied Meteorology 29 (2), 153–163.

Mitra, S. K., Vohl, O., Ahr, M., Pruppacher, H. R., Mar 1990. A wind tunnel and theoretical study of the melting behavior of atmospheric ice particles. iv: Experiment and theory for snow flakes. Journal of the Atmospheric Sciences 47 (5), 584–591.

Mohr, K. I., Famiglietti, J. S., Zipser, E. J., 1999. The contribution to tropical rainfall with respect to convective system type, size, and intensity estimated from the 85-ghz ice-scattering signature. Journal of Applied Meteorology 38 (5), 596–606.

Mugnai, A., Michele, S., Smith, E., Baordo, F., Bauer, P., Bizzarri, B., Joe, P., Kidd, C., Marzano, F., Tassa, A., Testud, J., Tripoli, G., 2007. Snowfall measurements by proposed european gpm mission. In: Levizzani, V., Bauer, P., Turk, F. (Eds.), Measuring Precipitation From Space. Vol. 28 of Advances In Global Change Research. Springer Netherlands, pp. 655–674.

Niu, F., Li, Z., 2011. Cloud invigoration and suppression by aerosols over the tropical region based on satellite observations. Atmospheric Chemistry and Physics Discussions 11 (2), 5003–5017.

Noel, V., Chepfer, H., Aug 2004. Study of ice crystal orientation in cirrus clouds based on satellite polarized radiance measurements. Journal of the Atmospheric Sciences 61 (16), 2073–2081.
URL http://dx.doi.org/10.1175/1520-0469(2004)061<2073:SOICOI>2.0.CO;2

Noh, Y.-J., Liu, G., Jones, A. S., Vonder Haar, T. H., 2009. Toward snowfall retrieval over land by combining satellite and in situ measurements. Journal of Geophysical Research: Atmospheres 114 (D24).

Noh, Y.-J., Liu, G., Seo, E.-K., Wang, J. R., Aonashi, K., 2006. Development of a snowfall retrieval algorithm at high microwave frequencies. Journal of Geophysical Research: Atmospheres 111 (D22).
URL http://dx.doi.org/10.1029/2005JD006826

Olson, W. S., Bauer, P., Kummerow, C. D., Hong, Y., Tao, W.-K., Jul 2001a. A melting-layer model for passive/active microwave remote sensing applications. part ii: Simulation of trmm observations. Journal of Applied Meteorology 40 (7), 1164–1179.
URL http://dx.doi.org/10.1175/1520-0450(2001)040<1164:AMLMFP>2.0.CO;2

Olson, W. S., Bauer, P., Viltard, N. F., Johnson, D. E., Tao, W.-K., Meneghini, R., Liao, L., Jul 2001b. A melting-layer model for passive/active microwave remote sensing applications.

part i: Model formulation and comparison with observations. Journal of Applied Meteorology 40 (7), 1145–1163.
URL http://dx.doi.org/10.1175/1520-0450(2001)040<1145:AMLMFP>2.0.CO;2

Pinty, J., Jabouille, P., 1998. A mixed-phase cloud parameterization for use in a mesoscale non-hydrostatic model: simulations of a squall line and of orographic precipitations. In: Conf. on Cloud Physics. pp. 217–220.

Prigent, C., Chevallier, F., Karbou, F., Bauer, P., Kelly, G., 2013/02/20 2005a. Amsu-a land surface emissivity estimation for numerical weather prediction assimilation schemes. Journal of Applied Meteorology 44 (4), 416–426.
URL http://dx.doi.org/10.1175/JAM2218.1

Prigent, C., Defer, E., Pardo, J. R., Pearl, C., Rossow, W. B., Pinty, J.-P., 2005b. Relations of polarized scattering signatures observed by the trmm microwave instrument with electrical processes in cloud systems. Geophysical Research Letters 32 (4).
URL http://dx.doi.org/10.1029/2004GL022225

Prigent, C., Jaumouille, E., Chevallier, F., Aires, F., feb. 2008. A parameterization of the microwave land surface emissivity between 19 and 100 ghz, anchored to satellite-derived estimates. Geoscience and Remote Sensing, IEEE Transactions on 46 (2), 344 –352.

Prigent, C., Pardo, J. R., Mishchenko, M. I., Rossow, W. B., 2001. Microwave polarized signatures generated within cloud systems: Special sensor microwave imager (ssm/i) observations interpreted with radiative transfer simulations. Journal of Geophysical Research: Atmospheres 106 (D22), 28243–28258.
URL http://dx.doi.org/10.1029/2001JD900242

Prigent, C., Rossow, W. B., Matthews, E., 1997. Microwave land surface emissivities estimated from ssm/i observations. Journal of Geophysical Research: Atmospheres 102 (D18), 21867–21890.

Prigent, C., Rossow, W. B., Matthews, E., 1998. Global maps of microwave land surface emissivities: Potential for land surface characterization. Radio Science 33 (3), 745–751.

Protat, A., Delanoë, J., O'Connor, E., L'Ecuyer, T., 2010. The evaluation of cloudsat and calipso ice microphysical products using ground-based cloud radar and lidar observations. Journal of Atmospheric and Oceanic Technology 27 (5), 793–810.

Purcell, E. M., Pennypacker, C. R., 1973. Scattering and absorption of light by nonspherical dielectric grains. The Astrophysical Journal 186, 705–714.

Reitter, S., Fröhlich, K., Seifert, A., Crewell, S., Mech, M., 2011. Evaluation of ice and snow content in the global numerical weather prediction model gme with cloudsat. Geoscientific Model Development 4 (3), 579–589.
URL http://www.geosci-model-dev.net/4/579/2011/

Rothman, L. S., Barbe, A., Benner, D. C., Brown, L. R., Camy-Peyret, C., Carleer, M. R., Chance, K., Clerbaux, C., Dana, V., Devi, V. M., Fayt, A., Flaud, J. M., Gamache, R. R.,

Goldman, A., Jacquemart, D., Jucks, K. W., Lafferty, W. J., Mandin, J.-Y., Massie, S. T., Nemtchinov, V., Newnham, D. A., Perrin, A., Rinsland, C. P., Schroeder, J., Smith, K. M., Smith, M. A. H., Tang, K., Toth, R. A., Auwera, J. V., Varanasi, P., Yoshino, K., 2003. The HITRAN molecular spectroscopic database: edition of 2000 including updates through 2001. J. Quant. Spectrosc. Radiat. Transfer 82, 5¡E2¿¡80¿¡93¿44.

Sassen, K., Matrosov, S., Campbell, J., 2007. Cloudsat spaceborne 94 ghz radar bright bands in the melting layer: An attenuation-driven upside-down lidar analog. Geophysical Research Letters 34 (16).
URL http://dx.doi.org/10.1029/2007GL030291

Saunders, R., Rayer, P., Brunel, P., von Engeln, A., Bormann, N., Strow, L., Hannon, S., Heilliette, S., Liu, X., Miskolczi, F., Han, Y., Masiello, G., Moncet, J.-L., Uymin, G., Sherlock, V., Turner, D. S., 2007. A comparison of radiative transfer models for simulating Atmospheric Infrared Sounder (AIRS) radiances. J. Geophys. Res. 112.

Saunders, R. W., Hewison, T. J., Stringer, S. J., Atkinson, N. C., 1995. The radiometric characterization of amsu-b. Microwave Theory and Techniques, IEEE Transactions on 43 (4), 760–771.

Schols, J. L., Weinman, J. A., Alexander, G. D., Stewart, R. E., Angus, L. J., Lee, A. C. L., Jan 1999. Microwave properties of frozen precipitation around a north atlantic cyclone. Journal of Applied Meteorology 38 (1), 29–43.

Schumacher, C., Houze, R. A., 2000. Comparison of radar data from the trmm satellite and kwajalein oceanic validation site. Journal of Applied Meteorology 39 (12), 2151–2164.

Sekhon, R., Srivastava, R., 1970. Snow size spectra and radar reflectivity. Journal of the Atmospheric Sciences 27 (2), 299–307.

Skofronick-Jackson, G., Johnson, B., july 2011. Thresholds of detection for falling snow from satellite-borne active and passive sensors. In: Geoscience and Remote Sensing Symposium (IGARSS), 2011 IEEE International. pp. 2637 –2640.

Skofronick-Jackson, G., Kim, M.-J., Weinman, J., Chang, D.-E., may 2004. A physical model to determine snowfall over land by microwave radiometry. Geoscience and Remote Sensing, IEEE Transactions on 42 (5), 1047 – 1058.

Skofronick-Jackson, G. M., Gasiewski, A. J., Wang, J. R., 2002. Influence of microphysical cloud parameterizations on microwave brightness temperatures. IEEE T. Geoscience and Remote Sensing 40 (1), 187–196.

Smith, E. A., Asrar, G., Furuhama, Y., Ginati, A., Mugnai, A., Nakamura, K., Adler, R. F., Chou, M.-D., Desbois, M., Durning, J. F., et al., 2007. International global precipitation measurement (gpm) program and mission: An overview. In: Measuring Precipitation From Space. Springer, pp. 611–653.

Spencer, R. W., Goodman, H. M., Hood, R. E., 1989. Precipitation retrieval over land and ocean with the ssm/i: Identification and characteristics of the scattering signal. Journal of Atmospheric and Oceanic Technology 6 (2), 254–273.

Sreerekha, T. R., Emde, C., Courcoux, N., Teichmann, C., Buehler, S. A., Loehnert, U., Mech, M., Crewell, S., Battaglia, A., Eriksson, P., Rydberg, B., Davis, C., Jiménez, C., English, S., Doherty, A., 2006. Development of an RT model for frequencies between 200 and 1000 GHz, final report. Tech. rep., ESTEC Contract No 17632/03/NL/FF.

Stephens, G. L., Vane, D. G., Boain, R. J., Mace, G. G., Sassen, K., Wang, Z., Illingworth, A. J., O'Connor, E. J., Rossow, W. B., Durden, S. L., Miller, S. D., Austin, R. T., Benedetti, A., Mitrescu, C., CloudSat Science Team, T., Dec 2002. The cloudsat mission and the a-train. Bulletin of the American Meteorological Society 83 (12), 1771–1790.
URL http://dx.doi.org/10.1175/BAMS-83-12-1771

Surussavadee, C., Staelin, D., oct. 2006. Comparison of amsu millimeter-wave satellite observations, mm5/tbscat predicted radiances, and electromagnetic models for hydrometeors. Geoscience and Remote Sensing, IEEE Transactions on 44 (10), 2667 –2678.

Troitsky, A., Osharin, A., Korolev, A., Strapp, J., 2003. Polarization of thermal microwave atmospheric radiation due to scattering by ice particles in clouds. Journal of the atmospheric sciences 60 (13), 1608–1620.

Troitsky, A., Osharin, A., Korolev, A., Strapp, W., Isaak, G., 2001. Studying the polarization characteristics of thermal microwave emission from a cloudy atmosphere. Radiophysics and Quantum Electronics 44, 935–948.

Turk, F. J., Park, K.-W., Haddad, Z. S., Rodriguez, P., Hudak, D. R., 2011. Constraining cloudsat-based snowfall profiles using surface observations and c-band ground radar. Journal of Geophysical Research: Atmospheres 116 (D23).
URL http://dx.doi.org/10.1029/2011JD016126

Urban, J., Lautié, N., Le Flochmoën, E., Jiménez, C., Eriksson, P., Dupuy, E., El Amraoui, L., Ekström, M., Frisk, U., Murtagh, D., de La Noë, J., Olberg, M., Ricaud, P., July 2005. Odin/SMR limb observations of stratospheric trace gases: Level 2 processing of ClO, N_2O, O_3, and HNO_3. J. Geophys. Res. 110, D14307.

Waliser, D. E., Li, J.-L. F., Woods, C. P., Austin, R. T., Bacmeister, J., Chern, J., Del Genio, A., Jiang, J. H., Kuang, Z., Meng, H., Minnis, P., Platnick, S., Rossow, W. B., Stephens, G. L., Sun-Mack, S., Tao, W.-K., Tompkins, A. M., Vane, D. G., Walker, C., Wu, D., 2009. Cloud ice: A climate model challenge with signs and expectations of progress. Journal of Geophysical Research: Atmospheres 114 (D8).
URL http://dx.doi.org/10.1029/2008JD010015

Wallace, J. M., Hobbs, P. V., 2006. Atmospheric science: an introductory survey. Vol. 92. Academic press.

Wang, J. R., Chang, L. A., 2013/02/21 1990. Retrieval of water vapor profiles from microwave radiometric measurements near 90 and 183 ghz. Journal of Applied Meteorology 29 (10), 1005–1013.
URL http://dx.doi.org/10.1175/1520-0450(1990)029<1005:ROWVPF>2.0.CO;2

Wang, J. R., Liu, G., Spinhirne, J. D., Racette, P., Hart, W. D., 2001. Observations and retrievals of cirrus cloud parameters using multichannel millimeter-wave radiometric measurements. Journal of Geophysical Research: Atmospheres 106 (D14), 15251–15263. URL http://dx.doi.org/10.1029/2000JD900262

Wiedner, M., Prigent, C., Pardo, J. R., Nuissier, O., Chaboureau, J.-P., Pinty, J.-P., Mascart, P., 2004. Modeling of passive microwave responses in convective situations using output from mesoscale models: Comparison with trmm/tmi satellite observations. Journal of Geophysical Research: Atmospheres (1984–2012) 109 (D6).

Willis, P. T., Heymsfield, A. J., Jul 1989. Structure of the melting layer in mesoscale convective system stratiform precipitation. Journal of the Atmospheric Sciences 46 (13), 2008–2025.

Xie, X., Löhnert, U., Kneifel, S., Crewell, S., 2012. Snow particle orientation observed by ground-based microwave radiometry. Journal of Geophysical Research 117 (D2), D02206.

Xie, X., Miao, J., Wang, W., july 2009. Microwave radiative transfer at frequencies of amsu-b: Effects of uncertainties in ice permittivity on brightness temperatures. In: Geoscience and Remote Sensing Symposium,2009 IEEE International,IGARSS 2009. Vol. 2. pp. II–714 –II–717.

Zawadzki, I., Szyrmer, W., Bell, C., Fabry, F., Oct 2005. Modeling of the melting layer. part iii: The density effect. Journal of the Atmospheric Sciences 62 (10), 3705–3723. URL http://dx.doi.org/10.1175/JAS3563.1

Appendix A

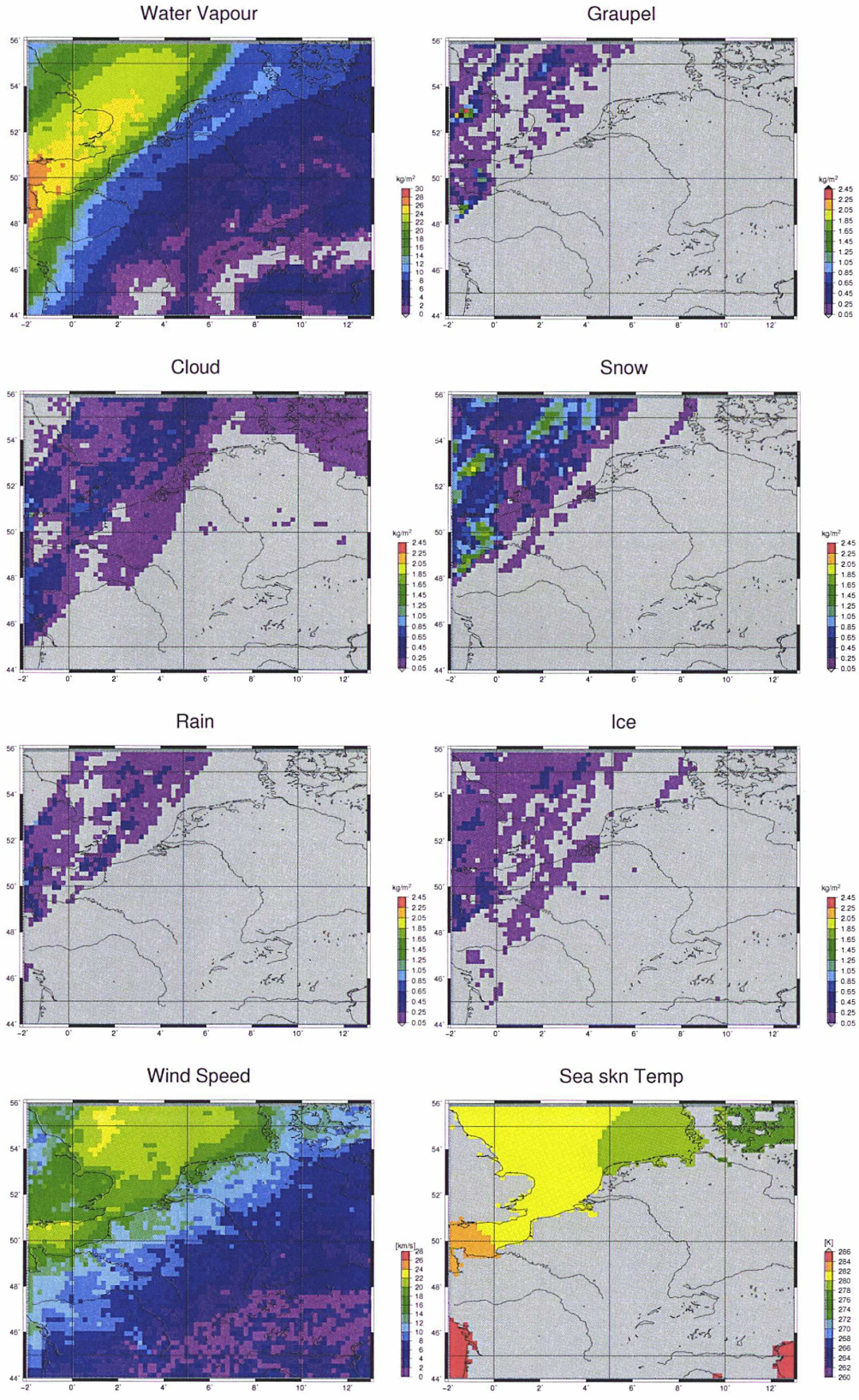

Figure 7.2: The Meso-NH fields of the RHINE scene on 10 February 2000 at SSM/I over-pass time (09:00UTC).

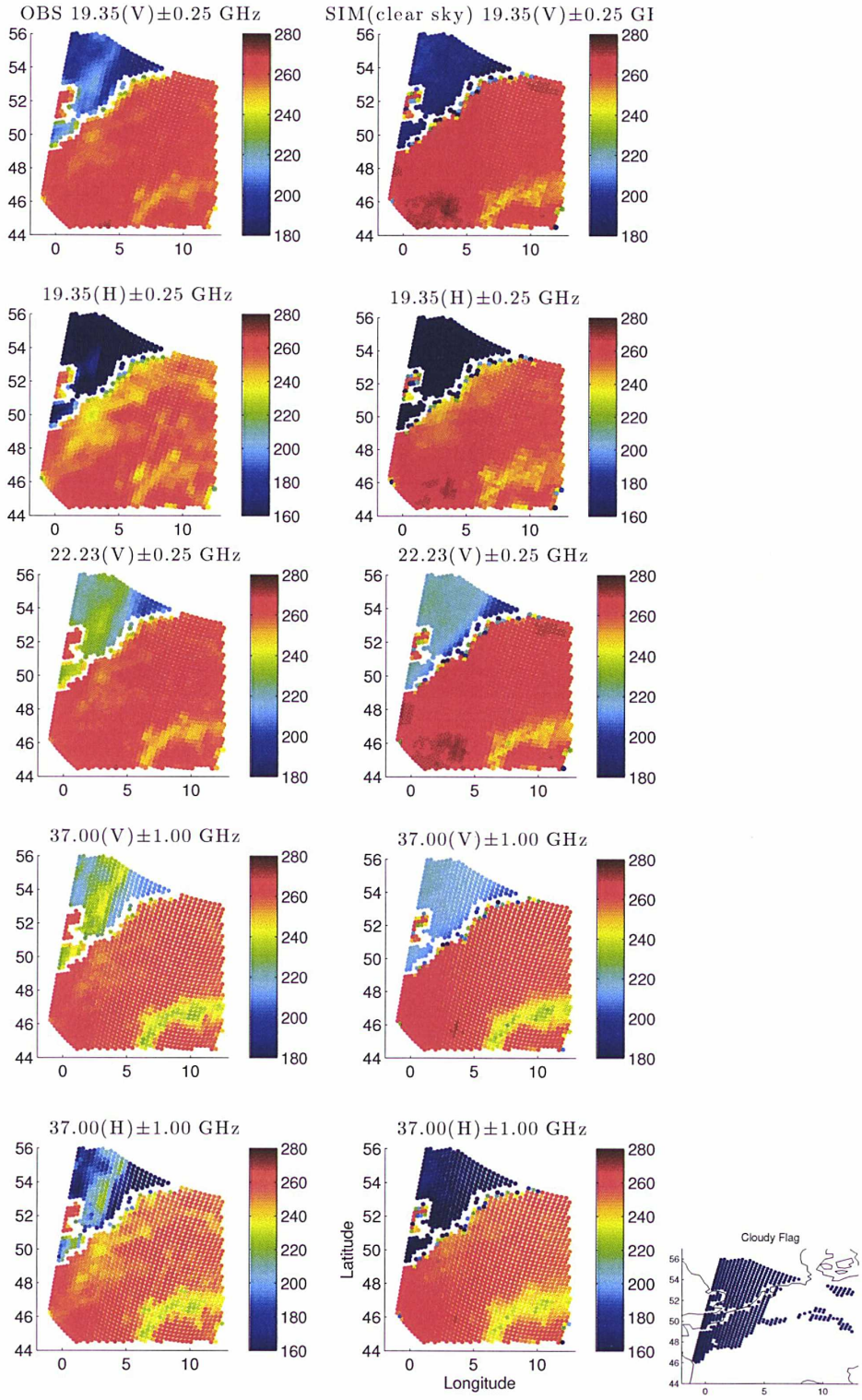

Figure 7.3: SSM/I low resolution observations (left) for the Rhine case on the 10 February 2000, along with ARTS radiative transfer simulations with Meso-NH inputs, ignoring the cloud components (right).

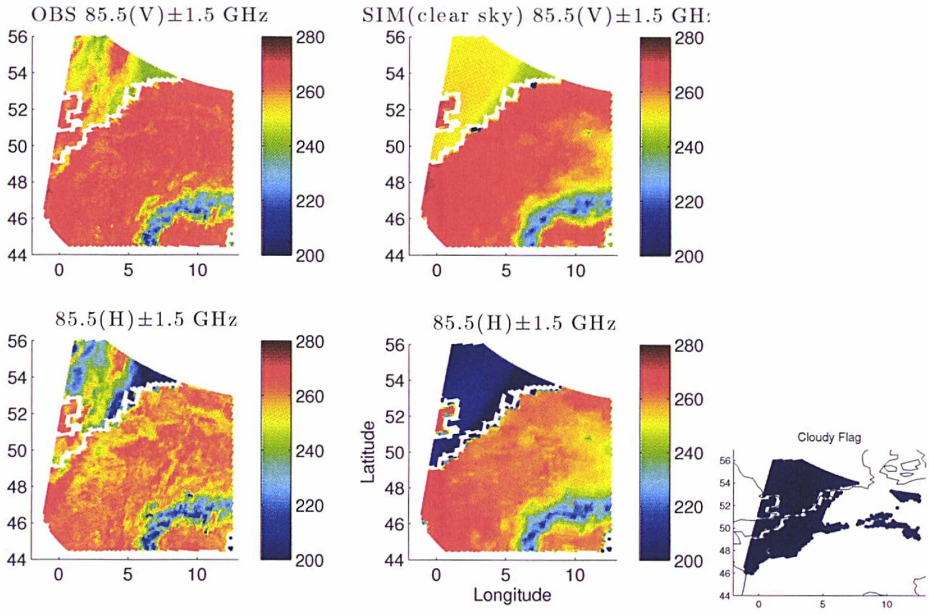

Figure 7.4: SSM/I hi resolution observations (left) for the Rhine case on the 10 February 2000, along with ARTS radiative transfer simulations with Meso-NH inputs, ignoring the cloud components (right).

Appendix B

Paper A

The Impact of the Melting Layer on the Passive Microwave Cloud Scattering Signal Observed from Satellites: A Study Using TRMM Microwave Passive and Active Measurements

Authors:
V. S. Galligani, C. Prigent, E. Defer, C. Jimenez, and P. Eriksson

Paper originally published in:
JOURNAL OF GEOPHYSICAL RESEARCH: ATMOSPHERES, 2013

The impact of the melting layer on the passive microwave cloud scattering signal observed from satellites: A study using TRMM microwave passive and active measurements

V. S. Galligani,[1] C. Prigent,[1] E. Defer,[1] C. Jimenez,[1] and P. Eriksson[2]

Received 31 October 2012; revised 17 April 2013; accepted 18 April 2013; published 13 June 2013.

[1] Concurrent passive and active microwave measurements onboard the Tropical Rainfall Measurement Mission (TRMM) show that under cloudy conditions, when a melting layer is detected by the precipitation radar, a polarized scattering signal at 85 GHz in passive mode is often observed. Radiative transfer simulations confirm the role of large horizontally oriented non-spherical particles on the polarized scattering signal and assess the effect of changes in particle phase, from solid ice to dry snow to melting snow, on the radiative properties. We conclude on the necessity to account for this polarization generated by the clouds in passive microwave rain retrievals and to use this specific signature to help diagnose the precipitation type and derive more accurate algorithms. In addition, analysis of the passive microwave polarized scattering is a unique way to get insight into microphysical properties of clouds at global scale, and this potential should be explored at millimeter and submillimeter frequencies that are more sensitive to the scattering generated by smaller particles.

Citation: Galligani, V. S., C. Prigent, E. Defer, C. Jimenez, and P. Eriksson (2013), The impact of the melting layer on the passive microwave cloud scattering signal observed from satellites: A study using TRMM microwave passive and active measurements, *J. Geophys. Res. Atmos.*, *118*, 5667–5678, doi:10.1002/jgrd.50431.

1. Introduction

[2] Several methods for estimating instantaneous precipitation rates from combined passive and active space-borne microwave observations have been developed and applied. These retrieval methods depend on the accuracy of the relationships between precipitating cloud properties and microwave observables. The lack of direct knowledge of the microphysical and associated radiative properties of certain precipitation particles like melting hydrometeors, which have an important radiative impact in stratiform regions, have led to subjective assumptions in the retrieval algorithms. In the stratiform regions of clouds, particles undergo complex melting processes as they fall through the freezing level. These processes have been described through aircraft microphysical measurements [e.g., *Willis and Heymsfield*, 1989], tunnel experiments [e.g., *Mitra et al.*, 1990] and modeling studies [e.g., *Zawadzki et al.*, 2005]. Around the 0°C isotherm, the aggregation of snow particles of different sizes and fall velocities forms larger flakes of similar velocity, leading to a large increase in the maximum-sized particles and a decrease in the total number of concentration. The low density flakes start to melt and turn into a mixture of water, ice, and air. During the melting process, the flakes collapse into raindrops of much smaller size than the original flakes of the same mass, but with an increased fall speed, yielding smaller particle concentration. Snow flakes typically melt within 100 to 500 m, and ice particles can be present at temperatures as high as 5°C.

[3] An increase in the radar backscattered signal close to the freezing level in stratified clouds, the so-called bright band, has been observed by ground based weather radars as early as the 1940s, and it was interpreted in terms of the melting of snow flakes [*Cunningham*, 1947]. Since the real part of the dielectric constant of water is more than three times larger than that of ice at 37 GHz, for example, the scattering caused by raindrops is greater than the one caused by ice particles of the same size. In the melting layer, wet snow flakes behave like large water drops, enhancing the backscattering whereas in the melted layer below, the decrease in number concentration and in particle size acts to reduce the radar reflectivity. The contrast between the higher reflectivity in the melting layer and the lower reflectivity below produces a bright band in the radar response, especially at low frequencies where attenuation by rain is not significant as seen from space. The signature of the melting layer is also significant from satellite instruments as observed with the Precipitation Radar (PR) onboard the Tropical Rainfall Measurement Mission (TRMM) since 1997. When the

[1]Laboratoire d'Etudes du Rayonnement et de la Matière en Astrophysique (LERMA), Centre National de la Recherche Scientifique, Observatoire de Paris, Paris, France.
[2]Department of Earth and Space Sciences, Chalmers University of Technology, Gothenburg, Sweden.

Corresponding author: V. S. Galligani, Laboratoire d'Etudes du Rayonnement et de la Matière en Astro-physique (LERMA), Centre National de la Recherche Scientifique, Observatoire de Paris, Paris, France. (victoria.galligani@obspm.fr)

2169-897X/13/10.1002/jgrd.50431

bright band is detected with the PR at 13 GHz, its effect on the reflectivity profile is taken into account in the rain retrieval algorithms. At CloudSat higher frequency, 94 GHz, only a sharp increase in the backscattering is observed at the melting layer: the decrease in the backscattering measured by TRMM at 13 GHz is not observed at 94 GHz due to the significant attenuation by rain [*Di Girolamo et al.*, 2003; *Kollias and Albrecht*, 2005; *Sassen et al.*, 2007].

[4] The impact of the melting layer on passive microwave observations has also been explored, mainly through modeling studies [*Bauer et al.*, 1999, 2000; *Olson et al.*, 2001a, 2001b]. Rather detailed melting processes have been implemented in cloud resolving models to produce realistic hydrometeor profiles, later used in radiative transfer simulations along with various dielectric models, size, and density distributions. The advanced melting scheme developed by *Olson et al.* [2001b] includes melting evaporation, particle interaction, and the effect of changing particle density within a three-dimensional cloud model over the radiatively cold ocean. Other simulation studies have also focused on the modeling of the dielectric properties of the mixed-phase melting particles [e.g., *Meneghini and Liao*, 1996, 2000]. All these studies result in an increase of the brightness temperatures (TBs) when the bright band is present. *Olson et al.* [2001a] found an increase of the TBs up to 15, 12, and 9 K at 19, 37, and 85 GHz respectively. From observations around a North Atlantic cyclone with SSM/I along with aircraft microphysical measurements, *Schols et al.* [1999] concluded that melting snow aggregates generate rather high TBs at 85 GHz compared to the regions where dense ice particles are present. *Battaglia et al.* [2003] conducted the first systematic analysis of observations to explore the effect of the melting layer on the passive microwave signal by looking at coincident radar and passive microwave observations during 5 years of TRMM data from December, January, and February over the East Pacific. They focus on frequencies below 40 GHz and conclude that the bright band has a significant impact on the microwave signal. At 10 and 19 GHz, at constant rain rate, the average TBs are always higher in the presence of a bright band suggesting the significant role of emission at those frequencies. The average TB difference read between presence and absence of the bright band decreases with increasing rain rate at 19 and 37 GHz, but at 85 GHz, TBs are lower in presence of a bright band, contradicting previous results (essentially from simulations) and suggesting the importance of the scattering effect above the melting layer. This scattering signal at 85 GHz has been used, for example, by *Mohr et al.* [1999] to estimate precipitation over ocean and land.

[5] In this study, we explore the impact of particle phase changes around the melting layer on the passive microwave observations using combined passive and active observations from TRMM, and we focus on the TRMM Microwave Imager (TMI) radiometric signatures. The PR and the TMI instruments provide simultaneous passive and active microwave observations, respectively, that document the hydrometeor contents of the sampled clouds at different wavelengths [*Kummerow et al.*, 1998, 2000]. We already analyzed the scattering polarized signatures at 85 GHz, with the help of coincident infrared observations from the International Satellite Cloud and Climatology Project (ISCCP) data set [*Prigent et al.*, 2001] and with the Lightning Imaging Sensor (LIS) [*Prigent et al.*, 2005]. We established the relationship between negative polarized signatures (difference between vertically and horizontally polarized brightness temperatures) at 85 GHz and the lightning activity in convective cores. Radiative transfer simulations showed that negative polarization differences can be explained by relatively large non-spherical particles, mostly vertically oriented. This is in contrast to small horizontally aligned plates populating cirrus clouds and large frozen particles in the form of aggregates that exhibit a horizontal preferential alignment due to aero-dynamical effects [*Xie and Miao*, 2011; *Xie et al.*, 2012]. In this study, we analyze TMI 37 and 85 GHz radiometric signals sensed in clouds and more specifically in bright band cloud regions based on PR measurements. The methodology and the data are described in section 2. Section 3 presents the observational results that suggest that polarized scattering at 85 GHz coincides with the presence of a melting layer. Section 4 uses radiative transfer simulations to examine the link between polarized scattering in the microwave and the properties of the hydrometeors, essentially their phase and density. Section 5 concludes this study, insisting on the interest of the analysis of the polarized signal at 85 GHz for more accurate precipitation retrievals.

2. The TRMM Observations

[6] The TRMM satellite, launched in 1997, carries a suite of instruments designed to study precipitation in the tropics [*Kummerow et al.*, 1998]. It includes two microwave instruments, one passive and one active, which are both used in this study. The TMI, a conical imager, measures at 10.7, 19.4, 21.3, 37, and 85.5 GHz with two orthogonal polarizations (except at 22 GHz) and a spatial resolution between 63 km × 37 km and 7 km × 5 km, depending on the frequency, and a swath of 780 km. The PR observes at 13.8 GHz with a 4 km resolution and a swath of 220 km located in the center of the TMI swath.

[7] The precipitation properties (near surface rain rate, convective/stratiform rain, and bright band properties) emanate from the 2A23 and 2A25 PR products. The algorithm 2A25 uses a Z-R relationship based on a particle size distribution model and retrieves profiles of the radar reflectivity factor with rain attenuation correction and rain rate for each radar beam [*Iguchi et al.*, 2000]. The algorithm 2A23 verifies if a bright band exists in rain echoes and determines the bright band height and intensity when it exists [*Awaka et al.*, 1997]. The rain type is classified into stratiform, convective and others, based on the detection of BB and, in case of warm rain, on the horizontal structure of the reflectivity field. The PR minimum detectable rain is usually considered to be 0.5 mm h^{-1}. *Schumacher and Houze* [2000] derive maps of rainfall rate and convective/stratiform classification for oceanic cases that compare well between PR and S-band validation radar records during the Kwajex experiment. *Schumacher and Houze* [2000] also report a tendency of the PR to under sample weaker echoes associated with stratiform rain near the surface and ice particles aloft, but the PR is still able to record most of the near-surface precipitation accumulation. *Liao and Meneghini* [2009] showed a fairly good agreement between the PR and Melbourne Weather Surveillance Radar-1988 Doppler

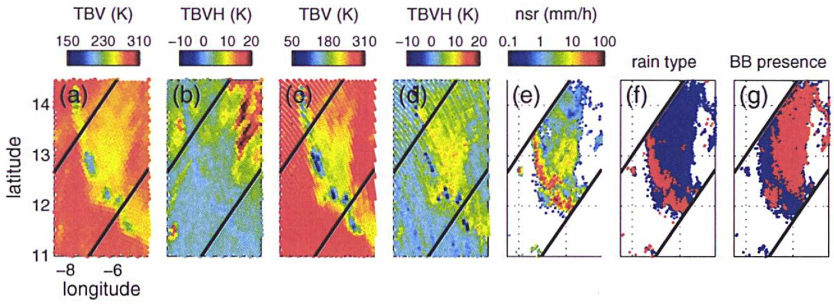

Figure 1. TRMM observations of a squall line in Africa during the AMMA campaign (19 August 2006) with (a) TBV(37 GHz), (b) TBVH(37 GHz), (c) TBV(85 GHz), (d) TBVH(85 GHz), (e) the near surface rain rate, (f) the PR rain type flag from the 2A23 PR product, convective in red and stratiform in blue, and (g) the presence of a BB in red.

(WSR) derived rain rates for the case of stratiform rain, while during convective rain the PR seems to overestimate light rain, and underestimate moderate to heavy rain in comparison with the WSR data, but different performances are expected worldwide, according to variability in climate, surface background, and raindrop size distributions [*Liao and Meneghini*, 2009]. More recently the analysis performed by *Berg et al.* [2010] reported a rather good agreement between PR and Cloud Profiling Radar (CPR) rain rates for the range 1 to 3 mm h^{-1} for a total precipitable water (TPW) estimate above 40 mm. In the present study, the PR observations are considered as valid and accurate enough to describe the properties of the precipitation (e.g., geographical distribution, rain rate type, and rain rate).

[8] TMI and PR observations, together with its derived products, have been merged together on a regular 0.2° × 0.2° grid mesh for 2 years (2006 and 2007). Each grid box contains, when available, the TMI 1B11 brightness temperatures located within the box, the TMI 2A12 derived rain parameters (not used in the analysis), and the PR level 2A products 2A23 and 2A25. The analysis of the database is performed over sea and land separately based on the 2A12 surface flag. In order to avoid contamination of the radiometric signal by snow on the ground, snow-covered pixels are filtered out using the National Snow and Ice Data Center (NSIDC) data [*Armstrong and Brodzik*, 2005].

3. Analysis of the Polarized Scattering Signatures of TMI Data in the Presence of Melting Layer

[9] A case study at a pixel level is presented in Figure 1 over land. It corresponds to a squall line in Africa as observed during the African Monsoon Multidisciplinary Analyses (AMMA) campaign (19 July 1998). Averaged vertical and horizontal brightness temperatures (TBV and TBH) and their polarization differences (TBVH) are shown in Figure 1. TBVH(85 GHz) signals of the order of 8 K and TBV(85 GHz) signals of the order of 220 K when the PR detects stratiform rain and the presence of BB can be observed, as presented by the statistical analysis that follows. Similarly, at 37 GHz some scattering is observed with the convective phase with lower TBVs but little polarization difference. In the stratiform part of the cloud, less pronounced scattering is present compared to 85 GHz. Near surface rain rate as provided by PR ranges over two orders of magnitude in the stratiform region in presence or not of BB. Regions of convective rain where there is no BB reported shows very low TBVs and negative or negligible polarization signals, high rain rate, and lightning activity (not shown).

[10] In order to assess the impact of the melting layer on the TMI observations, cases of stratiform rain are first identified with the PR and further divided into cases with and without melting layers as detected by the PR bright band (BB). Stratiform rain boxes of 0.2° × 0.2° are identified as having at least 20 PR observations with 50% of them stratiform; considered in this study are only those boxes where the bright band is detected for 100% of stratiform observations or for 0% of them. TBV, TBH, and TBVH at TMI frequencies are analyzed as a function of the stratiform near surface rain rate, with and without a melting layer. Figure 2 presents the variations as a function of stratiform rain rate of the TBH and TBVH over ocean (Figures 2a–2j) and land (Figures 2k–2t), along with their standard deviations, computed over the 0.2° × 0.2° grid at 37 and 85 GHz for stratiform rain with a BB (blue curve) and without a BB (red curve).

[11] The ocean has a rather low surface emissivity, with large polarization differences. At low frequencies, emission by cloud and rain increases the TBs over the radiometrically cold background, and the polarization generated by the surface decreases with increasing cloud and rain attenuation. For all frequencies above 10 GHz, the presence of BB tends to decrease the TBs. At 85 GHz, two phenomena compete, namely the emission and the scattering by cloud and rain. The difference between the presence and absence of a bright band is evidenced clearly at 85 GHz over land for high rain rates. TBs are lower when a BB is detected, likely associated with the increasing number of frozen particles associated to the melting layer. In addition TBs decrease with increasing RR for BB cases. The difference between BB and no-BB polarization difference increases with increasing rain rate, i.e., increasing ice quantities. This is clear evidence that the polarization difference (of the order of 7K) is generated by the hydrometeors, not by the polarized surface of the ocean.

[12] Land surface emissivities in the microwave region are usually very high (above 0.95) and low polarization differences, and the cloud and rain emission signatures are more difficult to detect due to the lack of contrast between the

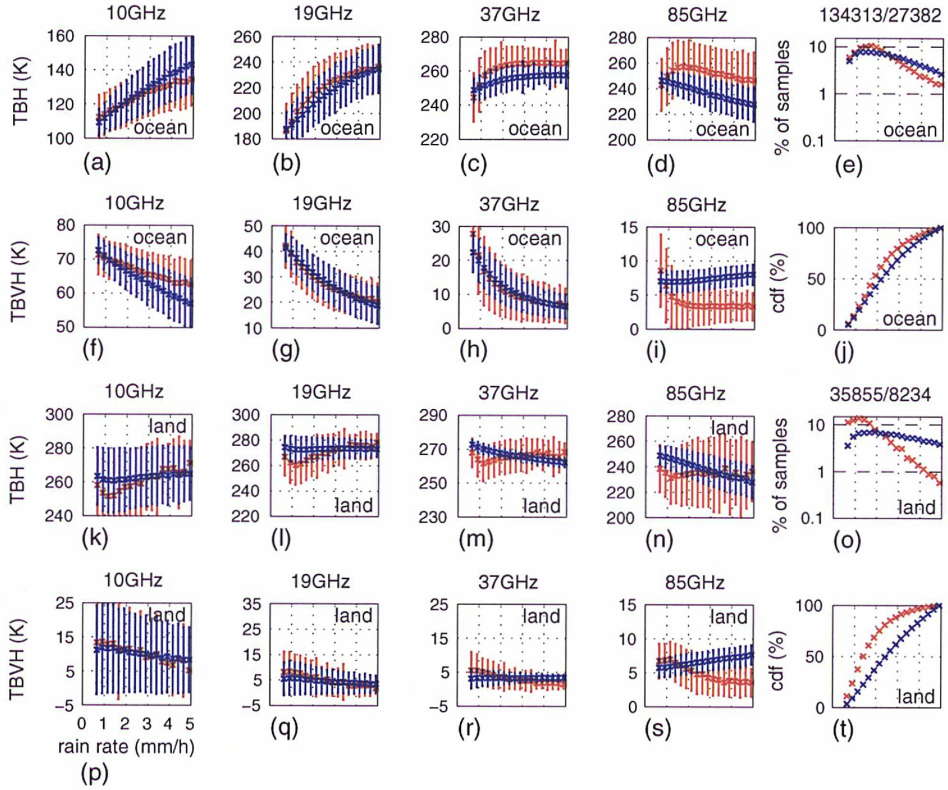

Figure 2. Variations of TMI (a–e, k–o) averaged brightness temperatures (TBH) and (f–j, p–t) averaged polarization differences (TBVH) along with their standard deviations as a function of the averaged rain rate as computed over a 0.2° × 0.2° grid over 2 years for the Tropical region. The 0.2° × 0.2° rain boxes are identified as having at least 20 PR observations with 50% of them being stratiform. Blue (red) represents grid boxes where the bright band (BB) was detected for 100% (0%) of stratiform observations. Figure 2e (Figure 2o) presents the percentages of grid-boxes relative to the total number of grid-boxes (indicated at the top of the panel—with/without BB) that satisfy the selection criteria as a function of rain rate over ocean (land). Their respective cumulative distribution function as a function of rain rate for cases with a BB (blue) and without a BB (red) is shown in Figures 2j and 2t for ocean and land, respectively.

surface and the atmosphere contributions. At 37 and 85 GHz, the variation of the brightness temperatures in presence of BB decreases for an increasing rain rate while the average brightness temperature is more or less constant in stratiform rain without a melting layer. The scattering signal by frozen particles is not only observable at 85 GHz when a melting layer is detected, but also at 37 GHz. Note nevertheless that, as expected, the magnitude of the TB decrease at 37 GHz is much more limited than at 85 GHz. Similar to what is observed over ocean, the polarization difference increases with increasing rain rate. On the average, a polarization difference of 4–5 K is observed for a rain rate of 5 mm/h between cases with and without melting layer.

[13] A sensitivity study (not shown) of the different thresholds over ocean shows that decreasing the percentage of BB for a given rain rate of 85 GHz induces warmer TBs, a decrease of the polarization difference, and a larger standard deviation of both TBs and polarization difference. When one increases the percentage of stratiform pixels, the number of non-BB rain pixels decreases and the averaged brightness temperatures get warmer at 85 GHz.

[14] Figure 3 presents the probability of precipitation cases (precipitation, convective precipitation, stratiform precipitation, and precipitation with BB) at 85 GHz as a function of TBV and TBVH using 2 years of data over both ocean and land, for 1 K × 1 K pairs of TBVH versus TBH. The probability of precipitation is defined as the averaged value of the number of PR pixels identified as precipitation divided by the number of PR observations within the same box. Only cases at least partly precipitating are considered, representing approximately 5% of the total population over both surfaces. In the case of precipitation over ocean (Figure 3a), the vertical branch with large polarization differences corresponds to situations with partial transmission of the surface's polarized signal despite the rain attenuation. The horizontal branch in the scatter plots corresponds to the decreasing TBs associated with the scattering signal of clouds. As expected, the probability of rain increases when the brightness temperatures decrease, i.e., when the convection deepens. Figure 3b (ocean) and Figure 3f (land) further show the percentage of PR pixels identified as convective rain pixels divided by the number

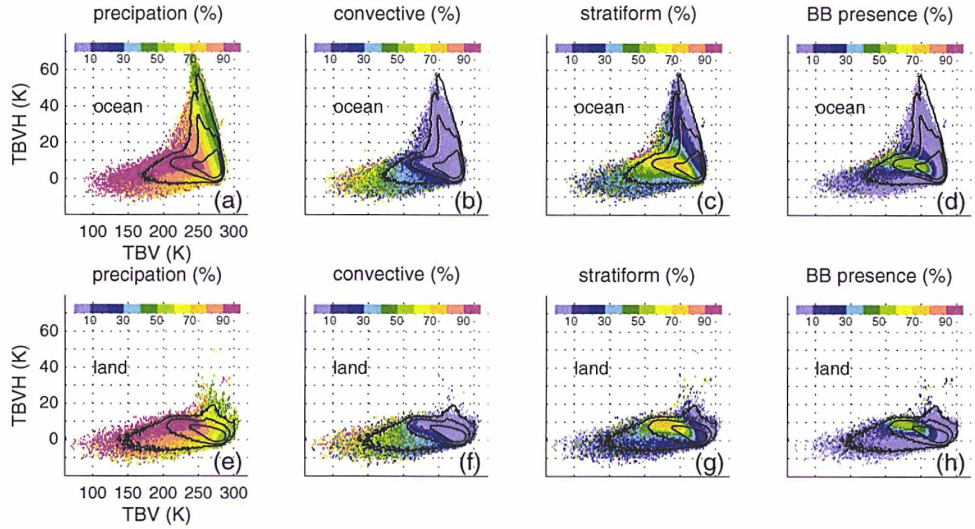

Figure 3. Scatter plot of the polarization difference (TBVH) versus the vertical polarization (TBV) at 85 GHz, for 2006 and 2007 data, over ocean (top) and over land (bottom), of the (a and e) probability of precipitation, of (b and f) convective rain, of (c and g) stratiform rain, and of (d and h) the presence of a BB. Black iso-lines delineate the population that represents 10^{-3}, 10^{-2}, and 0.1% of the total number of samples.

of PR observations within the same box. Colder brightness temperatures are more often observed over land than over ocean, which is consistent with the fact that continental convection is deeper than oceanic convection; deeper convection inducing more ice in the clouds and, consequently, more efficient scattering by large ice particles. Additionally, cold brightness temperatures associated with deep convection can exhibit negative polarization differences. *Prigent et al.* [2005] explain such radiometric behavior by the presence of predominantly vertically oriented graupel located in the convective cores. Convective rain (Figures 3b and 3f) and stratiform rain (Figures 3c and 3g) are clearly reported in two different regions of the TBV/TBVH space over both ocean and land. Convective rain is basically expected where TBVs at 85 GHz are below 250 K with a polarization difference negative or slightly positive. Stratiform rain is statistically dominant for TBV ranging from 200 K to 260 K and a positive TBVH from 5 K. Some basic threshold delimiting the specific regions of the TBVH space could be used as convective/stratiform classification for microwave-based retrieval schemes for TMI, but also for other space missions with similar frequencies and footprints after cross-calibration of the microwave sensors.

[15] For stratiform rain, one can expect a large spatial distribution of the rain field and a relatively homogeneous microwave signal within the box. Brightness temperatures with low percentage of stratiform rain correspond to clouds where there is also convection sampled in the same grid box. Note also that the sum of convective rain probability and stratiform rain probability is not necessarily equal to 100% because some of the PR pixels can be classified as non convective and non stratiform. Finally, Figure 3d (and Figure 3h) presents how the signal at 85 GHz correlates with the presence of BB over ocean (and land). Interestingly the high probability of BB presence spans over a relatively limited domain in the TBVH space around 7 K and, as expected, the high percentage of BB presence corresponds to regions where stratiform rain is also predominantly detected.

[16] For comparison, Figure 4 presents similar plots to Figure 3 but at 37 GHz. Stratiform and convective rains are clearly reported in two separate regions of the TBVH space for both ocean and land. Convective rain is predominantly detected (>70%) for brightness temperatures below 250 K and polarization differences up to 10 K (Figure 4b). Colder brightness temperatures can be recorded over land, because of more intense and therefore deeper convection over surfaces that can undergo strong solar heating. Stratiform rain (Figure 4c) is recorded for a large range of brightness temperatures (220 to 280 K) and a positive polarization difference of up to 40 K. Over land, the distribution peaks lie in a relative narrow area in the TBVH space.

[17] The possible links between the polarized scattering signatures at 85 GHz and the polarized observations in the visible [*Noel and Chepfer*, 2004; *Bréon and Dubrulle*, 2004] have also been investigated (Appendix A), but the relationship between the two phenomena was not conclusive.

4. Modeling the Sensitivity of the Passive Microwave Signal to Changes in Hydrometeor Phases

[18] As discussed, the melting layer is primarily characterized by a change in the particle composition from ice (more precisely a mixture of ice and air) to liquid water. This transformation has multiple impacts in terms of particle size, number concentration, and possibly shape and orientation. Our objective here is to assess qualitatively how changes in hydrometeor dielectric properties impact the polarized scattering signal in passive observations to investigate on the possible link between polarized scattering on the microwave

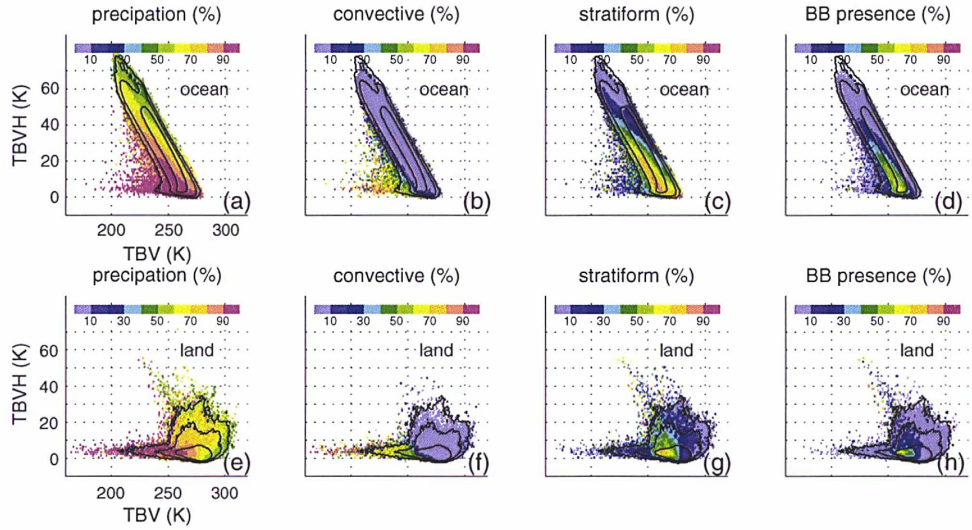

Figure 4. Same as Figure 3 but for 37 GHz.

and the dielectric properties in the BB melting layer. What causes the strongly polarized scattering signal observed at 85 GHz in stratiform situations? How do pure ice and snow compare in terms of scattering at 85 GHz for realistic particle habits? Does the snow wetness enhance the scattering effect and compensate for the decrease in size a melting particle goes through?

4.1. Dielectric Properties

[19] Water, air, and ice coexist in a single particle during the melting process. There is a large number of mixing formulas available to compute the effective dielectric constants of mixed phase hydrometeors and their results vary to a great extent when defining the order of the inclusions, being physically unclear as to how to select among these various formulas. Questions remain as to which of these mixing formulas can be applied to computations of polarimetric parameters from non-spherical melting particles. Furthermore, *Botta et al.* [2010] showed that the scattering behaviors as calculated from effective dielectric properties must be used with caution particularly at millimeter wavelengths. In summary, there are many ways to model the dielectric properties of mixtures which can directly lead to variabilities in the modelled BB effects [*Kollias and Albrecht*, 2005]. A review of the effective dielectric constants of mixed phase hydrometeors is proposed by *Meneghini and Liao* [2000].

[20] *Liao and Meneghini* [2005] insist that the effective dielectric properties of particles in the melting layer are the key problem in the simulation of the bright band signal in the active mode. *Kollias and Albrecht* [2005] assume that the physical model of the melting layer is correct and only test the reflectivity (i.e., the scattering properties) of the corresponding hydrometeor profiles. *Sassen et al.* [2007] argue that the details within the narrow melting layer are not too important because ultimately it is the difference between the scattering properties in the two phases that matters.

[21] *Meneghini and Liao* [2000] reviewed some of the available models and investigated their effect on extinction and backscattering coefficients at radar wavelengths and concluded that the Maxwell Garnett mixing rule for an air-ice mixture in a water matrix compares best to the Fast Fourier Transform numerical method. Since then, the Maxwell Garnett formulation has been commonly used [e.g., *Battaglia et al.*, 2003; *Olson et al.*, 2001a, 2001b]. Under this formulation, the effective dielectric constant (ϵ_{eff}) is

$$\epsilon_{\text{eff}} = \epsilon_{\text{mat}} + 3f\epsilon_{\text{mat}} \frac{(\epsilon_{\text{inc}} - \epsilon_{\text{mat}})}{\epsilon_{\text{inc}} + 2\epsilon_{\text{mat}} - f(\epsilon_{\text{inc}} - \epsilon_{\text{mat}})} \tag{1}$$

where ϵ_{mat} and ϵ_{inc} are the dielectric constants of the matrix and the inclusion phases respectively, and f is the volume fraction of the inclusions. Under the Maxwell Garnett formulation, snow is often described as a two phase mixture of ice-air (dry snow) and water. Its uniform density (ρ_m) varies with the melted fraction f_m, i.e., the volume fraction of water, as

$$\rho_m = \frac{\rho_s \rho_w}{f_m \rho_s + (1 - f_m)\rho_w} \tag{2}$$

where ρ_s and ρ_w are the density of dry snow and water, respectively. However, questions still remain as to how these three-phase mixtures are composed. A variety of different models arises depending on how the inclusion phases are defined, described well in *Fabry and Szyrmer* [1999] and *Brown and Ruf* [2007].

[22] *Olson et al.* [2001a, 2001b] conducted an intercomparison of dielectric models at 10.65, 19.35, 37.0, and 85.5 GHz for melting snow and graupel, showing that the refractive index curves of these hydrometeors were bounded by the Maxwell Garnett water matrix with ice inclusions (MGwi) and the Maxwell Garnett ice matrix with water inclusions (MGiw) model curves. *Olson et al.* [2001a, 2001b] also noted that the refractive indices of snow and graupel are subtly different, and their differences decrease as the meltwater fraction increases, and that overall, particle absorption and scattering efficiencies in these frequencies are enhanced greatly for relatively small meltwater fractions.

[23] In this study we use a model which literature has shown to agree with the average characteristics of the

Table 1. Density (ρ_s(D)) Parameterizations Used[a]

Label	Parameterization	Details
MA	$\rho_s = 0.015D_s^{-1}$	*Fabry and Szyrmer* [1999] relationship, as in *Mitchell et al.* [1990] and averaged for all types of snow.
MB	$\rho_s = 0.012D_s^{-1}$	*Fabry and Szyrmer* [1999] modification of the above relationship.
LH	$\rho_s = 0.015D_s^{-1.18}$	*Locatelli and Hobbs* [1974] relationship with assumptions made in *Fabry and Szyrmer* [1999].

[a]Equations are given in cgs units.

melting layer for long term observations [*Olson et al.*, 2001a, 2001b; *Battaglia et al.*, 2003; *Fabry and Szyrmer*, 1999; *Zawadzki et al.*, 2005]. This model applies equation (1) twice: one time to calculate dry snow (ice inclusions in an air matrix) and a second time to mix dry snow and water (water inclusions of melted volume fraction f_m in a dry snow environment). An important parameter left to define is the density of the snow, well known to decrease rapidly with size. Different relationships are seen in the literature where the upper limit is the density of pure ice (0.917 gcm^{-3}). Here a number of parameterizations found in the literature (see Table 1) are used to define ρ_s in equation (2). The overall density of the wet snow particle then follows equation (2).

4.2. Radiative Transfer Calculations

[24] Radiative properties of the melting layer are sensitive to a large number of parameters, such as the choice of dielectric models, density parameterization, or the integrated water paths (IWP, defined as the hydrometeor, ice, snow, or melting snow, column integrated water mass). Here we attempt to asses the sensitivity to such parameters in passive microwave observations.

[25] The Atmospheric Radiative Transfer Simulator (ARTS) is adopted for the sensitivity analysis. ARTS is a freely available, open source, software package with state-of-the-art gaseous absorption estimation and able to handle scattering (and full account of polarization effects) very efficiently [*Eriksson et al.*, 2011]. The discrete ordinate iterative (DOIT) method is one of the scattering algorithms in ARTS [*Emde et al.*, 2004] and the one used in this study. Tests were also conducted using the Monte Carlo method available in ARTS and similar results were found. The optical (single scattering) properties were calculated using the T-matrix code by *Mishchenko* [2000] which allows the treatment of oriented spheroids. It is important to keep in mind that modeling the optical properties of frozen particles is problematic even for pristine frozen particles that are not undergoing melting. The particle size distribution, the dielectric properties of the material, and the shape of the particle are all subject to large uncertainties that can translate into significant differences in terms of simulated brightness temperatures [e.g., *Surussavadee and Staelin*, 2006; *Meirold-Mautner et al.*, 2006; *Kulie et al.*, 2010].

[26] For the simulations in this study, a given atmospheric profile of temperature, pressure, water vapor, ozone, and height from the *Chevallier et al.* [2006] database was used

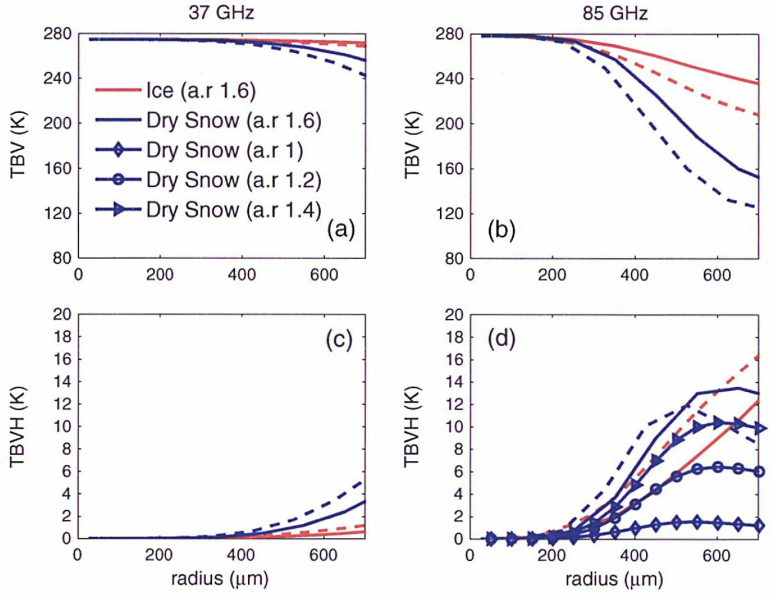

Figure 5. (a and b) The sensitivity of the vertical brightness temperature (TBV) and (c and d) the polarization difference (TBVH) at 37 and 85 GHz to the particle size (effective radius) of horizontally aligned pure ice and dry snow spheroids of aspect ratio 1.6, under different IWPs (solid lines for 0.2 kg/m^2 and dashed lines for 0.4 kg/m^2). Dry snow is composed of ice inclusions in an air matrix such that its density is parameterized by MA in Table 1. Additionally, the simulated polarization difference at 85 GHz for dry snow (0.2 kg/m^2) of different aspect ratios were added in Figure 5d.

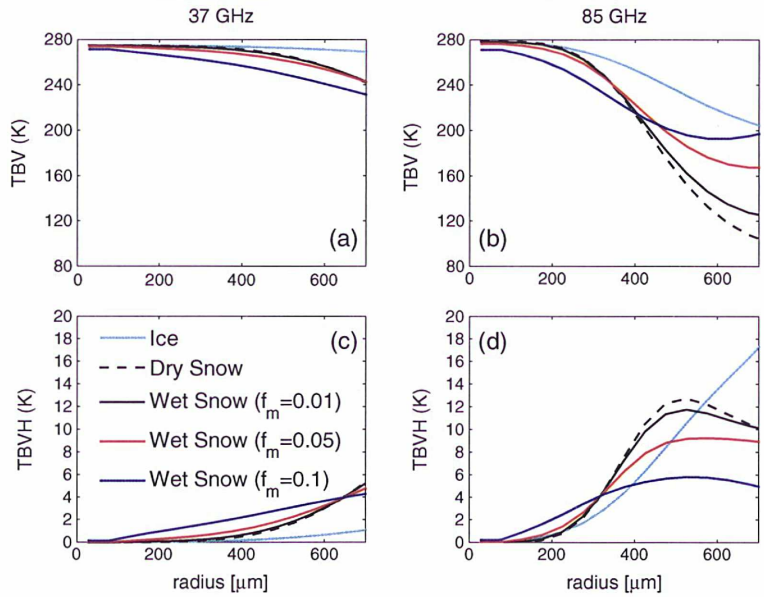

Figure 6. The simulated vertical polarization and polarization difference at 37 and 85 GHz for pure ice and wet snow hydrometeors (air-ice-water mixture) using the Maxwell Garnett mixing rule for a two phase mixture (air and ice) and water. Different melted fractions (f_m) are shown. The IWP is 0.4 kg/m^2.

(atmosphere of 8.3 kg/m^2 of water vapor). The land surface emissivity in the simulations is set to 0.9 for both polarizations and the nadir angle is set to 50°. A single layer (2 km thick) of hydrometeors populates the atmosphere around the 0° isotherm (4 km in altitude) with varying IWP (between 0.1 kg/m^2 and 2 kg/m^2). A mono-disperse particle size distribution of horizontally orientated spheroids was assumed and varied between 50 μm-700 μm (size refers to the size of a mass equivalent sphere).

[27] Simulations with hydrometeor profiles of more realistic characteristics (three plane parallel hydrometeor layers) are also analyzed (now shown). The three layers were composed of the following: (1) a layer of ice particles between 5 and 8 km with an equivalent ice water path of 0.4 kg/m^2 and single-size spherical randomly orientated particles of 150 μm radius; (2) a layer representing the melting layer between 3 and 5 km as described above; and (3) a rain layer of 4 mm/hr between 0 and 3 km containing liquid water, single size spherical randomly orientated particles of 400 μm radius. Such hydrometeor profiles yield similar results in terms of polarization difference at 85 GHz than the melting layer alone. The ice cloud above only adds limited extinction to the signal (a decrease of the polarization difference smaller than 2 K), and the rain below is not observed as the melting layer is quite opaque. We focus thus on the parameters of the particles populating the melting layer relevant to the observed polarized scattering signals described earlier in the presence of a BB, by simplifying the hydrometeor profiles to just the melting layer.

[28] With respect to defining the shape of these hydrometeors for the purpose of modeling the radar bright band at TRMM frequencies, the precise particle shapes are not very important, and scattering properties depend mostly on the overall shape of the particles as determined by the aspect ratio [*Dungey and Bohren*, 1993; *Matrosov et al.*, 2005]. From multiple aircraft observations, Heymsfield (personal communication, 2005) confirms the importance of the bulk aspect of particles as characterized by its aspect ratio, neglecting the simulation of individual complicated particle shapes: aspect ratios (longest/shortest axis of ellipse) of the order of 1.6 close to the 0° isotherm are selected, as suggested in *Korolev and Isaac* [2003]; *Hanesch* [1999]; and *Matrosov et al.* [2005].

[29] Considered in this study are perfectly horizontally aligned particles. Most particles are likely to suffer particle tumbling related to turbulence. The effect of tumbling has already been evaluated in *Prigent et al.* [2001]. *Xie et al.* [2012] showed that horizontally aligned particles behave similarly to oriented particles with a standard deviation of 10°, with TBs and polarization differences deviating less than 0.2 K compared to the perfect horizontal case. In this study, we will concentrate on perfectly horizontally aligned particles, for practical reasons.

[30] *Prigent et al.* [2005, 2001] explained the observed polarized scattering signal of pristine ice habits in terms of particle shape and orientation, where simulations with randomly oriented, large spheroidal particles cannot replicate the observed polarization differences at 85 GHz, but oriented non-spherical particles can. Following these studies, Figures 5a and 5b (resp. Figures 5c and 5d) show the vertical brightness temperature, TBV, (resp. polarization differences, TBVH) for 37 and 85 GHz as a function of particle size for pristine, horizontally distributed ice (ρ=0.917 kg/m^3) of aspect ratio 1.6. As expected, the TBVs decrease with increasing particle size, especially at 85 GHz: the larger the IWP, the larger the depression. In terms of the polarization signal, differences at 85 GHz also increase with increasing particle size and with increasing IWP. To evaluate the sensitivity of the scattering signal to particle composition, Figure 5 also shows the TBV and TBVH for dry snow

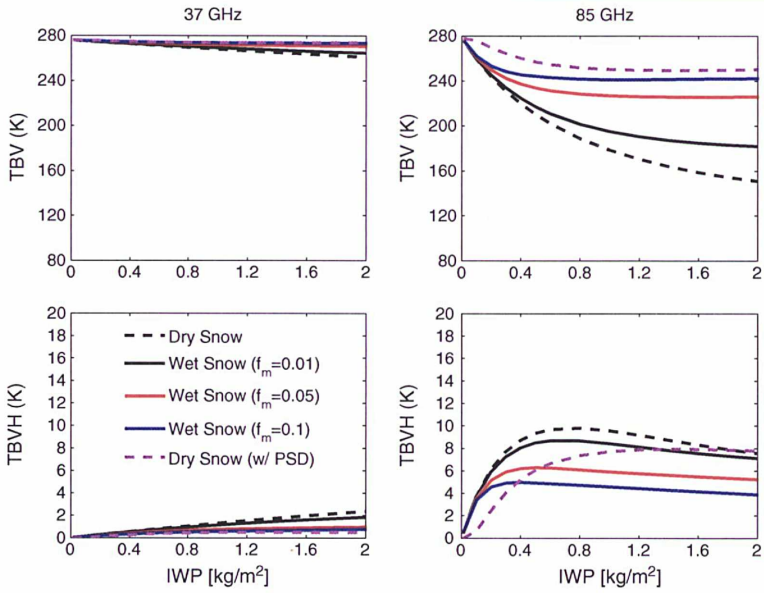

Figure 7. The simulated vertical polarization and polarization differences at 37 and 85 GHz for dry snow as a function of IWP for a particle of 400 μm. The radiative properties of the wet snow hydrometeors under different melted fractions (f_m) were simulated for the particle number concentration calculated for dry snow and their size allowed to decrease to conserve the IWP. The simulated vertical polarization and polarization differences for dry snow with the SS PSD applied is also shown.

(i.e., a mixture of air and ice). The dielectric properties for dry snow were calculated using ice inclusions in an air matrix, but it is worth noting that using air inclusions in a matrix of ice yielded very similar results (not shown). The volume fraction of the ice inclusions was determined by applying the density parameterization from *Mitchell et al.* [1990] (see Table 1) to the snowflake diameter (ρ_{ds}(D)). Using the other parameterizations listed in Table 1 yielded very similar results, with differences in TBVH of the order of 1 K and in TBV of the order of 2 K at 85 GHz. Figure 5 evidences that the scattering is much more important at 85 GHz than that at 37 GHz for both pristine ice and dry snow hydrometeors, while comparing pristine ice with dry snow shows that dry snow has enhanced the scattering and the polarization differences. For large particles of dry snow that have a large scattering effect (TBVs lower than 160 K), TBVH reaches a limit where multiple scattering effects become significant and TBVH approaches a saturation limit and starts decreasing. For higher IWPs, the TBVH saturation limit is approached with smaller particle sizes. It is important to keep in mind, however, that a comparison between ice and dry snow equal size particles takes into account a decrease in density in the dry snow particles: this decrease in density translates into an increase in the particle number concentration. Clearly, for a given particle size, the increase of particle number increases the scattering effect, as well as the polarization difference. Due to this effect, Figure 5 evidences how important density can be as a parameter, specially at 85 GHz. Note that in Figure 5d, TBVH for dry snow particles (IWP=0.2 kg/m^2) of aspect ratios of 1, 1.2, and 1.4 are also shown for comparison.

[31] Figure 6 explores the effect of snow wetness by including different melted fractions (f_m) in the ice-air-water mixture for an IWP of 0.4 kg/m^3. In the case of wet snow, since the integrated ice water path is maintained constant for a given particle size, an increase in melting fraction leads to an increase in density and to a decrease in particle number concentration. For realistically large particle sizes, when the melted fraction increases, the simulated TBV depressions and polarization differences are more limited. Tests were also run to evaluate the sensitivity of wet snow to the choice of $\rho_s(D)$ when calculating the dielectric properties of its dry snow matrix. This sensitivity was observed in the simulations to be not larger than 2 K for both TBVH and TBV at 85 GHz. In a cloud during the melting process, the transition from dry snow to melting snow does not induce a change of particle number concentration but a change in particle size, with the melting particle being smaller than the dry snow particle of the same mass. Figure 7 tests the effect of the melting fraction (f_m) for a given IWP, when conserving the particle number concentration. For each value of IWP and each hydrometeor phase, the particle number concentration is calculated for dry snow particles of 400 μm effective radius. For the wet hydrometeors simulated, in order to conserve IWP with the number concentration fixed to that of dry snow, their size is allowed to decrease. Figure 7 illustrates that for a given value of IWP and for a given particle number concentration, the change in dielectric properties from dry to wet snow does not compensate for the reduction in particle size that occurs in the melting layer.

[32] The simulations discussed so far with a monodisperse particle size distribution assess qualitatively the impact of hydrometeor dielectric properties on the polarization signal. In order to investigate more realistic clouds that contain particles of different size, the radiative transfer calculations for horizontally aligned ice particles were

repeated assuming an exponential particle size distribution for dry snow from *Sekhon and Srivastava* [1970]. The resulting magnitude of the depolarization (5–10 K) is comparable to the fixed particles size (Figure 7) and to the observed one (Figure 3). Then repeating the radiative transfer calculations with the *McFarquhar and Heymsfield* [1997] PSD parameterization for the same IWP range produces a maximum depolarization signal of approximately 3 K at 85 GHz (not shown).

[33] These simulations show that horizontally oriented oblate dry snow particles can generate the scattering signatures observed at 85 GHz, with polarization differences of the order of 5 K and higher. For a given IWP and particle size, dry snow is more efficient than pure ice at scattering and at generating polarized scattering at 85 GHz: the decrease in the real part of the refractive index from pure ice to dry snow, a mixture of ice and air, is largely compensated by the increase in particle number as a result of the lower density of dry snow. Melting of the snow does not enhance the brightness temperature depression nor the polarization difference. The changes in the real part of the refractive index from dry snow to melting snow do not compensate for the decrease in particle size that occurs with the melting of the particle.

5. Conclusion

[34] Scattering at 85 GHz over clouds is often associated with significant polarization differences (TBVH > 5 K), both over land and ocean. Coincident passive and active observations from TRMM show that a large portion of polarized scattering tends to occur when the radar observes a bright band, i.e., in the presence of a melting layer. The scattering signal by frozen particles is not only observable at 85 GHz when a melting layer is detected, but also at 37 GHz. Note nevertheless that, as expected, the magnitude of the TB decrease at 37 GHz is much more limited than at 85 GHz. Aggregation of snow particles around the 0°C isotherm produces large flakes that can significantly scatter the microwave. Our simulations show that the observations with TMI that coincide with a detected bright band on the PR can be interpreted in terms of dry snow particles of oblate bulk shapes with aspect ratios of the order of 1.6, and with horizontal orientation. The melting of the large snow flakes does not appear to increase the scattering effects.

[35] The sensitivity of passive microwave polarized scattering to the shape and orientation of the hydrometeors is unique among the current observations: it is an unexpected tool to gain understanding in complex microphysical processes in clouds.

[36] The presence of a melting layer can be deduced from the analysis of the polarized scattering signal, as shown in this study, with a rather stable relationship in the TBV and TBVH space when a radar bright band is observed. Neglecting the effect of the melting layer in the retrieval has been shown to lead to an overestimation of the precipitation for light stratiform rain [*Brown and Ruf*, 2007], a key issue in mid-latitude regions where the majority of the precipitation has a low freezing level. The Global Precipitation Measuring (GPM) mission will extend the TRMM capacity outside the Tropics to global and more frequent observations. Outside the regions where both passive and active observations from GPM will be available, the polarized scattering signal around 85 GHz can indicate the presence of the melting layer and will allow to redirect the retrieval scheme towards a more realistic precipitation scheme over land and ocean.

[37] The French-Indian Megha-Tropiques mission, launched in October 2011, carries a passive microwave conical scanner with polarized measurements at 18.7, 23.8, 36.5, 89, and 157 GHz. Analysis of the polarized scattering signal at 157 GHz is expected to begin soon: with a better sensitivity to the scattering by the ice phase, it will likely bring new insight into the cloud microphysics. These studies are also important in the framework of the development of the Ice Cloud Imager (ICI) for the next generation of European weather satellites, MetOp Second Generation (MetOp-SG). ICI is a radiometer planned to cover frequencies from 183 GHz up to 664 GHz.

Appendix A: Possible Links Between the Polarized Scattering Signatures at 85 GHz, and the Polarized Observations in the Visible

[38] The study was extended to a comparison of concurrent A-TRAIN observations of AMSR-E (Advanced Microwave Scanning Radiometer for EOS) and PARASOL instruments. The AMSR-E radiometer measures the microwave signal at 6.925, 10.65, 18.7, 23.8, 36.5, and 89.0 GHz. The PARASOL instrument, called POLDER (Polarization and Directionality of the Earth Reflectances) is a wide-field imaging radiometer/polarimeter [*Deschamps et al.*, 1994] that operates in the 443–1020 nm range with some polarized bands (443, 670, and 865 nm) [*Bréon and Dubrulle*, 2004]. PARASOL observations can be used to detect the sun glint, i.e., the reflection of the sun light in the visible and near infrared not only by the ice crystals located in the upper part of the clouds [*Noel and Chepfer*, 2004; *Bréon and Dubrulle*, 2004] but by lakes, oceans, or deserts. Some properties of the ice crystals that induce the sun glint such as their orientation can be deduced from PARASOL observations as well [*Noel and Chepfer*, 2004; *Bréon and Dubrulle*, 2004].

[39] The analysis was performed for all ascending orbits of 2006, i.e., daytime orbits over the 40°S–40°N latitude range. The method consists first in identifying and locating the sun glint in each PARASOL frame and, second, in deriving the properties of the ice crystals from the optical radiation measured at the sun glint locations. The radiometric signal at 89 GHz in V and H polarization comes from (almost) time-coincident AMSR-E observations measured at the nearest AMSR-E beam to the sun glint location pinpointed by PARASOL. The radiometric signal measured where sun glint occurs was investigated for ocean and land separately. It turns out that no specific radiometric signature at 89 GHz appears to be associated with sun glint. Indeed sun glint was detected in cloud regions characterized by a large range of brightness temperatures at 89 GHz (from 100 to 260 K). The absence of a specific radiometric signal associated with sun glint can be explained by the fact that even if horizontally oriented ice crystals are located at the top of the clouds, they can induce the sun glint measured by PARASOL, while the 89 GHz signal measured by AMSR-E is sensitive to a larger depth of hydrometeors below the

cloud top. However, submillimeter wave radiometers in conjunction with sun glint detection instruments should be used to study the properties of cloud ice and the interaction between hydrometeor orientation and polarization in the upper part of the clouds.

[40] **Acknowledgments.** The community behind ARTS is appreciated for providing an open source software, with a special thanks to Stefan Buehler for valuable advice. We would like to thank Andy Heymsfield and Jean-Pierre Pinty for carefully reading the manuscript and for their thoughtful comments. We are grateful to Francois-Marie Bréon for providing sun glint reports from PARASOL measurements and for fruitful discussions. The TRMM data were downloaded from the GSFC DAAC data center.

References

Armstrong, R. L., and M. J. Brodzik (2005), Northern hemisphere EASE-grid weekly snow cover and sea ice extent version 3 (Boulder, CO: National snow and ice data center, Digital Media), accessed May 2010 at http://nsidc.org/data/nsidc-0046.html.

Awaka, J., T. Iguchi, H. Kumagai, and K. I. Okamoto (1997), Rain type classification algorithm for TRMM precipitation radar, *Geoscience and Remote Sensing, 1997. IGARSS'97. Remote Sensing-A Scientific Vision for Sustainable Development*, vol. 4, pp. 1633–1635.

Battaglia, A., C. Kummerow, D.-B. Shin, and C. Williams (2003), Constraining microwave brightness temperatures by radar bright band observations, *J. Atmos. Oceanic Technol.*, *20*, 856–871.

Bauer, P., J. P. V. Poiares Baptista, and M. de Iulis (1999), The effect of the melting layer on the microwave emission of clouds over the ocean, *J. Atmos. Sci.*, *56*, 852–867.

Bauer, P., A. Khain, A. Pokrovsky, R. Meneghini, C. Kummerow, F. Marzano, and J. P. V. Poiares Baptista (2000), Combined cloud-microwave radiative transfer modeling of stratiform rainfall, *J. Atmos. Sci.*, *57*, 1082–1104.

Berg, W., T. L'Ecuyer, and J. M. Haynes (2010), The distribution of rainfall over oceans from spaceborne radars, *J. Appl. Meteorol. Clim.*, *49*, 535–543.

Botta, G., K. Aydin, and J. Verlinde (2010), Modeling of microwave scattering from cloud ice crystal aggregates and melting aggregates: A new approach, *IEEE Geosci. and Remote Sens. Lett.*, *7*, 572–576.

Bréon, F.-M., and B. Dubrulle (2004), Horizontally oriented plates in clouds, *J. Atmos. Sci.*, *61*, 2888–2898.

Brown, S. T., and C. S. Ruf (2007), Validation and development of melting layer models using constraints by active/passive microwave observations of rain and the wind-roughened ocean surface, *J. Atmos. Oceanic Technol.*, *24*, 543–563.

Chevallier, F., S. Di Michele, and A. P. Mc Nally, (2006), Diverse profile datasets from the ECMWF 91-level short-range forecasts, *Technical report, NWP SAF satellite application facility for numerical weather prediction*, Document no. NWPSAF-EC-TR-010, Version 1.0.

Cunningham, R. M. (1947), A different explanation of the bright line, *J. Meteor.*, *4*, 163.

Deschamps, P.-Y., F.-M. Breon, M. Leroy, A. Podaire, A. Bricaud, J.-C. Buriez, and G. Seze (1994), The POLDER mission: Instrument characteristics and scientific objectives, *IEEE Trans. Geosci. and Remote Sensing*, *32*, 598–615.

Di Girolamo, P., B. B. Demoz, and D. N. Whiteman (2003), Model simulations of melting hydrometeors: A new bright band from melting frozen drops, *Geophys. Res. Lett.*, *30*(12), 1626, doi:10.1029/2002GL016825.

Dungey, C. E., and C. F. Bohren (1993), Backscattering by non-spherical hydrometeors as calculated by the coupled-dipole method: An application in radar meteorology, *J. Atm. Oceanic Technol.*, *10*, 526–532.

Emde, C., S. A. Buehler, C. Davis, P. Eriksson, T. R. Sreerekha, and C. Teichmann (2004), A polarized discrete ordinate scattering model for simulations of limb and nadir longwave measurements in 1D/3D spherical atmospheres, *J. Geophys. Res.*, *109*, D24207, doi:10.1029/2004JD005140.

Eriksson, P., S. A. Buehler, C. P. Davis, C. Emde, and O. Lemke (2011), ARTS, the atmospheric radiative transfer simulator, Version 2, *J. Quant. Spectrosc. Radiat. Transfer*, *112*, 1551–1558.

Fabry, F., and W. Szyrmer (1999), Modeling of the melting layer. Part II: Electromagnetic, *J. Atmos. Sci.*, *56*, 3593–3600.

Hanesch, M. (1999), Fall velocity and shape of snowflakes, Dissertation ETH No 13322, Swiss Federal Institute of Technology, Zurich.

Iguchi, T., T. Kozu, R. Meneghini, J. Awaka, and K. Okamoto (2000), Rain-profiling algorithm for the TRMM precipitation radar, *J. Appl. Meteor.*, *39*, 2038–2052.

Kollias, P., and B. Albrecht (2005), Why the melting layer radar reflectivity is not bright at 94 GHz, *Geophys. Res. Lett.*, *32*, L24818, doi:10.1029/2005GL024074.

Korolev, A., and G. Isaac (2003), Roundness and aspect ratio of particles in ice clouds, *J. Atmos. Sci.*, *60*, 1795–1808.

Kummerow, C., W. Barnes, T. Kozu, J. Shiue, and J. Simpson (1998), The tropical rainfall measuring mission (TRMM) sensor package, *J. Atmos. Oceanic Technol.*, *15*, 809–817.

Kummerow, C., et al. (2000), The status of the tropical rainfall measuring mission (TRMM) after two years in orbit, *J. Appl. Meteor.*, *39*, 1965–1982.

Kulie, M. S., R. Bennartz, T. J. Greenwald, Y. Chen, and F. Weng (2010), Uncertainties in microwave properties of frozen precipitation: Implications for remote sensing and data assimilation, *J. Atmos. Sci.*, *67*, 3471–3487.

Matrosov, S. Y., A. J. Heymsfield, and Z. Wang (2005), Dual-frequency radar ratio of nonspherical atmospheric hydrometeors, *Geophys. Res. Lett.*, *32*, L13816, doi:10.1029/2005GL023210.

McFarquhar, G. M., and A. J. Heymsfield (1997), Parameterization of tropical cirrus ice crystal size distributions and implications for radiative transfer: Results from CEPEX, *J. Atmos. Sci.*, *54*, 2187–2200.

Meirold-Mautner, I., C. Prigent, E. Defer, J. R. Pardo, J.-P. Chaboureau, J.-P. Pinty, M. Mech, and S. Crewell (2006), Radiative transfer simulations using mesoscale cloud model outputs: Comparisons with passive microwave and infrared satellite observations for midlatitudes, *J. Atmos. Sci.*, *64*, 1550–1568.

Meneghini, R., and L. Liao (1996), Comparisons of cross sections for melting hydrometeors as derived from dielectric mixing formulas and a numerical method, *J. Appl. Meteor.*, *35*, 1658–1670.

Meneghini, R., and L. Liao (2000), Effective dielectric constants of mixed-phase hydrometeors, *J. Atmos. Oceanic Technol.*, *17*, 628–640.

Mishchenko, M. I. (2000), Calculation of the amplitude matrix for a nonspherical particle in a fixed orientation, *Appl. Opt.*, *39*, 1026–1031.

Mitchell, D. L., R. Zhang, and R. L. Pitter (1990), Mass-dimensional relationships for ice particles and the influence of riming on snowfall rates, *J. Appl. Meteor.*, *29*, 153–163.

Mitra, S. K., O. Vohl, M. Ahr, and H. R. Pruppacher (1990), A wind tunnel and theoretical study of the melting behavior of atmospheric ice particles. IV: Experiment and theory of snowflakes, *J. Atmos. Sci.*, *47*, 584–591.

Mohr, K. I., J. S. Famiglietti, and E. J. Zipser (1999), The contribution to tropical rainfall with respect to convective system type, size, and intensity estimated from the 85-GHz ice-scattering signature, *J. Appl. Meteor.*, *38*, 596–606.

Noel, V., and H. Chepfer (2004), Study of ice crystal orientation in cirrus clouds based on satellite polarized radiance measurements, *J. Atmos. Sci.*, *61*, 2073–2081.

Liao, L., and R. Meneghini (2005), On modeling air/spaceborne radar returns in the melting layer, *IEEE Trans. Geo. Remote Sens.*, *43*, 2799–2809.

Liao, L., and R. Meneghini (2009), Validation of TRMM precipitation radar through comparison of its multiyear measurements with ground-based radar, *J. Appl. Meteor. Climatol.*, *48*, 804–817.

Locatelli, J. D., and P. V. Hobbs (1974), Fall speeds and masses of solid precipitation particles, *J. Geophys. Res.*, *79*(15), 2185–2197, doi:10.1029/JC079i015p02185.

Olson, W. S., P. Bauer, N. F. Viltard, D. E. Johnson, W.-K. Tao, R. Meneghini, and L. Liao (2001a), A melting-layer model for passive/active microwave remote sensing applications. Part I: Model formulation and comparison with observations, *J. Appl. Meteor.*, *40*, 1145–1163.

Olson, W. S., P. Bauer, C. D. Kummerow, Y. Hong, and W. K. Tao (2001b), A melting-layer model for passive/active microwave remote sensing applications. Part II: Simulation of TRMM observations, *J. Appl. Meteorol.*, *40*, 1164–1179.

Prigent, C., J. R. Pardo, M. I. Mishchenko, and W. B. Rossow (2001), Microwave polarized scattering signatures in clouds: SSM/I observations interpreted with radiative transfer simulations, *J. Geophys. Res*, *106*, 28,243–28,258.

Prigent, C., E. Defer, J. R. Pardo, C. Pearl, W. B. Rossow, and J.-P. Pinty (2005), Relations of polarized scattering signatures observed by TRMM microwave instrument with electrical processes in cloud systems, *Geophys. Res. Lett.*, *32*, L04810, doi:10.1029/2004GL022225.

Sassen, K., S. Matrosov, and J. Campbell (2007), CloudSat spaceborne 94 GHz radar bright bands in the melting layer: An attenuation-driven upside-down lidar analog, *Geophys. Res. Lett.*, *34*, L16818, doi:10.1029/2007GL030291.

Schols, J. L., J. A. Weinman, G. D. Alexander, R. E. Stewart, L. J. Angus, and A. C. L. Lee (1999), Microwave properties of frozen precipitation around a North Atlantic Cyclone, *J. Appl. Meteor.*, *38*, 29–43.

Sekhon, R. S., and R. C. Srivastava (1970), Snow size spectra and radar reflectivity, *J. Atmos. Sci.*, *27*, 299–307.

Schumacher, C., and R. A. Houze Jr. (2000), Comparison of radar data from the TRMM satellite and Kwajalein Oceanic validation site, *J. Appl. Meteorol.*, *39*, 2151–2164.

Surussavadee, C., and D. H. Staelin (2006), Comparison of AMSU millimeter-wave satellite observations, MM5/TBSCAT predicted radiances, and electromagnetic models for hydrometeors, *IEEE Trans. Geo. Remote Sens.*, *44*, 2667–2678.

Willis, P. T., and A. J. Heymsfield (1989), Structure of the melting layer in mesoscale convective system stratiform precipitation, *J. Atmos. Sci.*, *46*, 2008–2025.

Xie, X., U. Lhnert, S. Kneifel, and S. Crewell (2012), Snow particle orientation observed by ground-based microwave radiometry, *J. Geophys. Res.*, *117*, D02206, doi:10.1029/2011JD016369.

Xie, X., and J. Miao (2011), Polarization difference due to nonrandomly oriented ice particles at millimeter/submillimeter waveband, *J. Quant. Spectrosc. Ra.*, *112*, 1090–1098.

Zawadzki, I., W. Szyrmer, C. Bell, and F. Fabry (2005), Modeling of the melting layer. Part III: The density effect, *J. Atmos. Sci.*, *62*, 3705–3723.

Paper B

First observations of polarized scattering over ice clouds at close-to-millimeter frequencies (157 GHz) with MADRAS on board the Megha-Tropiques mission

Authors:
E. Defer, V. S. Galligani, and C. Prigent

Reformatted version of paper submitted to:
JOURNAL OF GEOPHYSICAL RESEARCH: ATMOSPHERES, 2013

First observations of polarized scattering over ice clouds at close-to-millimeter frequencies (157GHz) with MADRAS on board the Megha-Tropiques mission

Eric Defer, Victoria Galligani, Catherine Prigent, and Carlos Jimenez

LERMA – CNRS/Observatoire de Paris

Submitted to JGR-Atmosphere

Corresponding Author: Eric Defer

eric.defer@obspm.fr

LERMA – CNRS/Observatoire de Paris

61 avenue de l'Observatoire

75014 Paris

France

Phone : +33 1 40 51 2135

Fax : +33 1 40 51 2002

Key points

1 - Cloud scattering induces polarization difference of the order of 10K at 157GHz

2 - Particle orientation must be considered in rain and cloud microwave retrievals

3 - MADRAS 89 and 157 GHz noises are in agreement with the required specifications

Index Terms and keywords

1) Remote sensing

2) Radiative processes

3) Clouds and aerosols

Abstract

Polarized scattering over ice clouds is investigated for the first time up to 157 GHz, based on the passive microwave observations of the MADRAS instrument on board the Indo-French Megha-Tropiques space-based mission. Compared to the 89 GHz channels, the 157 GHz channels offer the possibility to further characterize more the horizontal structure of the clouds and their cloud properties responsible for the observed scattering. The MADRAS noise levels at 89 and 157 GHz are in agreement with the required specifications of the mission. The analysis of the radiometric signal at 157 GHz reveals that the cloud scattering can induce a polarization difference of the order of 10 K at that frequency. Based on radiative transfer modelling the specific signature is interpreted as the effect of mainly horizontally oriented ice cloud particles. This then suggests that the effects of the cloud particle orientation should be considered in rain and cloud retrievals using passive microwave radiometry.

48 **Introduction**

49 Satellite remote sensing at millimeter waves has been proved to show a high sensitivity to
50 the cloud ice phase [Evans et al., 1998; Buehler et al., 2007; Jimenez et al., 2007; Defer et al.,
51 2008]. This led to the recent decision of having an Ice Cloud Imager (ICI) at frequencies between
52 160 to 660 GHz on board the next generation of operational satellites in Europe (MetOp-NG).

53 Within this framework, understanding and quantifying the scattering signals from ice
54 clouds, and more generally the frozen phase, at millimeter waves is a necessity for an optimal
55 retrieval of the ice cloud characteristics from the future satellite measurements. The interaction of
56 millimeter radiation with frozen hydrometeors is complex and involves not only the ice quantities
57 but also the size distribution of the particles, their dielectric properties, their shapes, and their
58 orientation.

59 Polarized scattering signals from the frozen phase have been evidenced up to 90 GHz,
60 from measurements with conical scanners such as the Special Sensor Microwave Imager (SSM/I)
61 or Tropical Rainfall Measurement Mission (TRMM) Microwave Imager (TMI) [Prigent et al.,
62 2001, 2005; Galligani et al., 2013]. It has been shown that this polarized scattering can be
63 explained by the interaction of the radiation with non-spherical and oriented particles and can
64 bring insight into the cloud microphysics. Up to recently, polarized measurements over 90 GHz
65 were not available. Current satellite observations are provided up to 190 GHz, but in cross track
66 mode without separate measurements of the orthogonal polarized signals.

67 Megha-Tropiques (MT) is a collaborative satellite mission, developed by ISRO (Indian
68 Space Research Organization) and CNES (Centre National d'Etudes Spatiales). The Indo-French
69 satellite, launched in 2011, carries several instruments, including a microwave imager MADRAS
70 (Microwave Analysis and Detection of Rain and Atmospheric Structures) and a microwave
71 sounder SAPHIR (Sondeur Atmosphérique du Profil d'Humidité Intertropicale par Radiométrie).
72 MADRAS is a conical scanner with frequencies between 19 and 157 GHz. Both orthogonal
73 polarizations are measured for most frequencies, including at 157 GHz. In this study, polarized
74 scattering over ice clouds is observed from satellite and analyzed for the first time at a frequency
75 above 100 GHz.

76 The MADRAS instrument is briefly described, insisting on the sensitivity of the high
77 frequency channels (section 1). The observed polarized scattering over ice clouds is then
78 analyzed with special attention to its frequency dependence (section 2). Radiative transfer
79 simulations help interpret the observations (section3). Section 4 concludes this study.

80

81 **1. MADRAS on board Megha-Tropiques**

82 The objective of the MT mission is to study the water cycle in the intertropical region, and
83 to evaluate its influence on the energy budget [Desbois et al., 2007]. The MT satellite was
84 successfully launched by ISRO from Sriharikota launch pad (India) and put on a circular orbit at
85 865 km, inclined by 20° to the equator. Thanks to this low inclined orbit, MT is providing
86 valuable observations over the tropics, between latitudes of +/-23° and is part of the Global
87 Precipitation Mission (GPM) constellation. MT carries two microwave instruments: SAPHIR, a
88 cross track humidity sounder with 6 channels around the H_2O line at 183 GHz, and a conical
89 imager an incidence angle of 53.5°, MADRAS, with frequencies at 18.7, 23.8, 36.5, 89 and 157

GHz for both orthogonal polarizations (except at 23.8 GHz that is vertical only) [Karouche and Raju, 2010].

Table 1 lists the different specifications of the MADRAS instrument including the required and goal noises set to 2.6 K and 2 K, respectively at 157 GHz [Goldstein and Karouche, 2013]. Analysis performed by CNES on in-flight records indicated better sensitivity than the requirements (as listed in Table 1), with even better performances compared to the assessment performed on ground during integration at ISRO, due to in flight vacuum pressure [Goldstein and Karouche, 2013]. Details on CNES flight tests and calibration as well as long term monitoring of MT payloads are available at http://smsc.cnes.fr/MEGHAT/Fr/A_recette_vol.htm.

The MADRAS V05 dataset studied here covers an observational period of the instrument from 13 October 2011 to 01 February 2013 by considering the MADRAS records (on the daily basis) every five days during the investigated period. Unfortunately, due to a serious anomaly observed in MADRAS mechanisms, since February 2013, the instrument is no longer operational and providing data.

2. Analysis of the MADRAS observations over ice clouds

An example of MADRAS observations is shown in Figure 1, over both ocean and land, over the south east coast of Africa, at 36, 89, and 157 GHz, for the vertical polarization (left) and for the polarization difference (right). The ocean surface emissivities are rather low and polarized, contrarily to the land that usually has a high emissivity with very limited polarization. For low atmospheric opacity at lower frequencies, the contrast between ocean and land is large. At 157 GHz, the atmospheric opacity in these tropical regions almost completely masks the surface signal. Note the differences in spatial resolution from 36 GHz to 157GHz, with rather blurred structures at 36 GHz as compared to the higher frequencies. At 36 GHz, the liquid water emission in the clouds induces an increase of the brightness temperatures (TB) over ocean but a decrease over the highly emitting land. The cloud emission also induces a decrease of the polarized surface emissions over ocean (Figure 1b). The observed large polarized signature over land at 37 and 89 GHz does not correspond to cloud structures, but to water surfaces (e.g. lake Malawi between 14S-10S and 34E-35E, lake Rukwa centered on 8S and 32E, or the south part of the lake Tanganyika around 7S and 35E). At 157 GHz, the cloud structure appears cold over both ocean and land, with low TBs, often much lower than the cloud temperature itself (down to 80 K on this example). This is due to scattering by the cloud ice phase. The low TBs are also associated to an increase in the signal polarization (Figure 1f). This cannot be due to the surface contribution, as the cloud free areas at 157 GHz do not show any polarization. Polarized signal of the order of 10 K cannot be generated either by scattering from spherical particles. However, as already observed close to 85 GHz, non-spherical horizontally aligned particles can generate significant positive polarized signal [Prigent et al., 2001; Prigent et al., 2005; Galligani et al., 2013]. These first polarized measurements at 157 GHz from MADRAS tend to show that polarized scattering is in clouds very common at 157 GHz, with even larger polarization than at 89 GHz, as could be expected from the interpretation of the polarized signal below 100 GHz.

Figures 2 and 3 show almost coincident TRMM and MADRAS observations in two zones of interest of Figure 1 (TRMM observed the same region about 6 min after MT). Comparison of MADRAS and TMI records is discussed in the Annex. Additional TRMM instruments are considered here: it includes the Precipitation Radar (PR) and the Visible and Infrared Scanner

(VIRS). Figure 2 focuses on deep convective clouds that exhibit significant cold TBs at 89 and 157 GHz (Figure 2a,c). As expected the radiation at 157 GHz emanates not only from the convective cloud regions as mapped at 89 GHz but also from adjacent thick anvils and thick clouds (figure 2c,e). The 157 GHz channels then offer the possibility to characterize further more the horizontal structure of the clouds and their inner properties at the origin of the scattering. The difference of polarization at 157 GHz tends to be of the order of 7-9 K (resp. close to 0 K) in thick clouds (resp. convective cores) (figure 2d).

Figure 3 zooms on another region of Figure 1 that was also sampled by TRMM PR (Figure 3f). Compared to Figure 2, the sampled clouds are less convective but the radiometric responses at 89 and 157 GHz are coherent between each other and with the IR records (Figure 3e). Except for few PR pixels, the precipitation measured along the PR swath was stratiform with the presence of bright band (not shown). The 157 GHz polarization difference exceeds 7 K in the precipitating clouds and maps a more extended area than at 89 GHz (Figure 3d,e).

Figure 4 presents scatterplots of the MADRAS brightness temperature polarization differences (TBVH) versus the brightness temperatures in vertical polarization (TBV). The plot is performed from 14 days out of the 84-day uploaded MADRAS dataset: these observations passed additional in-house verification performed on the radiometric signals at 89 GHz and 157 GHz. The ocean and land cases are treated separately, and for each 1 K by 1 K box the color indicates the relative number of pixels, with respect to the total for a given type of surface. Due to the different sampling rates, the number of quality-controlled samples at 157 GHz should approximately doubles the number of quality-controlled samples at lower frequencies. The emission and scattering regimes can be easily distinguished, especially over ocean. At 36, 89, and 157 GHz, clear sky and thin clouds have low TBV with significant polarization difference (the lower the frequency, the larger the polarization difference) but when the cloud opacity increases, TBV increases and the polarization difference decreases. At 157 GHz, even under clear sky condition, the opacity related to the water vapour can be high (large TBV) and masks the polarized surface signal (low TBVH). At 89 and 157 GHz, in presence of clouds with frozen hydrometeors, TBV decreases due to scattering by ice particles and can reach very low values.

Derived from Figure 4, Figure 5 represents the most probable polarization difference at 89 and 157 GHz versus TBV in the scattering regime for ocean and land separately. Ten percent of the TBV records are below 217 K for sea and land at 89 GHz and below 180 and 182 K over sea and land respectively at 157 GHz. With decreasing TBV, the polarization signal clearly increases up to 6-7 K at 89 GHz (Figures 5a and 5b), and up to 9-10 K at 157 GHz (Figures 5c and 5d), and then decreases again for very low TBV. Larger standard deviations are observed at 157 GHz compared to 89 GHz with a maximum of ~3.5 K. Figures 5a and 5b also show that colder brightness temperatures are recorded over land than over ocean, which is consistent with deeper convection over continent than over ocean. There is only 0.6 K difference at 200 K between the most probable polarization differences over ocean and land at 157 GHz. This confirms that the surface contribution to the polarization signal here is very limited, and it is likely that this difference is related to a difference in the cloud microphysics above land and ocean.

As shown in Figure 4, over land, the maximum of the 2D cumulative distribution is located at high TBV and close to 0 K polarization for all frequencies. This is expected: the land emissivity is only weakly polarized in average, and atmospheric emission processes are not polarized. At 157 GHz (Figure 4f) a significant number of pixels corresponding to high TBV shows negative polarization difference. We argue that the distribution of the polarization

difference at the maximum density of points for high TBV over land can provide an estimate of the instrument noise. This is also possible at 157 GHz over ocean, due to the high atmospheric opacity at this frequency. For these conditions, the dispersion of the TBVH around the mean value (close to 0 K) is an approximation of the noise on the polarized difference σ_{V-H}. With $\sigma_{V-H}^2 = \sigma_V^2 + \sigma_H^2$ and assuming that $\sigma_V = \sigma_H$, one can deduce an estimate of the instrument noise. Figure 6 shows the histograms of the TBVH at the TB value corresponding to the maximum density of points on Figure 4. This maximum density corresponds to TBV equal to 284 and 282 K over land at 89 and 157 GHz respectively, and 283 K over ocean at 157 GHz. At 157 GHz (Figure 6c and 6d), the maximum of the distribution is at -0.6 K (resp. 0 K) over land (resp. ocean) with a standard deviation of 3.44 K (resp. 3.48 K), while at 89 GHz over land (Figure 4b), the histogram peaks at 0 K with a standard deviation of 1.67 K. From the previous equation, and assuming a mean standard deviation of 3.46 K for the polarization difference at 157 GHz, we deduce that the instrument noise at 157 GHz is 2.45 K, whereas the instrument noise is 1.18 K at 89 GHz. These estimates are above the values provided by CNES (Table 1), but they are in agreement with the required instrument specification.

3. Confirmation of the interpretation of the polarized scattering with radiative transfer simulations

Radiative transfer simulations were performed with the Atmospheric Radiative Transfer Simulator [ARTS, Eriksson et al., 2011]. ARTS is a freely available, well documented, open source software package. ARTS handles scattering with a full and efficient account of polarization effects. It provides different methods to solve the radiative transfer equation and the Discrete Ordinate Iterative (DOIT) method is used in this study [Emde et al., 2004]. The single scattering properties are calculated using the T-matrix code [Mishchenko, 2000] that allows the treatment of oriented spheroids. The dielectric properties of the material, the particle size distribution, their shape and orientation are all subject to large uncertainties that can translate into significant differences in terms of simulated brightness temperatures [e.g., Surussavadee and Staelin, 2006; Meirold-Mautner et al., 2006; Kulie et al., 2010]. Recently Galligani et al. [2013] used ARTS to explore the impact of changes in hydrometeor phase around the melting layer on the upwelling polarized radiation for frequencies below 100 GHz. Two different sets of simulations are performed here to explore the polarized scattering up to 157 GHz. First, simplified atmospheric and hydrometeor profiles are used to carefully analyze the polarized radiation sensitivity to the particle characteristics (phase, size, shape, and orientation]. Second, more realistic simulations of the observed signals by MADRAS are conducted by exploiting the coincidence of TMI and MADRAS observations along a transect, in the middle of the PR swath presented in Figure 3b. This allows using the profiles of water and ice species estimated from the 2A12 TMI GPROF-based product available for that specific TRMM overpass. The focus for both simulations is on the impact of variations of the frozen phase microphysics on the microwave polarized scattering signals observed by MADRAS.

3.1 Hydrometeor microphysical properties

The scattering properties of hydrometeors are related to their dielectric properties, their size distribution, their shape, and their orientation. For pure water, the dielectric properties are relatively easy to estimate with limited uncertainties, for instance using Liebe et al. [1991] for

instance. For pure ice, Matzler et al. [2006] model is commonly adopted, but for other frozen species, the density is a key parameter in the calculation of the dielectric properties. Mesoscale cloud models (Meso-NH for instance, Lafore et al., 1998] usually provide the mass content (kg/m^3) of the species per atmospheric layer and the size distribution of the maximum dimension of the particle. However, the density and the shape of the species are not explicitly provided by the microphysical scheme. In Meso-NH for instance, the mass of each hydrometer category is derived from a relation of the type $m=aD^b$, with a and b specified for each type of hydrometeor, but the shape of the particle and as a consequence its volume and density are not explicitly given for all particles. For liquid clouds and rain, the particles are spheres with m proportional to D^3. Graupel and small ice crystals are not strictly spheres ($b=2.8$ and $b=2.5$, respectively), but are approximated so in the radiative transfer in microwaves as there is no real justification for a more complicated treatment. Graupel species are rimmed particles for which it is reasonable to assume a spherical shape. Small pure ice crystals can be approximated by spheres for microwave radiative transfer calculation as their scattering is very limited. However, for snow the particles are clearly not spheres, with m proportional to $D^{1.9}$. For passive microwave signals, it is viable to focus on the bulk aspect of particles as characterized by its aspect ratio, neglecting the simulation of individual complicated particle shapes [Mastrosov et al., 2005]. Aspect ratios between 1 and 2 will be tested, and a value of 1.6 is considered realistic from aircraft observations (Heysmfield, personal communication). The particle density for ice crystal is that of pure ice (0.941) and for snow and graupel, it is derived from the mass-size relationship from Meso-NH. In terms of dielectric properties, snow and graupel are heterogeneous media, made of ice and air (dry snow and graupel) and possibly ice, air and water (wet snow). The dielectric properties for heterogeneous media can be calculated with a number of mixing formulas. The most common, and the one used in this study, is the Maxwell-Garnett formula that gives the effective dielectric constant of a mixture as function of the dielectric constants of the host material and inclusions (see applications of this formula in e.g. Battaglia et al. [2003], Olson et al. [2001a, 2001b]). For dry snow and graupel, the host is air and the inclusion is ice. For wet snow, the Maxwell Garnett Formula is applied twice, once to calculate dry snow and a second time to mix dry snow and water.

By analyzing accurate Discrete Dipole Approximation (DDA) modelling of snow particles, Liu [2004] observed that snow has scattering and absorption properties between those of a solid ice equal-mass sphere of diameter $D0$ and an ice–air mixed sphere with a diameter equal to the maximum dimension of the particle D_{max}. For each frequency and particle shape, a softness parameter $SP=(D-D0)/(D_{max}-D0)$ is derived that gives the diameter of the best-fit equal-mass sphere. For each particle shape, this is actually equivalent to use a frequency dependent effective density along with modified diameters. This approach has already shown a high efficiency in reproducing real observations [Meirold-Mautner et al., 2007] and it will also be tested here.

Both randomly oriented and perfectly horizontally aligned particles are considered in our calculation. In the case of horizontally aligned particles, most particles are likely to suffer particle tumbling related to turbulence. The effect of tumbling has already been evaluated in Prigent et al. [2001]. Xie et al. [2012] showed that perfectly horizontally aligned particles behave similarly to horizontally oriented particles with a standard deviation of 10°, with TBs and polarization differences deviating by less than 0.2 K compared to the perfect horizontal case. We will concentrate on perfectly horizontally aligned particles for practical reasons.

3.2 Simulations with idealized profiles

These simulations involve a tropical standard atmosphere from the FASCOD database [Anderson et al., 1986], with a total column water vapor of 33 kg/m^2, a surface temperature of 300 K, and land surface emissivities set to 0.9 for both polarizations (to avoid any polarized contributions from the surface itself). The incidence angle of the simulated satellite observations is set to 53°, similar to TMI and MADRAS observation geometries. A single cloud layer (2 km thick from 6 to 8 km) is considered and populated with hydrometeors with varying Ice Water Path (IWP). A mono-disperse particle size distribution of spheroids is assumed, with radius of 50 μm to 800 μm (note that radius here refers to the radius of the sphere with equivalent mass, i.e., the effective radius). Figure 7 presents the sensitivity of TBV and the polarization difference TBVH to the particle size at 89 and 157 GHz, for pure ice and for dry snow, for horizontally aligned spheroids of different aspect ratios (aspect ratio of 1 corresponds to spheres). The TBV depression is very limited at 37 GHz (not shown), even for very large particles, but strongly increases with frequencies (Figure 7a,c). For dry snow the effect is stronger than for pure ice, because of the larger number of particles to reach the same IWP for snow than for ice (the density of ice is 0.917 g/cm^3 compared to a minimum density of 0.1 g/cm^3 for dry snow). At 89 and 157 GHz, the polarization difference increases with particle size and for a given particle size, it is larger at 157 GHz than at 89 GHz, until the TBVH signal reaches a maximum at 157GHz (Figure 7b,d). With randomly oriented spheroids of aspect ratio of 1.6 or 2, only very limited polarized scattering signals are simulated (not shown). On the contrary, for horizontally aligned particles, IWP of 0.2 kg/m^2, particle radius of ~ 500 μm, and a realistic aspect ratio of 1.6, a polarization difference between 9 and 15 K is obtained at 157 GHz (between 4 and 7 K at 89 GHz), depending on the density of the particle (pure ice or dry snow). This is in very good agreement with the MADRAS observations at these two frequencies.

Again for horizontally aligned spheroids, Figure 8 shows the sensitivity of the polarization difference at 89 and 157 GHz to the IWP and particle radius. Large polarization differences are simulated at 157 GHz for rather low IWP and limited radius. As observed in Figures 7 and 8, both an increase of IWC and particle size can result in the saturation of the polarization difference. This saturation is reached at lower sizes and lower IWP at 157 GHz than at 89 GHz, as expected. This saturation feature has been reported before [Miao et al., 2003; Xie and Miao, 2011) when a large number of scattering events occur. In that case, the V and H orthogonal streams of radiation tend to the same value, and their difference reaches zero.

Even though this atmospheric state is rather simplified, it helps conduct a sensitivity analysis of the impact of the microphysical properties on the polarization signal, and the simulations agree well with the MADRAS observations. Next section uses more realist realistic atmospheric parameters for the simulations.

3.3 Simulations with observational-based hydrometeor profiles

We focus on the stratiform system with large TBVH differences observed by both TMI and MADRAS off the coast of Madagascar in Figure 3. The PR nadir swath crosses this system and a longitudinal transect in the middle of the PR swath is selected for our analysis of coincident MADRAS and TMI observations. The profiles of water and ice contents retrieved from TMI (the 2A12 TMI product) are adopted along with coincident ECMWF re-analysis.

312 The PR 2A23 rain characteristics product [Awaka et al. 1998; Iguchi et al., 2000]
313 provides information on the presence and location of a melting layer, on the rain type (i.e.,
314 stratiform, convective, or other), on the freezing height, and on the cloud top height. The TMI
315 2A12 based on Goddard profiling algorithm (GPROF) 2010 algorithm generates surface rainfall
316 and vertical hydrometeor profiles of 5 species (snow cloud water, cloud liquid water, ice, graupel,
317 and rain) from the TMI brightness temperatures. It is derived from a Bayesian retrieval and it
318 gives the most probable structure of the hydrometeor profiles, given the TMI observations
319 [Kummerow et al., 2011].

320 Figure 9 shows the cloud liquid water content (CLWC), the rain water content (RWC), the
321 cloud ice water content (CIWC), the snow water content (SWC), the graupel water content
322 (GWC), and their integrated paths, as retrieved from the TMI 2A12 product for the transect of
323 interest. The PR bright band height (black circles) and the PR cloud top height (solid red curve)
324 are overlaid. The key step in these RT simulations is defining the microphysical assumptions to
325 describe this TMI 2A12 hydrometeor profiles. The TMI 2A12 algorithm only retrieves
326 hydrometeor profiles over ocean, and the RT simulations are conducted with FASTEM ocean
327 emissivities [English and Hewison, 1998] as derived using information on surface wind and
328 surface skin temperature from coincident ECMWF re-analysis.

329 The single scattering properties of the hydrometeors are calculated by the T-matrix
330 method, using the mass-size relationships introduced in Section 3.1. Figure 10 shows the
331 observations from MADRAS (left) and the corresponding simulations (right) for the cross-
332 section of interest for TBV and TBVH at 85 and 157 GHz. The first simulation (solid blue curve)
333 corresponds to the initially selected parameter for snow and graupel species where the particle
334 size distribution and the intrinsic mass of the particles are specified by the cloud mesoscale
335 model Meso-NH, with perfect snow spheres (aspect ratio of 1). It results in very limited
336 scattering with small TB depression and limited polarization (solid blue curve). In fact
337 TBV(clear)-TBV(snow) is of the order of 80 (resp. 50) K for 157 (resp. 89) GHz, which does not
338 compare well with the observed brightness temperature depressions by MADRAS of the order of
339 120 (resp. 70) K at 157 (resp. 89) GHz. Just west of 47°W, TBVH simulations increase
340 considerably to the TBVH observed during clear sky conditions (west of 46.5°W). This is due to
341 an underestimation of the retrieved hydrometeor contents, otherwise the atmosphere would be
342 opaque and the surface polarization would not be observed. A simulation where only the liquid
343 phase is taken into account is also shown to emphasize the importance of the ice phase at 157
344 GHz as compared to the 89 GHz (dashed blue line).

345 Changing the aspect ratio, the orientation or the PSD (to that of the Meso-NH PSD
346 parameterization for graupel for instance) of the dry snow particles, but using the same density
347 parameterization does not have an impact on TBV and TBVH (not shown). Multiplying the snow
348 content by 1.5 in each layer changes the result by less than 5 K at 157 GHz, far from the observed
349 TBV. Snow particle sizes that are likely to scatter and polarize the radiation at 89 and 157 GHz
350 have very low density under this parameterization, affecting the dielectric properties via the ice
351 volume fraction, and as a consequence are almost transparent to the microwaves (already seen in
352 e.g. Meirold-Mautner et al., 2006).

353 Assuming the Meso-NH particle size distribution for snow species but calculating the
354 dielectric properties for dry snow particles with a fixed density of 0.1 g/cm^3 (a value that is often
355 selected for snow) has an important impact on the single scattering properties via the ice volume
356 fraction and thus on the TBVs. Randomly oriented spheres show similar TBVs to those observed

(not shown) but do not polarize the scattering signal. Oblate horizontally oriented snow particles with aspect ratios 1.6 (solid red line) lead to TBVs and polarization signals of the order of those observed by MADRAS at both 157 and 89 GHz. Furthermore, the polarized scattering signals simulated for 157 GHz (9-12 K) are approximately twice those at 89 GHz (4-6 K) as expected and observed in Figure 4.

For the same configuration, the Meso-NH snow PSD was replaced by the Sekhon and Srivastava [1970] (SS) PSD (cyan circled line), thus assuming fewer large particles and more numerous smaller ones. With the SS PSD the TBV are increased by approximately 10 K and the TBVH are limited at 89 GHz.

The Liu parameterization of the scattering properties of snow is then tested, with the nominal PSD and density of the Meso-NH model (green dotted line). It provides TBV depressions and TBVH polarizations in very good agreement with the observations, without any additional fine-tuning.

The sensitivity to the snow content is then analyzed, multiplying the snow content by 1.5 in each atmospheric layer, with for the previous configuration with Liu's approximation (black dotted line). The scattering effect is significant, especially in terms of TB depression and polarization difference at 157 GHz. The snow quantities provided by the TMI inversion are realistic, and adding more snow does not improve the agreement between simulations and observations.

With realistic atmospheric profiles, it is thus possible to reproduce consistently the polarized scattering signals observed at 89 and 157 GHz. This confirms the validity of our previous interpretation of the signals up to 90 GHz, with additional stringent constraints imposed by the higher frequency.

4. Conclusion

The MADRAS instrument launched at the end of 2011 on board the Megha-Tropiques mission offers for the first time measurements of the two orthogonal polarizations at high microwave frequencies. Analysis of available quality controlled MADRAS data reveals that the noise levels at 89 and 157 GHz are in agreement with the required instrument specifications. Further analysis of the MADRAS observations also revealed that the instrument was very stable.

We observed that at 157 GHz, scattering by clouds is polarized with TBVH larger than 8 K in 50% of the cases for TBV below 250 K, as compared to 5.5 K in 50% of the cases at 89 GHz. Simulations confirm that this is due to horizontally oriented oblate particles in the cloud frozen phase. This polarized scattering signal at 157 GHz is consistent with the polarized signatures previously observed around 85 GHz, and as expected it is more common and stronger at higher frequencies. The large occurrence of the polarized scattering in the observations as well as the magnitude of the polarization suggest that horizontally oriented oblate particles are very frequent in the cloud ice phase.

This significant polarized scattering has to be taken into account in the development of the retrieval of precipitation and cloud properties from microwave radiometry, such as the GPM algorithms that are presently under development. Especially over land, most passive microwave retrievals for precipitation are based on the scattering signal at frequencies above 80 GHz. The

399 effect of these oriented particles has to be accounted for, at least as an additional source of noise,
400 if not explicitly.

401 With the recent decision of flying an Ice Cloud Imager between 170 and 675 GHz on
402 board the next generation of European operational meteorological satellites, relating the observed
403 scattering from the ice phase to accurate measurements of the cloud properties is a key challenge.
404 The analysis of the measurements provided by MADRAS contributes to the preparation of this
405 promising instrument.
406

ANNEX

Nearly-coincident MADRAS and TMI observations are available for the scene shown in Figure 1 and Figure A.1 respectively. The time difference is 6 min. Despite the different spatial resolutions and slightly different frequencies, the observations of the two radiometers are quite similar in terms of radiometric range and sensitivity over land and ocean. MADRAS measurements are very stable along a given scan, and from a scan to the next at high frequencies. No clear jump between scan lines is observed on the images of the polarization differences at 89 or 157 GHz, whereas at 85 GHz with TMI, a large noise is evident on the polarization difference maps, within a scan and from one scan to the next.

Figure A.2 shows the scatter plots of TBs and polarization differences for the common spectral bands (ocean and land together). At 35-37 GHz, the observations from the two radiometers span over the same radiometric domain even if TMI reported more convection-related scattering because of a better spatial resolution. At 85-89 GHz, even if the number of samples from two radiometers is almost the same, more negative polarization differences are reported by TMI, while the distribution of MADRAS polarization difference at TBs lower than 200 K seems to be centered around 5 K. This pinpoints to the need for thorough investigations on calibration of each radiometer if instruments have to be used jointly.

Figure A.3 shows the histograms and the cumulative distributions of the brightness temperatures for all surfaces together, for common radiometric band and polarization and for the two radiometers. These histograms are computed from the radiometric measurements shown in Figures 1 and A.1 but for the common area defined by the intersection of MADRAS and TMI swaths. At 37 GHz, both radiometers provide rather similar histograms at both sides of the distributions, i.e. in clear sky over sea and in most likely clear sky conditions over land. A difference exists at mid-TB range, i.e. mainly for beams located over ocean. At 85 GHz, for both polarizations, differences exist at cold brightness temperatures, i.e. for convective clouds. Those discrepancies can be explained by the different spatial resolutions between the two radiometers, the viewing geometry of the convective clouds depending on the orientation of the radiometer beams relative to the cloud structure, and the natural evolution of the sampled clouds between the two overpasses (delay of 6 min). While the histogram of the polarization difference at 37 GHz is rather similar, some differences are observed at 85 GHz: TMI recorded negative-to-null polarization differences while MADRAS did not, and smaller difference polarizations are recorded by MADRAS. These discrepancies could also be explained by the noisier measurements of TMI in this temperature range, as can be observed on the images.

From these comparisons, we can conclude that MADRAS performs well, with results very similar to TMI for their common (or close) channels. In addition, MADRAS is likely more stable than TMI.

Acknowledgements.

We thank ISRO and CNES for dissemination of the MADRAS data. We are grateful to Nadia Karouche (CNES), Christophe Goldstein (CNES) and Christian Tabart (ASTRIUM) for the fruitful discussions on the MADRAS instrument and on its calibration and performances. We would also like to thank the ARTS community for providing an open source radiative transfer code, with special thanks to Patrick Eriksson for valuable advices. MADRAS data were downloaded from ICARE data server (http://www-icare.univ-lille1.fr/). TRMM data were downloaded from TRMM data server (http://mirador.gsfc.nasa.gov/cgi-bin/mirador/presentNavigation.pl?tree=project&project=TRMM). CNES and Astrium supported VG. The French LEFE program and CNES-TOSCA supported this study.

455 **References:**

456 Anderson, G. P., S. Clough, F. Kneizys, J. Chetwynd, and E. P. Shettle (1986), AFGL
457 atmospheric constituent profiles (0.120 km), Tech. rep., DTIC Document.

458 Awaka, J., T. Iguchi, and K. Okamoto (1998), Early results on rain type classification by the
459 Tropical Rainfall Measuring Mission (TRMM) precipitation radar, Proc. 8th URSI
460 Commission F Open Symp., Aveiro, Portugal, pp.143-146.

461 Battaglia, A., C. Kummerow, Dong-Bin Shin, and C. Williams, (2003), Constraining microwave
462 brightness temperatures by radar bright band observations, J. Atmos. Oceanic. Technol., 20,
463 856–871.

464 Buehler, S. A. , C. Jimenez, K. F. Evans, P. Eriksson, B. Rydberg, A. J. Heymsfield, C. J.
465 Stubenrauch, U. Lohmann, C. Emde, V. O. John, T. R. Sreerekhai and C. P. Davis (2007), A
466 concept for a satellite mission to measure cloud ice water path, ice particle size, and cloud
467 altitude, Q. J. R. Meteorol. Soc., 133, 109-128.

468 Defer, E., C. Prigent, F. Aires, J. R. Pardo, C. J. Walden, O.-Z. Zanifé, J.-P. Chaboureau, and J.-
469 P. Pinty (2008), Development of precipitation retrievals at millimeter and sub-millimeter
470 wavelengths for geostationary satellites. J. Geophys. Res., 113, D08111,
471 doi:10.1029/2007JD008673.

472 Emde, C., S. A. Buehler, C. Davis, P. Eriksson, T. R. Sreerekha, and C. Teichmann (2004), A
473 polarized discrete ordinate scattering model for simulations of limb and nadir long-wave
474 measurements in 1-D/3-D spherical atmospheres, J. Geophys. Res., 109, D24207,
475 doi:10.1029/2004JD005140.

476 English, S. J., and T. J. Hewison (1998). Fast generic millimeter-wave emissivity model. In:
477 Asia-Pacific Symposium on Remote Sensing of the Atmosphere, Environment, and Space.
478 International Society for Optics and Photonics, pp. 282-300.

479 Eriksson, P., S. A. Buehler, C. P. Davis, C. Emde, and O. Lemke (2011), ARTS, the atmospheric
480 radiative transfer simulator, Version 2, J. Quant. Spectrosc. Radiat. Transfer, 112, 1551–1558.

481 Evans, K. F., J. R. Wang, P. E. Racette, G. Heymsfield, and L. Li (2005), Ice cloud retrievals and
482 analysis with the compact scanning submillimeter imaging radiometer and the cloud radar
483 system during CRYSTAL-FACE, J. Appl. Meteorol., 44, 839 – 859.

484 Galligani, V. S, C. Prigent, E. Defer, C. Jimenez, and P. Eriksson (2013), The impact of the
485 melting layer on the passive microwave cloud scattering signal observed from satellites: A
486 study using TRMM microwave passive and active measurements J. Geophys. Res., 118,
487 D05667, doi: 10.1002/jgrd.50431.

488 Goldstein, C., and N. Karouche (2013), CAL/VAL MADRAS Radiometric Sensitivity, report
489 MAD_RAD_02 TRO-NT-32-NT-2817- CNES, 8 pages, available at
490 http://smsc.cnes.fr/MEGHAT/PDF/MADRASRadiometricSensitivity.pdf.

491 Iguchi, T., T. Kozu, R. Meneghini, J. Awaka, and K. Okamoto (2000), Rain-profiling algorithm
492 for the TRMM precipitation radar, J. Appl. Meteor., 39, 2038–2052.

493 Jimenez, C., S. A. Buehler, B. Rydberg, P. Eriksson and K. F. Evans (2007), Performance
494 simulations for a submillimetre-wave cloud ice satellite instrument, Q. J. R. Meteorol. Soc.,
495 133, 129-149.

496 Karouche, N., C. Goldstein, A. Rosak, C. Malassingne, and G. Raju (2012), Megha-Tropiques
497 Satellite Mission : In Flight Performances Results, Geoscience and Remote Sensing
498 Symposium (IGARSS), 2012 IEEE International, 4684-4687,
499 10.1109/IGARSS.2012.6350420.

500 Karouche, N., and G. Raju (2010), Megha-Tropiques Satellite Mission: Sensors performances,
501 Proc. SPIE 7826, Sensors, Systems, and Next-Generation Satellites XIV, 78260Q (October 13,
502 2010), doi:10.1117/12.868048.

503 Kulie, M. S., R. Bennartz, T. J. Greenwald, Y. Chen, and F. Weng (2010), Uncertainties in
504 Microwave Properties of Frozen Precipitation: Implications for Remote Sensing and Data
505 Assimilation, J. Atmos. Sci., 67, 3471–3487.

506 Kummerow, C. D., S. Ringerud, J. Crook, D. Randel, and W. Berg (2011), An Observationally
507 Generated A Priori Database for Microwave Rainfall Retrievals. J. Atmos. Oceanic Technol.,
508 28, 113–130.

509 Lafore, J.-P., J. Stein, N. Asencio, P. Bougeault, V. Ducrocq, J. Duron, C. Fischer, P. Héreil, P.
510 Mascart, V. Masson, J.-P. Pinty, J.-L. Redelsperger, E. Richard, and J. Vilà-Guerau de
511 Arellano (1998) ; The Meso–NH Atmospheric Simulation System. Part I: adiabatic
512 formulation and control simulations. Scientific objectives and experimental design. Ann.
513 Geophys., 16, 90–109.

514 Liebe, H. J., G. A. Huord, and T. Manabe (1991), A model for the complex permittivity of water
515 at frequencies below 1 tHz, International Journal of Infrared and Millimeter Waves, 12 (7).

516 Liu, G. (2004), Approximation of single scattering properties of ice and snow particles for high
517 microwave frequencies, Journal of the atmospheric sciences 61 (20), 2441–2456.

518 Matrosov, S. Y., A. J. Heymsfield, and Z. Wang (2005), Dual-frequency radar ratio of
519 nonspherical atmospheric hydrometeors, Geophys. Res. Lett., 32, L13816,
520 doi:10.1029/2005GL023210.

521 Matzler, C., P.W. Rosenkranz, A. Battaglia and J.P. Wigneron (2006), Thermal Microwave
522 Radiation - Applications for Remote Sensing, IEE Electromagnetic Waves Series 52, London,
523 UK, Chapter 5.

524 Meirold-Mautner, I., C. Prigent, E. Defer, J.-R. Pardo, J.-P. Chaboureau, J.-P. Pinty, M. Mech,
525 and S. Crewell (2007), Radiative transfer simulations using mesoscale cloud model outputs:
526 comparisons with passive microwave and infrared satellite observations for mid-latitudes, J.
527 Atmos. Sci., 64, 1550-1568.

528 Miao, J., K.-P. Johnsen, S. Buehler, and A. Kokhanovsky (2003), The potential of polarization
529 measurements from space at mm and sub-mm wavelengths for determining cirrus cloud
530 parameters, Atmospheric Chemistry and Physics 3 (1), 39–48.

531 Mishchenko, M. I. (2000), Calculation of the amplitude matrix for a nspherical particle in a fixed
532 orientation, Appl. Opt., 39, 1026–1031.

533 Olson, W.S., P. Bauer, N.F. Viltard, D.E. Johnson, W.-K. Tao, R. Meneghini, and L. Liao
534 (2001a), A Melting-Layer Model for Passive/Active Microwave Remote Sensing
535 Applications. Part I: Model Formulation and Comparison with Observations, J. Appl. Meteor.,
536 40, 1145–1163.

537 Olson, William S., P. Bauer, C. D. Kummerow, Y. Hong, and W.-K. Tao (2001b), A Melting-
538 Layer Model for Passive/Active Microwave Remote Sensing Applications. Part II: Simulation
539 of TRMM Observations, Journal of Applied Meteorology 40, 1164–1179.

540 Prigent, C., E. Defer, J. Pardo, C. Pearl, W. B. Rossow, and J.-P. Pinty (2005), Relations of
541 polarized scattering signatures observed by the TRMM Microwave Instrument with electrical
542 processes in cloud systems, Geophys. Res. Let., 32, L04810, doi: 10.1029/2004GL022225.

543 Prigent, C., J. R. Pardo, M. I. Mishchenko and W. B. Rossow, Microwave polarized scattering
544 signatures in clouds: SSM/I observations interpreted with radiative transfer simulations,
545 Journal of Geophysical Research, 106, 28243-28258, 2001.

546 Surussavadee, C., and D. H. Staelin (2006), Comparison of AMSU millimeter-wave satellite
547 observations, MM5/TBSCAT predicted radiances, and electromagnetic models for
548 hydrometeors, IEEE Trans. Geo. Remote Sens., 44, 2667–2678.

549 Xie, X., U. Lohnert, S. Kneifel, and S. Crewell (2012), Snow particle orientation observed by
550 ground-based microwave radiometry, J. Geophys. Res., 117, D02206,
551 doi:10.1029/2011JD016369.

552 Xie, X., and J. Miao (2011), Polarization difference due to nonrandomly oriented ice particles at
553 millimeSpectrosc. Ra., 112, 1090–1098.
554

555

Name	*Central frequency (GHz)*	*Bandwidth (GHz)*	*Pol.*	*Cross track resolution (km)*	*Along track resolution (km)*	*NEDT (K)*		*NEDT (K)*	*NEDT (K)*
						Goal	*Req'd*	*Flight*	*Ground*
M1H	18.7	±0.1	H	40	67	0.5	0.7	0.33	0.37
M1V	18.7	±0.1	V	40	67	0.5	0.7	0.38	0.44
M2V	23.8	±0.2	V	40	67	0.5	0.7	0.34	0.39
M3H	36.5	±0.5	H	40	67	0.5	0.7	0.28	0.32
M3V	36.5	±0.5	V	40	67	0.5	0.7	0.28	0.33
M4H	89	±1.35	H	10	17	1	1.1	0.38	0.41
M4V	89	±1.35	V	10	17	1	1.1	0.36	0.39
M5H	157	±1.35	H	6	10	2	2.6	1.01	1.08
M5V	157	±1.35	V	6	10	2	2.6	0,94	1.08

556

557 Table 1. Characteristics of the MADRAS instrument on board Megha-Tropiques. Different noise
558 levels are given: the specification ones (Goal and Required) and the in-flight and ground
559 estimates from CNES at nominal MADRAS operations [Karouche et al., 2012; Goldstein and
560 Karouche, 2013].

561
562

563

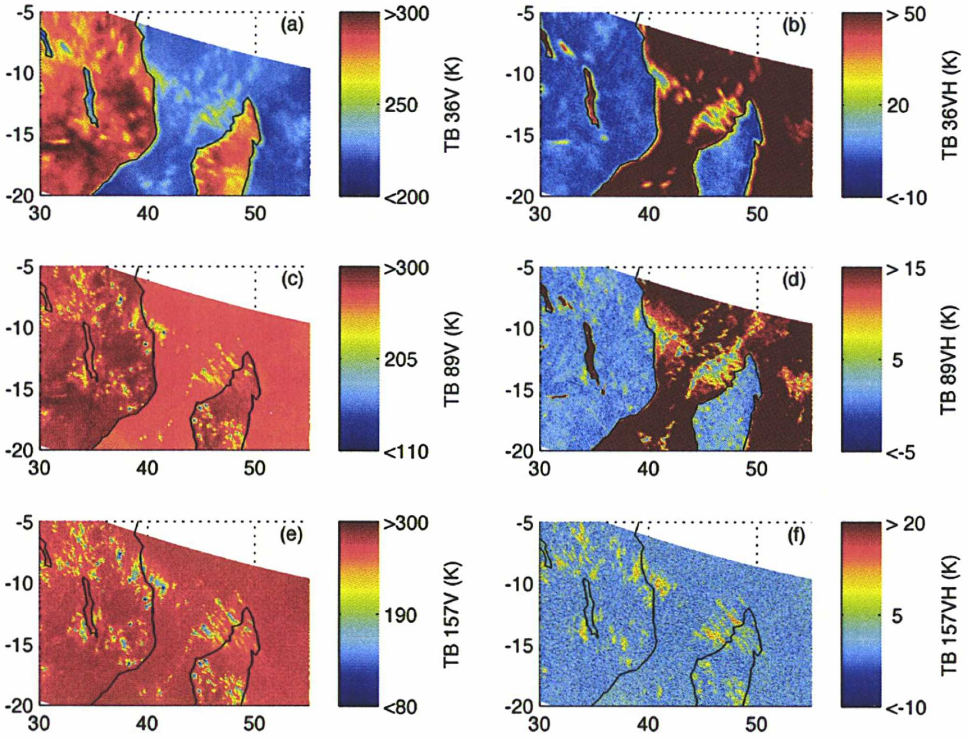

564

565

566 Figure 1 - A scene from MADRAS on board Megha-Tropiques, off the east coast of Africa, on
567 December 9th, 2011, between 12:05 and 12:12 TU. From top to bottom, 36, 89, and 157 GHz, on
568 the left the vertical polarization, on the right the difference between vertical and horizontal
569 polarizations.

570

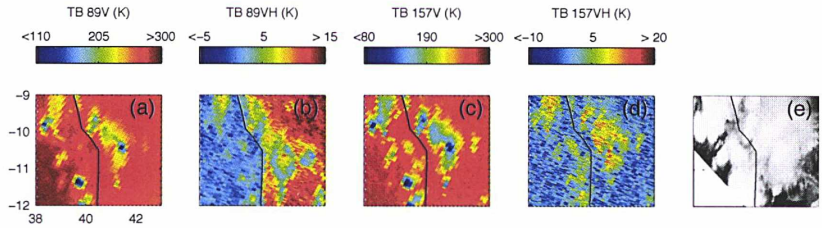

Figure 2 – Zoom on one area of Figure 1 with (a) TB89V map, (b) TB89VH map, (c) TB157V map, (d) TB157VH map, (e) TRMM VIRS 12-µm IR image.

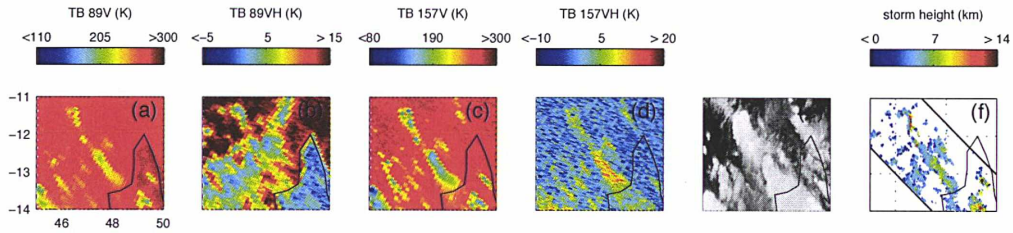

Figure 3 – Same as Figure 2 but for another region with (f) TRMM PR storm height. The solid lines in (f) delineate the borders of PR swath.

587

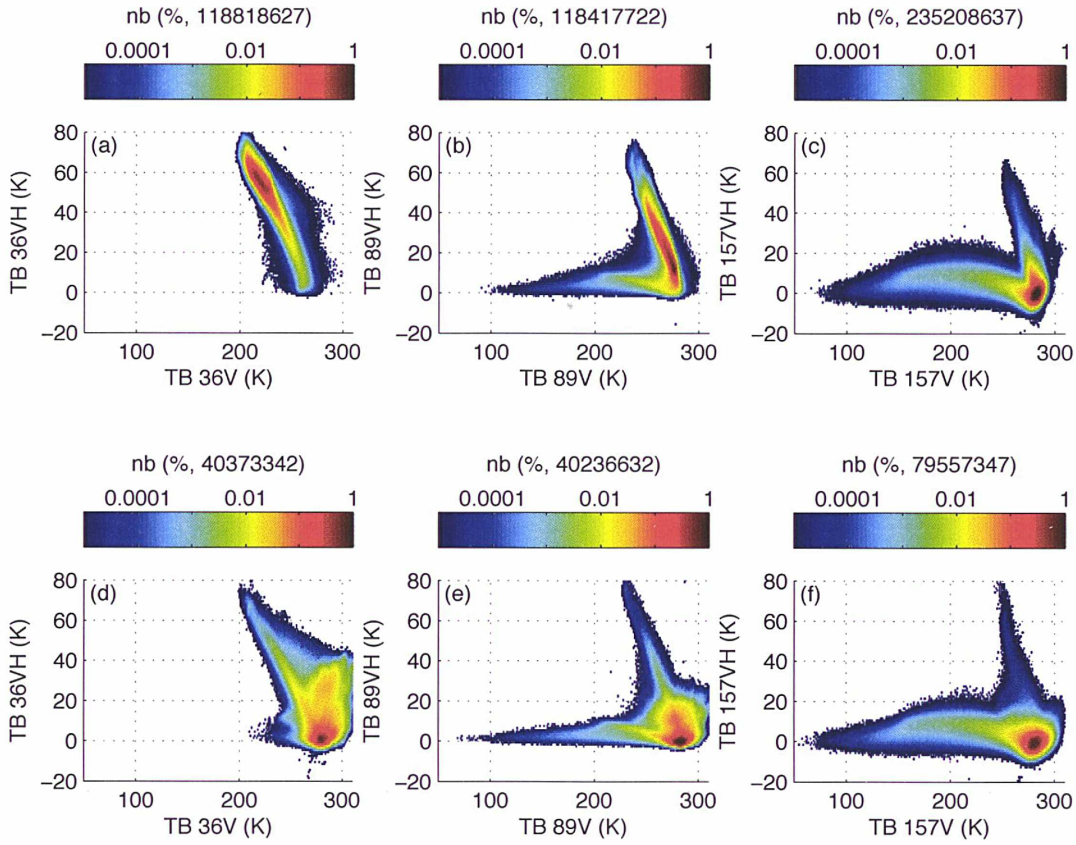

588
589

590 Figure 4 - The brightness temperature polarization differences (TBVH) versus the brightness
591 temperature in vertical polarization (TBV), for ocean (top) and land (bottom), for 36, 89, and 157
592 GHz from left to right. For each 1 K by 1 K box, the color indicates the relative number of pixels
593 that checked the quality control, with respect to the total number of pixels indicated on top of
594 each panel.
595

596

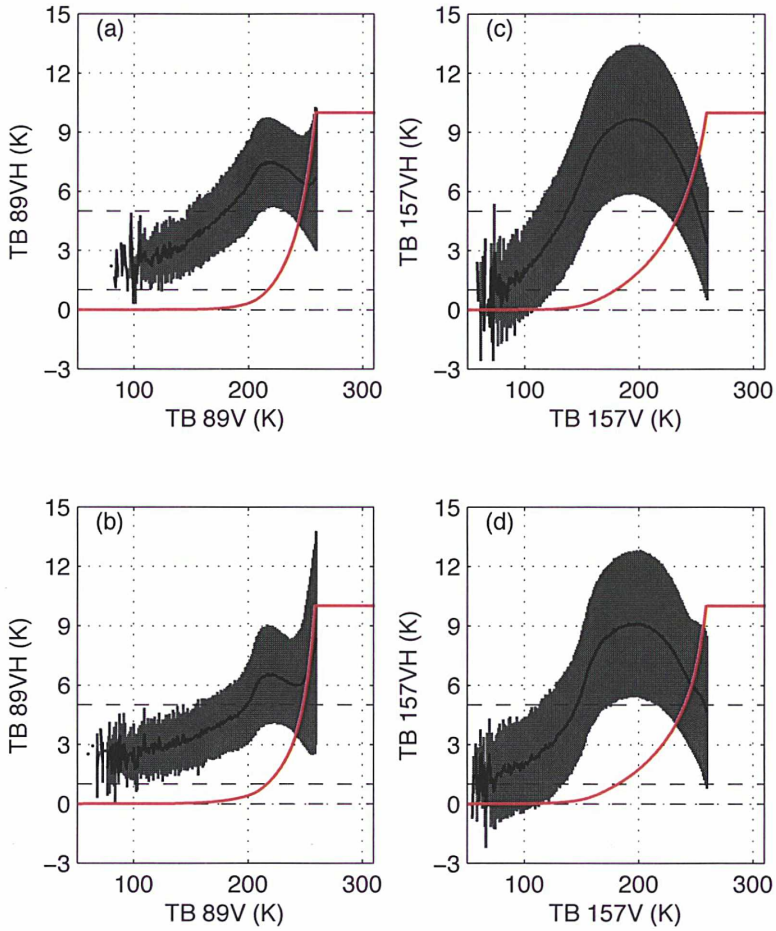

597

598

599 Figure 5 - Most probable polarization difference (solid black lines) and its standard deviation (in
600 grey) at 89 and 157 GHz for ocean (top) and land (bottom) in the scattering regime (see text for
601 the methodology to identify the scattering regime). The red curve shows the cumulative
602 distribution of the number of samples (rescaled between 0 and 10 K) with the dashed lines
603 corresponding to 0, 10 and 50% of the sample population in the scattering regime.

604

605

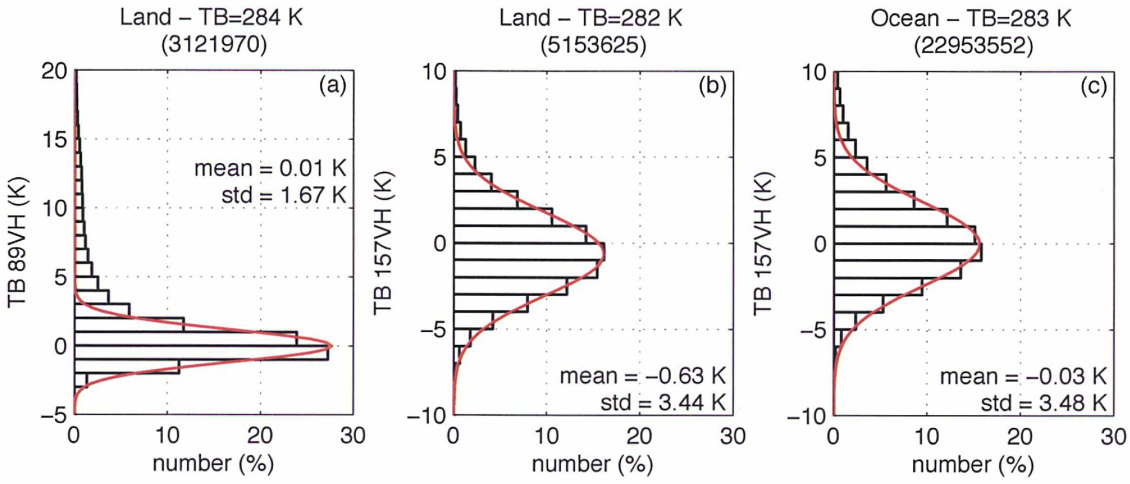

606

607

608 Figure 6 - Distribution of the polarization difference at the maximum of the distributions shown
609 in Figure 4 over land at 89 and 157 GHz (a, b) and over ocean at 157 GHz (c). The brightness
610 temperature that corresponds to the maximum is given at the top of each panel as well as the
611 number of TBV-TBVH pairs with that maximum brightness temperature.
612

613

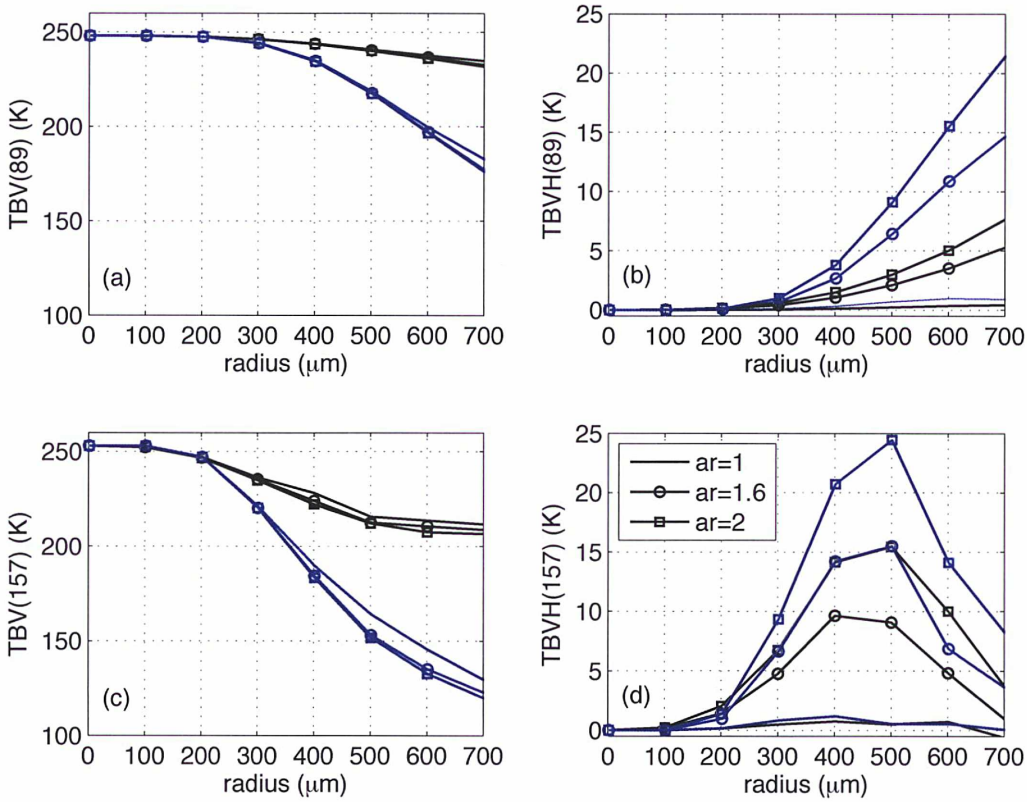

614

615

616 Figure 7 - The sensitivity of the vertical brightness temperature (TBV) and the polarization
617 difference (TBVH) at 89 GHz and 157 GHz to the particle aspect ratio as a function of the
618 effective radius for a mono disperse distribution of pure ice (black) and dry snow (blue)
619 horizontally aligned spheroids (fixed IWP at 0.2 kg/m^2).

620

621

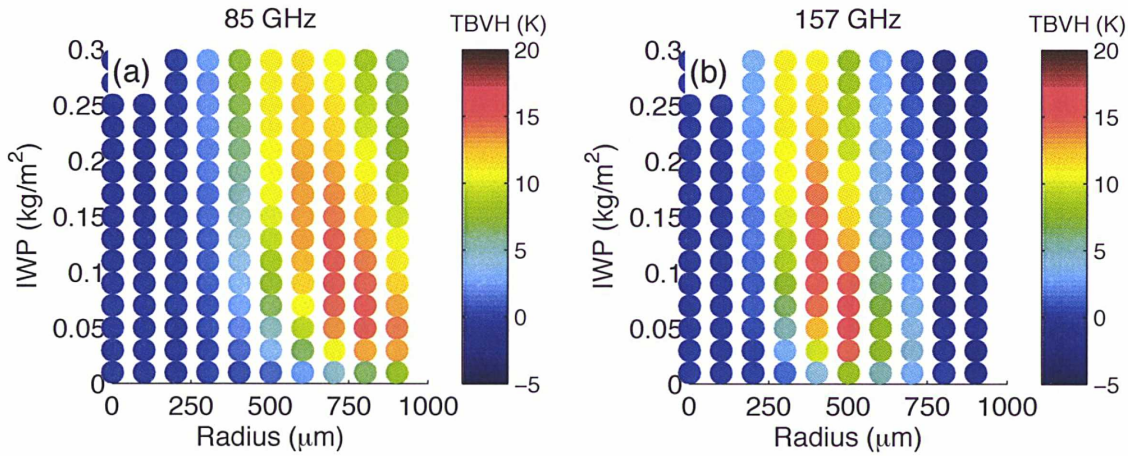

622

623

624 Figure 8 - The sensitivity of the polarization difference (TBVH) at (a) 89 GHz and (b) 157 GHz
625 for a mono-disperse distribution of dry snow horizontally aligned spheroids, as a function of the
626 IWP and as a function of the particle (effective) radius.

627

628

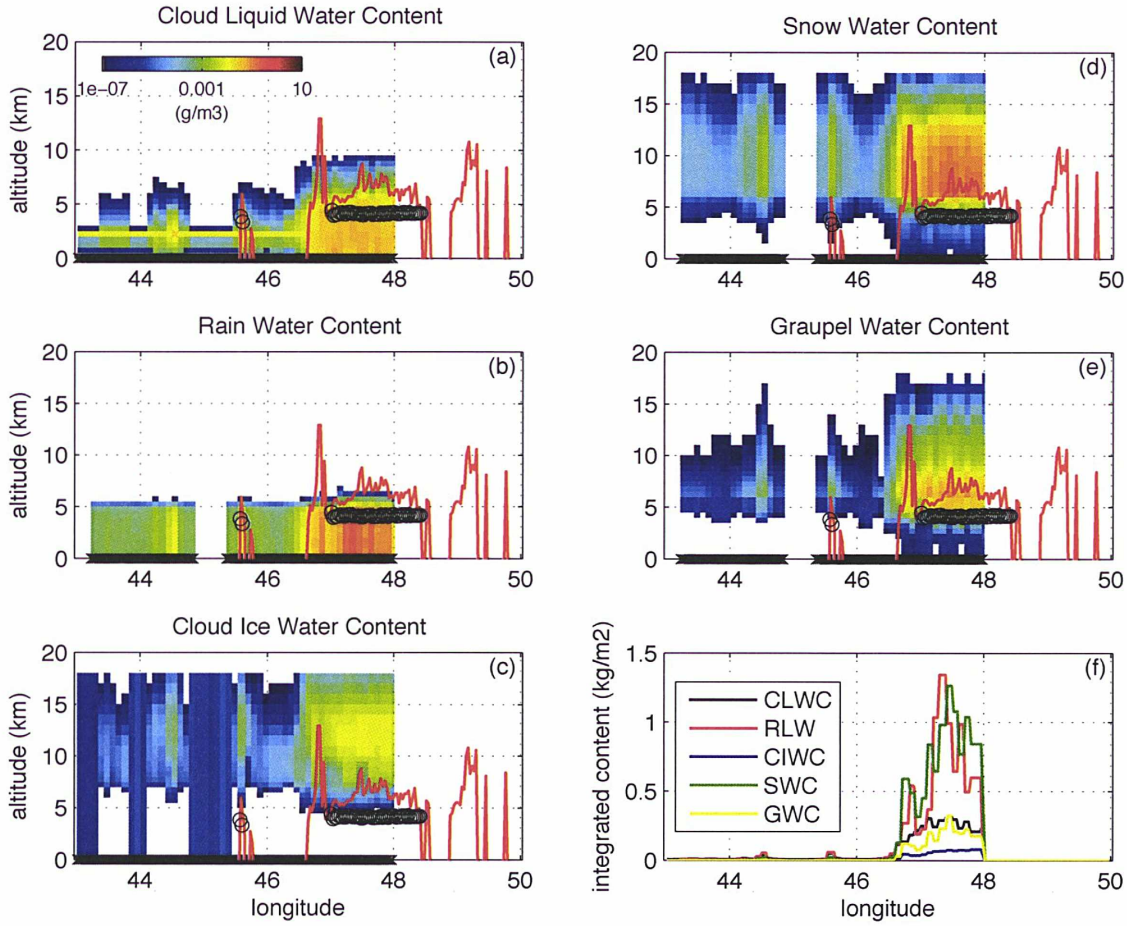

Figure 9 - The retrieved TMI 2A12 hydrometeor profiles for the transect of interest: (a) the cloud liquid water content (CLWC), (b) the rain water content (RWC), (c) the cloud ice water content (CIWC), (d) the snow water content (SWC), (e) the graupel water content (GWC), and (f) their integrated paths. Note that the PR bright band height (black circles) and the PR cloud top height (solid red curve) are overlaid. TMI 2A12 information is not available over land (East of 48E).

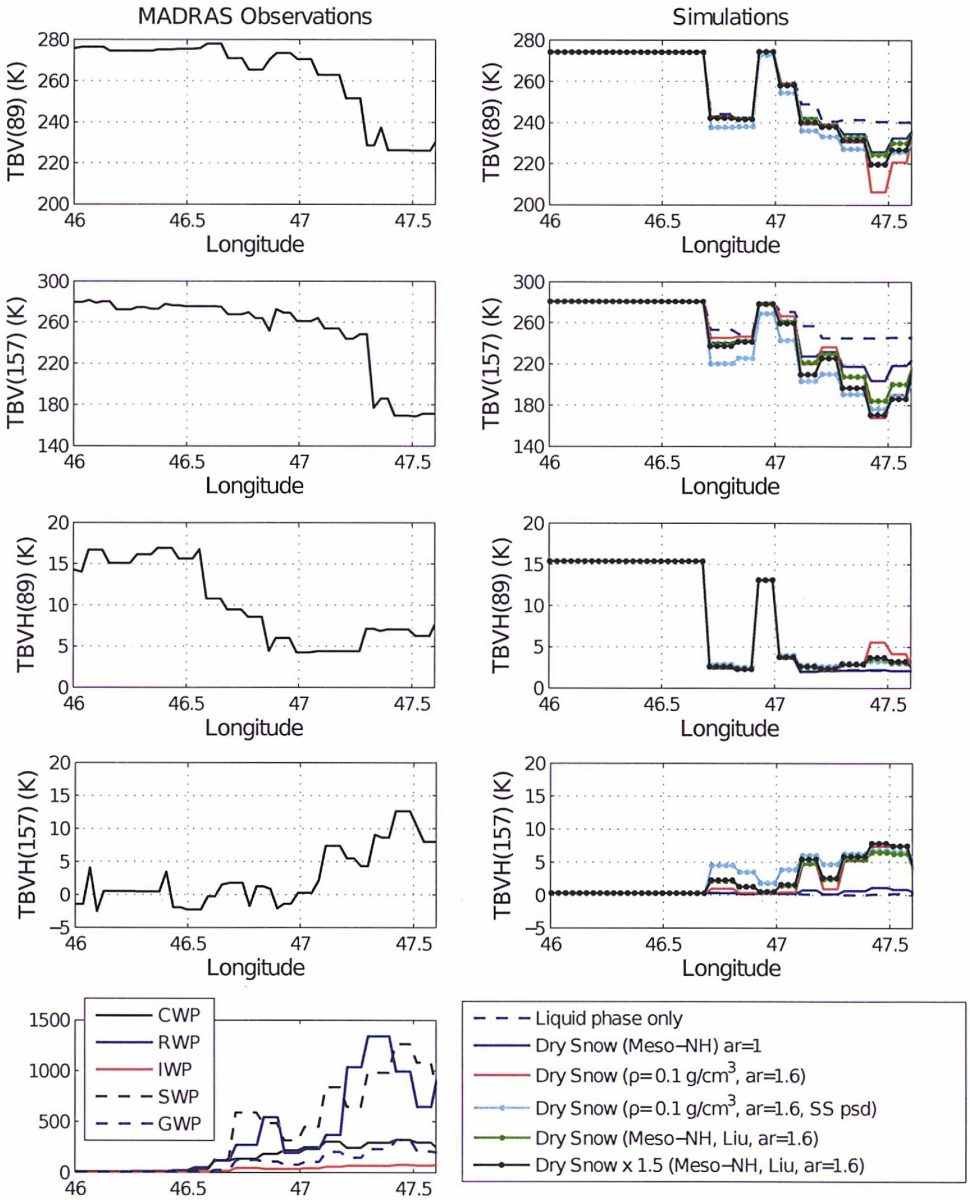

Figure 10 - The TBV and TBVH signals at 89 and 157 GHz observed by MADRAS (left) and simulated with ARTS (right) under different microphysical properties of snow species, for the transect of interest. See text for more detail.

644

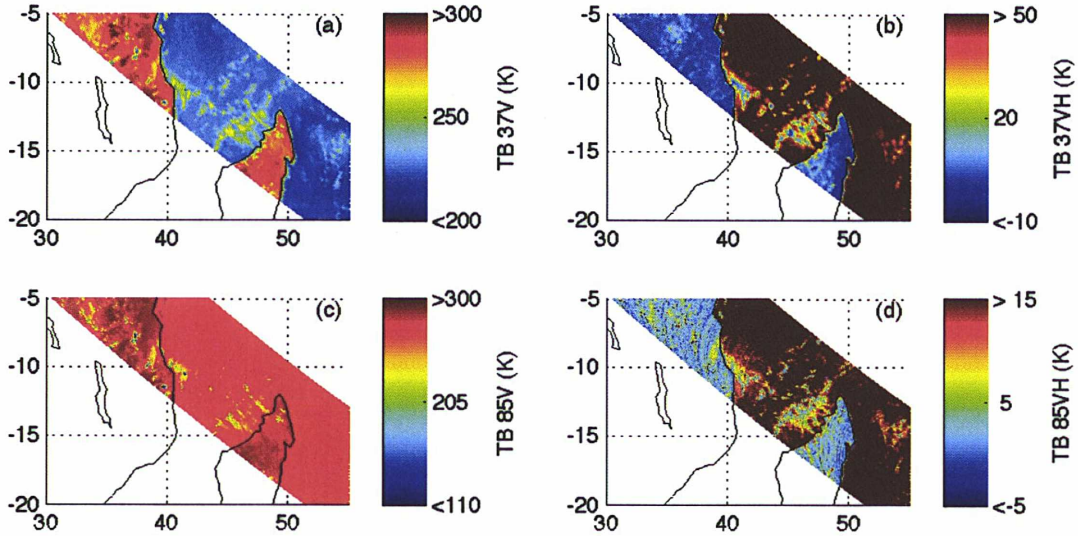

645
646
647 Figure A.1 - Same as Figure 1 but with TMI records.
648

649

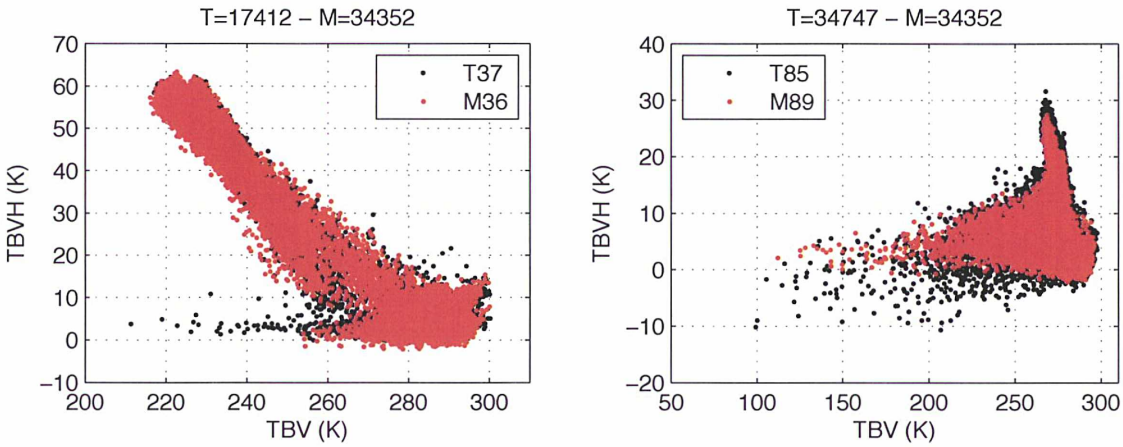

650

651

652 Figure A.2 - Scatter plots of brightness temperatures and polarization differences at the studied
653 bands for the two instruments. T and M stand for TMI and MADRAS respectively.

654

655

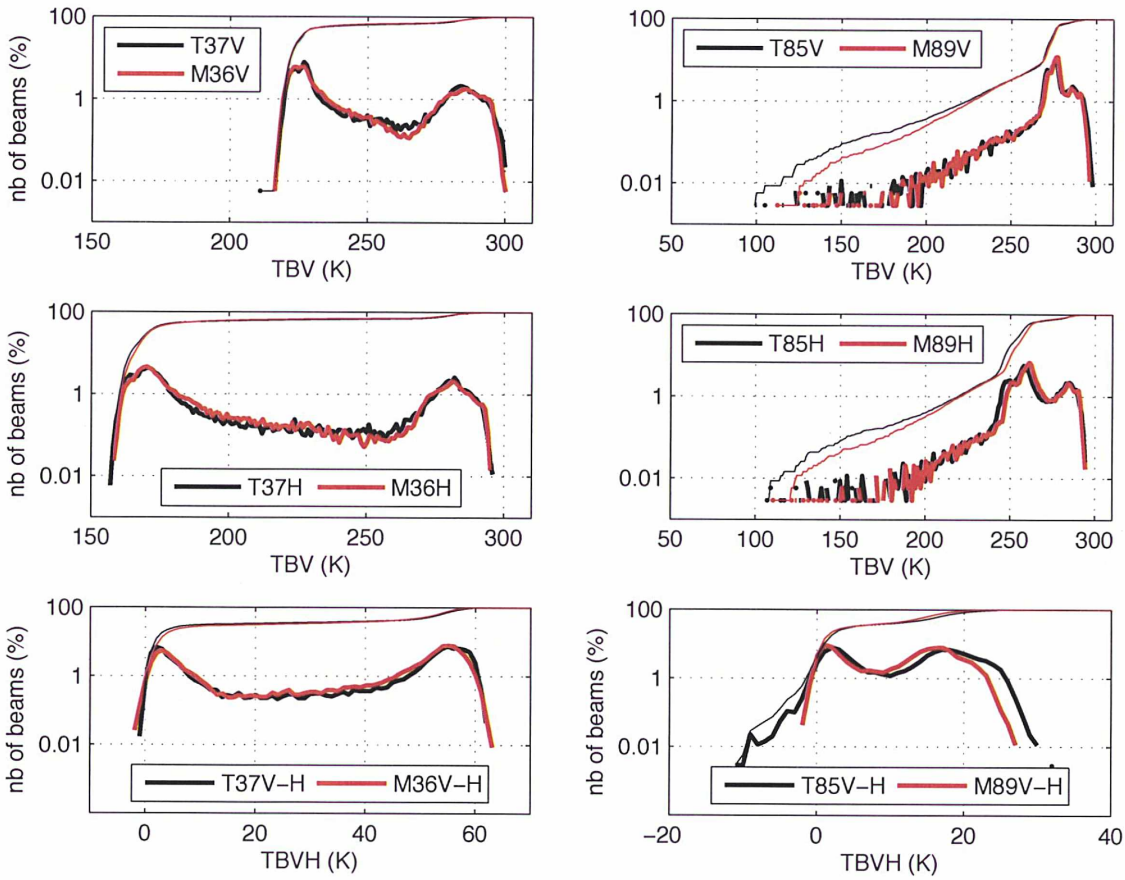

Figure A.3 - Histograms (in solid lines) and cumulative distributions (in thin lines) of the brightness temperatures mapped in Figures 1 and A.1 for common radiometric bands. Only beams located within the common area defined by the intersections of the overpasses of the two swaths were used to produce the plot. T and M stand for TMI and MADRAS respectively.